Imperial College London

Developing a 3D blood vessel-on-a-chip microfluidic *in vitro* model to study thrombosis in a controlled microenvironment

Josefin Jansson-Edqvist

Primary supervisor: Prof. Anna Randi
Co-supervisor: Dr. Joseph van Batenburg-Sherwood

National Heart and Lung Institute (NHLI)
Vascular Science section
and
Department of Bioengineering

Thesis submitted to Imperial College London for the degree of Doctor of Philosophy (PhD)

Abstract

Endothelial cells (EC) experience a heterogeneous microenvironment *in vivo*, which regulates EC phenotype and function. The three main groups of microenvironmental stimuli are: extracellular matrix (ECM), shear stress and crosstalk with tissue-specific cells. *In vitro* ECs are commonly studied as 2D monolayers on plastic, which cannot mimic this complex microenvironment, limiting the potential for tissue-specific disease modelling. *In vivo* models can capture all these microenvironmental parameters but cannot be easily manipulated; furthermore, there are pathophysiological differences between animals and humans. Significant progress has been made in the field of microfluidics to develop physiologically relevant *in vitro* models that can incorporate the endothelial microenvironment to allow disease modelling with human cells. We have developed a 3D blood vessel-on-a-chip microfluidic platform for studying ECs in health and disease, which allows independent control of ECM, shear stress and co-culture with tissue-specific cells. The custom-designed platform comprises a microfluidic device and 3D printed perfusion unit and supports both molecular and functional assays. A cylindrical vessel was created inside the microfluidic device by polymerising collagen around a needle and five chips could be cultured in parallel by attachment to the perfusion unit, which supports real-time imaging. Vessel formation was validated by immunofluorescence and by quantifying permeability. The blood vessel-on-a-chip model was used to study coagulation in real time by perfusing whole blood through the vessel following activation with pro-inflammatory cytokines. Labelled fibrinogen and anti-platelet antibodies were used to visualise thrombus formation. We showed significant increase in platelet adhesion and fibrinogen deposition following endothelial activation, compared to controls, for two different types of ECs. Blocking experiments identified tissue factor and thrombin as determinants of thrombosis in this model. Thus, we have demonstrated that the blood vessel-on-a-chip model provides a novel platform for *in vitro* studies on the coagulation cascade and mechanisms of thrombosis.

Table of Contents

Statement of Originality 9
Copyright Declaration 10
Acknowledgements 11
Abbreviations 12
Chapter 1: Introduction 15
1.1 The Vasculature 16
1.1.1 Structure 16
1.1.2 Function 17
1.1.2.1 Transendothelial transport 17
1.1.2.2 Angiogenesis 19
1.1.2.3 Inflammation 20
1.2 The endothelial microenvironment 20
1.2.1 Tissue-specific endothelial function 21
1.2.1.1 Lung 21
1.2.1.2 Kidney 22
1.2.1.3 Liver 22
1.2.2 ECM modulation of endothelial function 24
1.2.2.1 ECM composition 24
1.2.2.2 ECM mechanical properties 24
1.2.3 Shear stress in the vasculature 25
1.2.3.1 Quantifying shear stress 27
1.3 Controlling the EC microenvironment *in vitro* 29
1.3.1 Transwell models 30
1.3.2 Parallel flow channels 32
1.3.3 Vasculogenesis models 33
1.3.4 Microchannels 33
1.3.4.1 Membrane models 34
1.3.4.2 3-channel models 35
1.3.5 Needle model 36
1.3.6 Bioprinting 37
1.4 Disease modelling of thrombosis 39
1.4.1 Pathways regulating haemostasis and thrombosis 39
1.4.1.1 Heterogeneity in thrombotic disease 39
1.4.1.2 Platelet activation and plug formation 40
1.4.1.2.1 VWF and platelet adhesion 41
1.4.1.3 The coagulation cascade 42
1.4.1.3.1 The extrinsic pathway 42
1.4.1.3.2 The intrinsic pathway 43
1.4.2 Models for studying thrombosis 45
1.4.2.1 *In vivo* models 45
1.4.2.2 *In vitro* models 46
1.5 Aims and Hypotheses 50

1.5.1 Aims 50
1.5.2 Hypotheses 51
Chapter 2: Methods 52
2.1 Introduction 53
2.2 Optimised methods 53
2.2.1 Manufacturing the microfluidic device 55
2.2.2 Creating the vessel 55
2.2.3 Cell seeding 57
2.2.3.1 HUVEC 57
2.2.3.2 ECFC 57
2.2.4 Maintaining cell viability during long-term culture 58
2.2.5 Molecular assays 58
2.2.5.1 Immunocytochemistry 60
2.2.5.2 Bulk q-PCR 60
2.3 Model development 61
2.3.1 The microfluidic device 61
2.3.1.1 Material: PDMS 61
2.3.1.2 Design of the microfluidic device 61
2.3.1.2.1 ECM chamber 63
2.3.1.2.2 Inlets 63
2.3.1.2.2.1 Vessel inlets with a narrowing diameter 64
2.3.1.2.2.2 ECM inlets 65
2.3.1.2.3 Base substrate 66
2.3.2 Creating the vessel 66
2.3.2.1 ECM 67
2.3.2.2 Vessel size 72
2.3.3 Cell seeding 72
2.3.4 Endothelial monolayer formation 76
2.3.5 The incubator environment and cell viability 83
2.3.5.1 Humidity inside the incubator 83
2.3.5.2 pH-levels in cell culture media 86
2.3.6 Maintaining vessel integrity during long-term culture 86
2.3.6.1 Syringe pump 88
2.3.6.2 Hydrostatic pressure 91
2.3.6.2.1 Materials 91
2.3.6.2.2 Design 92
2.3.6.3 Gas-pressure controlled perfusion system 98
2.3.6.3.1 System validation 99
2.3.6.3.2 Connecting the vessel to the system for perfusion at physiological shear stress 106
2.3.7 Molecular analysis in the blood vessel-on-a-chip model 109
2.3.7.1 Immunocytochemistry 109
2.3.7.2 Single-cell qPCR 110
Chapter 3: Application 1 – Permeability 113
3.1 Introduction 114

3.1.1 Aims 115
3.2 Model development 115
3.2.1 Experimental setup 115
3.2.2 Capturing data 115
3.2.3 Data analysis 116
3.2.3.1 Pre-processing in Fiji (ImageJ) 116
3.2.3.2 Locate the vessel boundaries 116
3.2.3.3 Account for radial diffusion in the collagen 119
3.2.3.4 Define the image interval and measure the dextran concentration inside the vessel 124
3.2.3.4.1 Average intensity inside the vessel 124
3.2.3.4.2 Total number of data points in the collagen 126
3.2.3.5 Calculate permeability 126
3.2.3.5.1 Method 1 127
3.2.3.5.2 Method 2 129
3.2.3.5.3 Method 3 133
3.3 Model Validation 137
3.4 Discussion 137
Chapter 4: Application 2 – Disease modelling of thrombosis 140
4.1 Introduction 141
4.1.1 Endothelial activation 142
4.1.2 Blood collection and handling 143
4.1.2.1 Blood sample variability 143
4.1.2.2 Anticoagulant used for blood collection 144
4.1.2.3 Artificial platelet activation from phlebotomy 144
4.2 Model development of the 3D thrombosis assay 144
4.2.1 Fluorescent labelling of blood components 144
4.2.1.1 Fluorescent labelling of platelets 145
4.2.1.2. Fluorescent labelling of fibrinogen 145
4.2.2 Blood recalcification 145
4.2.3 Blood perfusion during real-time imaging 147
4.2.3.1 Perfusion setup 147
4.2.3.2 Acquiring data 149
4.2.4 Data analysis 152
4.2.4.1 Pre-processing in Fiji 152
4.2.4.2 Pre-processing in Matlab 154
4.2.4.3 Data analysis in Matlab 156
4.3 Model validation 156
4.3.1 3D thrombosis assay using HUVEC 157
4.3.1.1 The role of TF in the 3D thrombosis assay 161
4.3.1.2 The role of thrombin in the 3D thrombosis assay 161
4.3.2 3D thrombosis assay using ECFC 165
4.3.3 Molecular profiling of EC activation 168
4.4 Discussion 171
Chapter 5: Other applications 173

5.1 Co-culture with perivascular cells 174
5.1.1 Introduction 174
5.1.1.1 The role of pericytes in coagulation 175
5.1.1.2 Aims 176
5.1.2 Model development 176
5.1.2.1 Cell seeding 176
5.1.2.2 Studying vessel formation 177
5.1.3 Discussion 177
5.2 Angiogenesis 179
5.2.1 Introduction 180
5.2.1.1 Vascular malformations in VWD 180
5.2.1.2 *In vitro* models to study angiogenesis 180
5.2.1.3 Aims 182
5.2.2 Model development 182
5.2.2.1 Perfusing a growth factor cocktail through the vessel lumen 182
5.2.2.2 Establish a growth factor gradient in the collagen 184
5.2.2.2.1 Perfusing the growth factor cocktail through the ECM inlets 184
5.2.2.2.2 Incorporate a growth factor chamber in the microfluidic device 186
5.2.2.3 Co-culture with fibroblasts mixed in the collagen 186
5.2.3 Discussion 188
Chapter 6: Discussion 190
Bibliography 194
Appendix: Chapter 2 202
Appendix: Chapter 3 204
Appendix: Chapter 4 208
Appendix: Permission Documents 214

List of Tables

Table 1.1: Estimations of shear stress, shear rate and vessel dimensions in the human vasculature 29
Table 1.2: *In vitro* models to study thrombosis 47
Table 2.1: Antibodies validated for use in the blood vessel-on-a-chip model 60
Table 2.2: Resistances for comparison to iPerfusion measurements 81
Table 2.3: Cell numbers and volumes in 2D and 3D 88
Table 2.4: Resistances in 3D printed perfusion unit 96
Table 3.1: *In vitro* permeability measurements of endothelial monolayers 114
Table 3.2: Vessel diameters recorded during image processing. 119
Table 3.3: Comparing $I_{ECM,t1}$ and I_{vessel} for vessels with different barrier function 131

List of Figures

Chapter 1

Figure 1.1: Overview of the vasculature and blood vessel structure 18
Figure 1.2: Endothelial heterogeneity in the lung, kidney and liver 23
Figure 1.3: The substrate stiffness of different materials 26
Figure 1.4: *in vitro* models to control the endothelial microenvironment 31
Figure 1.5: The coagulation cascade 44

Chapter 2

Figure 2.1: Flow chart illustrating the steps and timelines for using the blood vessel-on-a-chip model 54
Figure 2.2: Manufacturing the microfluidic device 56
Figure 2.3: Method for creating the vessel 56
Figure 2.4: Cell seeding in the vessel 59
Figure 2.5: The 3D printed perfusion unit 59
Figure 2.6: Design evolution of the microfluidic device 62
Figure 2.7: Vessel inlets with a narrowing diameter are key to avoid collagen damage 62
Figure 2.8: Coating of the ECM chamber with low concentration collagen to prevent leaking 69
Figure 2.9: Air bubbles in the collagen can cause vessel deformation 69
Figure 2.10: Air bubbles inside the vessel can cause vessel deformation 70
Figure 2.11: Creating vessels with different diameters 71
Figure 2.12: Optimisation of sequential cell seeding in the vessel 74
Figure 2.13: Variability in the number of cells seeded in the vessel 74
Figure 2.14: EC migration into the collagen 75
Figure 2.15: EC adhesion to collagen 78
Figure 2.16: Time course of static cell culture in the blood vessel-on-a-chip model 79
Figure 2.17: Different methods for sealing the ECM inlets to avoid transverse pressure gradients 80
Figure 2.18: Using iPerfusion to measure the resistance of the vessel 82
Figure 2.19: EC monolayer disruption related to the incubator environment 84
Figure 2.20: The effect of humidity on EC monolayer disruption 85
Figure 2.21: Changes in cell morphology due to increased pH 85
Figure 2.22: Supplementing the cell culture media with HEPES prevents EC monolayer disruption 87
Figure 2.23: Cell viability is not maintained in the vessel during static culture conditions 89
Figure 2.24: Schematic and lumped-parameter model for perfusion using a syringe pump 89
Figure 2.25: Schematic, lumped-parameter model and shear stress in the 3D printed perfusion unit 93
Figure 2.26: Design 1 of the 3D printed perfusion unit 95
Figure 2.27: Additional design features of Design 2 of the 3D printed perfusion unit 95
Figure 2.28: Long-term culture of ECs in the vessel using the 3D printed perfusion unit for media turnover 97
Figure 2.29: Picture of the different components of the gas-pressure controlled perfusion system 100
Figure 2.30: Schematic of the gas-pressure controlled perfusion system showing the fluidic circuit 101
Figure 2.31: Sample perfusion of four channels in parallel (without ECs) 103

Figure 2.32: Incorporation of flush cycles to remove air bubbles in the tubing during perfusion.....103
Figure 2.33: Comparison of three approaches for preventing evaporative losses during perfusion 105
Figure 2.34: Sample 60-hour perfusion without any user interference or correction.....105
Figure 2.35: ECs perfused in the vessel at 10 dynes/cm^2 - experiment 1.....108
Figure 2.36: ECs perfused in the vessel at 10 dynes/cm^2 - experiment 2.....108
Figure 2.37: Over fixation significantly reduced the junctional staining that could be detected in the vessel112
Figure 2.38: Geometrical distortion of the vessel cross-section using confocal microscopy.....112
Figure 2.39: Gene expression data from single-cell qPCR 112

Chapter 3

Figure 3.1: Fluorescent images and intensity profiles for a high and low permeability case.....117
Figure 3.2: Using the intensity profile to locate the vessel boundaries 118
Figure 3.3: Accounting for radial diffusion into the collagen in the needle model 120
Figure 3.4: Calibration curves using different microscopy gains 123
Figure 3.5: Dextran calibration curve shows relationship between intensity and concentration 123
Figure 3.6: Intensity and dextran concentration profiles in the collagen 125
Figure 3.7: The average intensity inside the vessel as it is filling with dextran solution 125
Figure 3.8: Defining the imaging interval based on positive data points in the collagen 125
Figure 3.9: Calculating permeability using Method 1 128
Figure 3.10: Schematic illustrating radial diffusion through the vessel wall 130
Figure 3.11: Linear fit of I_{ECM} for four vessels with different barrier function 130
Figure 3.12: Permeability calculated using Method 2.....132
Figure 3.13: Dependence on X when calculating permeability using Method 2.....132
Figure 3.14: Graphs showing the key terms in the permeability equation for Method 3 135
Figure 3.15: Permeability calculated using Method 3.....136
Figure 3.16: Dependence on X when calculating permeability using Method 3.....136
Figure 3.17: Permeability measurements at different days post cell seeding 138
Figure 3.18: Immunofluorescent staining following permeability measurements.....138

Chapter 4

Figure 4.1: High fibrinogen concentrations result in fluorescent signal outside the vessel 146
Figure 4.2: Different approaches for blood recalcification to avoid clotting in the tubing 146
Figure 4.3: The perfusion setup for the 3D thrombosis assay.....148
Figure 4.4: Acquiring data for the 3D thrombosis assay using confocal microscopy 148
Figure 4.5: Characteristic response in the 3D thrombosis assay 150
Figure 4.6: Coagulation response along the vessel 151
Figure 4.7: Flow diagram for data analysis of the 3D thrombosis assay.....153
Figure 4.8: Investigating the use of the brightfield channel for identifying the vessel boundaries.....153
Figure 4.9: Using the platelet channel to define the vessel boundaries 155
Figure 4.10: Defining the image interval used for data analysis.....155
Figure 4.11: Platelet adhesion and fibrinogen deposition in HUVEC vessels 158

Figure 4.12: HUVEC dynamic response of platelet adhesion and fibrinogen deposition 160
Figure 4.13: The effects of blocking TF on platelet adhesion and fibrinogen deposition 162
Figure 4.14: Immunofluorescent images showing the effect of blocking TF on coagulation 163
Figure 4.15: The effects of blocking thrombin on platelet adhesion and fibrinogen deposition 164
Figure 4.16: Immunofluorescent images showing the effects of blocking thrombin on coagulation 164
Figure 4.17: Images of ECFC cultured in the vessel, confirming the formation of a confluent monolayer 166
Figure 4.18: Characteristic response of platelet adhesion and fibrinogen deposition in ECFC vessels 167
Figure 4.19: Platelet adhesion and fibrinogen deposition in ECFC vessels 167
Figure 4.20: ECFC dynamic response of platelet adhesion and fibrinogen deposition 169
Figure 4.21: ICAM1 gene expression in HUVEC and ECFC vessels following TNF-treatment 170
Figure 4.22: Bulk qPCR results for HUVEC and ECFC vessels following TNF-treatment 170

Chapter 5

Figure 5.1: Cell adhesion of pericytes to collagen 178
Figure 5.2: Immunofluorescent images showing vessel formation during co-culture with pericytes 178
Figure 5.3: Inducing angiogenesis by perfusing a growth factor cocktail through the vessel lumen 183
Figure 5.4: Perfusing a growth factor cocktail through the ECM inlets 185
Figure 5.5: The altered design of the microfluidic device to include a growth factor chamber 187
Figure 5.6: EC sprouting from the vessel wall in response to a growth factor gradient in the collagen 187
Figure 5.7: Co-culture with fibroblasts mixed in the collagen to induce sprouting from the vessel wall 189

Statement of Originality

I, Josefin Jansson-Edqvist, confirm that the work presented in this thesis is my own work. Work performed by other researchers is acknowledged in the necessary places in the thesis and work from other sources, including data and figures published by other research groups, has been appropriately referenced.

Copyright Declaration

The copyright of this thesis rests with the author. Unless otherwise indicated, its contents are licensed under a Creative Commons Attribution-Non Commercial 4.0 International Licence (CC BY-NC). Under this licence, you may copy and redistribute the material in any medium or format. You may also create and distribute modified versions of the work. This is on the condition that: you credit the author and do not use it, or any derivative works, for a commercial purpose. When reusing or sharing this work, ensure you make the licence terms clear to others by naming the licence and linking to the licence text. Where a work has been adapted, you should indicate that the work has been changed and describe those changes. Please seek permission from the copyright holder for uses of this work that are not included in this licence or permitted under UK Copyright Law.

Acknowledgements

I would like to give a special thanks to my supervisors, Anna Randi and Joseph van Batenburg-Sherwood for their support during the PhD. Anna, I have developed so much as a student in your lab, both personally and professionally. Thank you for always taking the time to help me when I needed it and for giving me creative freedom in the lab to explore my engineering ideas. Thank you for believing in me and for challenging me in every one of our meetings to become a better scientist. Joseph, I have learnt a lot about data analysis from you and how to bridge theory and experimental results, which I will carry with me throughout my career. Thank you for the many great discussions and for helping me to significantly develop as an engineer.

I have been very fortunate to work alongside some amazing people who have contributed to making this journey very memorable. A big thank you to my favourite postdoc, Claire Peghaire. You have been such an important mentor, colleague and friend to me over these past years. Thank you for your time and patience when teaching me molecular biology and for all our great scientific discussions. Thank you to our TC neighbours in the Mason group, Charis Pericleous, Robert Maughan and Lida Kabir. I spent the majority of my PhD in TC and you guys truly made it a wonderful working environment. I will always look back fondly on all the laughter and our many late-night talks. Thank you to everyone in the PhD-bay: Viktoria Kalna, Astrid Stroobants and Samata Pandey, your friendship means a lot to me. Kelly De Coteau, Noelle Pisacano, Luke Cave and Courtney Chatterton-Bartley, thank you for creating a great office atmosphere. To past and present members of the Randi group, thank you for your help and support: Neil Dufton, Matthew Dibble, Koralia Paschalaki, Oisín King, Graeme Birdsey, Daniela Pirri, Claudio Raimondi and Gaye Saginc Giannoustas. Thank you also to Tom McKinnon, Josefin Ahnström, Isabelle Salles and Mike Laffan for your valuable input on the coagulation story.

I also want to thank my friends and colleagues in Bioengineering: Foivos Chatzidimitriou, Adele Lam and Ester Reina-Torres. A special thank you to Michael Madekurozwa for your positive attitude and willingness to help. Your support has been invaluable. Thank you also for all the great times at the theatre!

Finally, I would like to thank my family for their continuous love and encouragement. You are the people who mean the most to me: My mum Inger, thank you for being my biggest supporter in life and for making it possible for me to pursue my dreams. My twin brother Magnus, you are one of my best friends, thank you for always being there to help me when I need it.

Abbreviations

ΔP: Pressure drop

Π: Osmotic Pressure

σ: Osmotic reflection coefficient

τ: Shear stress

μ: Fluid viscosity

ρ: Fluid density

A: Surface area

Ang: Angiopoietin

ATU: Anti-thrombin unit

BM: Basement Membrane

BSA: Bovine Serum Albumin

C: Concentration

CAD: Computer Aided Design

cP: Centipose (unit)

CO_2: Carbon Dioxide

CT: Computerised Tomography

CTA: Computed Tomography Angiography

D: Diffusion coefficient (also referred to as Diffusivity)

d: Diameter

Da: Dalton (unit)

E: Young's Modulus

EC: Endothelial Cells

ECFC: Endothelial Colony Forming Cells

ECGF: Endothelial Cell Growth Factors

ECM: Extracellular matrix

EDTA: Ethylenediaminetetraacetic acid

EGM: Endothelial Cell Growth Medium

FACS: Fluorescence-activated cell sorting

FBS: Fetal Bovine serum

FGF: Fibroblast Growth Factor

g: Acceleration due to gravity

HBMVP: Human Brain Microvascular Pericytes

HGF: Hepatocyte Growth Factor

HSPG: Heparan Sulphate Proteoglycans

HUVEC: Human Umbilical Vein Endothelial Cells

ICAM1: Intercellular Adhesion Molecule 1

ID: Inner diameter

I: Fluorescent intensity

IL: Interleukin

J: Flux

KLF: Krüppel-like Factor

L: Vessel length

L_p: Hydraulic conductivity

LPS: Lipopolysaccharides

MRI: Magnetic Resonance Imaging

O_2: Oxygen

OD: Outer diameter

P: Pressure

P_s: Solute permeability

PBS: Phosphate buffered saline

PDMS: Polydimethylsiloxane

PDGFR: Platelet Derived Growth Factor

PE: Phycoerythrin

PMA: Phorbol Myristate Acetate

PTFE: Polytetrafluoroethylene

Q: Fluid flow rate

R: Resistance

RBC: Red Blood Cell

Re: Reynolds number

RFP: Red Fluorescent Protein

RI: Refractive Index

RNA: Ribonucleic acid

ROI: Region of Interest

rpm: revolutions per minute

SLA: Stereolithography

SMA: Smooth Muscle Actin

SMC: Smooth Muscle Cell

TEER: Transendothelial Electrical Resistance

TF: Tissue Factor

TFPI: Tissue Factor Pathway Inhibitor

TGF: Transforming Growth Factor

TM: Thrombomodulin

TNF: Tumor Necrosis Factor

TRITC: Tetramethylrhodamine

u: Fluid velocity

VCAM1: Vascular Cell Adhesion Molecule 1

VEGF: Vascular Endothelial Growth Factor

VWD: Von Willebrand Disease

VWF: Von Willebrand Factor

Chapter 1: Introduction

1.1 The Vasculature

1.1.1 Structure

The vasculature is a closed network of blood vessels, circulating blood from the heart throughout the body to deliver oxygen and nutrients and remove waste products (produced from cell metabolism) from tissues as well as transporting cells and molecules between different tissues. Endothelial cells (ECs) line the inside of all blood vessels as a monolayer, which is in direct contact with circulating blood on the apical side and with the basement membrane (BM) on the basolateral side. The basement membrane comprises ECM proteins, including laminin and collagens and composition varies throughout the vasculature. There are broadly five categories of blood vessels: arteries, veins, arterioles, venules and capillaries (Figure 1.1 (A)), which are distinguished based on location, function and structure. Arterioles, venules and capillaries are collectively considered the microvasculature, which is where the majority of communication and exchange with surrounding tissue occurs (Potente and Mäkinen, 2017).

The circulation of blood through the vasculature starts in the aorta, which is the largest artery in the body (vessel diameter ~30 mm) and connects directly to the left ventricle in the heart. It also experiences the largest pressure drops within the vasculature between the heart relaxing and ejecting blood to deliver oxygenated blood into the vasculature with a pulsatile motion. Arteries have a thick vessel wall surrounding the basement membrane, comprising dense continuous layers of elastic tissue and smooth muscle cells (SMCs) (Figure 1.1 (C)), which allow the vessels to constrict and dilate to regulate the distribution of blood flow (also referred to as vascular tone). As the distance from the heart increases, arteries reach different organs to supply with oxygenated blood and branch into arterioles in a hierarchical fashion, with decreasing vessel diameters and with vessel walls comprising a thinner layer of elastic tissue and fewer SMCs. The arterioles connect to capillaries (vessel diameter <20 μm), which have a vessel wall comprising solely endothelial cells and basement membrane with a sparse coverage of pericytes that wrap around the endothelial cells to provide vessel stability and regulate the exchange with surrounding tissue (Potente and Mäkinen, 2017). Capillary beds are intricate vascular networks. Even though they hold only a small volume of the total circulating blood (estimated at ~10%) due to their small diameter, they represent more than 95% of all endothelial cells in the body and 95% of the total surface area for blood-EC exchange within in the vasculature (Rafii et al., 2016). Consequently, the exchange of oxygen, nutrients and waste products between blood and tissue primarily takes place in the capillary beds. Since oxygen is required for cell metabolic processes, and thereby also for cell viability, vascularisation within tissues is essential for maintaining homeostasis, resulting in individual

capillaries being located with a maximum distance of ~100-200 μm between each other to overcome the oxygen diffusion limit (Krogh, 1922). Following the exchange of fluids and solutes between the blood and the surrounding tissue, deoxygenated blood with waste products is collected from the capillary networks by the venules, which eventually connect to veins in a hierarchical fashion as they leave specific tissues, similar to the branching in the arterial side of the vascular tree. Compared to arteries, veins experience significantly lower pressure drops and therefore have a thinner layer of elastic tissue with a sparser coverage of SMCs comprising the vessel wall. Due to this lower pressure as well as having to perfuse blood against the force of gravity, veins are equipped with valves to prevent the blood from flowing backwards when transported towards the heart (Figure 1.1 (B)). Ultimately, the blood is returned to the heart from the veins through the vena cava and transported to the lungs via the pulmonary artery. In the lungs, carbon dioxide is released and blood is reoxygenated through breathing before returning to the left ventricle in the heart where it is recirculated into the vasculature through the aorta.

1.1.2 Function

As mentioned above, the vasculature is responsible for supplying blood to tissues, referred to as transendothelial transport. However, endothelial cells also have other important functions in the body including angiogenesis, haemostasis and regulation of inflammatory processes. Haemostasis is the coordinated response of the endothelium with blood components in order to stop bleeding following vascular injury (described in detail in later sections).

1.1.2.1 Transendothelial transport

Transendothelial transport refers to the fluid and solute exchange between blood inside capillaries and surrounding tissue. The endothelium functions as a semipermeable membrane where this exchange occurs through endothelial junctions between adjacent cells. Transendothelial transport can be characterised in terms of hydraulic conductivity (L_p) and solute permeability (P_s) for fluid and solute transport, respectively. Hydraulic conductivity describes the flow rate per unit area of the vessel wall at which fluid moves across the endothelium for a given hydrostatic pressure and osmotic pressure gradients, according to the revised Starling principle (Equation 1.1).

$$\frac{J_v}{A} = L_p\left[(P_c - P_i) - \sigma\left(\Pi_p - \Pi_g\right)\right] \quad (1.1)$$

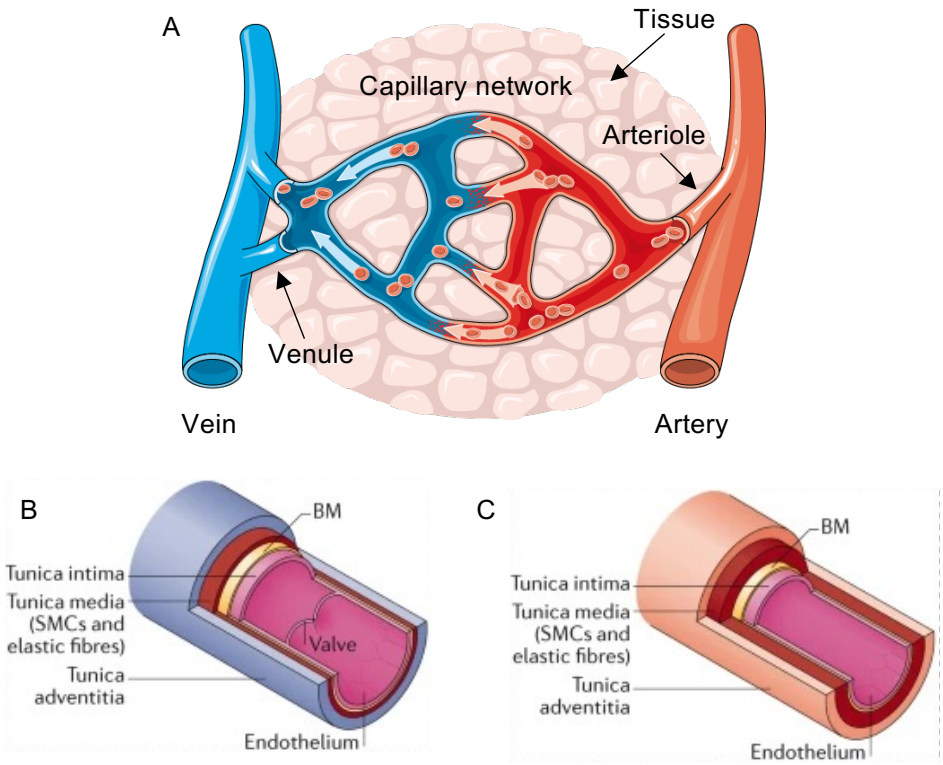


Figure 1.1: Overview of the vasculature and blood vessel structure. A: Schematic of a vascular bed, showing the five broad categories of blood vessels, arteries, veins, arterioles, venules and capillaries, and how they interact to perfuse blood through a tissue (Schematic obtained from smart.servier.com). B: Veins have a thin layer of elastic tissue and sparse coverage of SMCs comprising the vessel wall but are equipped with valves to prevent the blood from flowing backwards when transported towards the heart. C: Arteries have a thick vessel wall surrounding the basement membrane, comprising dense continuous layers of connective and elastic tissue and SMCs. Figures B-C were adapted by permission from Springer Nature Customer Service Centre GmbH: Springer Nature, Nature Reviews Molecular Cell Biology (Vascular heterogeneity and specialization in development and disease, Potente and Mäkinen), Copyright (2017).

where J_v is the volume filtration rate, A is the surface area of the endothelium through which fluid transport occurs, P_c is the capillary blood pressure (inside the vessel) and P_i is the hydrostatic pressure of the interstitial fluid (outside the vessel). Π_p and Π_g are the osmotic pressures of blood and fluid in the subglycocalyx space, respectively, so that (P_c-P_i) describes the hydrostatic pressure difference across the vessel wall and $(\Pi_p - \Pi_g)$ describes the concentration gradient of plasma proteins across the glycocalyx barrier. σ is the osmotic reflection coefficient, which describes the resistance to osmotic flow for a given solute.

Solute permeability, measured in units of distance over time, refers to the rate of molecular diffusion from the blood inside a capillary into the surrounding tissue, which is driven by the concentration difference across the capillary wall (ΔC), according to Equation 1.2. Fick's law of diffusion (Equation 1.3) can be used to describe the solute flux through a membrane with a specific diffusion coefficient (D). J_s is the solute flux, which is the amount of solute diffusing through the membrane per unit area and time, A is the surface area through which diffusion occurs and x is the membrane thickness. D (also referred to as diffusivity) describes the capability of a given molecule to diffuse through the membrane.

$$J_s = P_s A \Delta C \quad (1.2)$$

$$J_s = D \frac{\Delta C}{\Delta x} \quad (1.3)$$

1.1.2.2 Angiogenesis

Angiogenesis is the formation of new blood vessels branching from the pre-existing vasculature. This process occurs during development but also in adult tissue in response to nutrient deprivation, hypoxia (causing ischemia) or during wound healing following tissue injury, in order to restore tissue homeostasis. This process relies on quiescent endothelial cells switching into angiogenic and proliferative states in response to pro-inflammatory stimuli such as VEGF (Vascular Endothelial Growth Factor) or FGF (Fibroblast Growth Factor) to induce endothelial sprouting towards the growth factor source (Draoui et al., 2017). It requires coordination between tip cells and stalk cells, which are endothelial subtypes residing in the quiescent vasculature, where tip cells initiate the sprouting and stalk cells follow to extend the vessel to the required length. When the sprouting tip cells reach a vessel in its proximity, they connect to form a close network (referred to as anastomosis) and lumen formation is initiated to support blood flow in the new vessel.

1.1.2.3 Inflammation

Inflammation involves an immune response, where activated leukocytes (also referred to as white blood cells) infiltrate tissue from the blood stream, where they circulate in a quiescent state under healthy conditions, to destroy harmful substances (including bacteria and virus). Inflammation can be either acute (following infection) or chronic (due to prolonged exposure to inflammatory stimulus). The combination of leukocytes (including neutrophils, monocytes and T cells) involved in the process varies depending on the inflammatory stimuli. In a quiescent state the endothelium does not interact with circulating leukocytes; however, endothelial activation modulates transcription of adhesion molecules including E-selectin, VCAM1 (vascular cell-adhesion molecule 1) and ICAM1 (intercellular adhesion molecule 1), which promotes local recruitment and activation of leukocytes (Pober and Sessa, 2007). Endothelial cells are activated in response to cues from their local microenvironment, where receptors on the EC surface bind to pro-inflammatory mediators, including cytokines TNF-α (Tumour Necrosis Factor) and IL-1 (Interleukin-1). This alters EC phenotype, allowing leukocytes and plasma proteins to pass through the vessel wall by modulating the properties of adherens and tight junctions.

1.2 The endothelial microenvironment

In the microvasculature endothelial cells are affected by the microenvironment they experience, resulting in tissue-specific phenotype and function. These environmental signals include mechanical stimuli (primarily flow-induced shear stress), extracellular matrix (ECM) mechanical properties and composition, intercellular communication with surrounding cells as well as metabolism and organotypic growth factors (Potente and Mäkinen, 2017). The majority of cells in the body are in contact with the microvasculature (there are only a few avascular tissues, including cartilage and the transparent structures of the eye such as the lens). Consequently, a dysfunctional endothelium can contribute to a wide range of disease, including those that are currently the leading causes of death globally, such as ischemic heart disease, stroke, cancer and diabetes (WHO, 2019). Understanding specialised endothelial phenotype and how endothelial cells are affected by their microenvironment in health and disease is therefore important both as preventative measures as well as for finding effective treatments for these conditions, for example understanding why chronic inflammation, cancer metastasis and atherosclerotic plaque formation is more prone to certain vascular beds. Understanding of these specialised phenotypes through molecular signatures has progressed significantly in recent years through transcriptomic analysis techniques, including RNA sequencing, and mouse models with fluorescently tagged endothelial cells, where endothelial cells harvested from different organs show different transcriptomic profiles. Furthermore, vascular bed-specific arterial and venous phenotypes have also been identified, which

are associated with enrichment and repression of genes from specific transcription factor families, including SOXF, where deletion of the SOX17 gene in knockout-mice prevented the formation of arteries in these models (Potente and Mäkinen, 2017). Even though there are many known differences between human and mouse physiology, these findings highlight the importance of considering endothelial heterogeneity when predicting treatment efficiency, as genes within certain transcription factor families are up or down regulated depending on location within the vasculature.

1.2.1 Tissue-specific endothelial function

In the microvasculature, endothelial cells communicate with tissue-specific cells by secreting angiocrine factors, including growth factors, chemokines and ECM components and by expressing signalling molecules on the cell surface, which all contribute to the cells adapting specialised phenotypes and functions in order to maintain tissue homeostasis (Rafii et al., 2016). Using barrier function as an example, capillaries in the lung, kidney and liver are all specialised in different ways to allow efficient exchange with surrounding tissue. These vessels therefore have higher permeability compared to the capillaries in the brain, which have specialised tight and adherens junctions to protect neurons, resulting in a very restricted exchange with surrounding tissue to prevent foreign molecules, pathogens and immune cells to pass through the endothelium. Figure 1.2 (A-C) shows staining of the vasculature in mouse tissue in the lung, kidney and liver, where vessel morphology, structure and function of these capillary beds are highly specialised to support specific tissue function. These tissues are used as examples below to demonstrate the importance of tissue-specific endothelial function.

1.2.1.1 Lung

The lung alveoli have dense capillary networks. During breathing oxygen diffuses from the alveoli into the blood stream and carbon dioxide diffuses from the blood into the alveoli, where it is removed from the body. Alveolar capillaries have a continuous endothelium and basement membrane, where tight and adherens junctions regulate transendothelial transport (Figure 1.2 (D)) but a specialised thin barrier to allow efficient gas exchange through the vessel wall. Furthermore, since these blood vessels are in contact with air from the external environment, they have adapted a quick immune response to fight foreign substances. This has been confirmed with transcriptomic analysis in mouse tissue, where the lung endothelium showed upregulation of genes involved in immune function, such as leukocyte adhesion and migration (Jambusaria et al., 2020). The same study also showed that lung endothelial cells expressed genes typically found in lung epithelium, further confirming that the presence of tissue-specific cells influence endothelial phenotype.

1.2.1.2 Kidney

The kidney is responsible for removing waste products, which leave the body in the form of urine, while maintaining a healthy balance of water and electrolyte concentration, which influences the function of tissues that rely on electrical impulses, such as nerves and muscles. To achieve this, the capillary networks in the kidney, referred to as glomeruli, play an essential role in filtering the blood. These vessels have a fenestrated endothelium with well-defined pores to allow larger molecules and ions to pass through the vessel wall, while preventing removal of blood components such as red blood cells from the circulation (Figure 1.2 (E)). To facilitate efficient filtering this exchange is pressure-driven and therefore does not solely rely on diffusion.

1.2.1.3 Liver

The blood passes through the liver after leaving the stomach and intestines. The liver provides a range of functions, including producing nutrients for other organs and plasma proteins involved in clotting, removing bacteria, drugs and other poisonous substances from the blood stream as well as metabolising drugs to facilitate uptake by the rest of the body. Performing these vital body functions relies on crosstalk between liver cells (hepatocytes) and liver sinusoidal capillary networks, which have both a fenestrated endothelium as well as enhanced intercellular gaps and a discontinued plasma membrane (Figure 1.2 (F)). This vessel structure allows the exchange of a wide range of molecules, including macromolecules such as larger plasma proteins, which under healthy conditions cannot pass through the vessel wall elsewhere in the vasculature. Furthermore, through angiocrine signals liver sinusoidal endothelial cells regulate liver regeneration under healthy conditions and liver fibrosis in a pathological state. The liver is one of the organs in the body which has notable regenerative potential. Following surgical procedures such as partial hepatectomy, when a significant proportion of the total liver mass is removed due to disease such as cancer, the liver has the capacity to regenerate to its original size. Here, angiocrine signals from liver sinusoidal endothelial cells regulate hepatocyte expansion by secreting growth factors including hepatocyte growth factor (HGF) (Rafii et al., 2016). Mouse studies have shown that angiocrine signalling through the Angiopoietin-2-Tie2 pathways plays an important role in liver regeneration, to facilitate VEGF dependent angiogenesis and growth of the liver, as disrupting this signalling pathway resulted in delayed liver regeneration in adult mice following surgery. On the contrary, in response to chronic injury to the liver, liver sinusoidal endothelial cells instead secrete Transforming Growth Factor beta (TGF-β), which leads to the formation of scar tissue.

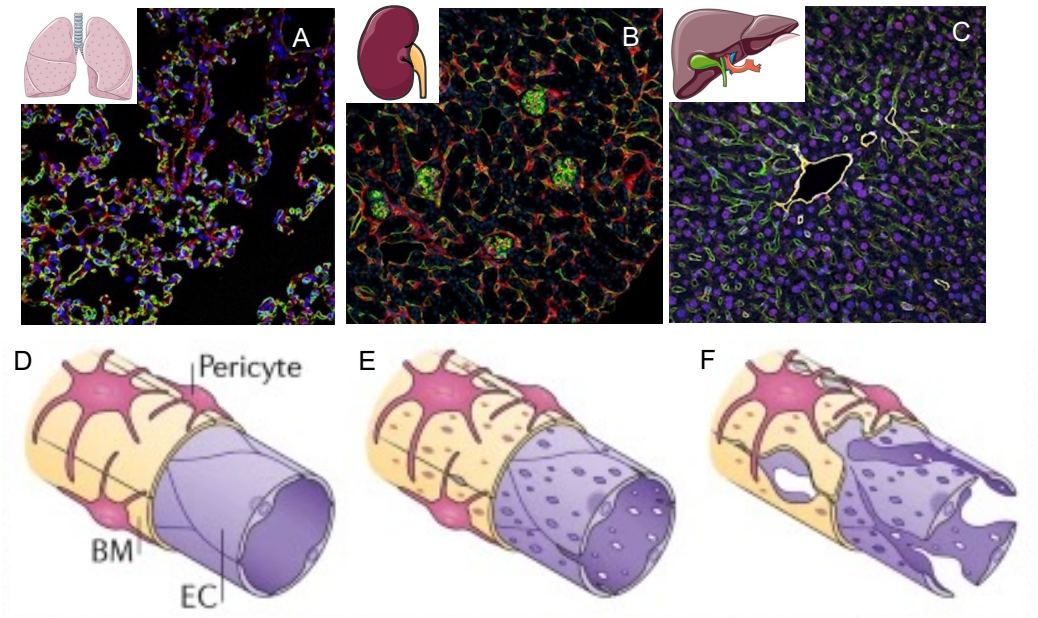


Figure 1.2: Endothelial heterogeneity in the lung, kidney and liver. A-C: Immunofluorescent staining of the vasculature in mouse tissue sections from the lung (A), kidney (B) and liver (C) (images provided by Dr. Neil Dufton). D: Capillaries in the lung have a continuous endothelium and basement membrane. E: Capillaries in the kidney (glomeruli) are fenestrated with pores through the endothelium to allow transport of larger molecules to move across the vessel wall when filtering the blood. F: Liver sinusoidal capillaries are both fenestrated and have a discontinued endothelium and plasma membrane to facilitate the transport of a range of solutes, including large plasma proteins. Figures D-F were adapted by permission from Springer Nature Customer Service Centre GmbH: Springer Nature, Nature Reviews Molecular Cell Biology (Vascular heterogeneity and specialization in development and disease, Potente and Mäkinen), Copyright (2017).

1.2.2 ECM modulation of endothelial function

The ECM is a scaffold that provides structural support for endothelial cells, which anchor to different ECM molecules through adhesive interactions with receptors on the cell surface, referred to as integrins (Davis and Senger, 2005). The ECM provides endothelial cells with mechanical and biochemical cues, based on ECM mechanical properties and tissue-specific composition, as different integrins are required for adhesion to different ECM proteins (Hussey et al., 2018). Cells are involved in rebuilding and remodelling the ECM, which occurs continuously in order to maintain tissue homeostasis but also during development and in response to injury. Cells modify their secreted ECM molecules in response to environmental stimuli including mechanical forces, oxygen gradients and nutrient concentrations (Hussey et al., 2018). These changes in the ECM are sensed by cell receptors through the binding to integrins, resulting in the activation of intracellular signalling cascades and regulation of gene expression (Nicolas et al., 2020). Dysfunction related to the secretion of specific ECM molecules is associated with disease, including fibrosis, which is the result of excessive ECM deposition.

1.2.2.1 ECM composition

In the microvasculature, endothelial cells are in contact with ECM molecules in the basement membrane, which also contacts the interstitial matrix in surrounding tissue. The basement membrane comprises mainly a network of collagens, laminins and heparan sulphate proteoglycans (HSPG) and the interstitial matrix comprises collagens and different glycoproteins, including fibronectin (Livanainen et al., 2003). Collagen is the most abundant category of proteins in the ECM, comprising ~30% of the ECM (Nicolas et al., 2020), which is why it is widely used in *in vitro* models. More than 28 different collagens have been identified (Hussey et al., 2018) and typically several different collagens can bind to the same integrins on the cell surface (Zeltz and Gullberg, 2016).

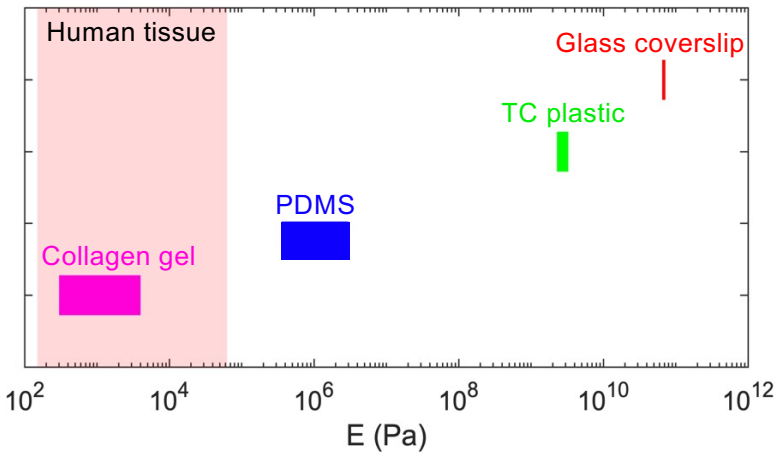
1.2.2.2 ECM mechanical properties

The stiffness of the substrate to which endothelial cells adhere is the most studied mechanical property of the ECM and has been shown to affect cell morphology (Yeung et al., 2005), migration (Levental et al., 2007), proliferation and barrier function. Furthermore, stiffness-sensitive differentially expressed genes including TGF-β2 have been identified in endothelial cells *in vitro* using RNA-sequencing, (Bastounis et al., 2019). Subendothelial stiffening occurs as a consequence of ageing and has been linked to age-related cardiovascular disease, including atherosclerosis and hypertension (Bastounis et al., 2019). ECM matrix

stiffening has also been observed as a consequence of tumour progression (LaValley et al., 2017). Since ECM stiffness has been found to play a role in disease, it is an important parameter to consider for mimicking the endothelial microenvironment *in vitro*. However, conventional tissue culture substrates including glass and plastic are several orders of magnitude stiffer compared to human tissue. Even though these substrates are commonly coated with ECM molecules to promote cell adhesion, ECs sense the presence of a stiff substrate from a 50-100 μm distance (Bogorad et al., 2017), which is not achieved by adsorbed matrix molecules on a 2D surface. Figure 1.3 shows the stiffness (measured by Young's modulus, E) of common 2D tissue culture substrates (glass, tissue culture plastic and PDMS) and 3D collagen gel used in *in vitro* models compared to the stiffness of vascularised human tissue. A glass coverslip has a Young's modulus of E~69GPa, which is at least 10^6 times stiffer than human tissue, where E~0.15-63kPa. Tissue culture plastic and PDMS have lower Young's modulus compared to glass, E~2-3GPa and E~0.3-1.4MPa respectively; however, only the 3D collagen gel falls within the range of vascularised human tissue with E~0.3-4kPa (depending on collagen concentration). Here collagen gel was used as an example of a 3D *in vitro* matrix; however, there might be other physiologically relevant alternatives that also fall within this range.

1.2.3 Shear stress in the vasculature

Endothelial cells are highly mechanosensitive and respond to mechanical stimuli in their environment, including blood flow-induced shear stress and stretch due to transmural pressure gradients (which will not be discussed here). Since all endothelial cells are in direct contact with circulating blood, they are affected by shear stress, which is the frictional force per unit area applied to the vessel wall as blood moves in the direction of flow tangential to the resting endothelium (Ballermann et al., 1998). How endothelial cells response to shear stress has been widely investigated *in vitro*, both in terms of magnitude and flow characteristics. Shear stress has been shown to regulate endothelial phenotype and function (Davies, 2009), including cell morphology, proliferation, quiescence and permeability. DeStefano et al. (2017) showed that perfusion with laminar shear stress resulted in cell elongation and alignment in the direction of flow, where the time required for cell alignment was correlated to shear stress magnitude. Proliferation has been shown to be dependent on flow characteristics, with results indicating increased proliferation in response to perfusion with disturbed flow, compared to static conditions, and inhibition of proliferation in response to laminar shear stress (Chiu et al., 2011). Proliferation rate can further be related to endothelial quiescence, where Wang et al. (2020) showed that prolonged (4 days) endothelial stimulation with laminar shear stress (at 10 dyne/cm^2) was required to induce quiescence in HUVEC, compared to static controls, which was validated in terms of increased



Substrate	Young's modulus (E)
Vascularised human tissue (including brain, pancreas, skin, spleen, muscle and tendon)	0.15-63 kPa [1]
Collagen gel (3-9 mg/ml)	0.3-4 kPa [2]
PDMS	0.36-1.4 MPa [3-4]
TC plastic (polystyrene)	2.28-3.28 GPa [5]
Glass coverslip	69 GPa [5]

Figure 1.3: The substrate stiffness of different materials. Graph showing substrate stiffness in terms of Young's modulus (E) for materials commonly used for tissue culture application compared to vascularised human tissue. The values shown in the graph are supported by the table. References: [1]: Liu et al., 2015, [2]: Raub et al., 2010, [3]: Liu et al., 2009, [4]: Johnston et al., 2014, [5]: Fundamentals of materials science and engineering, Callister.

glycocalyx thickness. Lastly, solute permeability has been shown to decrease with increasing shear stress, evaluated by Price et al. (2010) for 0-35 dyne/cm^2 with 70 kDa BSA and 10 kDa dextran. On a molecular level, shear stress has been found to modulate endothelial gene expression for a large range of genes (Braddock et al., 1998), and thereby directly regulating endothelial phenotype and function. Peghaire et al. (2019) showed a magnitude-dependent upregulation of shear stress sensitive genes KLF2 (Kruppel Like Factor 2) and TM (Thrombomodulin) in response to 24h perfusion at 5 dyne/cm^2 and 20 dyne/cm^2 compared to static controls. Wang et al. (2020) further studied KLF2 gene expression in response to bidirectional flow of 10 dyne/cm^2 but did not find a difference in gene expression compared to unidirectional laminar shear stress of 10 dyne/cm^2, indicating that KLF2 gene expression is primarily regulated by shear stress magnitude rather than flow characteristics.

1.2.3.1 Quantifying shear stress

The wall shear stress (τ) in a blood vessel can be calculated from Equation 1.4, according to the definition of dynamic viscosity, where μ is the fluid viscosity and du/dr describes how the fluid velocity changes across the vessel diameter, which can be obtained by knowing the velocity profile. $\dot{\gamma}$ is the shear rate, which describes the rate at which adjacent layers of fluid move relative to each other.

$$\tau = \mu\dot{\gamma} = \mu\frac{du}{dr} \tag{1.4}$$

Blood is a non-Newtonian and shear-thinning fluid, resulting in a shear-dependent viscosity that decreases with increasing shear stress (Papaioannou et al., 2005). Blood viscosity also depends on the blood composition and specifically on haematocrit, which is the volume ratio of red blood cells (RBCs) to total volume of blood (Lipowsky et al., 1980). Furthermore, red blood cells experience a vessel diameter-dependent behaviour when perfused through the vasculature, which alters the velocity profile. In capillaries where the vessel diameter is of comparable scale to the RBC diameter, single RBCs move through the vessels in series. However, in larger vessels (10-300 μm diameter) RBCs migrate away from the vessel wall (Sebastian et al., 2018).

These combined effects of shear-dependent viscosity and vessel diameter-dependent velocity profiles makes it difficult to accurately quantify shear stress for perfusion with blood. Therefore, shear rate ($\dot{\gamma}$) is commonly used when studying blood properties and blood flow *in vivo*. Shear rate can be quantified *in vivo* using imaging techniques such as Magnetic Resonance Imaging (MRI) or Doppler echocardiography (Papaioannou et al.,

2005) to measure the fluid velocity from particle movement inside a blood vessel and map the velocity profile. For studies *in vitro*; however, endothelial cells are commonly perfused with cell culture media rather than blood, which is considered an incompressible and Newtonian fluid. In this case shear stress can be derived from Poiseuille's law in response to a defined pressure drop (∆P) and average perfusion flow rate (Q), according to Equations 1.5-1.6, assuming the following conditions hold true

i) Uniform vessel with cylindrical cross-section (diameter d and length L)

ii) Perfusion with an incompressible and Newtonian fluid with viscosity μ

iii) Steady, laminar and fully developed fluid flow through the vessel

iv) Zero velocity at the vessel wall (no slip condition)

$$\tau = \frac{d\Delta P}{4L} \quad (1.5)$$

$$\Delta P = \frac{128\mu LQ}{\pi d^4} \quad (1.6)$$

In vitro perfusion models commonly use rectangular channels, rather than cylindrical vessels, which can be accounted for when calculating shear stress using Poiseuille's law. However, for *in vitro* studies where ECs are perfused with non-Newtonian fluids, including blood, using Poiseuille's law will not give an accurate quantification of shear stress. As an example, in blood vessels with high shear rates (>300 s^{-1}) blood viscosity is ~3.5 centipoise (cP), whereas blood viscosity is higher in vessels with lower shear rates (up to ~10 cP). Considering that water, as a Newtonian fluid, has a viscosity of 1 cP, not accounting for this during perfusion with blood would result in a significant (~4-10 times) underestimation of the actual shear stress experienced by endothelial cells. Understanding how endothelial cells respond to shear stress is important for understanding disease. Since shear stress depends on characteristics of the vessel as well as of the blood, which both vary throughout the vasculature, endothelial cells experience a wide range of shear stress depending on where in the vasculature they are located (Table 1.1).

Vessel	Shear stress (dyne/cm^2)	Shear rate (s^{-1})	Diameter (mm)	Wall thickness (mm)
Aorta	7-12	150-250	25-33	2
Arteries	10-48	300-1400	0.4-5	1
Arterioles	53	1600	0.1-0.3	0.02
Large Veins	1-6	125	5	0.5
Venules	10-16	400	0.02	0.002
Capillaries	44	1300	0.005-0.01	0.001

Table 1.1: Estimations of shear stress, shear rate and vessel dimensions in the human vasculature. Data adapted from Papaioannou et al. (2005) and Sakariassen et al. (2015).

Furthermore, changes in vessel geometry, including branch points, curvatures and bifurcations are regions with altered flow profiles and typically with disturbed flow, which are prone to atherosclerosis and promotes inflammatory activation, which can lead to thrombosis (Chiu et al., 2011). Blood composition, including haematocrit, can also be affected with age or disease, which can alter the shear stress that ECs sense and respond to.

1.3 Controlling the EC microenvironment *in vitro*

Conventional tissue culture techniques study endothelial cells in 2D as sheet monolayers on plastic substrates, which cannot capture any of the microenvironmental stimuli described above, apart from the response to growth factors, which can be delivered through cell culture media. Consequently, endothelial heterogeneity cannot be studied *in vitro* using these models. Therefore, the field is moving towards using more complex (and typically custom-made) *in vitro* models that can capture one or multiple of these features to bridge the gap between *in vivo* and *in vitro* models. The six main categories of *in vitro* models, which are capable of controlling the endothelial microenvironment in terms of ECM, shear stress or co-culture with tissue-specific cells are shown in Figure 1.4 and described below. However, it is important to notice that new models or modified versions of the models within these categories are constantly being proposed to get closer to modelling tissues under physiological or pathological conditions.

1. Transwell models
2. Parallel flow channels
3. Vasculogenesis models
4. Microchannel models
5. Needle model
6. Bioprinting

The capability of these *in vitro* models to control the endothelial microenvironment in terms of ECM, shear stress and co-culture with tissue-specific cells was defined as follows

i) ECM: endothelial cells do not sense the stiffness of the underlying non-physiological substrate, requiring a model which incorporates a 3D ECM gel with a thickness of >50-100 μm
ii) Shear stress: the shear stress that endothelial cells experience in the model in response to perfusion can be well characterised, requiring a pre-defined vessel geometry
iii) Co-culture: endothelial cells are cultured together with one or multiple other cell types in the same model but not necessarily in direct contact with each other

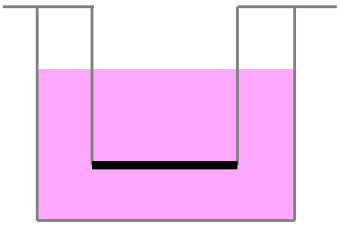
1.3.1 Transwell models

In a transwell model, a commercially available transwell insert comprising a membrane with a specific pore size is placed in a tissue culture well plate (different size inserts are available for compatibility with different size well plates). This separates each well into an upper and lower compartment by the porous membrane, resulting in three plastic surfaces where cells can be seeded (both sides of the membrane and on the surface of the well plate) and consequently the strength of this model is the possibility of culturing three different cell types in the same model. Furthermore, since it uses a tissue culture plate format, another advantage is the high throughput and easy to use characteristics of this model. However, co-culture in this setting is dependent on cell signalling via secreted soluble factors, where the cell response to specific soluble factors is concertation dependent. Due to the relatively large volumes of cell culture media required to cover cells in both compartments, a limitation of this model is that these concentrations might be significantly lower compared to what is expected *in vivo*.

Stone et al. (2019) used the transwell system to develop a model of the blood-brain-barrier comprising four different cell types: brain microvascular endothelial cells cultured in the top compartment, a mix of pericytes and astrocytes cultured on the other side of the membrane and neurons cultured on the base of the well plate. The study used oxygen-glucose deprivation to mimic the effects of ischaemic stroke and measured TEER (transendothelial electrical resistance) to quantify changes in barrier function in response to this event. Results showed significantly different responses comparing model setups with and without neurons, which highlights the value of physiologically relevant *in vitro* models in the field of drug discovery, to be able to predict drug efficacy.

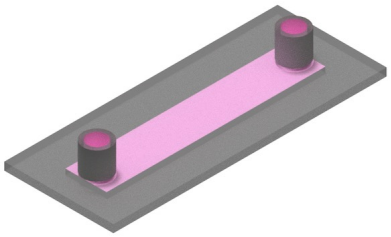
Transwell models

ECM: No
Shear stress: No
Co-culture: Yes



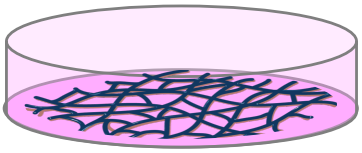
Parallel flow channels

ECM: No
Shear stress: Yes
Co-culture: No



Vasculogenesis models

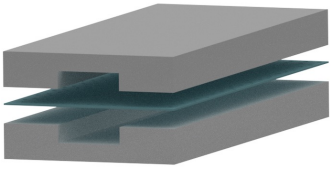
ECM: Yes
Shear stress: No
Co-culture: Yes



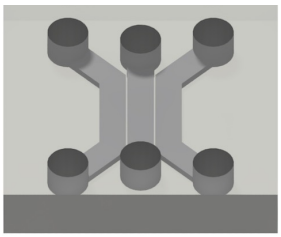
Microchannel models

ECM: No
Shear stress: Yes
Co-culture: Yes

Membrane models

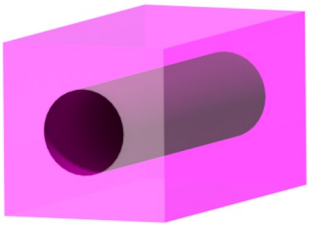


3-channel models



Needle model

ECM: Yes
Shear stress: Yes
Co-culture: Yes



Bioprinting

ECM: Yes
Shear stress: Yes
Co-culture: Yes

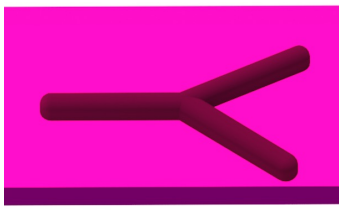


Figure 1.4: *in vitro* models to control the endothelial microenvironment. The six main categories of *in vitro* models discussed for controlling the endothelial microenvironment in terms of ECM, shear stress and co-culture with tissue-specific cells.

The transwell model is typically used under static conditions and seeding all cell types directly on the plastic substrates; however, it would be possible to seed cells on a polymerised 3D gel in both the upper and lower compartments to incorporate the contribution of the ECM in these studies. Furthermore, Warboys et al. (2010) used an orbital shaker to create a swirling motion over the cells to stimulate pig aortic endothelial cells cultured in the top compartment with shear stress. However, this method for applying shear stress results in a location dependent shear stress, which increases in the radial direction (0.2 to 3.6 dyne/cm^2 in this study based on the settings used on the orbital shaker). They further measured permeability by adding fluorescently labelled albumin to the top compartment and quantifying the rate of diffusion through the endothelial monolayer by measuring the concentration in the lower compartment using a fluorimeter. Results showed increased permeability in response to acute shear stress (1h stimulation) and decreased permeability in response to chronic shear stress (6-8 days stimulation), compared to static controls.

1.3.2 Parallel flow channels

In these models endothelial cells are seeded in rectangular channels and flow through the channel is achieved by attaching an external perfusion system, such as a syringe pump or a peristaltic pump. Custom-designed rectangular channels can be fabricated from PDMS using 3D printed moulds or soft lithography to cast the channels, which can then be bonded to a glass coverslip. Furthermore, channels with rectangular cross sections but with different geometries, such as a bifurcation, can also be obtained using these techniques, which allows studying changes in endothelial phenotype at different locations along the vessel, including in response to non-uniform shear stress at branching points (Sivarapatna et al., 2017). Depending on the channel dimensions chosen the flow profile will change, which can be characterised using CFD modelling. These 2D models under flow have had a large impact on *in vitro* studies as a tool for characterising endothelial cell response to shear stress. They are also commercially available from companies including ibidi and Cellix, who provide channels slides manufactured from tissue culture plastic as well as perfusion systems that can provide unidirectional or bi-directional laminar shear stress (with a range of frequencies available for changing flow direction) of 0.2-150 dyne/cm^2 (ibidi). Since these models isolates the effect of shear stress, they are directly comparable to cells cultured in static tissue culture plates; however, neither ECM nor co-culture can be incorporated in these studies.

1.3.3 Vasculogenesis models

Vasculogenesis refers to the assembly of endothelial cells into vessels. This process is primarily observed during development, driven by growth factors including VEGF and FGF (Potente and Mäkinen, 2017). *In vitro*, this is achieved by mixing endothelial cells into a 3D ECM gel and supplement the cell culture media with growth factors, resulting in endothelial cells self-assembling into capillary networks. Since endothelial cells are mixed in an ECM gel in this model, it is possible to incorporate other cell types as well; however, shear stress cannot be accurately controlled in this model. Even if perfusion through the vascular network is achieved, vessel parameters that affect shear stress including diameter and curvature vary throughout the network and are not known in advance, and hence culturing endothelial cells under controlled shear stress is challenging in this model.

This approach of creating a vascular network has been used in the field of regenerative medicine in co-culture with other cell types with the aim to create viable tissue constructs with dimensions that exceed the oxygen diffusion limit (~100-200 μm). From the perspective of studying endothelial cells, this method was initially established in the Matrigel tube-formation assay, which is carried out in a well plate format. However, Matrigel is not a very physiologically relevant substrate since it is derived from mouse tumours (Aisenbrey and Murphy, 2020). Perhaps the most sophisticated vasculogenesis model is that published by Wang et al. (2016), where a vascular network is established through vasculogenesis between two endothelialised channels in a microfluidic device, representing a capillary bed between arteries and veins. The vascular network is formed by mixing endothelial cells with lung fibroblasts in a fibrin gel, which is introduced into the microfluidic device following endothelialisation of the arterial and venular channels. Lumen formation of the vascular network as well as anastomosis between the arterial and venular side is confirmed by perfusion with fluorescently labelled dextran. Even though the vessels formed in this model are larger (~50 μm diameter) compared to capillaries found *in vivo* (~10 μm diameter), it is important to recognise the challenges including fabrication and endothelialisation associated with creating *in vitro* vessels of these dimensions, and hence this is an advantage of using a self-assembly technique for establishing vascular networks *in vitro*.

1.3.4 Microchannels

The microchannels category is based on PDMS microfluidic devices, using microfabrication techniques, including soft lithography and 3D printing, to create channels with rectangular cross-sections and precise dimensions in the micron scale to allow accurate control of the cell microenvironment. This includes shear

stress, as due to the small channel dimensions, perfusion through these channels result in laminar flow. Endothelial cells are seeded in the PDMS channels and due to the low volumes of reagents required, these models present a range of possibilities for *in vitro* studies. Independent access to the different channels allows great flexibility to for example seed different cell types using different protocols and introduce compounds at different time points during an experiment. Hence, the multidisciplinary field of microfluidics has opened doors for creating more complex and physiologically relevant *in vitro* models by capturing important features of the *in vivo* microenvironment (Wong et al., 2012) and these models therefore present an opportunity to replace animal testing. Furthermore, microfluidic technology has been essential for creating organ-on-a-chip systems, which refers to *in vitro* models with the capability to maintain tissue-specific functions of cells in culture and incorporate different cell types to create physiological models of whole tissue or organ function (Huh et al., 2010).

1.3.4.1 Membrane models

Pioneered by the "lung-on-a-chip" model (Huh et al., 2010) to mimic the interface between capillaries and lung epithelium, membrane models include two PDMS microchannels (the top and bottom channel) separated by a porous membrane, which allows exchange between the two channels. Facilitated by individual inlets, cell type, media, growth factors and shear stress in the two channels can be controlled independently. However, the relatively thick membrane (~10 μm) does not allow direct contact between the cells cultured in the top and bottom channels and therefore this model cannot capture the close interactions between for example endothelial cells and perivascular cells, which share a basement membrane *in vivo*.

In the lung-on-a-chip model, lung epithelial cells were seeded on the top surface of the membrane and endothelial cells are seeded on the opposite side. The top channel is filled with air to mimic the epithelial-air interface in the lung and the bottom channel is perfused with cell culture media to incorporate flow-induced shear stress and mimic the blood-endothelial interface. Furthermore, the model incorporates cyclic stretch of the epithelium to mimic breathing. This was the first model to integrate structural, functional and mechanical properties of the human alveolar-capillary interface in the same device, which cannot be achieved using conventional tissue culture techniques. Lung epithelial cells are commonly submerged in cell culture media when studied *in vitro*. Here, they were able to show that changing to a more physiological air-liquid interface of the cultured epithelium (in co-culture with endothelial cells) significantly influenced cell behaviour, including a tighter barrier function, which highlights the importance of physiologically relevant *in vitro* models for

translatability. In addition to barrier function, the study showed that the model could be used for investigating interactions with immune cells and pathogens as well as for toxicity studies, which is relevant in the field of drug discovery. The model has been used by several research groups and it is also commercialised (Emulate). Furthermore, optimising channel dimensions and mechanical stimuli, the model has been used for studying a range of different tissues, including bone, brain, intestine, kidney and liver.

1.3.4.2 3-channel models

Rather than arranging rectangular channels in a vertical direction, as the membrane models, in 3-channel models (although not limited to three channels) the channels are arranged parallel to each other in the horizontal plane and the device is bonded to a glass coverslip. The channels are separated by microposts or phaseguides, which support exchange through diffusion between the channels but due to surface tension there is no fluid mixing. The central channel is commonly filled with ECM and the outer channels with cell culture media and cells cultured on one or more of the channel surfaces. The main strength of this device design is the ability to setup chemical gradients across the central channel. Kim et al. (2013) used this model with five channels to study sprouting angiogenesis. In this study a pro-angiogenic ECM comprising fibrin matrix supplemented with collagen was introduced in the central channel and endothelial cells and lung fibroblasts were seeded in the channels on either side, resulting in endothelial sprouting through the ECM channel in response to a gradient of pro-angiogenic factors secreted by the lung fibroblasts. Strikingly, this study was able to show that the endothelial cells sprouted all the way across the central channel (width=700 μm) and eventually formed lumenised vessels, which could be perfused with fluorescently labelled dextran. Nashimoto et al. (2017) used a modified version of the same microfluidic device, but with a vertical hole through the central channel where a spheroid could be placed inside the ECM. In this study endothelial cells were seeded on both sides of the central channel and allowed to sprout into the ECM towards a spheroid created from lung fibroblasts. However, the sprouts were only able to connect to the spheroid when it was created from a co-culture of lung fibroblasts and HUVEC, resulting in a vascular network inside the spheroid, to which the sprouts could anastomose. In addition to studying endothelial response to chemical gradients, Song and Munn (2011) used a 3-channel microfluidic device to study the combined effect of transmural pressure gradients and VEGF on angiogenesis and found that the two stimuli cooperated to control endothelial sprouting.

The 3-channel model has been commercialised by Mimetas company, where 40 devices are fitted onto one 384-well tissue culture plate, allowing for high throughput studies. However, this does sacrifice flexibility as

this model cannot be connected to an external perfusion system limiting the range of shear stress that can be applied, supporting only hydrostatic pressure-driven flow induced by a rocker platform. In addition to angiogenesis, the model has been used for co-culture studies as a tool for drug discovery, allowing for crosstalk between different cell types without separation by a membrane. Petrosyan et al. (2019) used this device to create a glomerulus-on-a-chip model from co-culture of human podocytes and glomerular endothelial cells, which maintained their phenotype and function for over a month in culture. The study focussed on barrier function, studying albumin leakage and the response to drug compounds following glucose-induced cell damage in the context of diabetic nephropathy. The model has also been used to create gut, brain and liver-on-a-chip models.

1.3.5 Needle model

The needle model is based on the concept of polymerising ECM (commonly collagen) around a needle to create a straight hollow cylindrical vessel into which endothelial cells can be seeded, which was first published by Chrobak et al. (2006), encapsulating the ECM in a PDMS microfluidic device. This model offers the possibility to control ECM, shear stress and co-culture as endothelial cells are seeded directly onto the polymerised ECM surface, experience luminal flow as they line the vessel wall and a second cell type can be mixed into the matrix (Wong and Searson, 2014). Being able to create vessels with cylindrical cross-sections is an advantage of this model, which is challenging to achieve in microchannel models, which rely on microfabrication techniques including soft lithography. However, geometry is a limiting factor as the rod that the ECM is polymerised around needs to be removed while leaving the ECM gel intact. Chrobak et al. (2006) achieved tapered vessels by etching sections of the needles prior to collagen polymerisation and Jiménez-Torres et al. (2016) achieved bifurcations using PDMS rods; however reproducibly of these techniques was not confirmed by either study.

The needle model has been used for studying barrier function, motivated by the aim to create a more physiological environment for drug discovery. Here, Price et al. (2010) studied barrier function in response to mechanical stimuli and showed that vessel permeability decreased in response to exposure to higher shear stress. Furthermore, Chrobak et al. (2006) showed increased vessel permeability in response to inflammatory stimuli (TNF-α, thrombin and histamine) and increased leukocyte adhesion in an inflammatory state, where inhibition of both these outcomes could be achieved using blocking antibodies to relevant molecules. The model has also been used to study angiogenesis by perfusing the vessel with pro-angiogenic media,

supplemented with VEGF (Takahashi et al., 2017) (Pauty et al., 2018). Only one study so far has taken advantage of controlling all three microenvironmental parameters in this model. Wong and Searson (2014) mimicked the interface between the ECM, the vasculature and tumour cells, creating a 1.6 mm diameter vessel, which was embedded in collagen containing fibrosarcoma cells and perfused at physiological shear stress (12-15 dyne/cm^2). Similar to the majority of studies using microchannel models, studies using the needle model commonly do not perfuse the vessels at physiological shear stress, which is likely due to challenges with interfacing with an external perfusion system.

1.3.6 Bioprinting

3D printing is an additive manufacturing technique, where a specific geometry is built from layer-by-layer precise positioning of materials. Bioprinting refers to the 3D printing of biomaterials, including hydrogels, living cells and biochemicals. The technique is commonly associated with the field of regenerative medicine, with the aim to reconstruct parts of tissues (or organs) with biological and mechanical properties suitable for implantation, which is motivated by the worldwide shortage of available organs for transplantation. However, accurately mimicking the ECM remains the main technical challenge for achieving this, which is essential to be able to populate the 3D printed construct with all the different cell types required for organ function (Murphy and Atala, 2014). To address this, decellularised tissue might provide a more promising solution.

3D bioprinting can also be used as a research tool, where flexibility over vessel geometry is the main parameter that separates bioprinting from other *in vitro* models. Vascular networks can be 3D printed based on Computerised Tomography (CT) or MRI images; however, creating an *in vitro* model from 3D bioprinting requires access to specialist equipment (3D printers), which are very expensive and not readily available in research laboratories. Consequently, these models are very much still in the development and proof-of-concept stage. Furthermore, due to the complexity of creating these models, the studies using them tend to focus on creating pre-vascularised constructs suitable for implantation (presented below).

Wu et al. (2011) reported a method for omnidirectional printing, which is based on 3D printing sacrificial ink (comprised of Pluronic F127), inside a reservoir filled with non-polymerised liquid hydrogel with finely tuned material properties to support interfacing with the sacrificial ink. Following 3D printing the hydrogel is polymerised using photocuring with UV light and the sacrificial ink is removed by liquefication at 4°C, leaving a hollow vascular network inside the hydrogel. This method can create vascular networks with complex

geometries and hierarchical branching with 200-600 μm diameter vessels; however, the main limitation is the need for photocurable hydrogel, which presents a challenge for introducing live cells into the hydrogel before polymerisation. Miller et al. (2012) developed a method for 3D printing a vascular network as a mesh structure in sugar with diameters of 150-750 μm. Following 3D printing, a containing mixed in stem cells was polymerised around the network, which was immersed in an aqueous solution to dissolve the 3D printed sugar. The study validated that HUVECs could be seeded in the hollow channels following sugar degradation and that blood could be perfused through the network, which was connected from the inlet to the outlet. 3D printing with sugar has also been used by Lei et al. (2019), who showed the feasibility of 3D printing a vascular network which more closely mimicked the geometry of a capillary bed. Furthermore, they showed increased cell survival of rat cardiomyocytes when cell culture media was introduced through the 3D printed vascular network, compared to bulk hydrogel; however vessels were not endothelialised in this study.

Kolesky et al. (2016) reported a method for 3D printing with cell inks that incorporated live cells, to create thick (1 cm) vascularised tissue constructs that remained viable in culture for more than six weeks. In this study, human mesenchymal stem cells and neonatal dermal fibroblasts are mixed into cell inks and 3D printed in pre-defined patterns. Similar to the studies using sugar, a sacrificial ink is used to 3D print the vascular network, which is dissolved with temperature following hydrogel polymerisation, after which endothelial cells are seeded in the hollow vessel structures using an external pump. Following long-term perfusion with growth factors, the study shows *in situ* differentiation of human mesenchymal stem cells towards an osteogenic lineage.

Zhu et al. (2017) developed a method which relied on vasculogenesis for vessel formation rather than seeding endothelial cells in vascular networks created by 3D printing with a sacrificial material, which is a limitation in terms of vessel diameter due to the manual endothelialisation step required. In this model, endothelial cells and mesenchymal stem cells were mixed into a cell ink, which were polymerised in layers using UV light according to a mask defining the pattern of the vascular network and any uncured ink was washed off. Results showed that endothelial cells remained inside the defined vascular networks and formed lumens. Furthermore, they implanted a pre-vascularised 3D printed tissue construct under the dorsal skin of a mouse and vessels with human endothelial cells and red blood cells could be detected in the graft two weeks following implantation, suggesting anastomosis between the graft and host vasculature. This method allows very high-resolution, 3D printing a rat capillary network with vessels ranging from 5-50 μm in diameter as proof-of-concept; however, endothelialisation of this vascular network was not shown. Also based on layers of polymerisation of hydrogels Grigoryan et al. (2019) use projection stereolithography with food dyes as photo

absorbers to 3D print complex vascular networks in a quick way, such as the entire vasculature surrounding a lung air sac. A less complex vascular network geometry was 3D printed in hydrogel containing hepatocytes and endothelial cells were seeded in the vessels following hydrogel polymerisation. This pre-vascularised construct was implanted into mice with chronic liver injury and showed host blood inside the vascular network, indicating anastomosis with the host vasculature.

1.4 Disease modelling of thrombosis

1.4.1 Pathways regulating haemostasis and thrombosis

Coagulation, or clotting, refers to the process of clot formation in a blood vessel. In a healthy state, haemostasis occurs as a protective mechanism to prevent excessive blood loss following endothelial injury, which further is the first stage of wound healing. Haemostasis involves interactions between the vessel wall (comprising both the endothelium and subendothelium), platelets and circulating coagulation factors to form a blood clot and stop bleeding. This occurs in three main stages where stages 2 and 3 occur simultaneously as the coagulation process is sustained

1. Endothelial activation from vessel damage
2. Exposure of the subendothelium and initiation of platelet adhesion to the exposed regions
3. Platelet plug formation
4. Fibrin deposition following activation of the coagulation cascade

Clot formation is commonly divided into primary and secondary haemostasis, where primary haemostasis involves immediate platelet activation and aggregation at the site of injury to form a platelet plug and secondary haemostasis refers to the activation of the coagulation cascade, which is a complex biochemical process resulting in fibrin deposition to form a stable clot.

1.4.1.1 Heterogeneity in thrombotic disease

Thrombosis is a pathological state where coagulation is initiated without vascular injury (and consequent bleeding) resulting in the formation of a blood clot, which is referred to as a thrombus. In a healthy state the endothelium provides an anticoagulant and non-adhesive surface, which prevents platelet adhesion and clot formation. However, in a thrombotic state, components of the endothelial anticoagulant system are

downregulated in response to stimuli from the local microenvironment, where inflammation is one such stimuli, which has been associated with thrombotic disease in different parts of the vasculature.

Thrombosis can lead to the obstruction of blood flow and consequently result in ischemia or tissue death due to oxygen deprivation (Smith et al., 2015). This can occur both in arterial, venous and microvascular beds and is one of the leading causes of death in the world (Wu, 2015), contributing to disease including stroke and myocardial infarction. Arterial thrombosis is commonly initiated by vascular endothelial erosions and/or rupture of an atherosclerotic plaque, which occurs following build-up of lipid deposits on the vessel wall. Arterial thrombosis is the most prominent cause of myocardial infarction and of about 80% of strokes (Mackman, 2008). Furthermore, a thrombus can break free from the vessel wall and travel through the vascular system, for example pulmonary embolism is caused by thrombi that travel from the veins in the legs and block a pulmonary artery in the lung as a consequence of deep vein thrombosis (Grover and Mackman, 2019). Deep vein thrombosis and pulmonary embolism are collectively referred to as venous thromboembolism, which is the third leading cause of cardiovascular-associated death, after myocardial infarction and stroke. Venous thrombosis mainly stems from blood stasis or reduced blood flow, which results in accumulation of procoagulant factors including thrombin or from endothelial activation in response to inflammatory stimuli, which can alter the anticoagulant properties of the endothelium to a less protective phenotype (Mackman, 2012). Thrombosis in the microvasculature is associated with a range of disease and can lead to severe organ damage. In many cases microvascular thrombosis is associated with inflammation, referred to as thromboinflammation, for example in sepsis, ischemia-reperfusion injury, antiphospholipid syndrome and sickle-cell disease (Jackson et al., 2019). Endothelial cells have a central role in thromboinflammation, which is characterised by a loss of antithrombotic and anti-inflammatory functions of the endothelium resulting in dysregulation of both coagulation and leukocyte recruitment.

1.4.1.2 Platelet activation and plug formation

In haemostasis platelet plug formation is the initial response to vascular injury, where platelet adhesion occurs at the site of vessel damage to quickly stop bleeding. Platelets bind via receptors on their membrane surface to VWF, exposed ECM (including collagen) or to activated endothelial cells or leukocytes. Other adhesive molecules include fibronectin, laminin, fibulin and thrombospondin. This binding results in platelet activation, when platelets release the contents of their granules into the circulation, including adhesive glycoproteins such as P-selectin, fibrinogen, and VWF, coagulation factors, mitogenic factors, angiogenetic factors, fibrinolytic

inhibitors and immunoglobulins (Yun et al., 2016). This results in activation of the coagulation cascade and the recruitment of other platelets to achieve platelet aggregation, growing the size of the clot.

1.4.1.2.1 VWF and platelet adhesion

Von Willebrand Factor (VWF) is produced by endothelial cells and stored inside the cells in WPBs (Weibel-Palade bodies). It is secreted into the circulation to maintain a baseline concentration and also released upon endothelial activation. Although platelets can adhere to the vessel wall through multiple different molecules, plasma VWF is required for platelet adhesion under high shear, starting from shear rates of 500-800 s^{-1} (Ruggeri and Mendolicchio, 2007). During high shear conditions, VWF serves as a bridge between the vessel wall and platelets, anchoring to collagen and to the platelet membrane (Riddel et al., 2007). Platelets can also adhere to VWF on the EC surface. This higher shear rate where VWF is required for platelet adhesion is normally found in arteries, arterioles and in some capillary beds. However, this mechanism also plays an important role in vessels that normally would not experience high shear if they have decreased diameters due to thrombotic regions or atherosclerotic plaque. In this case there is a local increase in the fluid velocity, and consequently in the shear rate, in order to maintain a constant flow rate of blood in the vasculature. Plasma VWF and platelets do not interact in the circulation as VWF needs to undergo a confirmational change to provide a binding site for platelets. This happens when VWF gets immobilised when it binds to collagen or through self-assembly with other VWF multimers. The functional differences between endothelial VWF and platelet VWF in thrombotic and thrombosis-related diseases are unclear.

The mechanisms involved in platelet adhesion and activation will affect the characteristics of thrombus formation. *In vitro* experiments showed that surfaces coated with fibrinogen resulted in platelet adhesion and activation but generated only small thrombi in the absence of other adhesive molecules. Furthermore, *ex vivo* perfusion experiments with fibrinogen deficient mice showed that thrombi mediated by VWF in the absence of fibrinogen would grow rapidly under high shear but were unstable and would detach from the wall; however with both VWF and fibrinogen present the thrombi grew more slowly and remained bound to the vessel wall (Ruggeri and Mendolicchio, 2007). Regions of atherosclerotic plaque are also associated with thrombus formation. Atherosclerotic plaques are rich in collagen, which provides a surface for platelet adhesion and furthermore, the rupture of atherosclerotic plaque can lead to endothelial damage and consequently EC activation (Yun et al., 2016).

1.4.1.3 The coagulation cascade

The coagulation cascade refers to the sequential activation of coagulation factors that eventually leads to fibrin deposition at the site of endothelial activation. There are 13 main coagulation factors (labelled I-XIII), which normally circulate in the blood in their inactive state and contribute to clot formation upon activation through proteolysis. Coagulation is initiated either by the intrinsic (contact) pathway or the extrinsic (tissue factor) pathway in the coagulation cascade. Both result in the activation of factor X, converting factor X into factor Xa, where a indicates its activated state. This initiates the common pathway and the cleavage of pro-thrombin to thrombin, followed by conversion of fibrinogen to fibrin (Figure 1.5). Fibrinogen is a soluble glycoprotein that is produced in the liver and circulate in blood. In the coagulation cascade it is converted to fibrin, which comprises polymer chains that cross-link to form a gel to stabilise the clot (Riddel et al., 2007). Thrombin and fibrinogen in the common pathway are also involved in platelet activation and hence both platelet adhesion and fibrin deposition will continue in parallel, following activation of the coagulation cascade, until the size of the clot is sufficient to stop bleeding.

1.4.1.3.1 The extrinsic pathway

The extrinsic pathway is essential for haemostasis *in vivo*. Following vascular injury, the extrinsic pathway is activated when blood comes in contact with tissue factor (TF), which is expressed on the surface of cells surrounding the endothelium, including mural cells (pericytes and smooth muscle cells) as well as fibroblasts and epithelial cells (Bode and Mackman, 2014). TF can also be detected in the bloodstream, referred to as circulating or blood-borne TF. Continuing down the extrinsic pathway, TF is a receptor for factor VIIa. When circulating factor VII in the blood comes in contact with tissue factor, it is activated and upon binding to the receptor it forms a complex, which activates factor X and thereby initiates the common pathway.

Healthy endothelium does not express tissue factor (or very low levels) and thereby serves as a protective barrier, separating tissue factor expressing cells from direct contact with blood components and resulting in a haemostatic envelope that activates the coagulation pathway only if tissue factor from surrounding cells is exposed to blood following vessel injury. However, in pathological states, such as sepsis, it has been shown that endothelial cells and activated monocytes also express tissue factor, which can lead to thrombosis. TF expressed and produced by monocytes is the main source of blood-borne TF; however, this form of TF is also associated with microparticles originating from ECs, vascular smooth muscle cells, or platelets. TF from monocytes is believed to play a significant role in chronic inflammation as monocytes adhere to inflamed tissue

(Jackson et al., 2019). Atherosclerotic plaques also contain significant levels of tissue factor, originating from monocytes and smooth muscle cells, which therefore increases thrombotic risk in patients. Furthermore, *in vitro* studies have shown that a range of stimuli, including VEGF, inflammatory stimulation with TNF-α, IL-1β or Lipopolysaccharides (LPS), stimulation with histamine or thrombin as well as hypoxia can induce significant tissue factor expression in endothelial cells (Bode and Mackman, 2014) (Smith et al., 2015). Similar to endothelial cells, TF expression in monocytes is induced by inflammatory stimuli but also from enhanced glucose levels in the blood, showing elevated levels in patients with diabetes (Steffel et al., 2006).

1.4.1.3.2 The intrinsic pathway

The intrinsic pathway describes clotting from direct contact between blood and negatively charged surfaces and can be initiated without interaction with the vessel wall, for example when blood is collected in glass tubes. The intrinsic pathway is initiated by the activation of factor XII, which anchors to the charged surface and initiates clot formation at that location. It involves sequential activation of factors XII, XI, IX and VIII and in the presence of calcium activated factors IX and VIII form a complex that leads to the activation of factor X and the initiation of the common pathway.

The intrinsic pathway has an important role *in vitro*, when blood comes in contact with artificial surfaces; however, it has also been shown that factor XII binds to and can be activated by collagen, which is negatively charged (Wu, 2015), as well as other physiological surfaces including RNA or DNA released from damaged or dying cells or negatively charged inorganic polyphosphates secreted by platelets (Jackson et al., 2019). Furthermore, activated endothelial cells have molecules on their surfaces that might contribute to activation of the intrinsic pathway (Gailani and Renné, 2007). Evidence suggest that the intrinsic pathway does not contribute to haemostasis *in vivo*, as humans or mice lacking factor XII do not present with excessive bleeding (Smith et al., 2015) and the intrinsic pathway is therefore not required to stop bleeding. However, the contribution of the intrinsic pathway in pathological conditions is not fully understood. It may play a role, or there may be cross-activation of both pathways, in thrombotic disease. This is of great interest therapeutically for lowering thrombotic risk in patients as anticoagulation drugs that target the extrinsic or common pathways, such as heparin which inhibits the activation of several coagulation factors including factor X, inevitably also increase the risk of bleeding, which can lead to haemorrhage (Harter et al., 2015). The role of the intrinsic pathway in thrombosis has primarily been studied using animal models of specific gene knock-out mice, where it has been reported that mice deficient in factor VIII were protected from venous thrombosis with no effect on

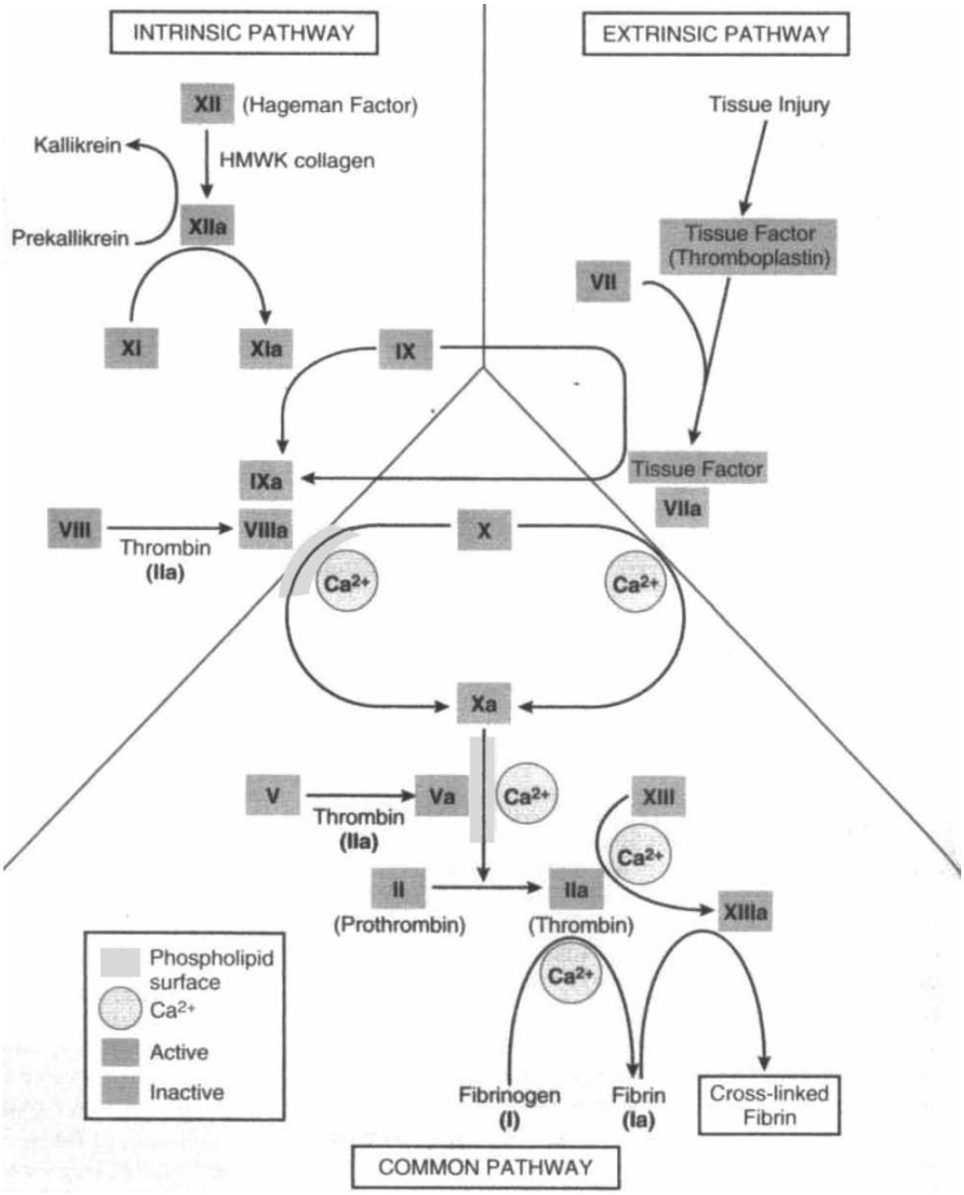


Figure 1.5: The coagulation cascade. Schematic illustrating the sequence of events in the intrinsic, extrinsic and common pathways of the coagulation cascade. Figure adapted from Riddel et al. (2007) with permission from SAGE Publications.

bleeding. Furthermore, mice deficient in factor XII were protected from arterial thrombosis with results comparable to wild type mice treated with a high dose of heparin. How translatable these results are to disease modelling in humans is still not clear as *in vivo* thrombosis models commonly result in collagen exposure (Gailani and Renné, 2007). Clinical trials with therapies targeting the intrinsic pathway are ongoing, where coagulation factors XI and XII are preferred candidates due to their limited involvement in haemostasis *in vivo* (Grover and Mackman, 2019).

1.4.2 Models for studying thrombosis

The pathophysiology of thrombosis varies throughout the vasculature, due to variations in stimuli from the microenvironment and different properties of the vessel wall, which consequently leads to different interactions with blood components. As mentioned previously, recent studies of RNA-sequencing of endothelial cells from different tissues show tissue-specific endothelial phenotypes, and importantly, these variations in gene expression profiles have been shown to includes genes involved in coagulation, such as thrombomodulin and VWF (Goveia et al., 2020) (Sabbagh et al., 2018). This further highlights the need for studying thrombosis in different parts of the vasculature to be able to find treatments for this disease. Due to the complexity of coagulation, involving both an activated endothelium and circulating blood, thrombosis has primarily been studied *in vivo*, taking advantage of genetically modified mice for gene deletion or overexpression, which exist for the majority of genes involved in haemostasis (Westrick et al., 2007). However, as a result of recent advances in microfluidics, *in vitro* models are starting to emerge as well. In terms of understanding endothelial heterogeneity in the context of thrombosis this presents an opportunity for the field by being able to accurately control independent aspects of the endothelial microenvironment. Furthermore, the current *in vivo* models of thrombosis are technically complicated and limited to a few vascular beds. Finally, there are significant differences in mouse and human physiology regarding the interface between the endothelium and blood. This includes flow-induced shear stress, which is typically an order of magnitude higher in mice compared to the human vasculature.

1.4.2.1 *In vivo* models

Several different *in vivo* thrombosis models exist, using different approaches to achieve local activation of the endothelium and measuring the time to occlusion or thrombus resolution (reviewed in Westrick et al., 2007). A few of the more commonly used models are summarised below, including the ferric chloride model, the mechanical wire injury model, the Rose Bengal model and the direct laser injury model, which fall into different

categories for endothelial activation. In the ferric chloride model, ferric chloride is manually applied with tissue to a region of the outer surface of the vessel wall. The chemical causes damage to the endothelial monolayer and results in collagen exposure to circulating blood and the initiation of platelet adhesion and activation of the coagulation cascade. In the mechanical wire injury model, a wire is inserted through the vessel wall and similarly to the ferric chloride results in disruption of the endothelium and exposure of underlying components in the vessel wall. Both these models require surgical exposure of the blood vessels where thrombosis is to be studied, and therefore, they are primarily suitable for larger vessels, including the femoral and carotid arteries and the inferior vena cava. The Rose Bengal model and the Direct laser injury model are more sophisticated and use laser to activate the endothelium. Furthermore, these models are considered easier to use compared to surgical intervention and can be used in different vascular beds. Rose Bengal is a photosensitizing dye, which is injected into the vasculature through the tail of the mouse. A green laser is aimed at a specific vessel location, resulting in injury to the endothelium, which is believed to be caused by the generation of reactive oxygen species when Rose Bengal comes in contact with the light from the laser. The direct laser injury model uses heat from the laser to create local activation of the vessel wall. Blood components are labelled by injection into the blood stream and through these the growing thrombus can be monitored in real time using microscopy and consequently allows precise quantification of clot formation. Although this model provides the highest resolution, it is limited by the vascular beds where thrombosis can be studied, which currently include the microvasculature in the ear and the mesenteric and cremaster arterioles, as the model requires blood vessels to be located in close proximity to the skin due to the microscopy requirements.

1.4.2.2 *In vitro* models

Inspired by the direct laser injury model, *in vitro* thrombosis models rely on real-time microscopy to monitor thrombus growth and characteristics using fluorescently labelled blood components. Studying the synergistic contribution of platelet adhesion and fibrin deposition in thrombosis requires the following three criteria for model design

1. ECs should cover all surfaces that are in direct contact with blood to prevent non-physiological activation of the intrinsic pathway from artificial (plastic) surfaces
2. ECs cultured in the model should be activated in culture after having grown to confluency, to switch to a pro-thrombotic phenotype. Such stimuli includes pro-inflammatory cytokines

3. The model should allow to perfuse the established endothelium with blood at a pre-defined shear stress during real-time microscopy

Due to the complexity required to achieve this, only a handful of custom-made microfluidic models, which meet these criteria have been published for the study of thrombosis *in vitro.* The characteristics of these models are shown in (Table 1.2), which further includes the capabilities of these models to control the EC microenvironment and thereby mimic tissue-specific aspects of the vasculature. These technical challenges appear to be related to studying platelet adhesion and thrombin generation simultaneously, and therefore, in the haematology field the majority of *in vitro* studies decouple these events to focus on either platelet adhesion or thrombin generation. Platelet perfusion assays are based on anticoagulated blood perfused on collagen surfaces, to study platelet adhesion, as the initial step in thrombosis or haemostasis resulting in platelet plug formation (Li et al., 2013). Since the blood is anticoagulated, fibrin deposition does not occur. Thrombin generation assays use whole blood or plasma supplemented with tissue factor in a well-plate format to study the rate of thrombin generation and the potential of the blood to clot following activation of coagulation factors in the extrinsic pathway. This is further used in the clinic to evaluate if patients are at risk for clotting or bleeding (Kintigh et al., 2018). The advantage of these two categories of assays is that they are straightforward to perform. However, they account only for the contribution of blood components and do not consider how the vessel wall influences thrombotic events, thereby missing a key element for modelling this disease.

		Control over the microenvironment			**Thrombosis model**		
Study	**Model category**	**ECM**	**Co-culture**	**Pre-conditioning ECs to shear stress**	**EC activation**	**Readout: platelet adhesion**	**Readout: fibrin deposition**
Zheng et al. (2012)	Parallel channels	Collagen	No	0.1 dyne/cm^2 hydrostatic pressure	PMA	yes	no
Sakurai et al. (2018)	Parallel channels	No	No	500s^{-1} or 2500s^{-1} syringe pump	EC damage	yes	yes
Mathur et al. (2019)	Parallel channels	No	No	0.81 dyne/cm^2 syringe pump	Diabetic endothelium	yes	yes
Costa et al. (2017)	Parallel channels	No	No	No	stenotic vessel	yes	no
Jain et al. (2018)	Membrane models	No	Lung alveolar epithelial cells	0.1 dyne/cm^2 syringe pump	TNF-α	yes	yes
Barrile et al. (2018)	Membrane models	No	No	0.1 dyne/cm^2 syringe pump	TNF-α	yes	yes

Table 1.2: Summary of published *in vitro* models where blood is perfused through endothelialised channels to study thrombosis or haemostasis.

From Table 1.2 it is clear that these studies have not focussed on regulating the endothelial microenvironment in the context of thrombosis as none of the studies control all three microenvironmental parameters, namely

the ECM, co-culture with tissue-specific cells and pre-conditioning of ECs to physiological shear stress. The studies are summarised below.

Zheng et al. (2012) published one of the first studies where blood was perfused through endothelialised channels in a microfluidic device. The model was created using soft lithography with channels created in a rectangular grid. A collagen gel was introduced during the microfabrication process so that endothelial cells would be in direct contact with collagen gel rather than with PDMS. This method also resulted in more circular channel cross-sections, where endothelial cells would coat the entire lumen of the channels. Anticoagulated blood was perfused through the channels. Activation of the endothelium with PMA (phorbol myristate acetate), which induces release of VWF from its storage, increased platelet adhesion to the vessel wall, compared to controls. In addition to studying platelet adhesion, this study shows the potential of using this model for studying angiogenesis by inducing sprouting into the collagen gel in response to perfusing proangiogenic media through the vessel lumen, studying permeability by measuring the diffusion of fluorescent dextran into the collagen gel and they also show that perivascular cells can be cultured in the collagen gel. However, the vessel design as a rectangular grid with right angle corners makes perfusion at physiological shear stress challenging in this model and potentially also perfusion with recalcified blood, which could be one explanation as to why the study focuses on platelet adhesion, rather than thrombosis.

Mathur et al. (2019) studied the role of disease-specific vascular dysfunction in the context of thrombosis, modelling the endothelium of patients with type 1 diabetes using ECFC (Endothelial Colony Forming Cells) isolated from blood samples from diabetic pigs. Perfusing these endothelial cells with blood from healthy human donors showed significant increase in platelet adhesion compared to controls. Furthermore, results suggest increased oxidative stress in these cells, which agrees with clinical findings in patients with type 1 diabetes. Even though the main limitation of this study is that they do not use human endothelial cells, it highlights the importance of accounting for a pathological endothelial phenotype when evaluating thrombotic risk in patients.

Thrombosis has also been studied in the presence of co-culture *in vitro*, motivated by studying organ-level contributions to vascular inflammation-driven thrombus formation. Using the lung-on-a-chip model, Jain et al. (2018) cultured endothelial cells on all surfaces in the bottom chamber of the membrane model, through which blood was perfused, and lung epithelial cells were cultured on the top surface of the membrane. The study shows a significant increase in platelet adhesion and fibrin deposition when the endothelium is activated by

TNF-α, both when it was introduced in the top or bottom channels. The model has also been validated for investigating the response to anti-inflammatory drugs relevant for pulmonary thrombosis.

As mentioned previously, changes in vessel geometry present regions with altered flow profiles, which can promote endothelial inflammatory activation and consequently thrombosis. Costa et al. (2017) studied platelet aggregation in a stenotic vessel geometry based on thoracic Computed Tomography Angiography (CTA) scans of coronary arteries from patients. The model was manufactured by 3D printing a mould using stereolithography (SLA), which incorporated the stenotic vessel geometry. PDMS was then cast in the mould, which was broken following PDMS polymerisation to release the microfluidic device, leaving a hollow 400 μm diameter vessel inside with 55% and 67% diameter constrictions. Although the study does not confirm endothelial activation, which is supposed to be induced due to altered flow characteristics and/or shear stress, results show significant platelet aggregation downstream of the stenotic region after 15 minutes perfusion with blood, representing a region with disturbed flow, compared to no platelet aggregation in control vessels without a stenotic region.

Sakurai et al. (2018) have developed a model to study haemostasis, where local endothelial activation is initiated in response to physical damage of the endothelium, which is achieved using pneumatic pressure to rupture the PDMS wall on which endothelial cells are cultured. They use “bleeding time” as the readout for haemostasis, which is defined as the time required for clot formation, when blood is no longer escaping from the hole in the vessel wall. In healthy controls, coagulation is initiated within minutes of EC damage and haemostasis is achieved within 20 minutes. This is the only published model which aims to match the shear stress used for pre-conditioning of the endothelium to the shear stress used during blood perfusion. However, it should be noted that the study uses the same flow rate for perfusion with blood and cell culture media, which is likely to result in different shear stress between the two cases, since blood is a non-Newtonian fluid (as described in earlier in this chapter). For model validation, they show prolonged bleeding time at high shear stress when blocking VWF dependent platelet adhesion; however, there was no significant difference in bleeding time in response to tissue factor inhibition. This suggests that fibrin deposition was not achieved through the extrinsic pathway in this model, which is surprising considering that haemostasis is tissue factor dependent *in vivo*. The authors imply that this is due to the absence of subendothelial cells, which are a main source of TF and suggest coating the channel with collagen and TF before cell seeding, which the blood would only come in contact with following vascular injury. However, they do not characterise the expression of TF on the endothelial cells. Furthermore, disease modelling using blood from haemophilia A patients resulted in a

significant decrease in fibrin deposition at the site of injury and consequently haemostasis was not reached within the 15 minutes perfusion time, which would be expected since haemophilia A is a bleeding disorder.

Reviewing existing *in vitro* studies of thrombosis, and focussing on tissue-specific thrombosis, it is clear that this field is very much still in the model development phase. Important progress has been made by other groups to define the parameters for mimicking thrombotic events *in vitro*; however, only a few studies have moved beyond the validation stage to use their developed model for disease modelling. Technical challenges as well as the lower throughput and longer experimental times associated with these models together with the fact that no commercial platforms exist are likely explanations for this. Even though no thrombosis model has been published which can simultaneously mimic multiple aspects of the microenvironment, significant progress has been made outside the field of thrombosis to control the endothelial microenvironment. Parallel channels are an essential tool to study the effect of shear stress on endothelial cells and membrane models have been used to mimic a range of different tissues, based on the lung-on-a-chip model where endothelial cells are co-cultured with tissue-specific cells. However, these models are commonly established to focus on function of the co-culture cells rather than the endothelium. The needle model and models based on bioprinting have the capability to incorporate both ECM, shear stress and co-culture with tissue-specific cells; however, none of these models have been used or developed in the context of studying thrombosis. Furthermore, the advantage of using a model that can control all these three microenvironmental parameters to study thrombosis is the possibility to use the same model for different *in vitro* assays, which would be a useful tool in vascular science to link different aspects of endothelial function to disease.

1.5 Aims and Hypotheses

1.5.1 Aims

The aim of this PhD was to develop a reproducible 3D blood vessel-on-a-chip platform based on the needle model category of microfluidic devices as a tool in vascular science and biomechanics, which

1. Allows high reproducibility and culturing multiple devices in parallel with minimal manual intervention
2. Allows studying endothelial cells in a controlled microenvironment, supporting independent control of ECM, shear stress and co-culture with tissue-specific cells
3. Allows real-time imaging and perfusion with whole blood
4. Supports studying cellular and molecular mechanisms of endothelial cells

1.5.2 Hypotheses

Having developed the model according to Aims 1-4, I then proceeded to apply the model to the study of thrombosis in the context of vascular inflammation with the following hypotheses

i) TNF-α induces a pro-thrombotic EC phenotype sufficient to detect a coagulation response in the model

ii) Blocking antibodies and compounds can be used to manipulate both the ECs and the blood to rescue a healthy non-thrombotic phenotype in the model

Chapter 2: Methods

2.1 Introduction

The blood vessel-on-a-chip platform that was developed in this project is based on the “needle model” design, where ECM is polymerised around a needle to create a pre-defined cylindrical vessel in a microfluidic device (described in Chapter 1). This approach was chosen as it has the potential to incorporate the three main microenvironmental stimuli: ECM, flow-induced shear stress and co-culture with tissue-specific cells. The platform comprises a microfluidic device and a 3D printed perfusion unit, which were both designed and optimised based on the below design criteria to allow independent control of these microenvironmental parameters

1. The platform should allow high reproducibility and culturing multiple devices in parallel
2. The platform should allow culture without manual intervention for a minimum of 16 hours (overnight culture)
3. The microfluidic device should support real-time imaging of the vessel using confocal microscopy
4. The microfluidic device should allow interfacing with an external perfusion system for perfusion at physiological shear stress
5. ECs cultured in the vessel should sense the mechanical properties and composition of an ECM substrate with physiological relevance
6. The microfluidic device should support co-culture with mural and/or tissue-specific cells
7. The platform should support studying cellular and molecular mechanisms, including protein and gene expression.

This chapter first outlines the optimised design and methods for creating the blood vessel-on-a-chip model. This is followed by a detailed description justifying methods and design choices, as these require prior knowledge of the model. A structure outlining the problem, details and outcome was used for clarity when discussing troubleshooting approaches.

2.2 Optimised methods

The steps and timelines for using the blood vessel-on-a-chip model is illustrated in the flow chart in Figure 2.1 and described in detail below.

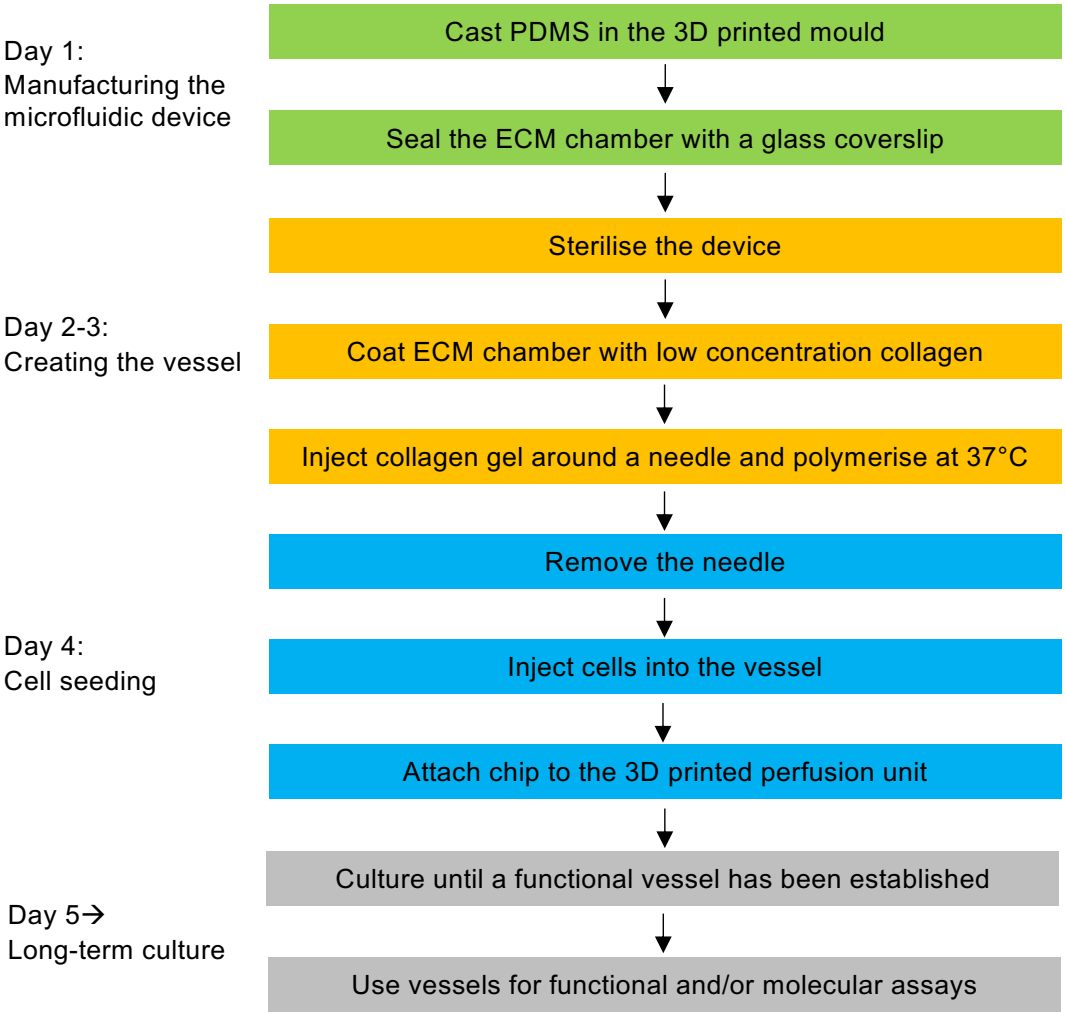


Figure 2.1: Flow chart illustrating the steps and timelines for using the blood vessel-on-a-chip model

2.2.1 Manufacturing the microfluidic device

The microfluidic device was manufactured by casting PDMS (Polydimethylsiloxane) in a 3D printed mould (3D printer: Objet 30 Prime, Stratasys, 3D printing material: VeroClear) (Figure 2.2 (A)). The mould was designed using the Computer Aided Design (CAD) software Autodesk Inventor. The microfluidic device has four inlets: two ECM inlets and two vessel inlets, all leading to a hollow ECM chamber (diameter=5 mm, height=1.3 mm). The ECM inlets were created by inserting tubing (Fine bore polythene tubing, Portex, Smiths Medical, ID=0.28 mm, OD=0.61 mm) through holes in the mould into the ECM chamber. The vessel inlets were created by inserting a 300 µm diameter stainless-steel acupuncture needle (Seirin) across the ECM chamber and attaching tubing on both ends, leaving a ~2 mm distance between the tubing and the ECM chamber (Figure 2.2 (B)). PDMS (Sylgard 184, the Dow Chemical Company) was prepared at a 10:1 elastomer to curing agent ratio at room temperature, mixed thoroughly and poured into the mould until full. The mould filled with PDMS was polymerised at 65°C in an oven for one hour, after which all tubing and the needle was removed, leaving hollow inlets in the PDMS. The microfluidic device (diameter=19 mm, height=1.7 mm) was then released from the mould (Figure 2.2 (C)). The ECM chamber was sealed with a glass coverslip (diameter=19 mm, Borosilicate glass thickness no 1, VWR), which was bonded to the PDMS using oxygen plasma treatment of both the glass and PDMS surfaces for 30 seconds, using a laboratory corona treater (Electro-Technical Products), followed by post-treatment baking at 65°C in an oven for one hour (Figure 2.2 (D)).

2.2.2 Creating the vessel

The device was sterilised by injecting 70% ethanol, using a 200 µl pipette to fill all inlets and the ECM chamber. The ethanol was removed using a tissue culture vacuum aspirator and the device was washed with PBS, following the same procedure as for injecting and removing the ethanol. To promote adhesion of collagen to PDMS, the ECM chamber and ECM inlets were coated with 50 µg/ml neutralised collagen I overnight at room temperature, using the same method for injection as described above. The coating collagen solution was prepared from a 5 mg/ml collagen stock solution (rat tail collagen I, 3D culture matrix, Cultrex, R&D systems), which was diluted in PBS to reach a 65 µg/ml concentration. The collagen solution was neutralised in HEPES (1M, sigma) and $NaHCO_3$ (37 g/l reconstituted in MilliQ water, sigma) at an 8:1:1 ratio (neutralisation protocol from van Duinen et al., 2017), resulting in a final collagen concentration of 50 µg/ml. The collagen neutralisation steps were performed on ice. To prevent evaporation during incubation, the devices were placed floating in PBS inside a petri dish, which was sealed with parafilm laboratory film (Bemis company). Following the collagen coating step, the ECM chamber and all inlets were filled with PBS and a stainless-steel acupuncture

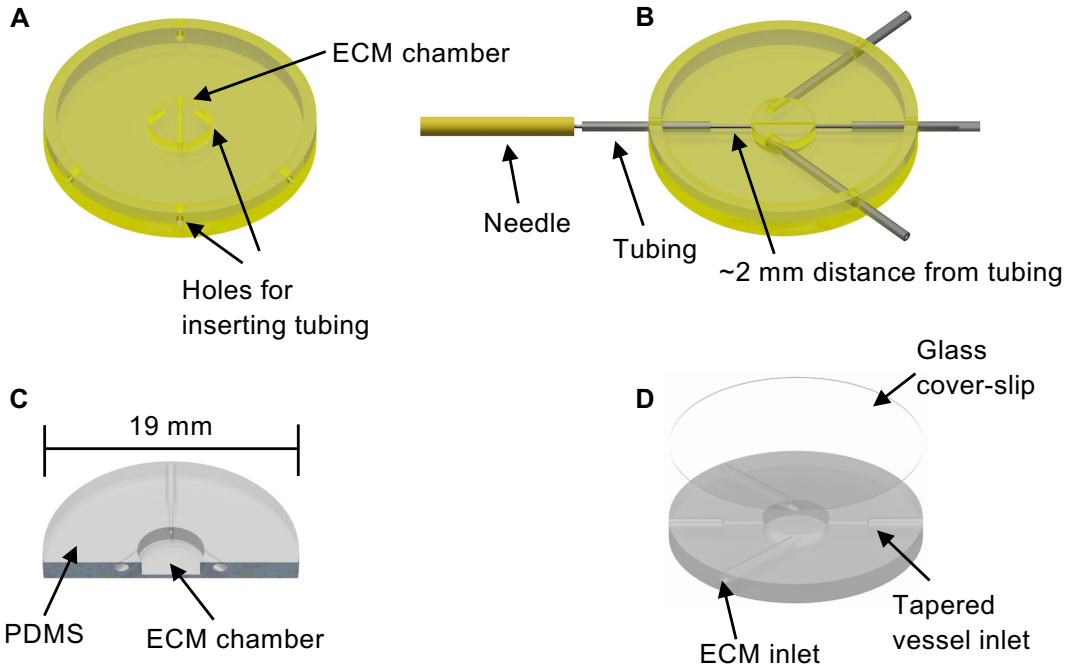


Figure 2.2: Manufacturing the microfluidic device. A: The circular 3D printed mould has a 5 mm diameter extrusion at the centre to create the ECM chamber and holes through the walls and ECM chamber for inserting tubing. B: The mould is prepared by inserting tubing and a 300 µm diameter sharp needle is through holes in the 3D printed mould to create two ECM inlets two tapered vessel inlets, after which PDMS is poured into the mould and polymerised. C: The tubing and needle are removed before releasing the microfluidic device from the mould, leaving an empty ECM chamber and hollow inlets inside the PDMS. D: The ECM chamber is sealed with a glass cover slip using oxygen plasma treatment.

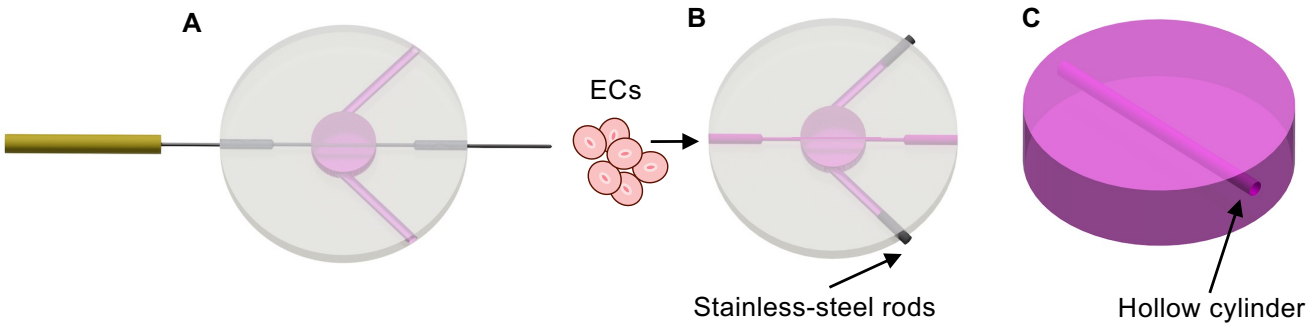


Figure 2.3: Method for creating the vessel. A: The vessel inlets are filled with PBS (ECM inlets and ECM chamber are empty) and a 300 µm diameter acupuncture needle is inserted between the vessel inlets after which collagen is injected through one of the ECM inlets until the ECM chamber and both ECM inlets are filled with collagen. B: The collagen is polymerised for 24h at 37°C after which the needle is removed and stainless steel rods are inserted to seal the ECM inlets. C: Zoomed-in image of the ECM chamber showing a hollow cylindrical vessel across the polymerised collagen.

needle (300 μm diameter, Seirin, sterilised with 70% ethanol before use) was inserted across the ECM chamber, sealing the vessel inlets. The ECM chamber was then emptied by aspirating PBS from one of the ECM inlets but leaving the vessel inlets filled with PBS. Neutralised collagen gel (4 mg/ml, same neutralisation protocol as for the pre-coating) was injected through the ECM inlet around the needle, using a 200 μl pipette, filling the ECM chamber and both ECM inlets with collagen (Figure 2.3 (A)). The devices were placed floating in PBS inside a petri dish and collagen was polymerised at 37°C overnight. Following collagen polymerisation, the needle was withdrawn, leaving a hollow cylindrical vessel inside the collagen, across the ECM chamber, and stainless-steel rods were inserted to seal the ECM inlets (OD=0.8 mm, length: ~2-3 mm, Crazy Wire Company), which had been manually cut to the desired length from a wire using pliers (Figure 2.3 (B-C)).

2.2.3 Cell seeding

Prior to cell seeding in the vessel, a vial containing 250,000 endothelial cells (HUVEC and ECFC have been validated in the model) was thawed and cells were seeded into two wells of a 6-well tissue culture plate (125,000 cells/well) and allowed to grow to ~80% confluence in Endothelial Cell Growth Medium (EGM2, Lonza), changing the cell culture media every 2-3 days. For cell seeding in the vessel, endothelial cells were trypsinised from one well of the 6-well tissue culture plate, counted, centrifuged at 1200 rpm (revolutions per minute) for 5 minutes at room temperature and resuspended at a cell density of $5x10^6$ cells/ml. Endothelial cells were seeded on the bottom surface of the vessel by injecting 2.5 μl of cell suspension through one of the vessel inlets using a 10 μl pipette (Figure 2.4 (A)). The device was then placed in PBS in a 12-well tissue culture plate (Figure 2.4 (B)) and incubated at 37°C for 30 minutes to allow cell adhesion to the collagen; then the cell seeding procedure and 30-minute incubation was repeated after rotating the device 180° to seed cells on the top surface, using endothelial cells freshly trypsinised from the remaining well of the 6-well tissue culture plate for the second cell seeding.

2.2.3.1 HUVEC

Human Umbilical Vein Endothelial cells (HUVEC) were purchased from Lonza as a pool with cells from 10 individual donors and were seeded at passage 4-6 in the device.

2.2.3.2 ECFC

Endothelial Colony Forming Cells (ECFC) were isolated from blood samples from healthy donors. An ECFC pool with five donors was created by combining cells from five individual donors at passage 4 and expanding the pool for one passage, using the pooled ECFC in the device at passage 5. All ECFC isolations were

performed by Dr. Charis Pericleous and Dr. Robert Maughan following the protocol from Martin-Ramirez et al, (2012). The isolation and use of human cells was approved by the local ethics committee.

2.2.4 Maintaining cell viability during long-term culture

To maintain cell viability in the vessel, the device was connected to a 3D printed perfusion unit (Figure 2.5 (A)), facilitating continuous media turnover of at least one vessel volume per minute when media is replaced once per day. The unit has five separate inlet and outlet reservoirs and allows culturing of five vessels in parallel. Hydrostatic pressure-driven flow moves cell culture media from the inlet reservoirs to the outlet reservoirs through the vessel, resulting in a flow-induced shear stress of <0.3 dyne/cm^2 (Figure 2.5 (C) shows the analytical solution). The perfusion unit was 3D printed from nylon (PA2200) using Selective Laser Sintering (SLS, Forge Labs), which yields permeable structures. To prevent leaking from the reservoirs, they were coated with PDMS after 3D printing and incubated overnight in an oven at 65°C for polymerisation. The unit has the dimensions of a rectangular tissue culture plate to fit on a microscope stage and allows optical access through holes in the base, on top of which the devices are placed. The perfusion unit was prepared the day before cell seeding by autoclaving and connecting Polytetrafluoroethylene (PTFE) microtubing (ID=0.3 mm, OD=0.8 mm, Adtech Polymer Engineering) between the inlet and outlet reservoirs (Figure 2.5 (B)), adding 3 ml PBS to each of the inlet reservoirs and aspirating from the tubing at the outlet reservoir to initiate fluid flow. The unit was incubated at 37°C overnight to precondition the tubing to incubator conditions (temperature and gas concentration). One hour before cell seeding, all air bubbles in the tubing were cleared by aspirating from the tubing at the outlet reservoir and the PBS in the inlet reservoirs was replaced with 3 ml of EGM2 cell culture media supplemented with 25 mM HEPES. Following cell seeding, the devices were connected to the perfusion unit by cutting away the tubing on top of each hole in the base using scissors and attaching the two pieces of tubing to the vessel inlets. Cell culture media was replaced once per day by adding fresh media to the inlet reservoirs, reaching a total volume of 3 ml per reservoir, and aspirating the media from the outlet reservoirs. All cell culture media contained 25 mM HEPES and had been pre-conditioned to incubator conditions by placing the media in a T25 tissue culture flask inside the incubator overnight to avoid problems with air bubbles.

2.2.5 Molecular assays

The blood vessel-on-a-chip model was validated for immunocytochemistry and qPCR, described below.

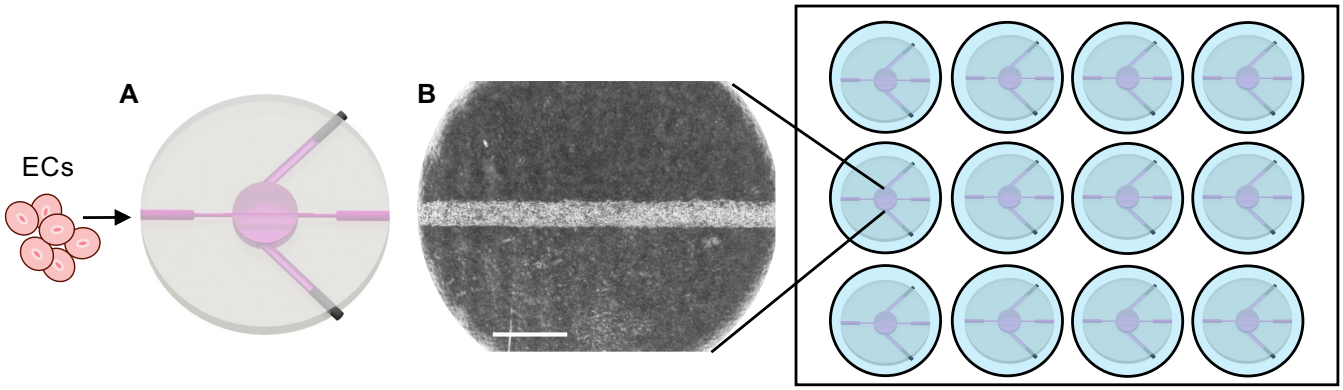


Figure 2.4: Cell seeding in the vessel. A: ECs were injected through one of the vessel inlets. B: Phase contrast image showing ECs in the vessel after injecting cell suspension. The devices were placed in PBS in a 12-well tissue culture plate and incubated at 37°C to allow cell adhesion to the collagen. Scale bar=1 mm.

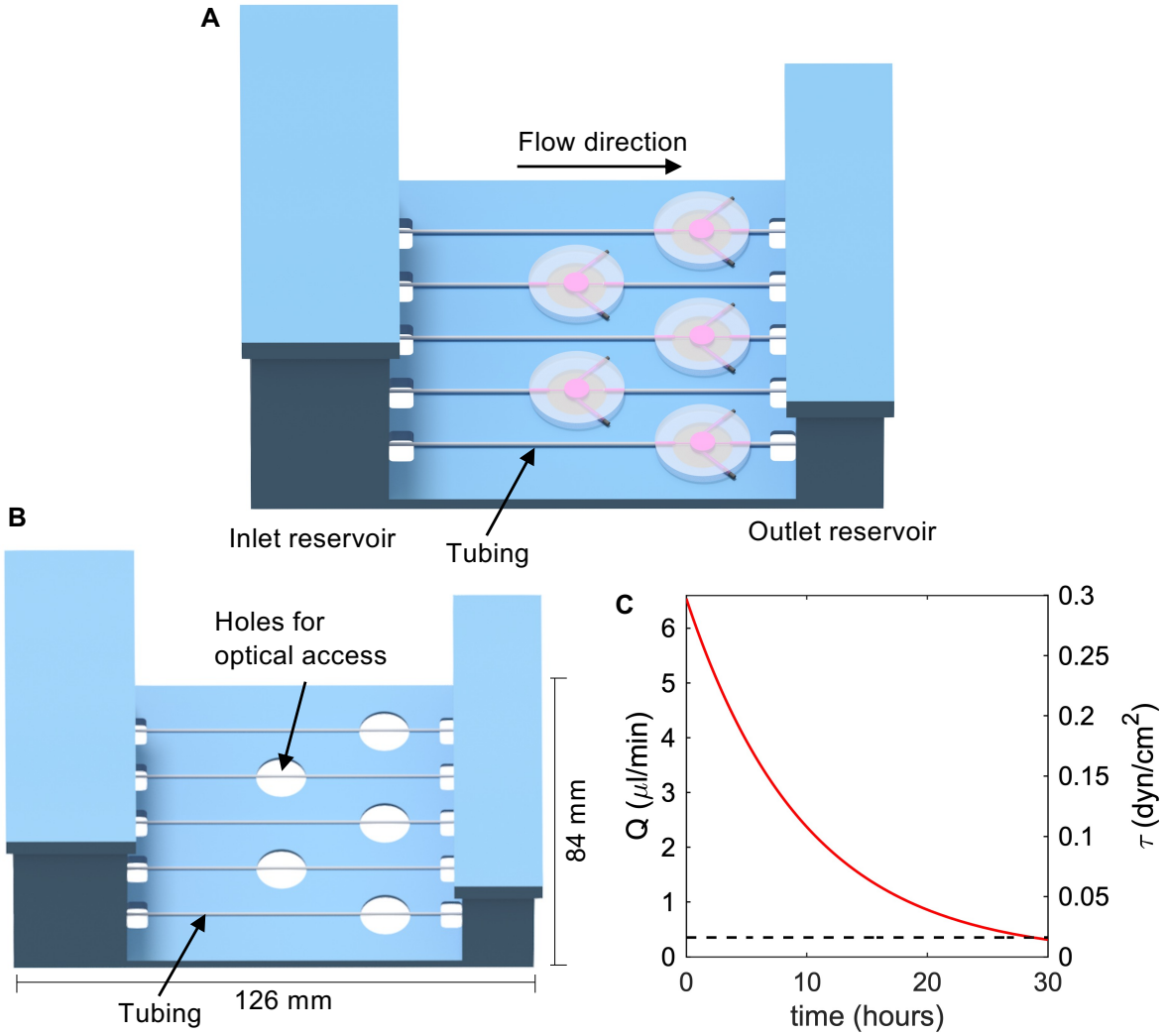


Figure 2.5: The 3D printed perfusion unit. A: CAD-model of the 3D printed perfusion unit holding five microfluidic devices. Continuous media turnover is achieved from hydrostatic pressure-driven flow between the inlet and outlet reservoirs. B: The unit has the dimensions of a tissue culture plate to fit into a microscope holder as well as holes through the base, on top of which the devices are placed to allow real-time imaging. The unit was prepared the day before cell seeding by connecting tubing between the inlet and outlet reservoirs and preconditioning the tubing (filled with PBS) to incubator conditions. C: Graph showing how the perfusion flow rate changes over time, resulting in a shear stress of <0.3 dyne/cm^2. If media is replaced once per day, the flow rate is always greater than one vessel volume per minute (indicated by the dashed line).

2.2.5.1 Immunocytochemistry

All steps in the protocol were performed on the same day and at room temperature. Fixation, permeabilisation, blocking and PBS washes were performed by perfusion using a 3D printed perfusion unit similar to the culture unit. To minimise antibody waste, the primary and secondary antibodies were delivered with a pipette using the same method as for cell seeding. Vessels were fixed with 4% formaldehyde solution (diluted in PBS from 37% stock solution, Sigma) for 15 minutes. The cells were permeabilised with 0.2% Tween-20 (diluted in PBS) for 20 minutes followed by 30 minutes blocking with 10% Bovine Serum Albumin (BSA, diluted in PBS, Sigma). The primary antibodies were delivered in two steps, injecting 5 µl antibody solution (diluted in 1% BSA) and incubating for 45 minutes and then rotating the device 180°, adding an additional 5 µl antibody solution and incubating for another 45 minutes. The vessel was then washed for 10 minutes followed by incubation with the secondary antibodies, which were delivered using the same method as for the primary antibodies but with 30-minute incubations. The vessel was washed with PBS for 10 minutes prior to microscopy or storage at 4°C in a 12-well tissue culture plate, sealed with parafilm laboratory film and floating in PBS to prevent the collagen from drying out.

Antibodies	**Concentration**
DAPI	1/1000
VE-cadherin	1/100
2nd antibodies (488, 555 and 647-conjugated)	1/400

Table 2.1: Antibodies and concentrations validated for use in the blood vessel-on-a-chip model

2.2.5.2 Bulk q-PCR

Cells were isolated from the microfluidic device for RNA extraction by breaking the coverslip and removing the collagen gel inside the ECM chamber using a pipette tip. The collagen was digested by placing it in a 1.5 ml Eppendorf tube containing 1 ml of collagenase A solution (Sigma, 2 mg/ml) reconstituted in EGM2 cell culture media that had been pre-warmed to 37°C in a water bath. It was then placed in a 37°C water bath for 2-5 minutes until the collagen was no longer visible inside the tube. It is crucial to digest all the collagen as any remnant would block the spin column, resulting in low RNA purity and non-detectible Ct values during qPCR. The solution was centrifuged at 1200 rpm at room temperature for 5 minutes, after which the collagenase solution was discarded and the cells were lysed by adding 50 µl extraction buffer from the PicoPure RNA isolation kit (Thermofisher). Samples were kept at -80°C until the RNA extraction protocol was performed, according to instructions provided in the RNA isolation kit. Following RNA extraction, total RNA was reverse

transcribed into cDNA using Superscript III Reverse Transcriptase (Invitrogen). Quantitative real-time PCR was performed using PerfeCTa SYBR Green Fastmix (Quanta Biosciences) on a Bio-Rad CFX96 system.

2.3 Model development

Published studies based on the needle model all use custom-designed PDMS microfluidic devices, likely designed and optimised based on specific applications. The below sections describe the troubleshooting carried out in this project, to justify methods and design choices applied to the blood vessel-on-a-chip model.

2.3.1 The microfluidic device

2.3.1.1 Material: PDMS

PDMS is a translucent silicone elastomer. It is commonly used in custom-designed cell culture models as it is non-toxic to cells and allows imaging due to its optically transparent properties (Young and Beebe, 2010). It is gas permeable to carbon dioxide (CO_2) and oxygen (O_2) (Firpo et al., 2015), which is an advantage for cell culture applications. However, PDMS is also permeable to water vapour, which can cause problems with evaporation of cell culture media (Heo et al., 2007) and PDMS has been shown to absorb small molecules, making it non-ideal for drug studies (Toepke and Beebe., 2006) if the compounds are in direct contact with a material surface. If these limitations can be overcome, PDMS is convenient to work with in a research laboratory especially at the prototype stage as it does not require specialist equipment and is inexpensive (cost of manufacturing the blood vessel-on-a-chip microfluidic device is <£0.5/device, using less than one gram of PDMS/device). However, manufacturing is labour-intensive and low throughput as every device is individually made, compared to techniques that support mass production with plastic, such as injection moulding. PDMS polymerises with temperature where polymerisation time decreases with increasing temperature. In this project, 65°C was chosen as the polymerisation temperature as it results in a low polymerisation time of one hour and does not melt or cause deformation to the 3D printed mould. Furthermore, oxygen plasma treatment provides a water-tight seal between PDMS and glass, eliminating the need for introducing sealants that may be toxic or damaging to cells.

2.3.1.2 Design of the microfluidic device

The design of the microfluidic device was modified over the duration of the project based on results on functionality and usability. The key alterations in design are summarised in Figure 2.6 showing the evolution

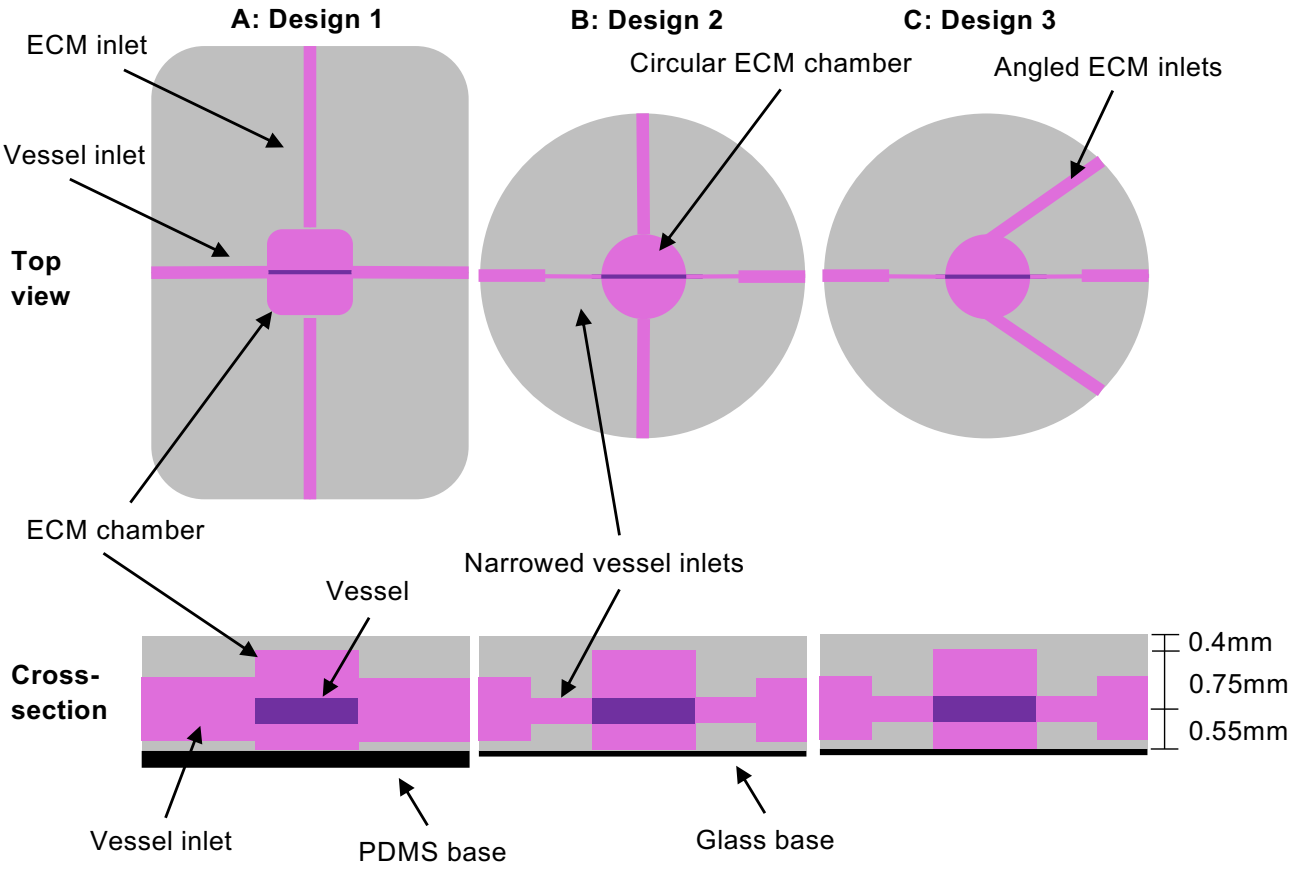


Figure 2.6: Design evolution of the microfluidic device. A: Design 1 has a rectangular geometry and square ECM chamber, PDMS base and same-diameter ECM and vessel inlets. B: Design 2 is improved from Design 1 to have a circular device geometry and using a glass coverslip as a base. It also has a circular ECM chamber and tapered vessel inlets. C: Design 3 is improved from Design 2 to have angled ECM inlets.

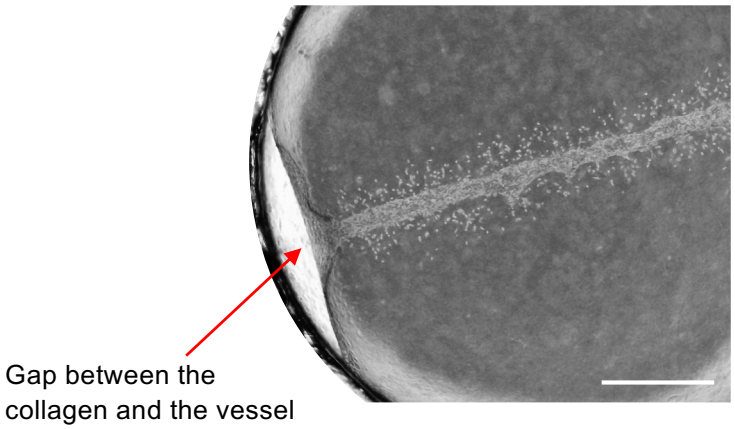


Figure 2.7: Vessel inlets with a narrowing diameter are key to avoid collagen damage. Top view brightfield image showing the ECM chamber. Without vessel inlets with a narrowing diameter, there is a risk of pushing on the collagen during perfusion or cell seeding, resulting in deformation of the collagen. Scale bar=1 mm.

of the design in three steps (Design 1, Design 2 and Design 3). Vessel length (5 mm) and the number of inlets (two ECM inlets and two vessel inlets) are shared between all versions. The 5 mm vessel length was chosen arbitrarily; it was considered long enough so that the vessel in the collagen could be imaged without including signal from the PDMS, but not too long to require an excessive volume of collagen in the ECM chamber. Furthermore, in all cases the PDMS bonding area is significantly larger than the ECM chamber, to facilitate high quality bonding to the base substrate and avoid leakage. The following sections describe troubleshooting to justify the different design features (the ECM chamber, the inlets, and the base substrate) and consequently the rationale behind modifying the design of the microfluidic device.

2.3.1.2.1 ECM chamber

Problem 1: Air bubbles in the collagen in the ECM chamber resulted in low success rate for creating the vessels.

Details: Design 1 used a rectangular ECM chamber with rounded corners, where air bubbles would get trapped when collagen was injected into the chamber.

Outcome: Using a circular ECM chamber (Design 2 and Design 3) prevented air bubbles from getting trapped in the ECM chamber during collagen injection.

Problem 2: ECs sense the stiffness of the device substrates (PDMS or glass coverslip)

Details: ECs can sense the presence of a give substrate from a 50-100 μm distance (Bogorad et al., 2017). In the ECM chamber, the centre of the vessel was placed 550 μm from the glass coverslip, resulting in a 300 μm distance from the glass to the bottom surface of the vessel for a 300 μm diameter vessel. The PDMS top surface of the ECM chamber was placed 750 μm from the centre of the vessel, resulting in a 500 μm distance between the PDMS and the top surface of the vessel (device cross-section shown in Figure 2.6).

Outcome: The dimensions of the ECM chamber are sufficient to allow ECs cultured in the microfluidic device to sense the ECM composition and mechanical properties of the collagen alone, and not from the glass or PDMS.

2.3.1.2.2 Inlets

Problem 1: The orientation (horizontal or vertical) of the inlets is related to reproducibility of the blood vessel-on-a-chip model.

Details: Tubing is conventionally attached to microfluidic devices in a vertical orientation after manually creating holes through the PDMS with a biopsy punch. Due to the rubber-like properties of PDMS it is a good sealant and tubing can be attached directly through the PDMS without needing bulky connectors, which reduces dead volume and allows greater flexibility over design. The needle model relies on inserting a needle across the microfluidic device in a horizontal orientation, which requires holes through the PDMS to hold the needle in place during ECM polymerisation. Chrobak et al (2006) sealed those holes after ECM polymerisation, which required an additional PDMS polymerisation step and thereby increasing the sources of error in the manufacturing process. Furthermore, using vertical inlets to interface with the polymerised ECM gel makes it difficult to clear potential air bubbles from the vessel inlets, which further reduces reproducibility.

Outcome: In this model, tubing was attached directly in line with the vessel in a horizontal orientation. To manufacture these inlets, PDMS was polymerised around tubing, which was inserted horizontally through the 3D printed mould. Using this method, the minimum thickness of the device was limited by the tubing outer diameter (OD). The inlets were created using 0.6 mm OD tubing and 0.8 mm OD tubing was then used during perfusion to create a good seal between the tubing and the PDMS. This method allowed high reproducibility with close to 100% success rate in casting the microfluidic device.

Problem 2: 3D printing resolution affects PDMS-glass bonding using plasma treatment.

Details: The method for creating inlets described above requires a 3D printed mould and cannot be created using soft lithography, which is conventionally used in microfluidics, as it is dependent on incorporating cylindrical holes through the outer walls of the mould and the ECM chamber. Soft lithography typically allows higher resolution, compared to 3D printing, which is essential for successful bonding between glass and PDMS.

Outcome: The 3D printer used in this project has a 16 µm layer thickness. Using 3D printers with lower resolution resulted in well-defined printing lines along the mould, creating an uneven PDMS surface. This would result in leakage from the bottom of the ECM chamber during cell culture due to poor bonding.

2.3.1.2.2.1 Vessel inlets with a narrowing diameter

Problem 1: Collagen damage during perfusion and collagen blocking the vessel inlets

Details: In Design 1 the vessel inlets were significantly larger than the vessel diameter, 600 µm compared to 300 µm, respectively. When a pressure drop was applied along the vessel, during perfusion from hydrostatic pressure, this would cause damage to the collagen as shown in Figure 2.7. Furthermore, when injecting

collagen into the ECM chamber, after inserting the acupuncture needle, collagen could escape through the vessel inlets. It was difficult to remove collagen from these regions following polymerisation, resulting in restricted fluid flow through the vessel inlets.

Outcome: In Design 2, the vessel inlets were changed to narrow in the PDMS, to have the same diameter as the vessel when they reached the ECM chamber. This solved the problem with collagen damage, as cell culture media would not push on the collagen outside the vessel during perfusion or cell seeding. Furthermore, it solved the problem with blocked vessel inlets, as the narrowed regions would grip the needle during collagen injection and thereby prevent collagen solution from leaking into and polymerise inside the vessel inlets in the PDMS.

Problem 2: The length of the narrowing vessel inlets affects flow characteristics

Details: Using a vessel inlet that narrows in the PDMS, to match the vessel diameter, allowed having fully developed flow along the entire length of the vessel in the ECM chamber during perfusion. For laminar flow through a vessel with cylindrical cross-section, the entrance length can be calculated according to Equation 2.1 (Buresti, 2012), after which the flow will be fully developed, where d is the vessel diameter and Re is the Reynolds number. The Reynolds number can be calculated using Equation 2.2, based on the fluid density (ρ), viscosity (μ) average velocity (u) and the vessel diameter (d). Fluid flow is considered laminar for Reynolds numbers below ~1200.

$$L_{entrance} = 0.06dRe \quad (2.1)$$

$$Re = \frac{\rho u d}{\mu} \quad (2.2)$$

Outcome: Using a vessel inlet with a ~2 mm narrowing section in the PDMS, this represents the maximum entrance length possible for fully developed flow at the start of the vessel in the ECM chamber. A 2 mm entrance length corresponds to a Reynolds number of ~110, which holds true for flow rates up to ~1125 μl/min or shear stresses up to ~50 dyne/cm^2 for perfusion with cell culture media.

2.3.1.2.2.2 ECM inlets

Problem: The ECM inlet orientation prevents fitting multiple devices in parallel in the 3D printed perfusion unit.

Details: The initial purpose of the ECM inlets was to allow delivering compounds to the ECM after a vessel was formed. This would have required easy access to the ECM inlets and therefore they were cast as shown

in Figure 2.6 (B). The possibility of using the ECM inlets to introduce a concentration gradient in the ECM was investigated (described in Chapter 5); however, due to the large distance from the outer surface of the device to the vessel wall (~9 mm) this proved difficult. The ECM inlets were therefore only used for injecting collagen and then sealed with stainless-steel rods. The possibility of removing the ECM inlets was considered since they did not serve a purpose after the vessel was created. However, this required injecting collagen through the vessel inlets and then inserting the needle, which reduced reproducibility as collagen would block the vessel inlets, reducing the success rate for cell seeding and for perfusion through the vessel (as described previously in this chapter).

Outcome: In Design 3 the ECM inlets were cast in the PDMS at an angle to allow connecting five devices in parallel to the 3D printed perfusion unit (Figure 2.5).

2.3.1.2.3 Base substrate

Problem: The thickness of the base substrate limits optical access to the vessel using confocal microscopy.

Details: In Design 1 a PDMS base was used instead of a glass cover slip. Due to the thickness of the base (>1 mm) this limited optical access in terms of objective working distance. Furthermore, due to the non-rigid properties of PDMS, achieving a flat surface was difficult, resulting in issues with focussing on the same plane along the vessel.

Outcome: In Design 2, a glass coverslip was used as a base substrate, which has a thickness of <200 µm and provided a levelled surface for imaging due to the rigidity of the glass surface. A circular coverslip was chosen to avoid right angled interfaces and corners, as they are weak points for bonding that can cause leakage due to separation between glass and PDMS. In Design 2 the mould geometry was therefore altered to match these dimensions. The diameter (19 mm) was chosen so that the device would fit into the well of a 12-well tissue culture plate (diameter=22 mm), which was convenient when working with multiple devices in parallel. However, glass coverslips are very fragile and could easily crack during the bonding step or when holding the device for injecting collagen or during cell seeding. A broken glass coverslip would result in leaking from the base of the device during cell culture and therefore needed to be discarded.

2.3.2 Creating the vessel

To allow future use of this model by different research groups, all steps for creating the vessel require only conventional tissue culture equipment readily available in molecular biology laboratories, including pipettes and vacuum aspirators for injecting and removing fluids.

2.3.2.1 ECM

In this project, all experiments used commercially available collagen I isolated from rat tail at a concentration of 4 mg/ml. Collagen was chosen for optimisation and validation purposes as it is the most abundant category of ECM proteins *in vivo* (described in Chapter 1) and is therefore also commonly used *in vitro*. However, this technique should support any type of ECM that can be injected using a pipette and which creates a gel that is rigid enough to prevent the vessel from collapsing when the needle is removed.

Problem 1: Non-homogeneous collagen polymerisation inside the microfluidic device.

Details: Collagen polymerises with temperature and with increasing pH (referred to as neutralisation). Injection with high-concentration collagen therefore needs to be a quick process to avoid non-homogeneous collagen polymerisation inside the microfluidic device. Neutralised collagen was left on ice for 10-15 minutes before injection to ensure the lowest possible viscosity for injection. Two different delivery techniques were investigated: using tubing connected to a 1 ml syringe and using a 200 µl pipette. Issues with the tubing method included collagen polymerisation in the tubing, likely due to increased temperature from holding the tubing when connecting it to the device, as well as low accuracy of injection speed associated with using a 1 ml syringe to inject ~30 µl neutralised collagen.

Outcome: Using a 200 µl pipette was the better option for achieving quick delivery and was therefore used for creating the vessel, even though it was a more challenging technique. 45 µl neutralised collagen was used for each device, discarding the pipette tip after each injection, as it was found that collagen started polymerising on the inner walls of the pipette tip between injection and withdrawing new collagen solution.

Problem 2: Leakage of fluid around the collagen during perfusion due to weak bonding of the collagen to the PDMS surface.

Details: To improve bonding between a given hydrogel and the PDMS surface in a microfluidic device, Pagano et al. (2014) suggested to coat the PDMS surface with low concentration collagen (50 µg/ml) prior to injecting the hydrogel. The effect of coating the PDMS surface in the ECM chamber was validated by perfusing Xanthan gum (250 ppm, Sigma) reconstituted in Milli-Q water and red food colouring through the vessel as an analogue for blood (Gijsen et al., 1999), comparing the two conditions (coating or no coating). The experiment was repeated for three individual vessels for both conditions, perfusing the vessel for 90 seconds at a flow rate of 500 µl/min (~90 dynes/cm^2) and visually observing if there was any red colour outside of the vessel boundaries.

Outcome: Results clearly indicate poor collagen bonding to the PDMS without the coating step, with significant fluid flow outside the vessel. Introducing the coating step solved this problem and no fluid leakage was observed in any of these vessels (Figure 2.8). Furthermore, these results suggest that the device can be perfused at higher flow rates, and consequently higher shear stress, without causing leakage or damaging the collagen.

Problem 3: Microbubbles in the collagen during polymerisation.

Details: During collagen polymerisation inside the incubator, visible microbubbles would appear in the collagen in the ECM chamber, which disappeared over time. However, if a microbubble would appear in contact with the needle, this would cause a defect in the shape of the vessel (Figure 2.9 (A)) even though the air bubble disappeared over time. If the air bubbles in the ECM chamber were not cleared before cell seeding, they would grow over time and cause damage or deformation to the vessel by compressing the collagen (Figure 2.9 (B-D)).

Outcome: All devices were polymerised overnight at 37°C inside an incubator before cell seeding to facilitate removal of microbubbles in the collagen. If there were any larger air bubbles visible inside the ECM chamber before polymerisation in the incubator, (related to problems with the injection process) the device would be discarded as these air bubbles would not disappear over time.

Problem 4: Air bubbles introduced through the vessel can cause vessel deformation.

Details: Following collagen polymerisation, the needle was withdrawn through the vessel inlets. It was essential that the vessel inlets were filled with PBS prior to inserting the needle and injecting collagen to make sure that the vessel filled with PBS and not with air as the needle was withdrawn. If air bubbles would enter the vessel as the needle was withdrawn, it would typically be possible to clear them manually; however, they could permanently damage the vessel. Figure 2.10 shows a vessel where an air bubble entered the vessel from the left vessel inlet, and even though the air bubble was successfully removed it resulted in permanent expansion of the vessel diameter in this location.

Outcome: The devices were placed floating in PBS in a petri dish during polymerisation. This ensured no air-liquid interface at the vessel inlets, and consequently no fluid evaporation from the inlets, to prevent the vessel from filling with air as the needle was withdrawn.

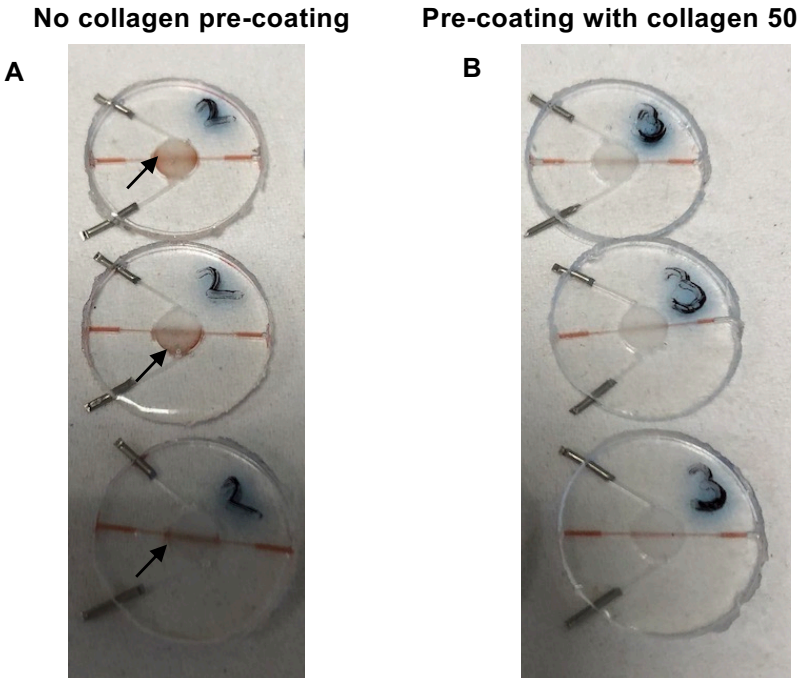


Figure 2.8: Coating of the ECM chamber with low concentration collagen to prevent leaking. The effect of coating the ECM chamber with 50 µg/ml neutralised collagen to improve collagen-PDMS bonding is shown in pictures A and B for n=3 vessels for each condition. Both conditions were repeated for three individual vessels. A: No collagen coating resulted in fluid being perfused outside the vessel boundaries, around the collagen (leakage areas indicted with arrows). B: Coating the ECM chamber with 50 µg/ml neutralised collagen prevented leakage of the perfusion fluid around the collagen.

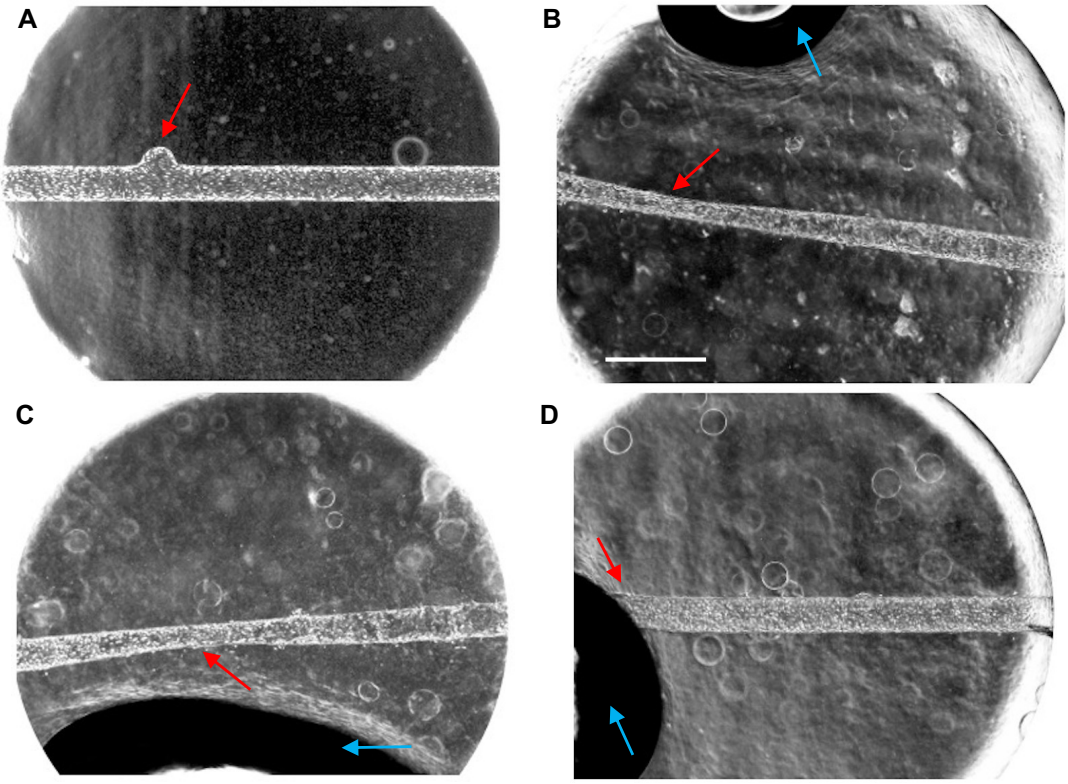


Figure 2.9: Air bubbles in the collagen can cause vessel deformation. Top view of phase contrast images of the ECM chamber for four different vessels. A: The red arrow indicates a change in vessel shape due to a microbubble in contact with the needle during collage polymerisation. B-D: Three examples showing how air bubbles in the collagen in the ECM chamber caused damage to the vessel during cell culture. Air bubbles are indicated with blue arrows and locations of vessel deformation are indicated with red arrows. Scale bar=1 mm (applies to all images).

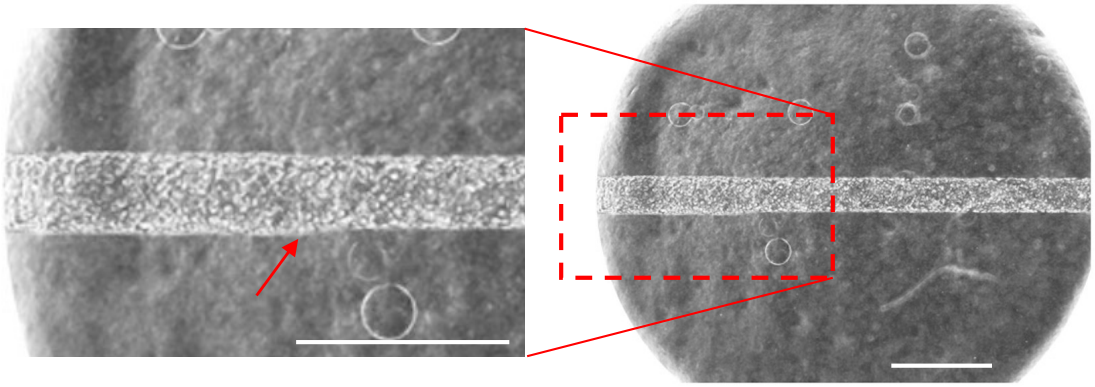


Figure 2.10: Air bubbles inside the vessel can cause vessel deformation. Phase contrast top view image of the ECM chamber, where the left image shows a zoomed-in section of the vessel where an air bubble entered the vessel after withdrawing the needle, causing permanent deformation to the vessel, having increased diameter in this location. Scale bars=1 mm.

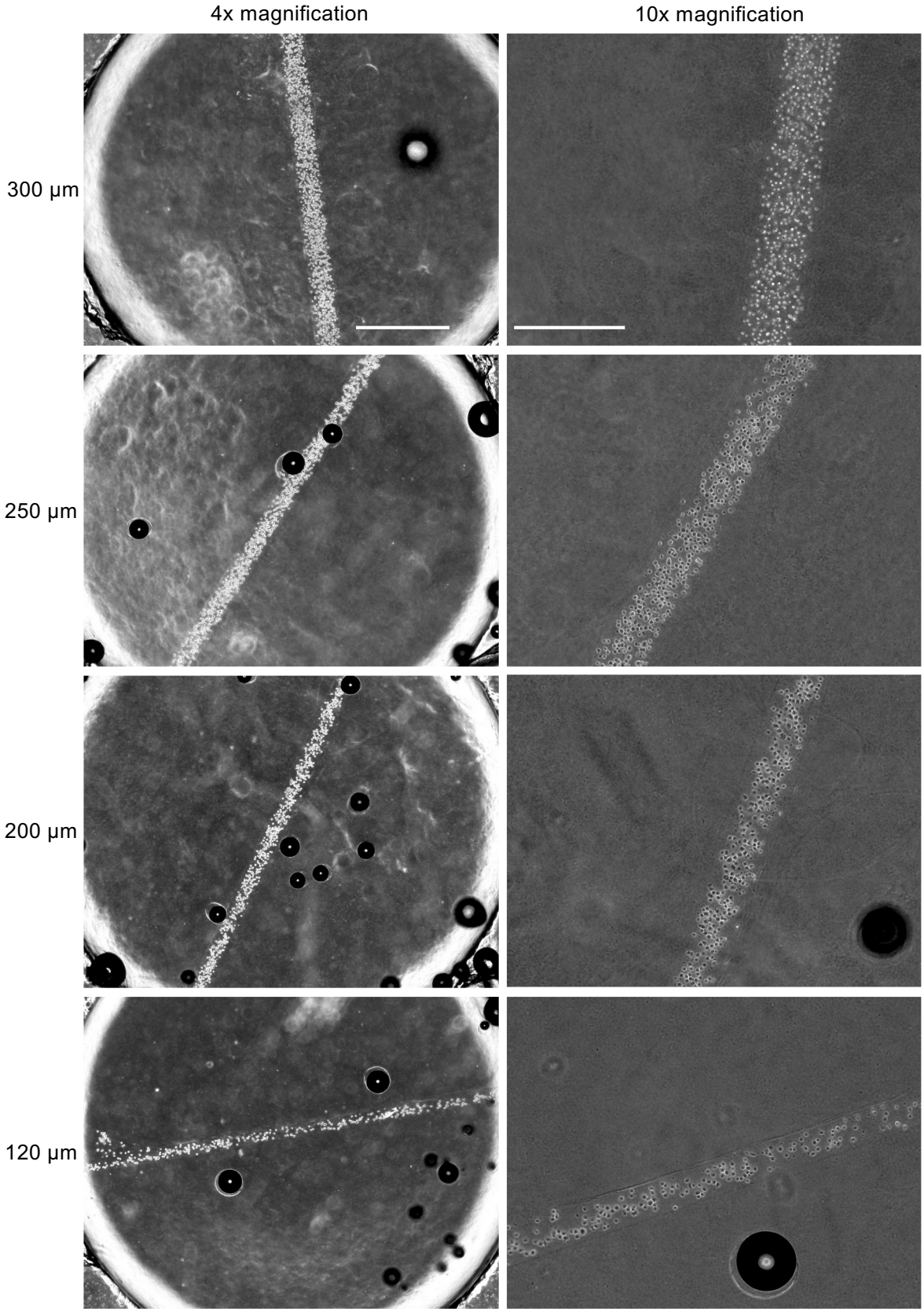


Figure 2.11: Creating vessels with different diameters. Top view phase contrast images of four different vessels seeded on the same time, showing the ECM chamber with 4x magnification and the centre of the vessel with 10x magnification for four different vessel diameters; 300 µm, 250 µm, 200 µm and 120 µm, confirming that creating the vessel and cell seeding is possible in all cases. Scale bars 4x magnification=1 mm, scale bars 10x magnification=500 µm (applies to all images).

2.3.2.2 Vessel size

For optimisation and validation purposes the same vessel diameter (300 µm) was used for all experiments in this project. However, the feasibility of decreasing the vessel diameter was investigated. Smaller diameter vessels could be successfully created in this model; as proof-of-concept, four different vessel diameters (300 µm, 250 µm, 200 µm and 120 µm) were investigated in terms of creating the vessel and cell seeding. Results show that it is feasible to use this model for all those vessel diameters (Figure 2.11); however, it was technically more challenging to work with smaller diameter vessels, which might result in lower reproducibility due to vessel damage from injecting cell suspension or from clearing air bubbles. 120 µm is the smallest available diameter for acupuncture needles and therefore, this was the smallest vessel size investigated. The use of a 50 µm diameter stainless-steel wire was considered; however, the rough edge of the wire from cutting with pliers damaged the collagen when it was withdrawn following collagen polymerisation. It might have been possible to use different cutting techniques that would result in a sharp edge of the wire (similar to the acupuncture needles), in which case the commercially available sizes of stainless-steel needles would not be a limiting factor for choosing a vessel diameter.

2.3.3 Cell seeding

Cell suspension was injected through the vessel inlet using a pipette. A volume of 2.5 µl cell suspension was chosen, which replaced all the fluid inside the vessel inlet at the side of injection, all the fluid inside the vessel in the ECM chamber and the fluid in the narrow section of the vessel inlet on the opposite side. After cell injection, phase contrast microscopy was used to confirm successful cell seeding, visualising ECs along the entire vessel, which had a round morphology (Figure 2.12 (A)). The devices were then incubated at 37°C to allow cell adhesion to the collagen surface, which would happen within 15-30 minutes after cell seeding and was visible by a change in cell morphology, referred to as spreading (Figure 2.12 (B)). After confirming cell adhesion to the collagen, the device was rotated 180°C before the second cell seeding and incubation. If sufficient time for cell adhesion was not allowed between cell seedings, a significant number of cells from the first cell seeding would be washed out during the second cell seeding.

Problem 1: Using the same cell suspension for the two cell seedings resulted in clusters of cells injected into the vessel during the second cell seeding.

Details: The left-over cells from the first cell seeding could not be kept in suspension and re-used for the second cell seeding as this resulted in clusters of cells being injected into the vessel (Figure 2.12 (C)). This occurred even if the cell suspension was well mixed prior to injection.

Outcome: The cell culture format of seeding cells in two wells in a 6-well tissue culture plate was introduced. This allowed creating two separate cell suspensions, one for each cell seeding, by sequential trypsinisation of each well just prior to cell seeding.

Problem 2: Variability of the total number of cells seeded in the vessel.

Details: The cell seeding step can result in variability. Figure 2.13 (A-B) shows two vessels that were seeded on the same day using the same cell suspension, showing a clear difference in cell seeding density between the two vessels. The reason for the variability in cell seeding density between different vessels is not fully understood. Very low cell seeding density could originate from not inserting the pipette correctly into the vessel inlet when injecting the cell suspension. If this was the case, the cell seeding step was repeated.

Outcome: Before connection to the 3D printed perfusion unit, all vessels were imaged using phase contrast microscopy and if there were outliers showing obvious differences in cell seeding density compared to the rest of the batch, these vessels were discarded.

Problem 3: Very high cell seeding densities resulted in cell death in the vessel.

Details: When a very large number of cells were injected into the vessel, all cells were not able to adhere to the collagen, which resulted in dead cells inside the vessel that would remain there for long periods of time (Figure 2.13 (C)).

Outcome: A range of cell seeding densities were used during the optimisation phase of the project (5-8 $x10^7$ cells/ml). Even though higher cell seeding densities resulted in reaching a confluent vessel in a shorter period of time, the lower cell seeding density of $5x10^6$ cells/ml was chosen as the final concentration to avoid issues with dead cells inside the vessel.

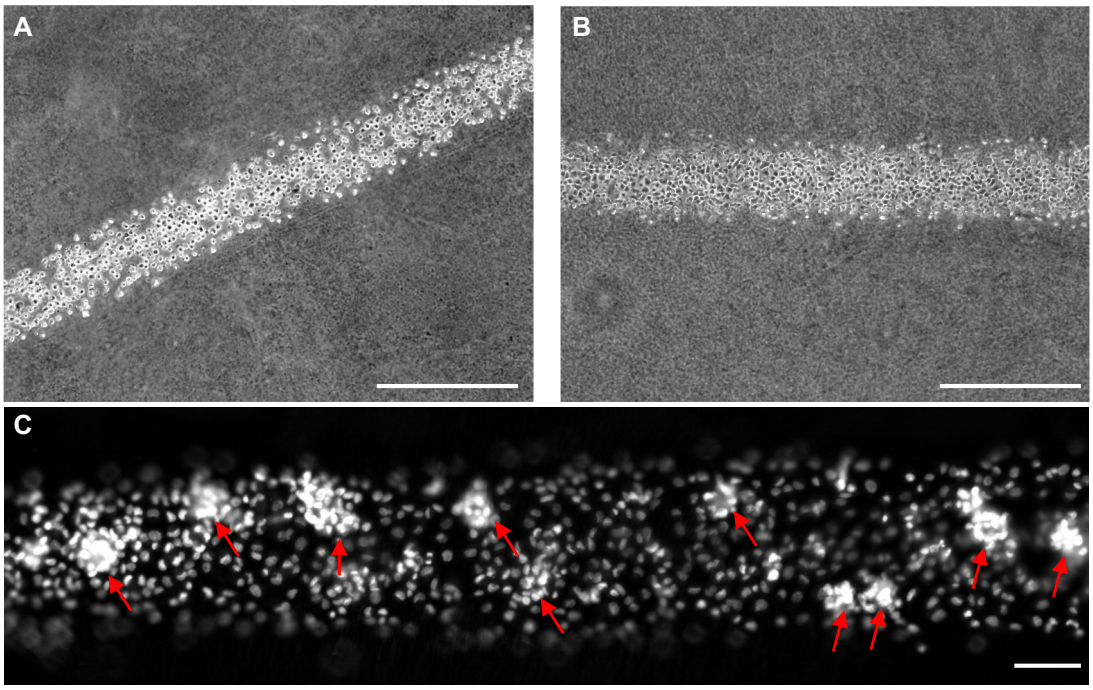


Figure 2.12: Optimisation of sequential cell seeding in the vessel. A: ECs have a round morphology when seeded in the vessel (scale bar=500 µm). B: Following 30 minutes incubation at 37°C ECs have adhered to the collagen surface, indicated by a change in cell shape (scale bar=500 µm). C: Using the left-over cell suspension from the first cell seeding results in clusters of cells being injected during the second cell seeding (scale bar=100 µm).

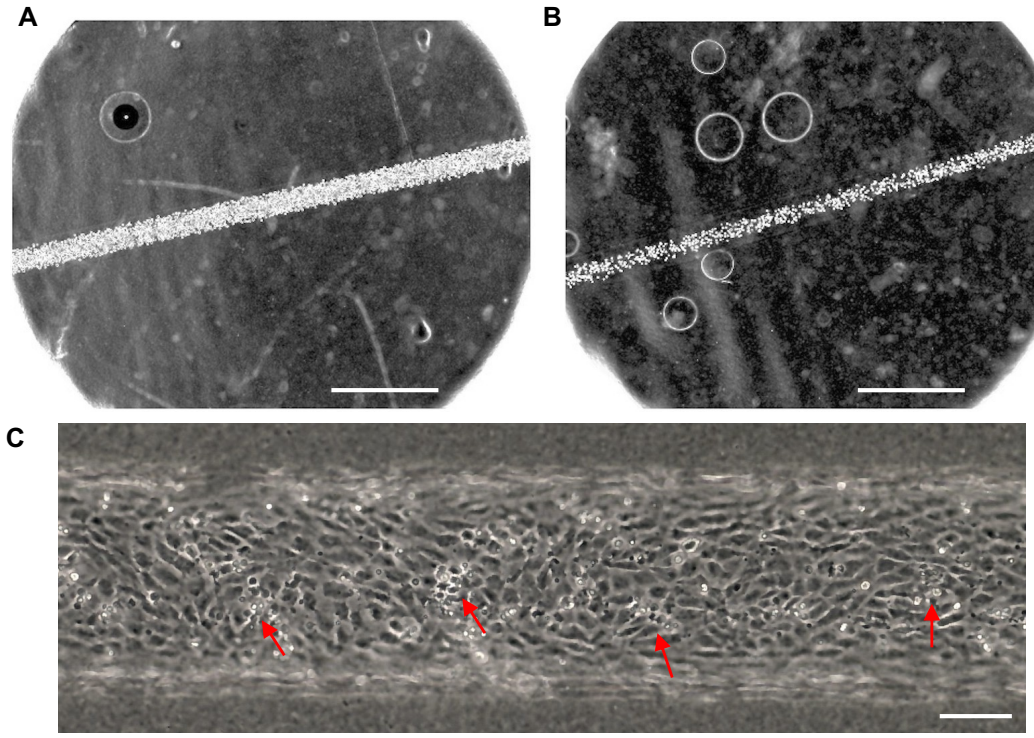


Figure 2.13: Variability in the number of cells seeded in the vessel. A-B: Top-view brightfield images of the ECM chamber clearly indicating variability in cell seeding density between, where the vessel in image A has much higher cell seeding density compared to the vessel in image B even though the same cell suspension was used in both cases (scale bar=1 mm). C: Very high cell seeding densities results in dead cells inside the vessel that are not washed out with perfusion. The image was taken 17h post cell seeding (scale bar=100 µm).

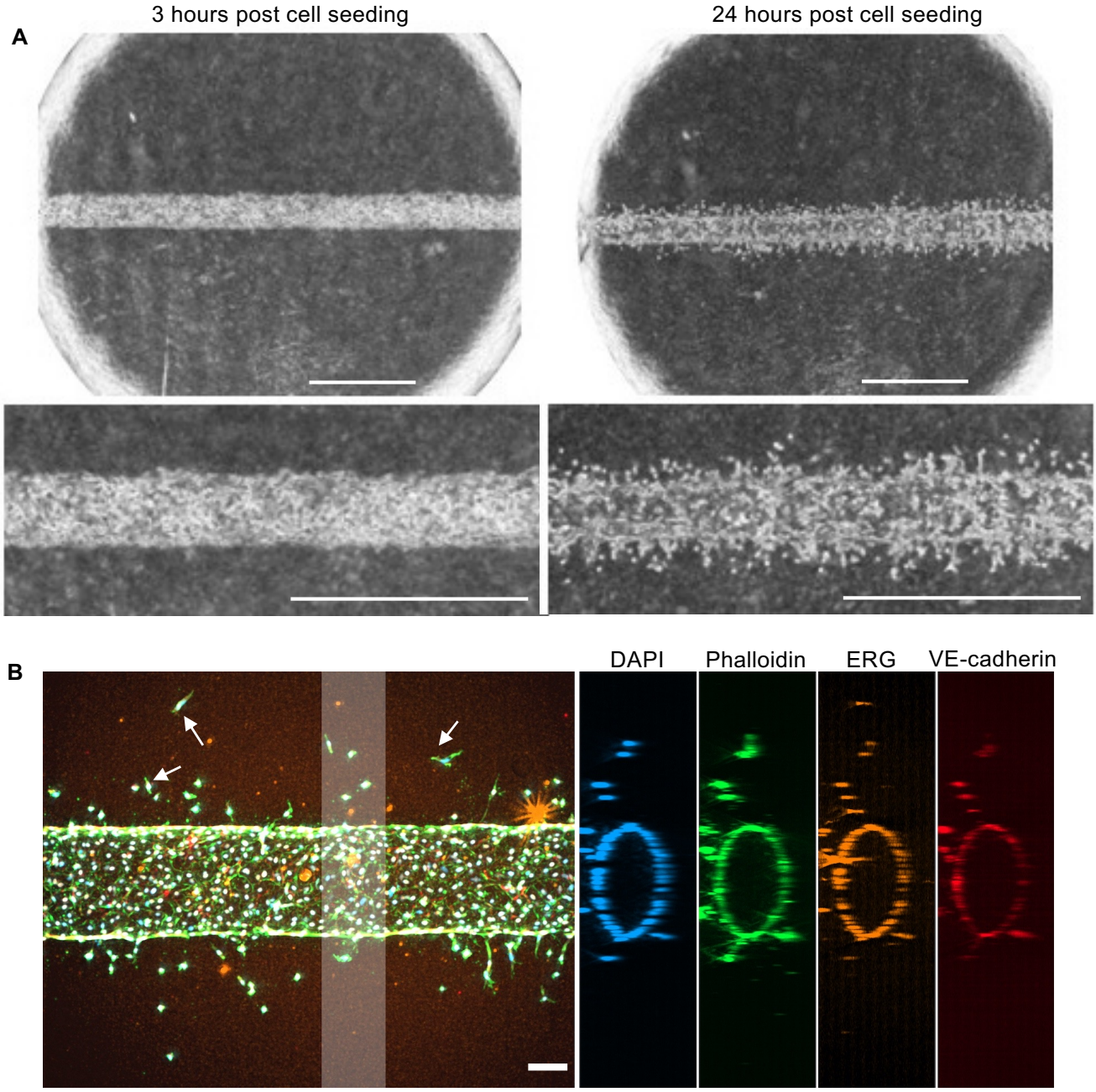


Figure 2.14: EC migration into the collagen. A: Endothelial cells are migrating into the collagen at 24 hours post cell seeding, which was not observed 3 hours post cell seeding. Scale bars=1 mm B: Immunofluorescent staining with DAPI (blue), phalloidin (green), ERG (orange) and VE-cadherin (red), showing endothelial cells detached from the vessel wall and migrating into the collagen (examples highlighted with white arrows). Scale bar=100 µm.

2.3.4 Endothelial monolayer formation

Problem: During cell culture in the microfluidic device, endothelial cells would migrate into the collagen rather forming a monolayer lining the lumen of the vessel.

Details: Figure 2.14 (A) shows that HUVEC remained within the vessel boundaries for 3 hours following cell seeding but were migrating into the collagen at 24h post cell seeding. This was further confirmed with immunofluorescent staining after overnight culture, observing endothelial cells in the collagen, which had detached from the vessel wall (Figure 2.14 (B)). We investigated if this was a problem with the setup in the microfluidic device or with the substrate on which the cells were cultured.

Test 1 (substrate): EC adhesion was investigated outside of the microfluidic device, in a 24-well tissue culture plate. Collagen was polymerised in a 24-well tissue culture plate, HUVEC seeded on top and cell culture media changed once a day.

Outcome 1 (substrate): Results showed that HUVEC adhered to the collagen and formed a monolayer on top of the polymerised collagen, which remained viable for at least six days (Figure 2.15), suggesting that there is no problem with culturing endothelial cells on pre-polymerised collagen at this concentration.

Test 2 (setup): The vessel was observed for nine hours following cell seeding to investigate changes in monolayer formation before it was connected to the perfusion unit. Cell culture media was changed manually every two hours using a pipette.

Outcome 2 (setup): Figure 2.16 indicates that no cell migration into the collagen occurred within the first 9h following cell seeding. We therefore hypothesised that cell migration into the collagen was related to perfusing the vessel, as there was no visible cell migration into the collagen under static conditions.

Test 3 (transverse pressure gradients): Song and Munn (2011) showed that transverse pressure gradients resulted in endothelial cell invasion into a collagen gel in a 3-channel microfluidic device with collagen in the centre channel and HUVEC cultured on PDMS substrates in the outer channels. We therefore investigated transverse pressure gradients across the vessel, which would be caused by a leak from the ECM inlets. Due to small volumes, this could occur without observing fluid leakage as any fluid that escaped through the ECM inlets could evaporate inside the incubator. Four different approaches for preventing transverse pressure gradients were investigated

1. Closing the ECM inlets using tubing connected to a blunt 27G needle, both filled with cell culture media, and using a luer plug at the end of the needle (Cole Parmer) to close the inlet (Figure 2.17 (A)). This was the initial method used for sealing the ECM inlets to allow opening the luer plug to deliver compounds through the ECM.
2. A device manufactured without any ECM inlets was used as a positive control to eliminate any transverse pressure gradients across the vessel (Figure 2.17 (B)).
3. Sealing the ECM inlets with stainless-steel rods (diameter=0.8 mm) (Figure 2.17 (D)). Stainless-steel 316 was chosen as it has high corrosion resistance, which is important when used with liquids and in a humid environment, and the material causes no thrombogenic, toxic or inflammatory response when used *in vivo* (Eliaz, 2019), which is important to prevent the release of foreign molecules into the collagen during cell culture.
4. Closing one ECM inlet with a stainless-steel rod and the other with tubing with a blunt 27G needle and a luer plug, for direct comparison of the two methods (Figure 2.17 (C)).

Outcome (Transverse pressure gradients): Transverse pressure gradients across the vessel could be eliminated by changing the method for sealing the ECM inlets. The initial approach using luer plugs resulted in significant cell migration into the collagen during perfusion. When removing the ECM inlets, no cell migration into the collagen was observed 18 hours post cell seeding, indicating that transverse pressure gradients due to insufficient sealing of the ECM inlets was the cause of this problem. However, by removing the ECM inlets from the design collagen needed to be injected through the vessel inlets, which introduced problems with reproducibility due to blocked vessel inlets (described earlier in this chapter). Comparing sealing one ECM inlet with a luer plug and the other with a stainless-steel rod, cell migration was visible only in the direction of the ECM inlet sealed with the luer plug. Furthermore, sealing both ECM inlets with the stainless-steel rods showed no cell migration into the collagen, comparable to the results from the devices without ECM inlets, and therefore this method was chosen for sealing the ECM inlets.

To confirm that sealing the ECM inlets with stainless-steel rods did not introduce any unwanted pressure gradients in the device, the platform technology *iPerfusion* (Sherwood et al., 2016) was used to compare resistances between a device without any ECM inlets and one where the ECM inlets were sealed using stainless-steel rods. Obtaining comparable measurements of resistance for the two cases would demonstrate the absence of leaks. Using *iPerfusion*, the resistance (R) of the vessel was measured by recording the flow

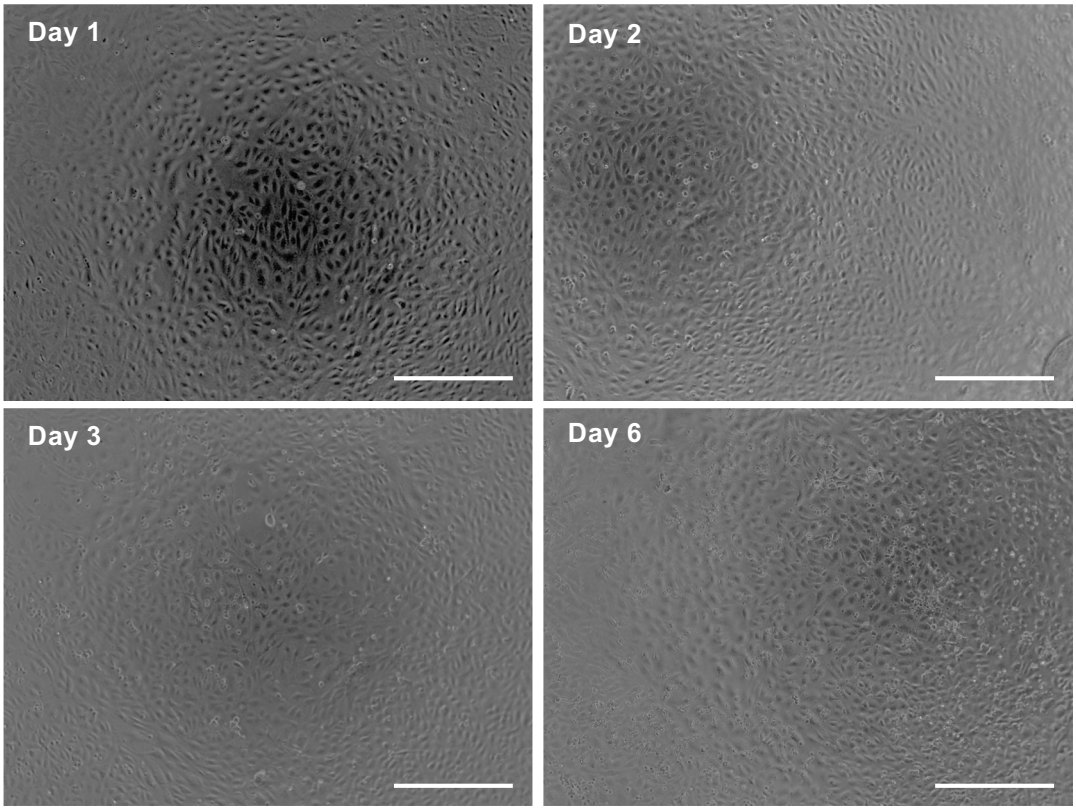


Figure 2.15: EC adhesion to collagen. Phase contrast images showing HUVEC cultured on top of polymerised collagen in a 24-well tissue culture plate. Representative images based on n=3 wells. The cells formed a monolayer on top of the collagen, which remained viable for six days in culture when changing the cell culture media once every day. Scale bars=1 mm.

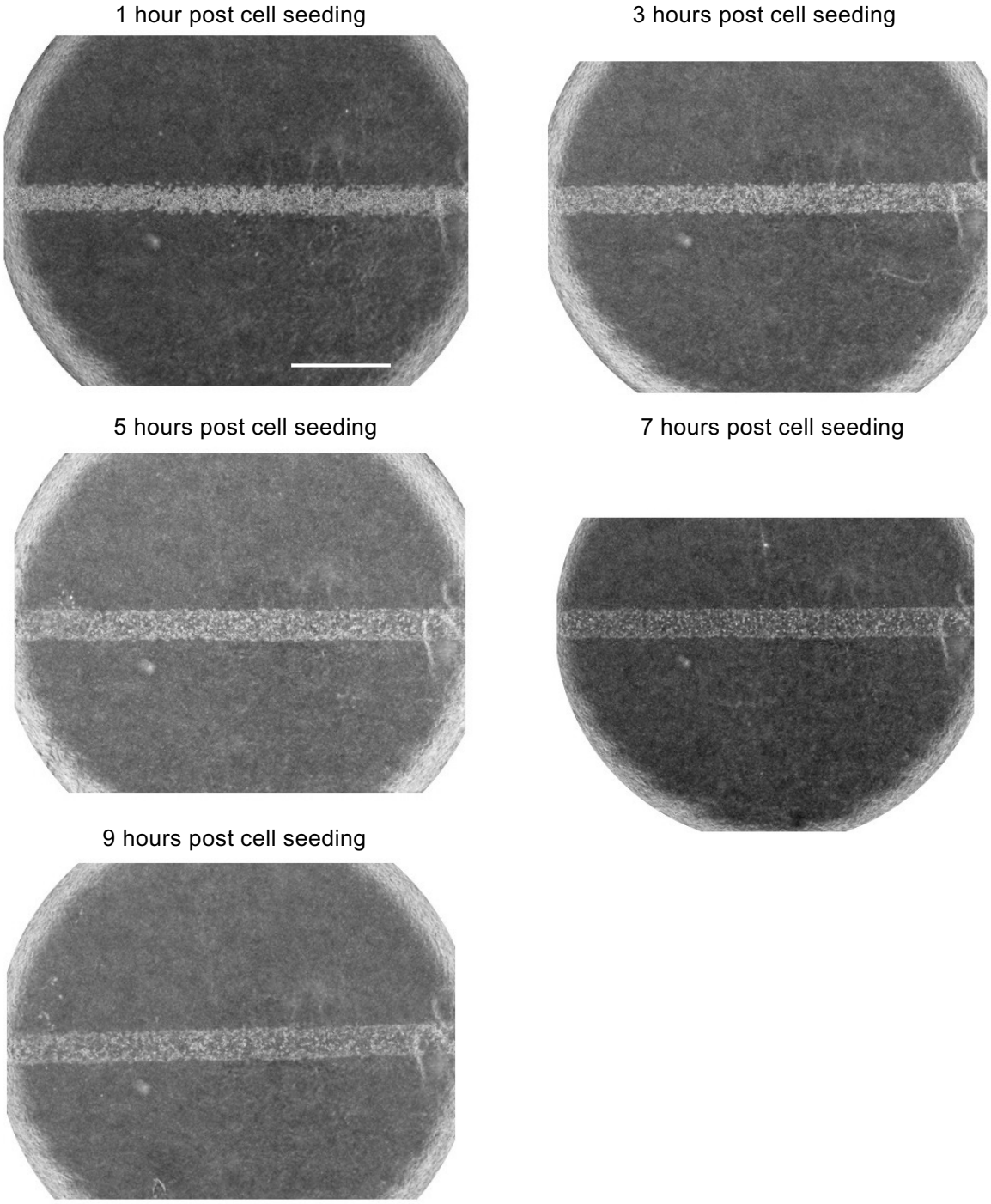


Figure 2.16: Time course of static cell culture in the blood vessel-on-a-chip model. No cell migration into the collagen was observed for the first nine hours after cell seeding when the device was incubated under static conditions and cell culture media was changed manually every two hours using a pipette. Representative images based on n=2 vessels. Scale bar=1 mm (applies to all images).

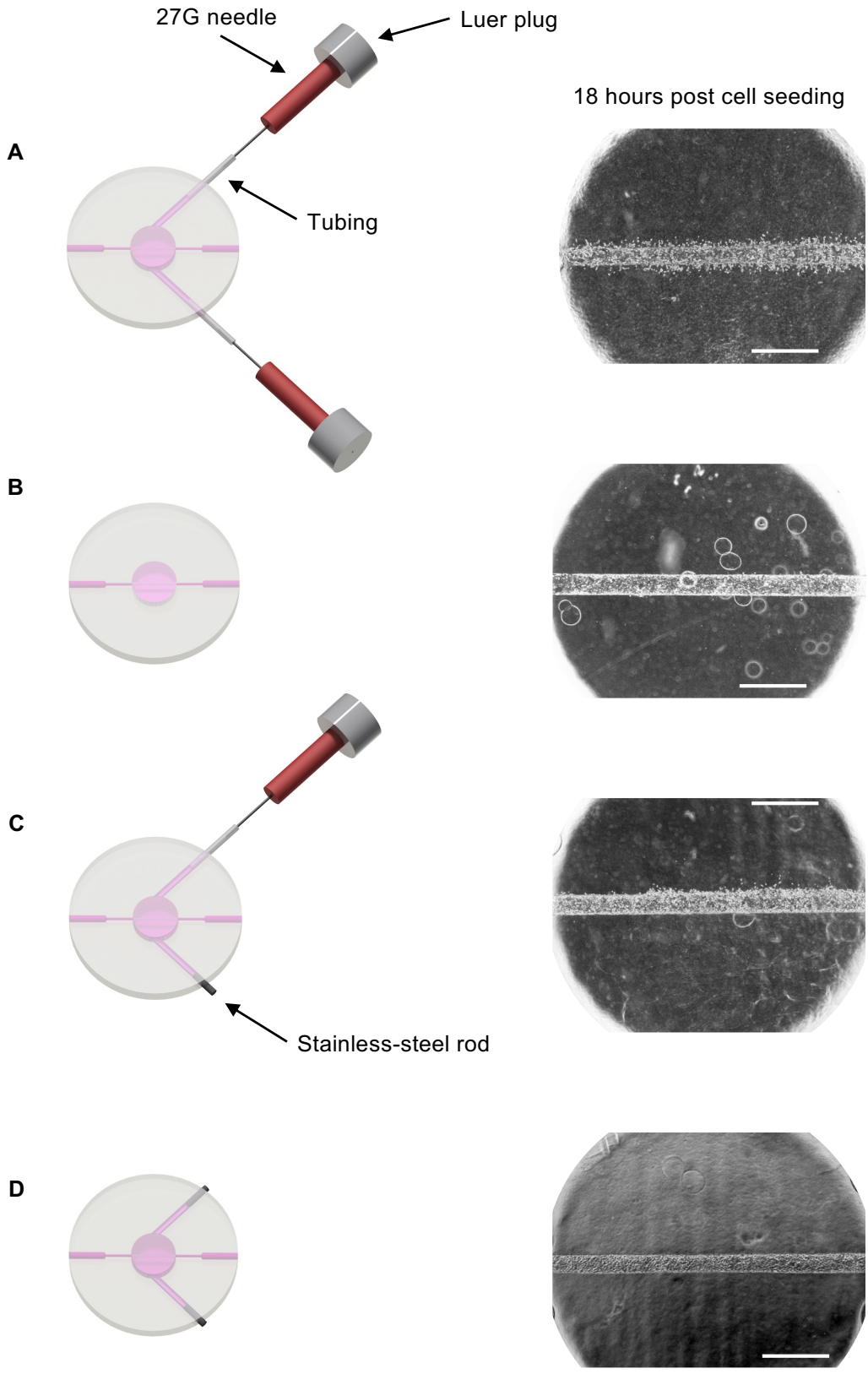


Figure 2.17: Different methods for sealing the ECM inlets to avoid transverse pressure gradients. A: Both ECM inlets are sealed by connecting tubing to the inlet, through which a 27G blunt needle is inserted, which is closed using a luer plug. This method results in EC migration into the collagen. Condition repeated for n>10 vessels. B: The microfluidic device is manufactured without any ECM inlets, resulting in no cell migration into the collagen. Condition repeated for n=3 vessels. C: Comparing two methods for sealing the ECM inlets: the 27G needle setup (as described in A) and using stainless-steel rods. Here cell migration is only observed in the direction of the 27G needle. Condition repeated for n=2 vessels .D: Using stainless-steel rods to seal both inlets does not result in any cell migration into the collagen. Condition repeated for n>10 vessels. Scale bars=1 mm.

rate (Q) though the vessel at defined pressure drops (∆P), according to Equation 2.3 (assuming Poiseuille flow), where μ is the viscosity of the perfusate, L is the length of the vessel and d is the vessel diameter.

$$R_{Analytical} = \frac{\Delta P}{Q} = \frac{128\mu L}{\pi d^4} \quad (2.3)$$

If there was fluid escaping through the ECM inlets, the resistance of the vessel would be lower than the analytical solution. The analytical values of resistance calculated for the vessel (and connected tubing) are shown in Table 2.2.

	Analytical resistance mmHg/(μl/min)
Vessel (including narrowing inlets)	0.0057
40 cm tubing (ID=0.3 mm)	0.2515
Total	0.2572

Table 2.2: Analytical resistances for the tubing and the vessel, for comparison to iPerfusion measurements.

In this experiment, the device was connected to the iPerfusion system using approximately 20 cm of tubing (ID=0.3 mm) on either side of the device. The flow rate of water through the vessel and the pressure drop along the vessel was recorded using a flow sensor and pressure sensor respectively, in response to six different pressure drops between the inlet and outlet reservoirs, which was achieved by changes in hydrostatic pressure from vertically displacing the inlet reservoir. The experimental setup is shown in Figure 2.18 (A-B) and the lumped-parameter model for the fluidic circuit is shown in Figure 2.18 (G). Measurements were taken twice, once when increasing the pressure drop and once when decreasing the pressure to reach the starting value. Pressure drops and flow rates were recorded for 60 seconds on each step. Data analysis was carried out using Matlab (MathWorks) using the average signal over 30 seconds (indicated by the grey shaded area in (Figure 2.18 (C-D)). Values of resistance were obtained using a linear fit between data points of pressure and flow rates, where the slope of the fit represents resistance (Figure 2.18 (E-F)). The measurements resulted in resistances of 0.2538 (±0.0036) mmHg/(μl/min) and 0.2684 (±0.0156) mmHg/(μl/min), respectively for no ECM inlets and ECM inlets sealed with stainless-steel rods, results reported with 95% confidence bounds on the fits. Comparing to the analytical solution where a diameter of 300 μm was used, the experimentally obtained resistance values for the device without ECM inlets predicts a diameter of 301 μm (±1μm) and the device where the ECM inlets were sealed using stainless-steel rods predicts a diameter of 297 μm (±4μm). From these results it was concluded that there were no problems with transverse pressure gradients caused by leaks when sealing the ECM inlets with stainless-steel rods, as the pressure drops used here (~5-9 mmHg)

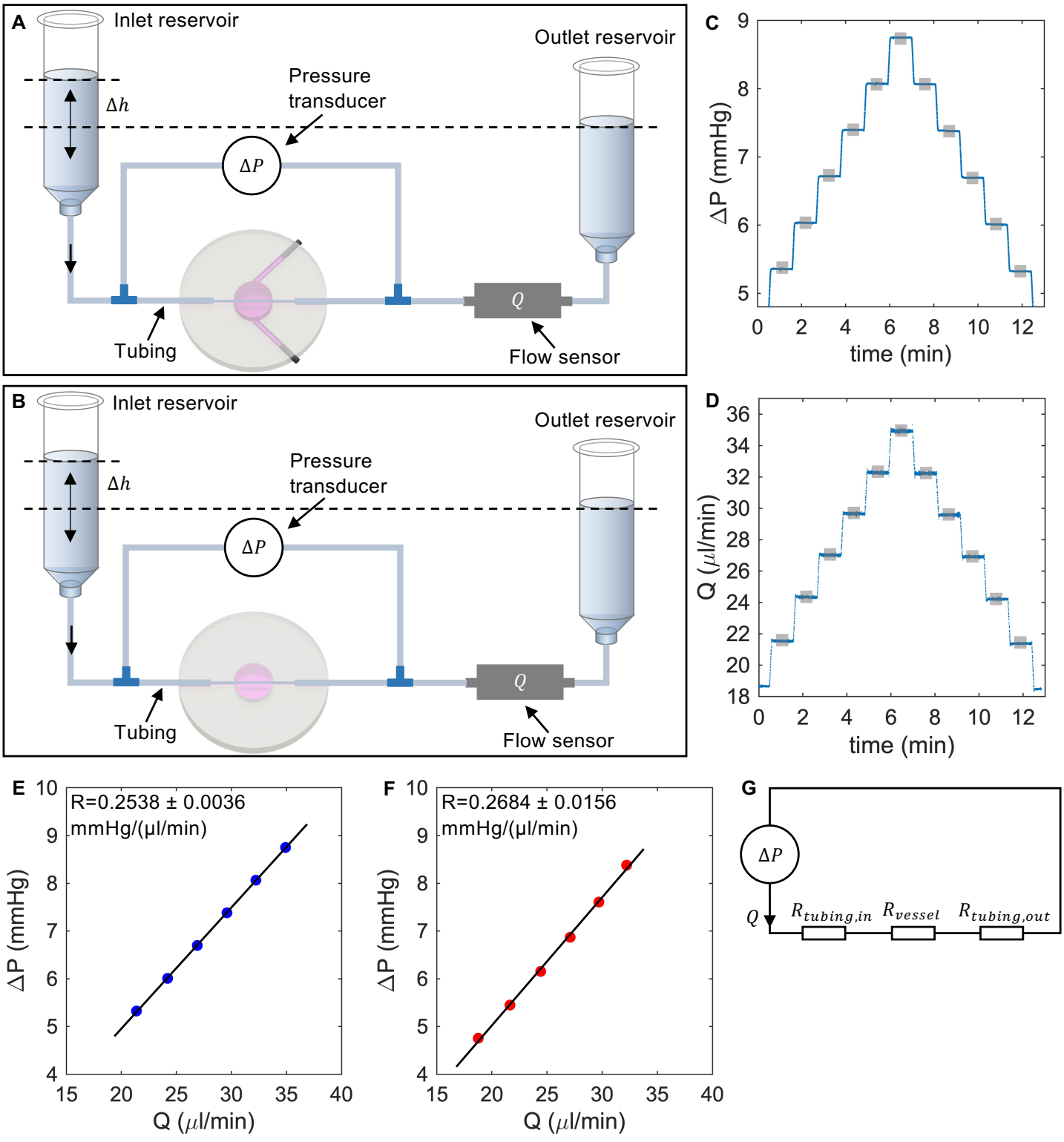


Figure 2.18: Using iPerfusion to measure the resistance of the vessel. A-B: Schematics of the experimental setups using iPerfusion for measuring the resistance of a vessel where the ECM inlets are sealed using stainless-steel rods (A) and a device without ECM inlets (B). C-D: Pressure drops and flow rates were recorded for 60 seconds on each pressure step and the average over 30 seconds was used for analysis (shaded grey area in the graphs). E-F: Resistance values were obtained as the slope when fitting a linear curve between pressure and flow data (black line indicates the fit). The measured resistance of the vessel in a device without ECM inlets is shown in E and the measured resistance of the vessel where the ECM inlets were sealed with stainless-steel rods is shown in F. Data based on n=1 vessels per condition, performing the experiments sequentially.

were significantly higher compared to what is used during culture in the 3D printed perfusion unit (<1 mmHg for a 11 mm height difference between the inlet and outlet reservoirs).

2.3.5 The incubator environment and cell viability

After forming an endothelial monolayer lining the lumen of the blood vessel, it was observed that the monolayer would get disrupted when placed in the incubator after changing the cell culture media. Figure 2.19 (A-C) shows representative images of how the monolayer changed in response to environmental conditions when it was placed in the incubator. Figure 2.19 (A) shows a vessel 24 hours post cell seeding, when it was taken out from the incubator to refill the inlet reservoirs. Here the monolayer shows a confluent vessel with a cobblestone morphology. The vessel was then placed back in the incubator and taken out again after about 10 minutes (Figure 2.19 (B)), at which point the morphology of the monolayer had changed and was disrupted. However, if the vessel was then placed back in the incubator for about two additional hours, the morphology would recover to again show a cobblestone morphology (Figure 2.19 (C)). This experiment was performed using M199 cell culture media (supplemented with 1% Penicillin/Streptomycin, 2% L-Glutamine, 20% FBS (Fetal Bovine serum), heparin (1000 U/ml) and 30 mg/ml endothelial cell growth factors, ECGF). In comparison, no obvious changes in cell morphology could be observed in HUVEC cultured in a 6-well tissue culture plate 10 minutes after placing the plate back in the incubator (Figure 2.19 (D-E)). The main difference between the two setups, the microfluidic device and the 6-well tissue culture plate, is the volume of cell culture media, <1 µl inside the vessel compared to 1 ml in the 6-well tissue culture plate, suggesting that any environmental changes related to the cell culture media would affect the vessel in the microfluidic device much quicker compared to the cells cultured in the 6-well tissue culture plate. To investigate the cause of this problem, two environmental parameters were independently studied: humidity and pH.

2.3.5.1 Humidity inside the incubator

Problem: Evaporation of cell culture media from the microfluidic device could cause EC monolayer disruption.
Details: The humidity level inside the incubator will decrease in response to opening the door, which could result in evaporation of cell culture media. It has been shown that evaporation of cell culture media through PDMS microfluidic devices can lead to a shift in osmolality (Heo et al., 2007). To investigate if this was the cause of the monolayer disruption the microfluidic device was submerged in water (after connection to the 3D printed perfusion unit ensuring that no inlets were open to the surrounding water). This experimental setup

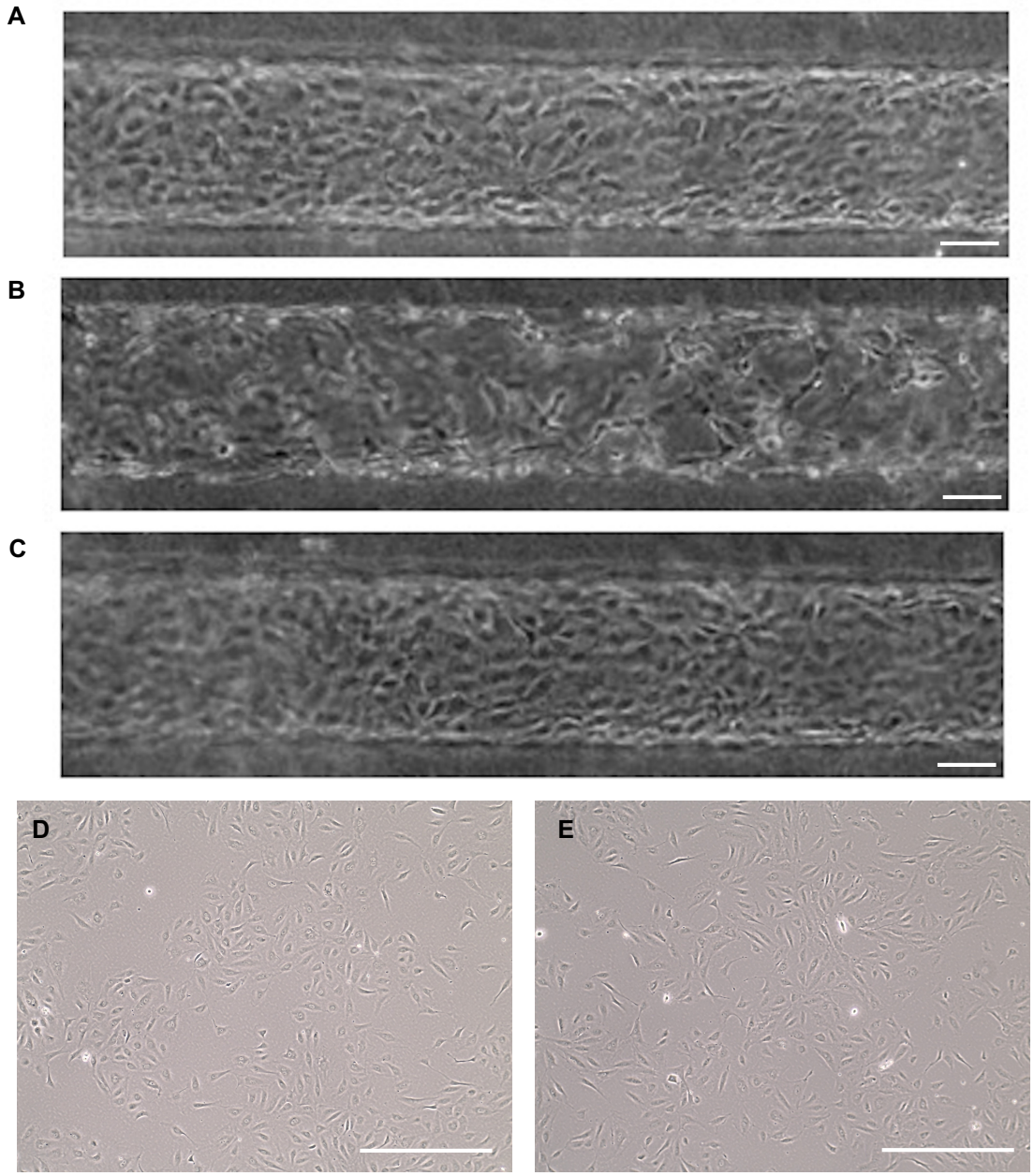


Figure 2.19: EC monolayer disruption related to the incubator environment. A-C: Representative images based on n=2 vessels. Scale bars=100 µm. A: The vessel after overnight culture, showing a characteristic cobblestone morphology. B: After refilling the inlet reservoirs with cell culture media the vessel is placed back into the incubator for ~10 minutes and then imaged, showing a disrupted monolayer. C: Placing the vessel in the incubator for another two hours, the monolayer recovers to again show a cobblestone morphology. D-E: Phase contrast images of HUVEC in a 6-well tissue culture plate with 1 ml cell culture media per well. Scale bars=500 µm. D: 24 hours after cell seeding. E: Placing the plate back inside the incubator for ~10 minutes and then taking it out again does not seem to affect the cell morphology in this culture setting.

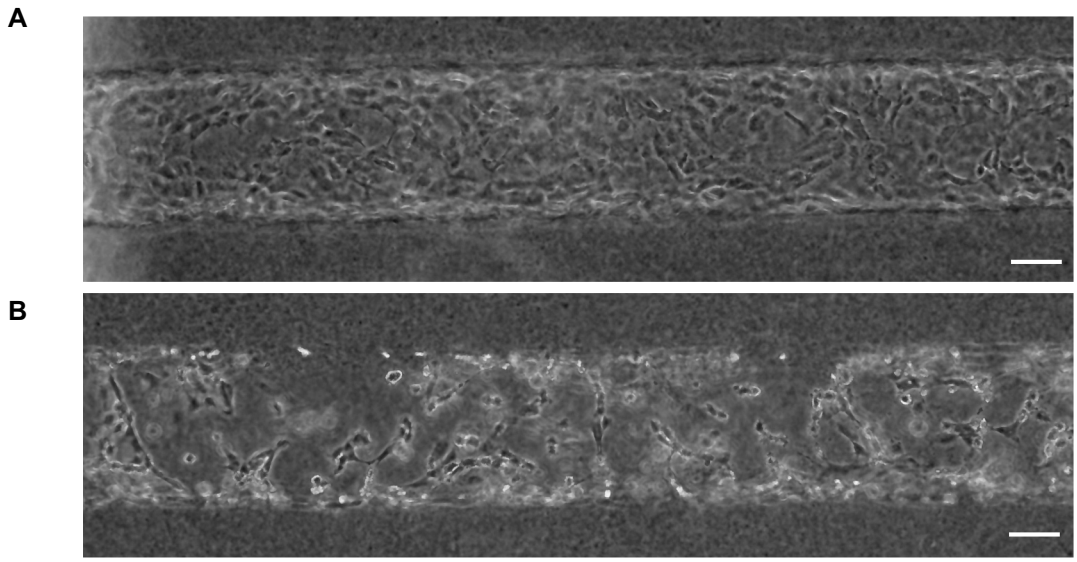


Figure 2.20: The effect of humidity on EC monolayer disruption (n=1 vessel). The microfluidic device was submerged in water to prevent evaporation of cell culture media through the PDMS surface. A: The vessel monolayer shows a cobblestone morphology when taken out two hours after being placed inside the incubator and submerged in water. B: Placing the device in the incubator and taking it out after ~10 minutes results in monolayer deformation even when the device was submerged in water. Scale bars=100 μm.

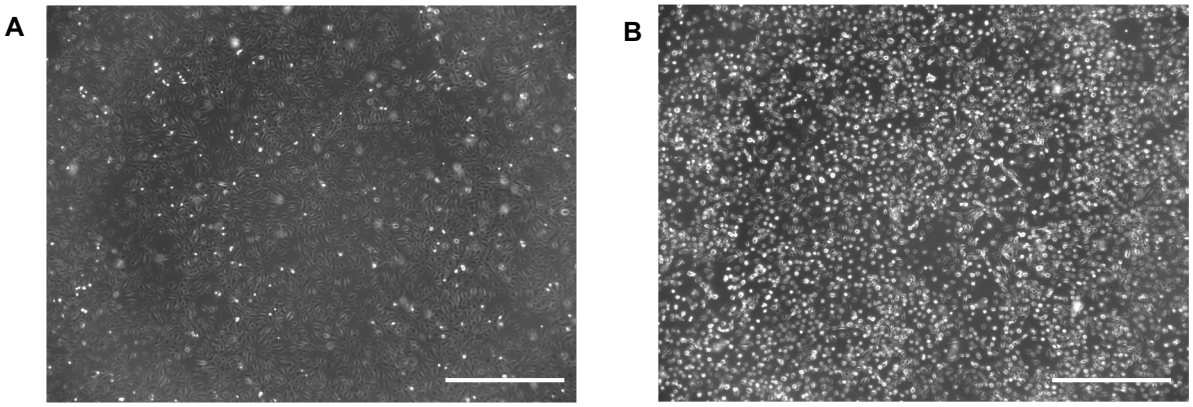


Figure 2.21: Changes in cell morphology due to increased pH. 4x magnification phase contrast images of HUVEC cultured in a 6-well tissue culture plate in M199 cell culture media (1 ml per well). A: The EC monolayer directly after it was taken out from the incubator. B: After 90 minutes at 37°C with atmospheric CO_2 detached cells are clearly visible (white dots indicate round cells). Scale bars= 500 μm.

would eliminate any PDMS-air interfaces and thereby remove the possibility of evaporation of cell culture media through the PDMS surface.

Outcome: Results show that preventing evaporation through the microfluidic device did not solve the problem with monolayer disruption when placing the device inside the incubator (Figure 2.20).

2.3.5.2 pH-levels in cell culture media

Problem: Changes in the pH of cell culture media could cause EC monolayer disruption.

Details: Cell culture media is conventionally pH buffered using sodium bicarbonate, M199 included. Sodium bicarbonate is CO_2 dependent, resulting in decreased pH in response to increased CO_2 levels. When opening the incubator, CO_2 levels inside the incubator will decrease (from 5%), due to lower CO_2 levels in ambient air (~1%). To investigate the response to CO_2 dependent changes in pH, HUVEC cultured in a 6-well tissue culture plate (1 ml M199 media per well) were placed inside a temperature-controlled microscope stage, heated to 37°C and at atmospheric CO_2. Figure 2.21 shows the monolayer before placing it on the stage (Figure 2.21 (A)) and 90 minutes later (Figure 2.21 (B)). This was sufficient time for the pH to change, at which point detached cells were clearly visible, suggesting that a cell environment that causes the pH to increase results in a disrupted EC monolayer. To reduce the impact of CO_2 dependence on pH buffering, the cell culture media was supplemented with 25 mM HEPES buffer, which is a pH-independent buffer (10-25 mM recommended by the manufacturer, Sigma). The same experiment where the monolayer was imaged 10 minutes after placing the device back in the incubator was repeated using M199 or EGM2 (Lonza) cell culture media, both supplemented with 25 mM HEPES.

Outcome: Figure 2.22 clearly shows that the pH dependence cannot be overcome using M199 cell culture media, even when it is supplemented with HEPES; however, when using EGM2 the monolayer remained intact and only very small pH dependent effects were observed. Therefore, the cell culture media used in the blood vessel-on-a-chip model was changed to EGM2 supplemented with 25 mM HEPES.

2.3.6 Maintaining vessel integrity during long-term culture

The cell number to volume ratio is significantly lower in microfluidic devices than in conventional cell culture techniques. Considering a 6-well tissue culture plate, with a cell density of 50,000 cells/cm^2 and 1 ml volume per well as per the manufacturers' instructions, this tissue culture format results in >10 times higher volume of available cell culture media per cell, compared to culture in the 300 µm diameter vessel in the blood vessel-on-a-chip platform (Table 2.3).

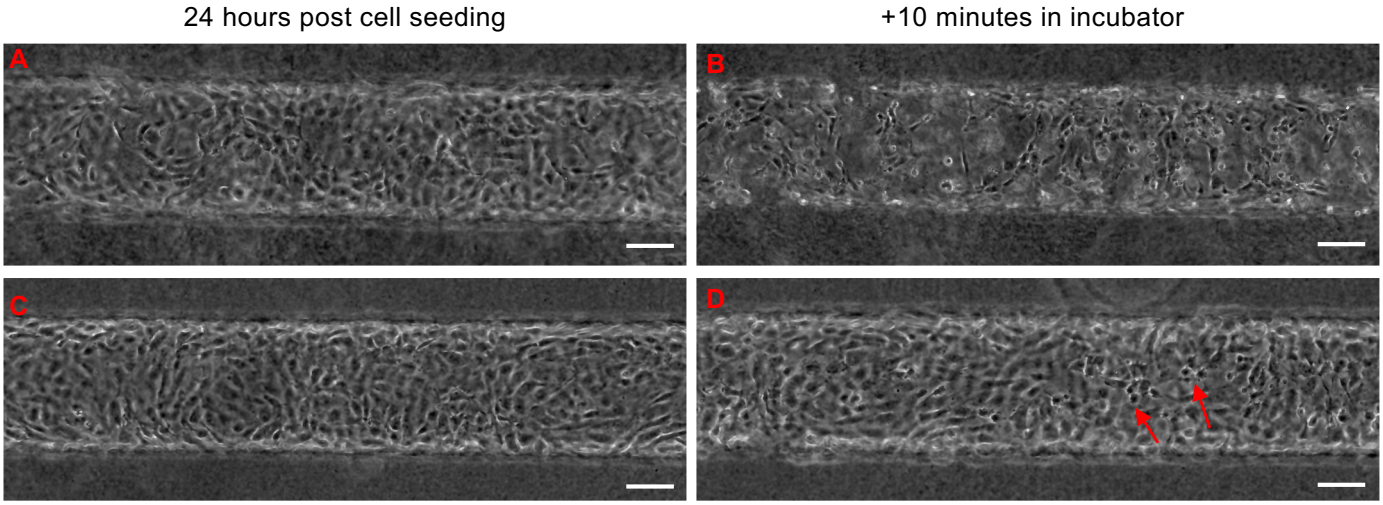


Figure 2.22: Supplementing the cell culture media with HEPES prevents EC monolayer disruption. Repeating the experiment where the monolayer is imaged 10 minutes after placed in the incubator for cell culture media (M199 or EGM2) supplemented with 25 mM HEPES buffer, both conditions show vessels with cobblestone morphologies following 24 hour culture. Representative images based on n=2 vessels. A-B: Even after supplementing the M199 cell culture media with HEPES pH dependent affects on the EC monolayer cannot be overcome. C-D: Using EGM2 cell culture media, the monolayer remains intact and only small pH dependent effects could be observed (indicated with red arrows). Scale bars=100 μm.

	300 µm diameter vessel	6-well tissue culture plate
Surface area (mm^2)	4.7	960
Cell number	2356	480000
Volume (µl)	0.35	1000
Volume/cell (nl)	0.15	2.1

Table 2.3: Surface areas, cell numbers and volumes for the 300 µm diameter vessel in the microfluidic device and a conventional 6-well tissue culture plate, at a cell density of 50,000 cells/cm^2.

Consequently, due to the very low volume within the vessel (~0.35 µl) vessel integrity was not maintained in the microfluidic device during overnight culture under static conditions. Figure 2.14 shows representative images of endothelial cells in the vessel when the device was left in a 24-well plate under static conditions for four hours and then at 16 hours post cell seeding, indicating cell detachment, and showing that the vessel did not maintain its integrity for 16 hours without media turnover. For practical reasons, the model should support culture without manual intervention for a minimum of 16 hours (overnight culture) and therefore, perfusion was required in this model to maintain vessel integrity during long-term culture. Three different methods for perfusing the vessel were investigated to facilitate media turnover during overnight culture: a syringe pump, hydrostatic pressure and a gas-pressure controlled perfusion system.

2.3.6.1 Syringe pump

Syringe pumps provide flow-driven perfusion, using a stepper motor to push or withdraw a syringe to deliver fluid at a pre-defined constant flow rate. The fluidic circuit was designed using manifolds to split the flow into five parallel channels, which allowed five devices to be perfused in parallel (schematic and lumped-parameter model shown in Figure 2.24). This setup was used in the early stages of the project, before the ECM inlets were sealed with stainless-steel rods and therefore, the valves connected to the ECM inlets were kept closed during perfusion. Using a fixed flow rate (Q), the pressure drop (ΔP) in the system is dependent on the total resistance (R_{tot}), assuming Poiseuille flow according to Equation 2.4, where the resistance is determined by the tubing and vessel dimensions (diameter d and length L), according to Equation 2.5. Using the same length tubing to connect all channels, the resistance of all channels should be the same ($R=R_1=R_2=R_3=R_4=R_5$) (Equation 2.6). This further results in the same flow rate across all devices ($Q_1=Q_2=Q_3=Q_4=Q_5=Q/5$).

$$Q = \frac{\Delta P}{R_{tot}} \tag{2.4}$$

$$R = \frac{128\mu L}{\pi d^4} \tag{2.5}$$

$$\frac{1}{R_{tot}} = \frac{1}{R_1} + \frac{1}{R_2} + \frac{1}{R_3} + \frac{1}{R_4} + \frac{1}{R_5} = \frac{5}{R} \tag{2.6}$$

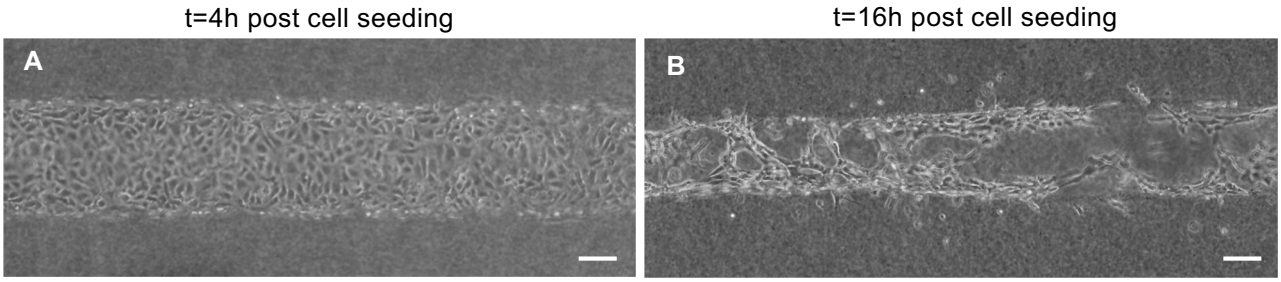


Figure 2.23: Cell viability is not maintained in the vessel during static culture conditions. Top view brightfield images showing representative examples of two different vessels cultured under static conditions (when the microfluidic device is placed in a 24-well tissue culture plate). Representative images based on n>10 vessels A: Four hours post cell seeding endothelial cells have adhered to the collagen and a characteristic cobblestone morphology can be observed. B: 16 hours post cell seeding the monolayer is disrupted. Scale bars=100 µm.

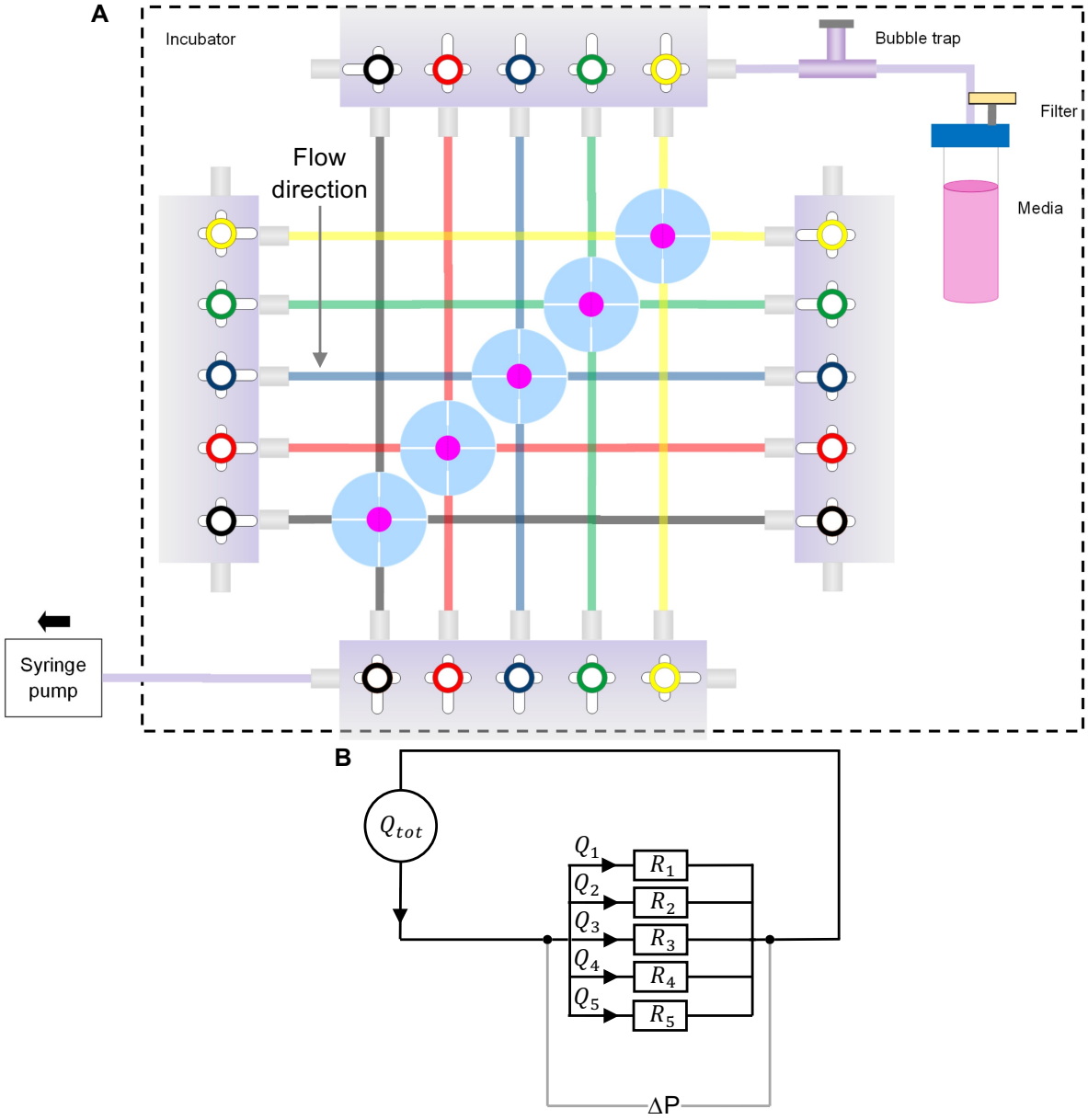


Figure 2.24: Schematic and lumped-parameter model for perfusion using a syringe pump. A: Schematic of the fluidic setup for perfusion with a syringe pump, which is placed outside the incubator. Cell culture media is withdrawn from a reservoir inside the incubator and manifolds are used to split the fluid into five channels, allowing perfusion of five devices in parallel. B: Lumped-parameter models showing how the flow rate is split between the five channels. If the combined resistance of the vessel and tubing is the same for all five channels, all vessels will have the same flow rate.

However, if the resistance in one or more of the channel changes (for example due to air bubbles in the tubing or a leak) the flow will be split differently. Therefore, using this setup the flow rate and shear stress experienced by the individual vessels could not be accurately controlled.

Problem 1: Air bubbles in the system could obstructs flow.

Details: As shown in the schematic in Figure 2.24, the vessels were perfused by withdrawing fluid from a reservoir with cell culture media inside the incubator, which was open to atmospheric pressure through a syringe filter. This setup was prone to air bubble formation as when fluid is withdrawn it moves from atmospheric pressure to a pressure below atmospheric pressure. This decrease in pressure causes gas bubbles to form as the amount of gas that can be held in solution decreases with pressure (according to Henry's law). However, since the syringe pump is placed outside the incubator cell culture media would not be pre-conditioned to incubator conditions when entering the vessel if the opposite direction was used.

Outcome: A bubble trap was introduced in line with the media reservoir to remove air bubbles upstream of the manifold.

Problem 2: The setup was difficult to use and resulted in low success rate for long-term culture of multiple devices in parallel.

Details: Connecting four pieces of tubing per device to the manifolds, which were all prone to air bubble formation, required long setup times and frequently resulted in one or more devices not being perfused due to air bubbles blocking the tubing. Furthermore, connecting and disconnecting tubing for imaging the vessel could result in vessel or collagen damage if not handled very carefully. Syringe pumps are generally easy to use as the fluidic circuit can be assembled in a tissue culture hood and then attached to the pump, since fluid is not in direct contact with any components of the pump. However, an important limitation of using a syringe pump for this application was the limited range of shear stress that could be achieved with this setup. Since a syringe pump provides one-directional perfusion, rather than circulating the media, it requires large volumes of cell culture media for perfusion as physiological shear stress. For example, using a 50 ml syringe with cell culture media could perfuse five devices at 10 dynes/cm^2 only for less than one hour.

Outcome: This setup with a syringe pump was only used in the initial stages of the project and was not taken forward for model validation or for long-term perfusion at physiological shear stress.

2.3.6.2 Hydrostatic pressure

The second method investigated for perfusing the vessel was hydrostatic pressure. In a hydrostatic pressure-driven perfusion system, the flow rate through the vessel is determined by the height difference between the inlet and outlet reservoirs (∆h), according to Equation 2.7, together with the total resistance in the fluidic circuit (R_{tot}), where ρ is the fluid density and g is the acceleration due to gravity.

$$\Delta P = \rho g \Delta h = Q R_{tot} \quad (2.7)$$

The main advantage of using hydrostatic pressure-driven flow is that it does not require an external perfusion system, which therefore does not limit the number of experiments that can be carried out in parallel. However, as cell culture media is not circulated there is a limit on the flow rates (and shear stresses) that can be achieved during overnight culture without requiring unfeasibly large height differences and amounts of cell culture media. Hence, the goal with this perfusion method was to facilitate continuous media turnover for cell survival inside the vessel rather than applying physiological shear stress. The following design criteria were used for designing the perfusion unit, which was designed using the CAD software Autodesk Inventor and manufactured by 3D printing. The optimised version of the 3D printed perfusion unit was used for all experiments presented in Chapters 3-5.

1. The perfusion unit should provide continuous media turnover of at least one vessel volume per minute that lasts for more than 16 hours.
2. The perfusion unit should allow real-time imaging so that once the microfluidic devices are connected to the tubing they do not need to be disconnected until the end of the experiment.
3. The perfusion unit should be autoclavable to allow repeated use in a sterile cell culture environment.
4. Each device should have an individual flow circuit so if one or more vessels fail this does not affect the rest of the experiment.

2.3.6.2.1 Materials

Two different 3D printing materials were investigated for manufacturing the perfusion unit: VeroClear and Nylon.

Problem 1: The 3D printing material used was not autoclavable and deformed inside the incubator.

Details: Initially, the perfusion unit was manufactured from VeroClear (the same material as the 3D printed moulds for casting PDMS), which is not autoclavable. Furthermore, the device was permanently deformed from exposure to the incubator environment during long periods of time, which reduced imaging capabilities.
Outcome: The perfusion unit was manufactured from nylon instead, which is autoclavable and non-toxic to cells.

Problem 2: 3D printing in nylon yielded parts that were permeable to water.
Details: A different 3D printing technique, Selective Laser Sintering (SLS), was required for manufacturing the perfusion unit from nylon, where powdered material is fused together using the heat from a laser. This 3D printing technique yields parts that are permeable to water and consequently, when filling the reservoirs with cell culture media it would leak through the walls of the unit.
Outcome: To create watertight reservoirs, all inner surfaces of the reservoirs were coated with a thin layer of PDMS and polymerised overnight at 65°C in an oven. It is well known that PDMS is autoclavable and therefore, the coating did not get damaged with repeated autoclaving, so this step was only performed once, directly after 3D printing.

2.3.6.2.2 Design

The perfusion unit was designed with the outer dimensions of a tissue culture plate to be compatible with real-time imaging on a microscope stage. This section describes how the fluidic circuit was designed, considering these restrictions in dimensions, to allow continuous media turnover for >16h.

To maximise perfusion time for a given height difference between the inlet and outlet reservoirs, an overflowing design was used to maintain the fluid level in the outlet reservoir at a constant height. This was achieved by having a small reservoir, into which the tubing was placed, which would overflow into a larger reservoir (Figure 2.25 (C)). The fluid level in the inlet reservoir decreases with an exponential decay (Figure 2.25 (A-B)) with increased perfusion time according to Equation 2.8 (derivation shown in Appendix: Chapter 2). R_{tot} is the equivalent resistance of the fluidic circuit, including the vessel and the tubing (Equation 2.9), as show in in the lumped-parameter model in Figure 2.25 (D). Even though this results in an initial flow rate greater than the minimum design requirement of one vessel volume per minute, it is important to consider that the initial height difference needs to be large enough to facilitate flow even if the incubator is not completely level.

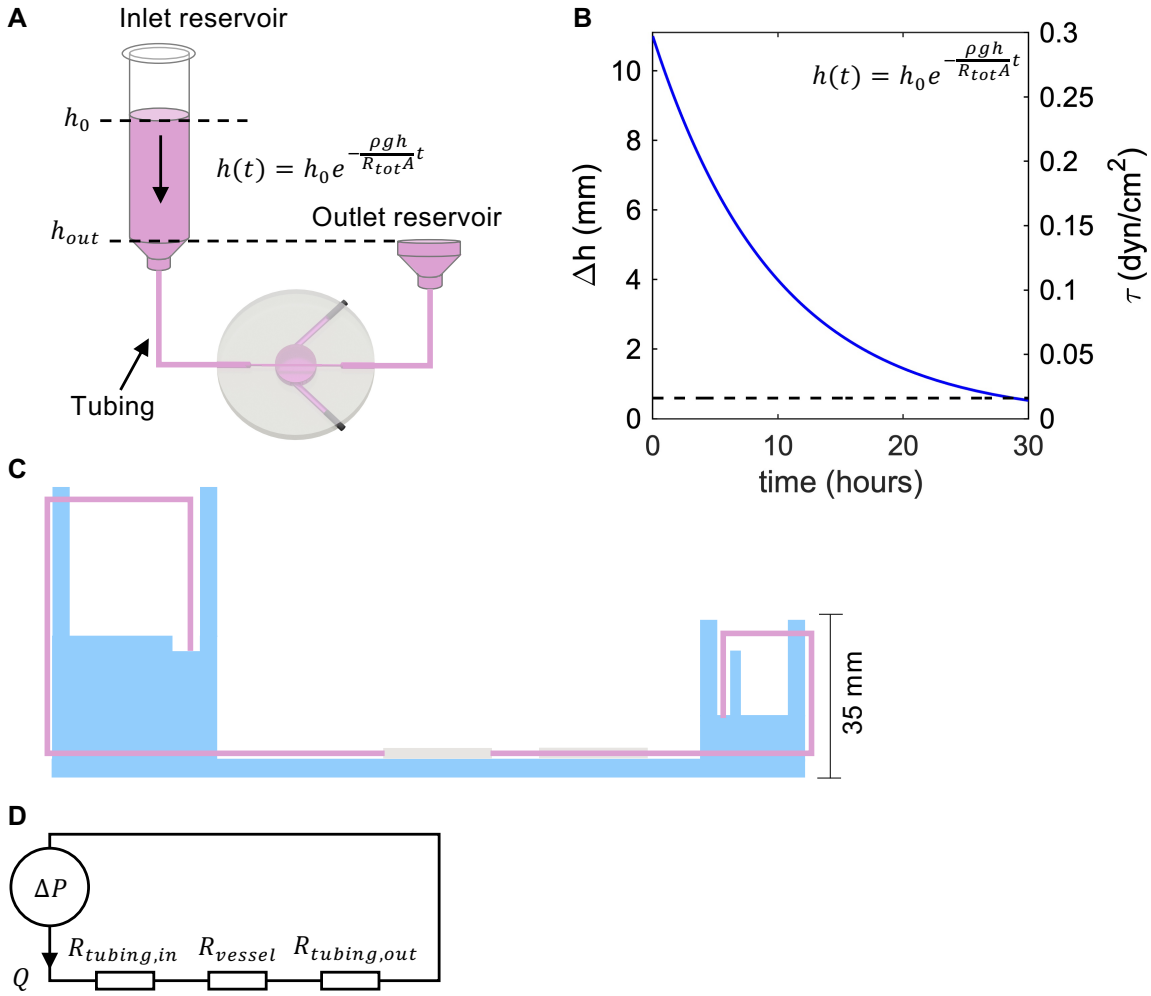


Figure 2.25: Schematic, lumped-parameter model and shear stress in the 3D printed perfusion unit. A: Schematic of the hydrostatic pressure-driven fluidic circuit, using an overflowing design to maintain a constant height fluid level in the outlet reservoir (h_{out}). B: The fluid level in the inlet reservoir decreases with an exponential decay with increasing perfusion time. The values in the graph refer to perfusion using the final version of the 3D printed unit. C: Cross-sectional view of the connector-free 3D printed perfusion unit showing the tubing from the inlet reservoir to the outlet reservoir through the microfluidic device. The outlet reservoir needs to be <38 mm to fit underneath the condenser on a confocal microscope. D: Lumped parameter model of the connector-free design, where the resistance in the fluidic circuit is only dependent on the tubing length and the vessel dimensions.

$$\Delta P = QR_{tot} = \rho g h(t) = \rho g h_0 e^{-\frac{\rho g h}{R_{tot} A} t} \quad (2.8)$$

$$R_{tot} = R_{tubing,in} + R_{vessel} + R_{tubing,out} \quad (2.9)$$

From Equation 2.8, the initial height of the inlet reservoir (h_0), the total resistance across one vessel (R_{tot}) and the surface area of the inlet reservoir (A) need to be chosen to meet the design criteria. A and h_0 are indirectly restricted by the maximum height of the outlet reservoir, which needs to be <38 mm to fit underneath the microscope condenser, limiting the volume of fluid that can be perfused from the inlet reservoir to the outlet reservoir.

Problem: Interfacing with fluidic connectors caused leaking with repeated use and allowed only four vessels to be cultured in parallel.

Details: The first version of the design (Figure 2.26) supported four vessels to be cultured in parallel. Each microfluidic device was connected to an individual inlet reservoir through a series of fluidic connectors: a threaded male luer lock fitting (Cole Parmer) was attached to the inlet reservoir, which had pre-defined holes that had been tapped following 3D printing. A 4 mm diameter syringe filter (Merck Millipore) was connected to the luer fitting, with the purpose of increasing the resistance in the circuit, followed by a blunt 0.5-inch length 27G needle (ID=0.21 mm, OD=0.41 mm, Linton Instrumentation). The microfluidic device was connected by attaching tubing (Fine bore polythene tubing, Portex, Smiths Medical, ID=0.4 mm, OD=0.79 mm) around the blunt needle. To achieve media turnover for at least 16 hours the surface area of the inlet reservoir needled to be larger than what could fit within the dimensions of a tissue culture plate and therefore, an external reservoir was included in the design, which was attached to the inlet reservoir using male luer slip connectors (Cole Parmer). The main issues with this design were problems with the filters getting blocked over time (assumed to be from serum from the cell culture media getting trapped in the filter) as well as fluid leaking from the fluidic connectors. Glue was used to prevent problems with leaking; however, it was not compatible with autoclaving and was therefore not a feasible long-term solution as it needed to be reapplied before every experiment.

Outcome: To avoid all problems with fluid leaking from fluidic connectors, the final version of the 3D printed perfusion unit (which was used for all functional experiments in this project), was a connector-free design, where tubing was threaded between the inlet and outlet reservoirs through 3D printed holes in the unit (Figure 2.25 (C)).

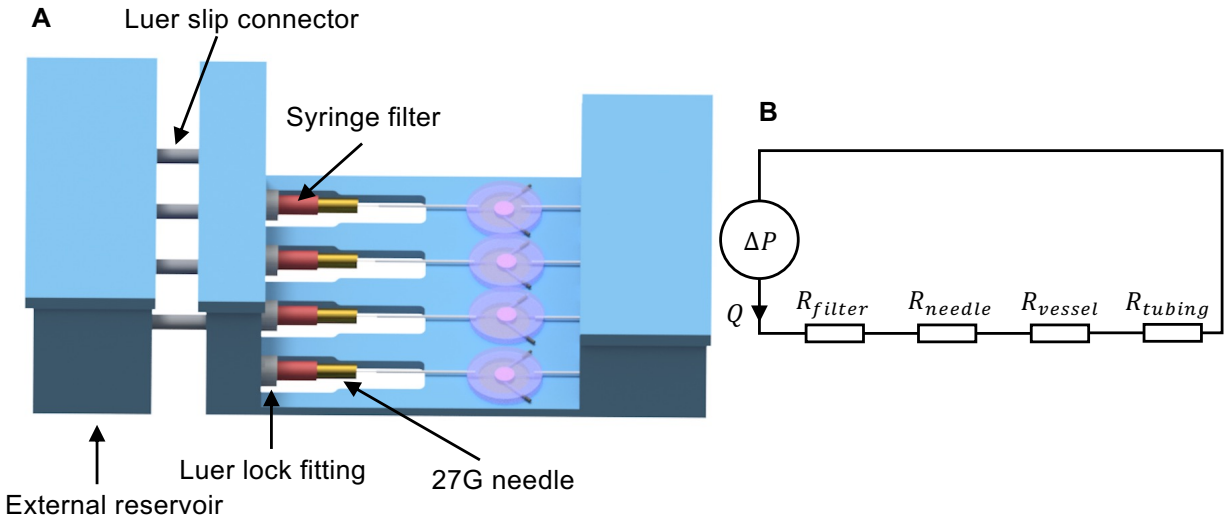


Figure 2.26: Design 1 of the 3D printed perfusion unit. A: The first version of the design of the 3D printed perfusion unit, allowing perfusion of four devices in parallel. Each microfluidic device is connected to the inlet reservoir through a luer lock fitting, a syringe filter and a 27G needle in series. An external reservoir is connected to the inlet reservoir using luer slip connectors. B: Lumped-parameter model of the perfusion circuit.

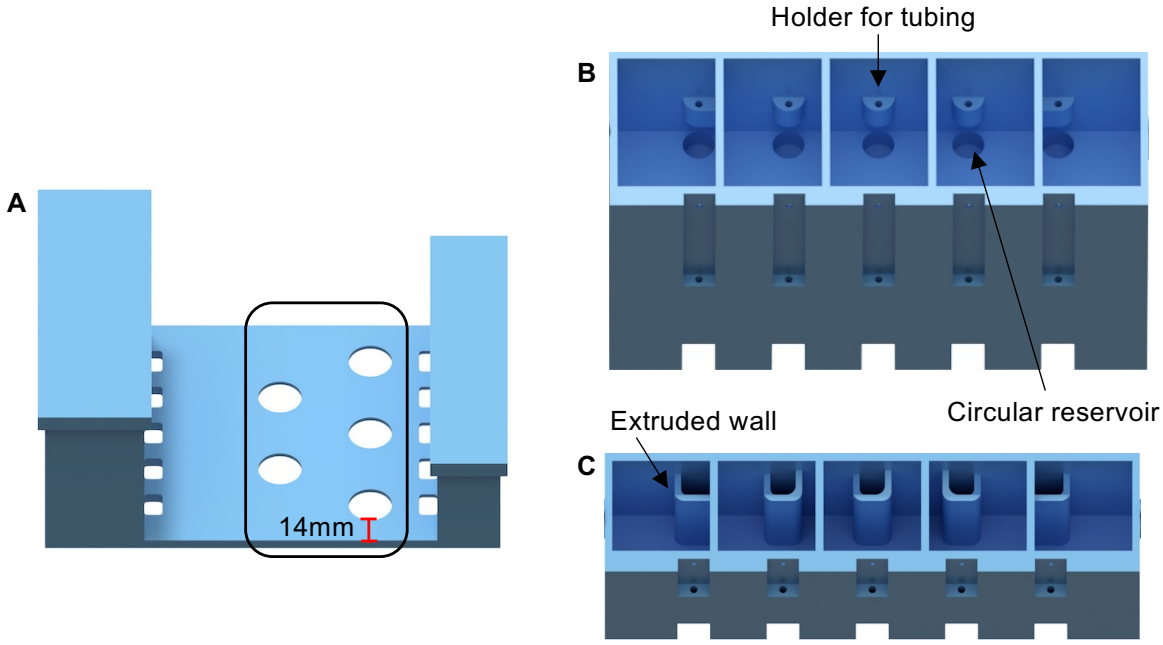


Figure 2.27: Additional design features of Design 2 of the 3D printed perfusion unit. A: The holes for optical access are shifted towards the outlet reservoir and away from the edge to be compatible with confocal microscopy. B: Figure showing the inlet reservoir, indicating the holders for the tubing on the wall, which also serves to indicate the fluid level corresponding to 3 ml, as well as the smaller circular reservoirs, into which tubing is placed and which are placed lower than the outlet reservoir to make sure that the tubing never empties. C: Figure showing the outlet reservoir where tubing into a smaller reservoir and fluid overflows into the larger reservoir to maintain a constant height of the fluid level in the smaller reservoir over time. On of the walls on the smaller reservoir has been extruded down 1.5 mm to break surface tension and facilitating fluid flowing into the larger reservoir.

Having removed the needle and syringe filter in the fluidic circuit, the tubing served as the main source of the resistance for controlling the flow rate in the vessel, due to the increased tubing length required between the inlet and outlet reservoirs (~130 mm in Design 1 and ~300 mm in Design 2). Furthermore, in Design 2, the tubing was changed to PTFE tubing, which had a smaller inner diameter (ID=0.3 mm). The modifications made to Design 2 resulted in a ~2-fold increase in resistance, as shown in Table 2.4, and consequently, ~2-fold decrease in flow rate. This allowed decreasing the size of the inlet reservoir and hence eliminating the need for attaching a separate reservoir. Furthermore, due to the space gained from removing the bulky fluidic connectors, an additional device could fit on the unit, by slightly offsetting the devices, to allow a total of five devices to be cultured in parallel.

	Resistance in Design 1 mmHg/(µl/min)	**Resistance in Design 2 mmHg/(µl/min)**
Vessel	0.004	0.004
Tubing	0.019	0.136
Needle	0.024	No needle in this design
Filter	0.015	No filter in this design
R_{tot}	**0.062**	**0.14**

Table 2.4: Comparing resistances in the fluidic circuits between Design 1 and Design 2 of the 3D printed perfusion unit.

Additional design features of Design 2 are outlined below and shown in Figure 2.27

i) The holes in the base of the unit, which facilitate optical access through the device, were offset towards the outlet reservoir so that all devices could be imaged using confocal microscopy, as the inlet reservoir was too tall to fit underneath the condenser. The holes were also offset 14 mm from the edge, optimised based on the x-y range of the microscope objective

ii) The walls of the inlet reservoirs have holders for the tubing, which also serve the purpose of indicating the fluid level that corresponds to a volume of 3 ml, which is useful when the inlet reservoir is refilled before it has completely emptied.

iii) There is a small circular reservoir (4 mm deep) inside the inlet reservoir into which the tubing is placed. This smaller reservoir is below the level of the outlet reservoir and will therefore never empty completely, making sure that air is never introduced inside the tubing, which prevents fluid flow.

iv) In the outlet reservoir, one of the walls of the smaller reservoir is extruded down 1.5 mm to break surface tension so that when the smaller reservoir is full fluid empties over this wall rather than creating a droplet on top of the reservoir.

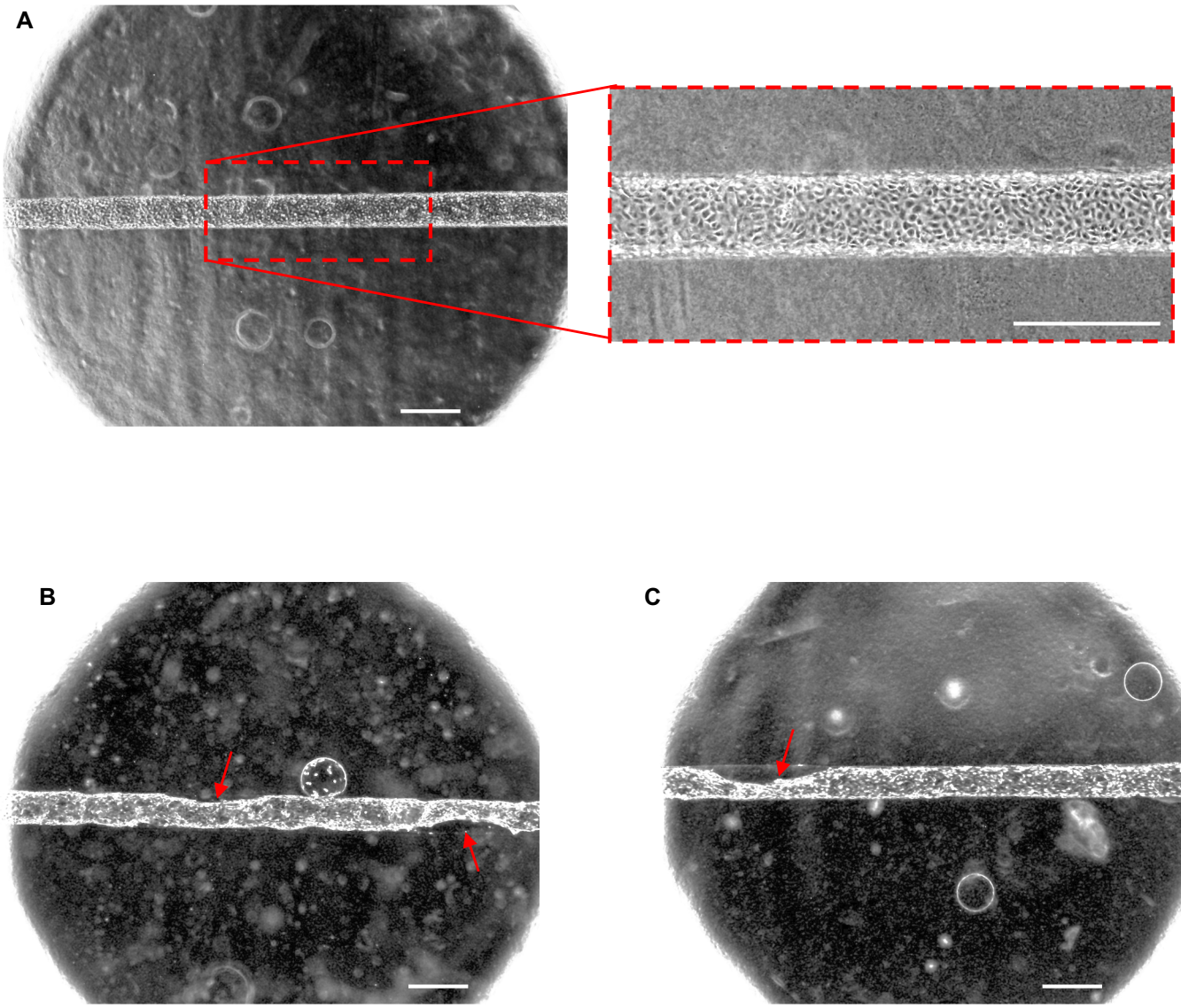


Figure 2.28: Long-term culture of ECs in the vessel using the 3D printed perfusion unit for media turnover (n>10 vessels). A: Using EGM2 cell culture media, the integrity of the monolayer can be maintained in culture, showing a confluent vessel with a cobblestone morphology eight days after cell seeding. B-C: Two examples of vessels where damage to the monolayer occurred when keeping the vessel in culture for several days post confluency. Scale bars=500 µm.

Following all the optimisation steps described in this chapter, the integrity of the endothelial monolayer could be maintained for several days in the blood vessel-on-a-chip model. Figure 2.28 (A) shows a confluent vessel with a characteristic cobblestone morphology eight days post cell seeding. A confluent monolayer will not remain viable in the model for long periods of time. In Figure 2.28 (B-C), the monolayer in certain regions of the vessel has collapsed. This phenomenon was also observed by Price et al. (2010) in the needle model; however, the number of days for which the monolayer remains viable and can be used for functional or molecular assays is not fully understood.

2.3.6.3 Gas-pressure controlled perfusion system

The hardware and software for the gas-pressure controlled perfusion system was developed by Dr. Michael Madekurozwa and Dr. Joseph van Batenburg-Sherwood in the Department of Bioengineering, Imperial College London with input regarding design and user interface from Josefin Jansson-Edqvist. All experiments presented in this section were performed by Josefin Jansson-Edqvist.

A custom-designed gas-pressure controlled perfusion system was developed for the purpose of perfusing the vessels at a constant level of physiological relevant shear stress (0-50 dynes/cm^2) during long-term culture. The system is still under development and was not used for the work presented in Chapters 3-5.

Several systems have been designed by other manufacturers (including Cellix and ibidi) and groups with the intent of subjecting cells to a set amount of shear stress. The systems designed by other manufacturers and groups are not suitable for this work for one or more of the following reasons:

i) restrictive in their capabilities as they must be used with cells seeded on purchased chips of specific size and dimensions.
ii) unintended oscillatory shear stress due to the fluid pumping mechanism (diaphragm, peristaltic, syringe pumps etc).
iii) lack of real time parameter (pressure, flow rate and temperature) monitoring and recording.
iv) not designed for long term experiments.
v) expensive to run due to their rate of media consumption.
vi) transporting cell culture media between the inside and outside of the incubator.

The gas-pressure controlled perfusion system was designed according to the following specifications:

i) requires ~15ml of media per channel and recycles the media without changing the direction of fluid flow across the vessel.

ii) allows the user to set the pressure across the vessel (and by association, the shear stress).

iii) provides real-time non-contact measurement of the flow rate through the vessel.

iv) capable of running continuously for >2 days.

2.3.6.3.1 System validation

To achieve these goals, the system shown in Figure 2.29 was built and programmed to run in LabVIEW (National Instruments). It comprises an electronics enclosure, which resides outside the incubator, and a fluidics box, which contains the fluidic circuit and resides inside the incubator. In this perfusion system fluid flows from each of the four pressurised gas tight bottles (in Figure 2.30, the perfusate filled bottles to the right of the vessels) into the four gas tight bottles at atmospheric pressure (in Figure 2.30 the perfusate filled bottles to the left of the vessels). When the fluid in the pressurised bottles falls below a setpoint (measured with a level detector), all the solenoids in the system switch their position resulting in the previously pressurised gas tight bottles being set to atmosphere and the gas tight bottles previously set to atmosphere being pressurised. The solenoids immediately adjacent to the vessels ensure that the direction of fluid flow through the channel is constant throughout the perfusion and consequently, the direction of shear stress is also constant throughout the perfusion.

The perfusion system was designed to use gas pressure to drive the flow of cell culture media through the vessel. The use of gas pressure as a driving source prevents unintentional pulsatile flow and eliminates the need for replenishing the media gas concentration, which must be maintained for pH buffering of cell culture media and ensures that the cells are cultured under aerobic conditions. Strain gauges were used to measure the mass of the gas tight bottles on one side of the pinch valves (Figure 2.30), which would increase or decrease as cell culture media was perfused into or out from the bottles, respectively. The flow rate through each vessel was calculated by taking the derivative of the mass (m) of each bottle with respect to time and dividing by the density (ρ) of cell culture media, according to Equation 2.10, resulting in units of µl/s as shown in square brackets.

$$Q = \frac{1}{\rho}\frac{\partial m}{\partial t}\left[\frac{\mu l}{g}\frac{g}{s}\right] \quad (2.10)$$

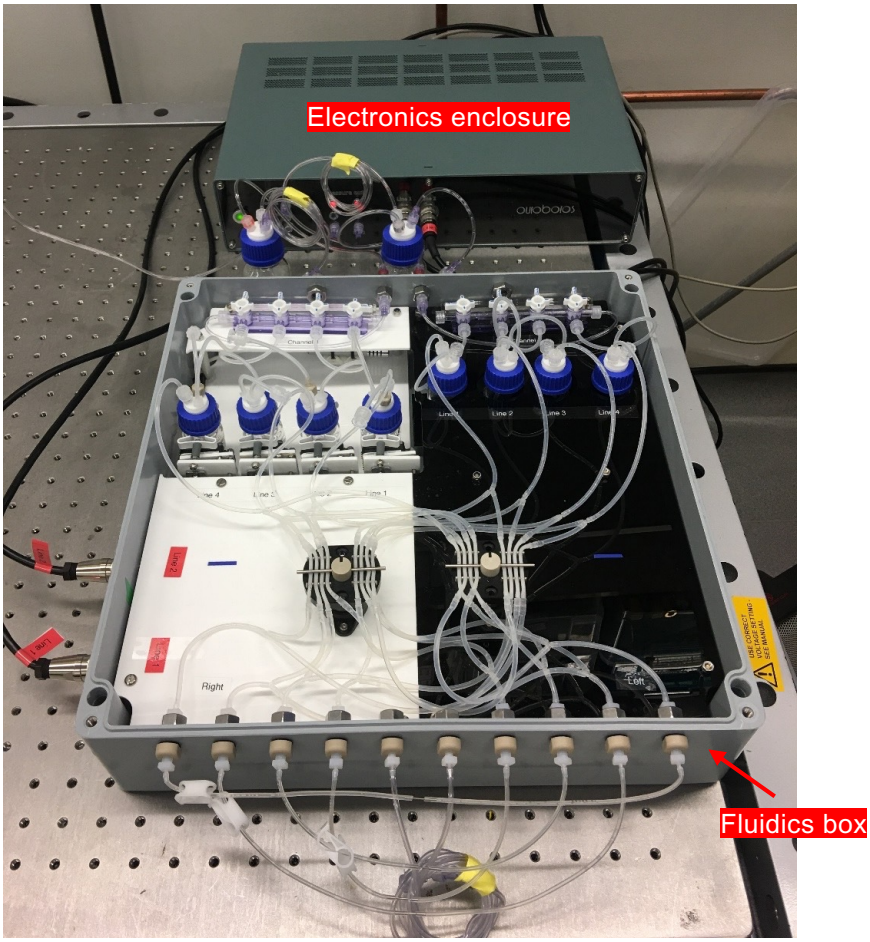


Figure 2.29: Picture of the different components of the gas-pressure controlled perfusion system. The gas-pressure controlled perfusion system, comprising an electronics enclosure, which resides outside the incubator and is powered by mains. The grey box is the fluidics box, which contains the fluidic circuit. It resides inside the incubator and is powered by 24 and 48V dc lines, which are user safe.

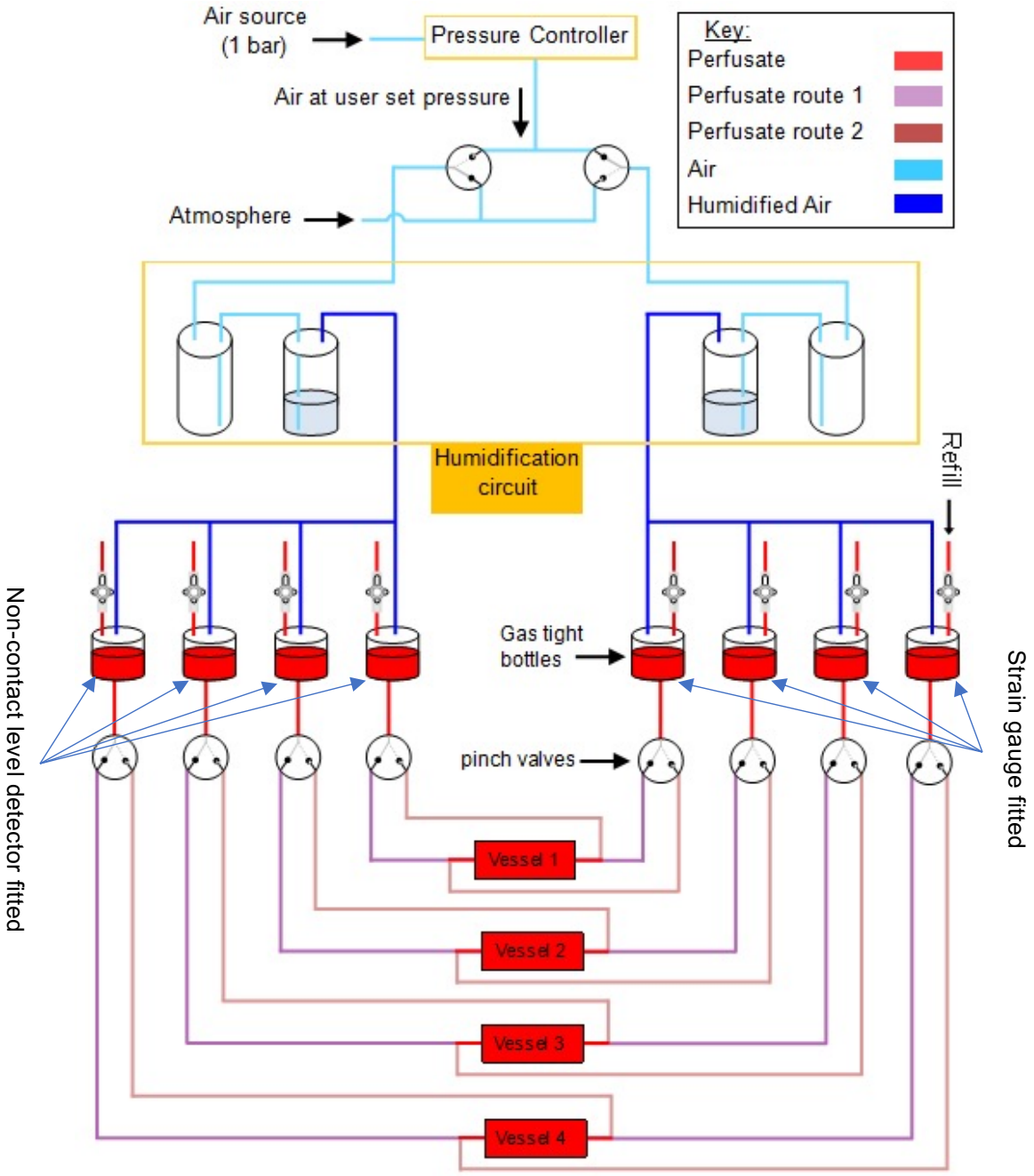


Figure 2.30: Schematic of the gas-pressure controlled perfusion system showing the fluidic circuit. The perfusate (cell culture media) in each channel is isolated. An external gas cylinder with 5% Carbon Dioxide/Air is used to pressurise gas tight bottles and drive flow across the vessels. A humidification circuit ensures that pressurised air is humidified before it comes into contact with the perfusate (prevents perfusate evaporation). Pinch valves are used to recirculate perfusate while ensuring that the direction of flow across each vessel does not change. Figure produced by Dr. Michael Madekurozwa.

The gas tight bottles on the other side of the pinch valves were all fitted with two non-contact fluid level detectors (one for bottle fluid level high and the other for bottle fluid level low), which were used to automatically determine when to change the direction of flow in all channels, as the perfusion system has only one pressure controller. When to switch flow direction was based on the following asymmetric conditions:

i) when fluid is flowing from the strain gauge fitted gas tight bottles to the bottles with non-contact level detectors, it will continue to do so until the fluid level is registered as high by the non-contact level detectors in at least three gas tight bottles.
ii) when fluid is flowing from bottles with non-contact level detectors to the strain gauge fitted gas tight bottles, it will continue to do so until the fluid level is registered as low by the non-contact level detectors in at least 2 gas tight bottles.

The asymmetry of the test conditions gives the system stability as well as allows the perfusion system to continue to function if one bottle (but not more than one) fails. A sample of the performance of the perfusion system with all four channels perfused in parallel is showed in Figure 2.31. In the sample perfusion, the yellow channel (Figure 2.31 (b)) contained an air bubble in the tubing and as the system makes measurements in real-time, failure of the yellow channel was visible. The sample tracing was acquired by perfusing water at room temperature. Furthermore, all system validation experiments were carried out without attaching a microfluidic device. A piece of PTFE tubing (ID=300 μm) was used to represent the resistance of the vessel. The shear stress experienced by endothelial cells in the vessel can be calculated using Equation 2.11 (assuming Poiseuille flow), where L is the length of the vessel, ΔP is the pressure drop along the vessel, d is the vessel diameter, μ is the viscosity of the perfusate and Q is the flow rate through the vessel.

$$\tau = \frac{\Delta P\, d}{4\, L} = \frac{32 \mu Q}{\pi d^3} \qquad (2.11)$$

The applied pressure specified for driving perfusion can only be used to measure shear stress if this also represents the pressure drop along the vessel. In this system, ΔP also includes the pressure drop along the tubing. Therefore, the estimations of flow rate through the vessel, based on recordings of mass transfer, were used to determine shear stress, despite its reliance on the third power of the vessel diameter (diameter=300 μm was used). The temperature and humidity inside the box were monitored to ensure that the system

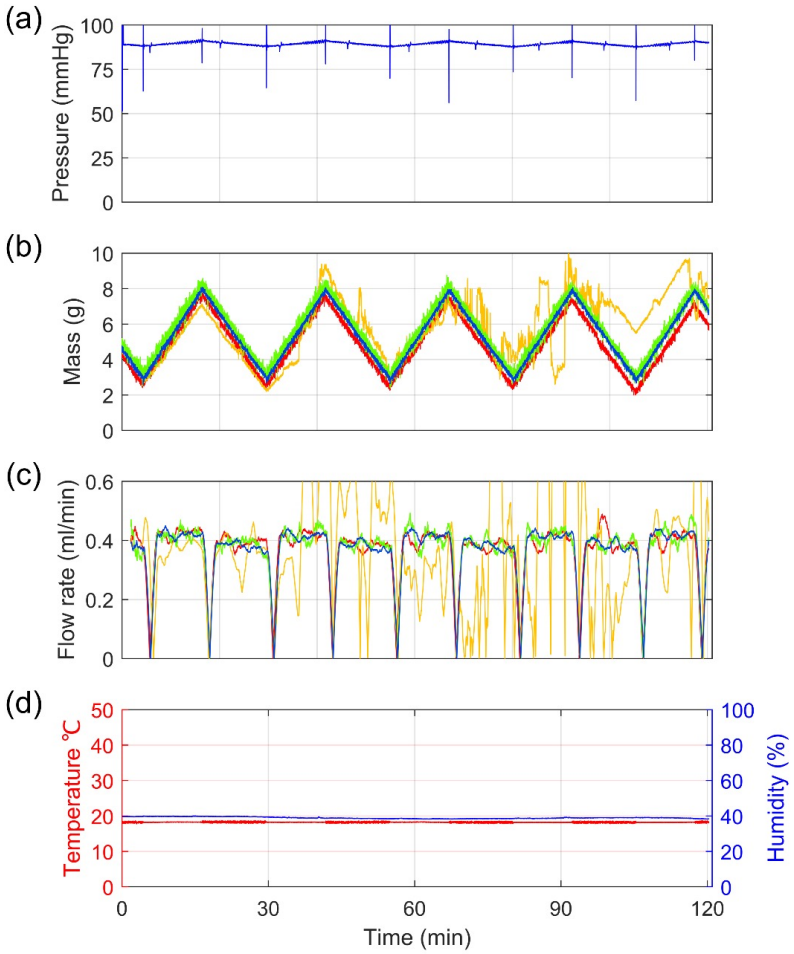


Figure 2.31: Sample perfusion of four channels in parallel (without ECs). Perfusion of 4 blank channels (without connecting the microfluidic device). Plot (a) shows the applied pressure during perfusion. In plots (b) and (c), Channel 1 is plotted in red, Channel 2 in yellow, Channel 3 in green and Channel 4 in blue. (b) Mass of bottles for each channel, showing that fluid is being continuously perfused with the same flow rate in all channels, except for channel 2 (yellow), which has failed. (c) Magnitude of the flow rate in each channel. (d) Temperature and humidity inside the box housing the bottles and solenoid is kept constant during the 2 hour perfusion.

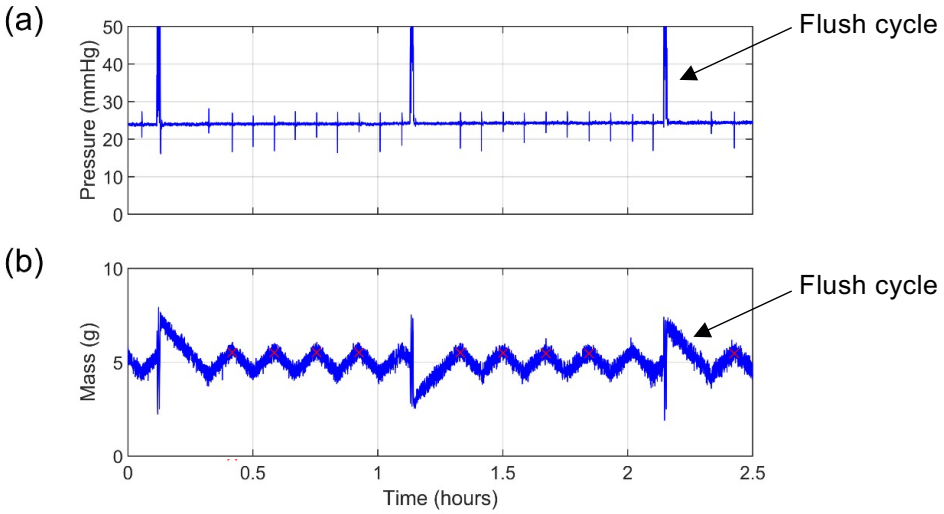


Figure 2.32: Incorporation of flush cycles to remove air bubbles in the tubing during perfusion. Figure showing the effect of flush cycles (indicated as the peaks in both graphs) on applied pressure (a) and recorded mass (b) for one channel perfused at room temperature without connecting a microfluidic device.

remained dry during use inside the incubator (to avoid damaging electrical components) as well as ensure that the temperature of cell culture media was maintained at 37°C.

Problem 1: Air bubble formation inside the tubing.

Details: When performing experiments with the perfusion system inside the incubator it was found that air bubbles would form inside the tubing, which would grow over time and could affect the flow rate in a specific channel or cause damage to the vessel if allowed to enter the microfluidic device.

Outcome: Flush cycles were incorporated to remove any air bubbles that might form inside the tubing by forcing them into one of the gas tight bottles. Flush cycles are demonstrated in Figure 2.32, where after every 10 cycles the system bypasses the vessel, sets the applied pressure to 50 mmHg and flushes the tubing three times before returning to normal operation.

Problem 2: Evaporative losses from the gas tight bottles caused the perfusion system to fail as the amount of fluid in the system became too little to permit switching via the non-contact level sensors.

Details: The compressed air mixture (5% CO_2) used to set the pressure drop is dry and can therefore cause evaporative loss at the air-liquid interface with cell culture media inside the gas tight bottles. This needs to be prevented as it can alter the osmotic pressure and composition of cell culture media, as well as cause problems with long-term perfusion as the volume of cell culture media decreases over time. Three approaches were investigated for eliminating evaporative losses in this system

i) Using anti-evaporation silicone oil (purchased from ibidi, validated for cell culture applications) at the fluid surface inside the gas tight bottles
ii) Introducing a humidification circuit at room temperature to pressurise the bottles using humidified air
iii) Introducing a humidification circuit inside the incubator to pressurise the bottles using heated and humidified air

Figure 2.33 shows a comparison of the three approaches, when using the perfusion system inside the incubator. Using the anti-evaporation oil fluid loss remained at a substantial rate, indicated by a reduction in mass over time. The humidified driving gas prevented evaporative loss more effectively than silicone oil whether the water used to humidify the air was heated or not, with the heated humidification giving the best results.

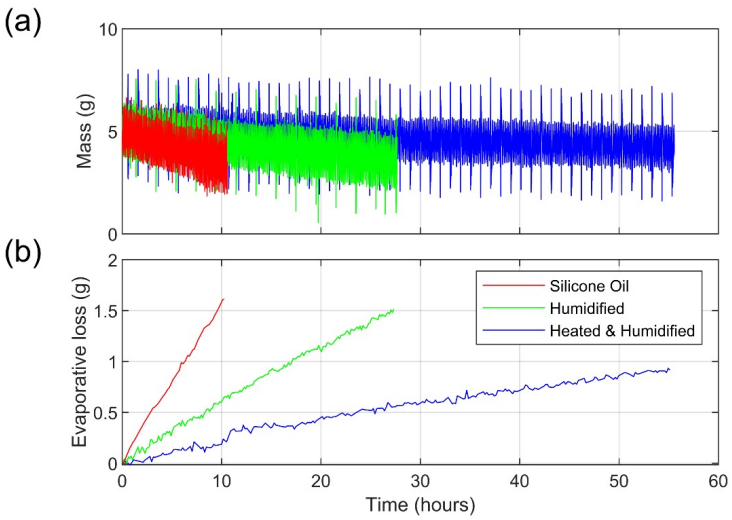


Figure 2.33: Comparison of three approaches for preventing evaporative losses during perfusion. Figure showing media evaporative loss for n=1 perfusion for each condition. (a) The mass of 3 bottles in 3 independent experiments was monitored over several hours. (b) Evaporative losses in the system derived from tracking the peak mass of the gas tight bottles when undergoing different evaporative prevention treatments. Each channel in the system is designed to contain a total of ~15 ml of media.

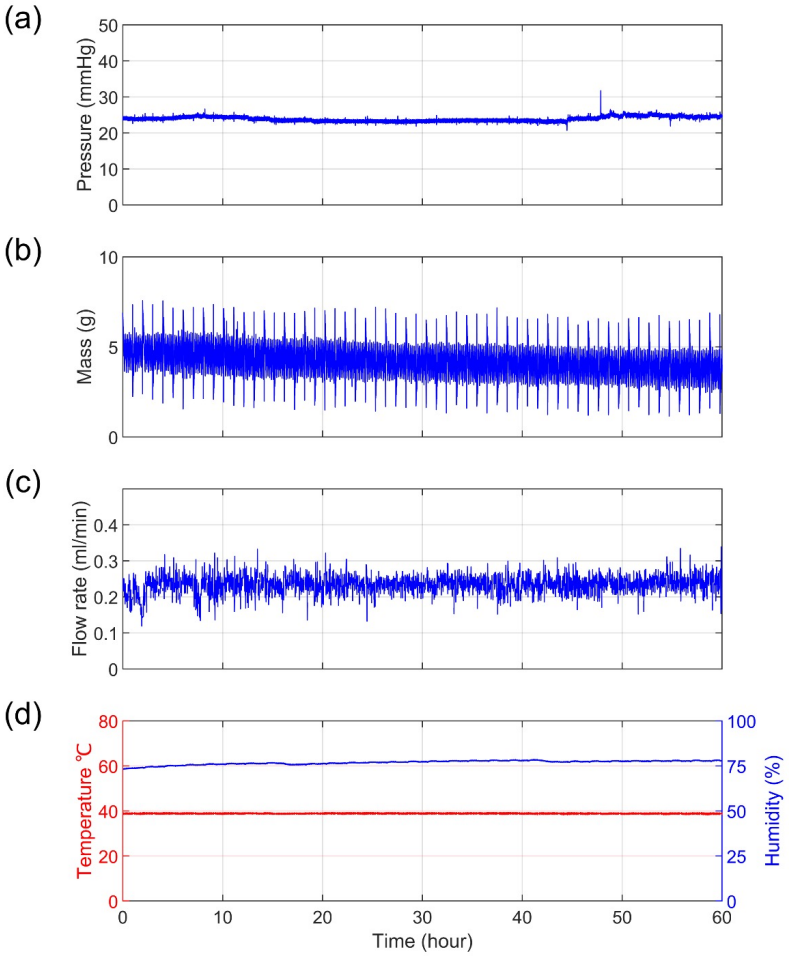


Figure 2.34: Sample 60-hour perfusion without any user interference or correction. (a) Gas pressure with periods during flushes and flow direction changes excluded. (b) Mass of the gas tight bottle. (c) Flow rate through the system was calculated by taking the absolute value of the derivative of 60-second intervals of the mass as plotted in panel (b) and excluding times that are ±30 seconds from periods when the flow direction changes. (d) Temperature and Humidity recordings inside the fluidics box inside the incubator.

Outcome: With the heated humidification circuit incorporated, to the perfusion system, the system was validated without a microfluidic device for continuous perfusion inside an incubator for more than two days, without requiring any user interface (Figure 2.34).

2.3.6.3.2 Connecting the vessel to the system for perfusion at physiological shear stress

Having validated the perfusion system for continuous perfusion at 37°C, a microfluidic device was connected to the system two hours following cell seeding with HUVEC and perfused at 10 dynes/cm^2 for 36 hours before detaching the device and imaging the vessel using phase contrast microscopy. Figure 2.35 (A-B) shows the vessel two hours post cell seeding, before it was connected to the perfusion system, and after 36 hours of perfusion (Figure 2.35 (C)), at which point all endothelial cells had been washed out from the vessel. However, results also indicate that the collagen or the vessel geometry did not get damaged from interfacing with the perfusion system at a physiological shear stress of 10 dynes/cm^2.

Problem: Loss of cells from the vessel during continuous perfusion at 10 dynes/cm^2.

Details: The protocol recommended for perfusion of HUVEC at 10 dynes/cm^2 using the ibidi perfusion system was followed, which includes the below steps

1. Pre-conditioning of the perfusion system to the incubator environment: Following assembly of the perfusion system, it was filled with cell culture media (including all tubing) and left inside the incubator overnight at static conditions.
2. Connect the vessel to the perfusion system only after a confluent monolayer has been established: The vessel was seeded with HUVEC (5x10^6 cells/ml) the day before perfusion and cultured in the 3D printed perfusion unit for 24h before it was connected to the perfusion system. This resulted in a confluent monolayer 24h post cell seeding (Figure 2.36 (A-B)).
3. Ramp up the shear stress after connecting the vessel: After connecting the microfluidic device to the perfusion system, the shear stress was ramped up during 30-minute intervals at 2 dynes/cm^2 and 5 dynes/cm^2 before reaching the desired shear stress of 10 dynes/cm^2.

Outcome: When disconnecting the device after 24 hours of perfusion, significant cell death was observed inside the vessel (Figure 2.36 (C-D)). The reason for this is still unknown, but could be due to unfavourable environmental conditions, as it does not seem like the monolayer is being “peeled off” from the vessel due to large pressure gradients or high shear stress.

The gas-pressure controlled perfusion system was difficult to work with, which was a significant limitation for carrying out experiments at physiologically relevant shear stress. This includes assembling the fluidic circuit and avoiding leaks from the large number of bottle connections as well as assembling the different components of the system and connecting to the electronics enclosure outside of the incubator. Furthermore, the system requires a much larger space in the incubator compared to conventional tissue culture experiments and lacks the possibility of real-time monitoring of the vessel during perfusion, which makes it inconvenient to use. The relatively large volume of cell culture media required for each vessel (~15ml) is also a limiting factor, considering the small number of cells cultured in each vessel (<2400); however, this can be motivated by the eliminated need to change media during long term perfusion, which is a difficult step that requires manual intervention. It should be noted that there is currently no perfusion system available on the market, which has overcome all these limitations while meeting the requirements specified earlier in this Chapter.

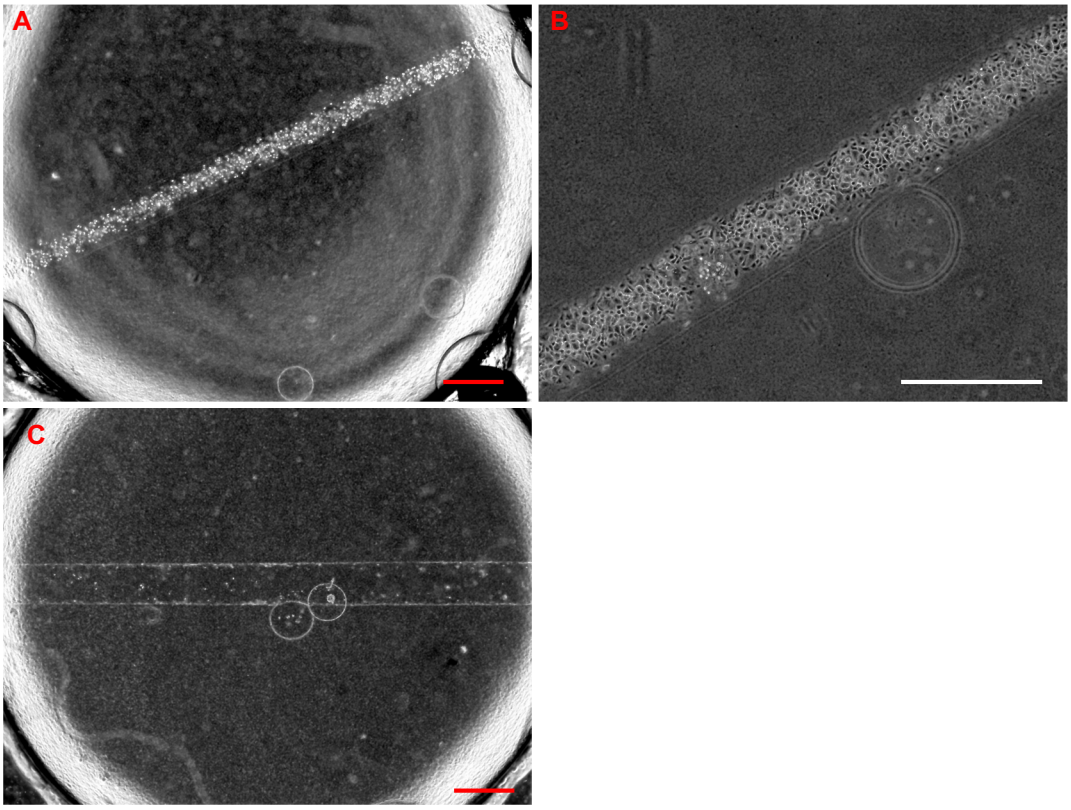


Figure 2.35: ECs perfused in the vessel at 10 dynes/cm^2 - experiment 1 (n=1 vessel). A-B: Endothelial cells are adhered to the collagen 2 hours post cell seeding before attaching the device to the perfusion system. C: After 36 hours of perfusion at 10 dynes/cm^2 all endothelial cells have been washed out from the vessel. Scale bars=500 μm.

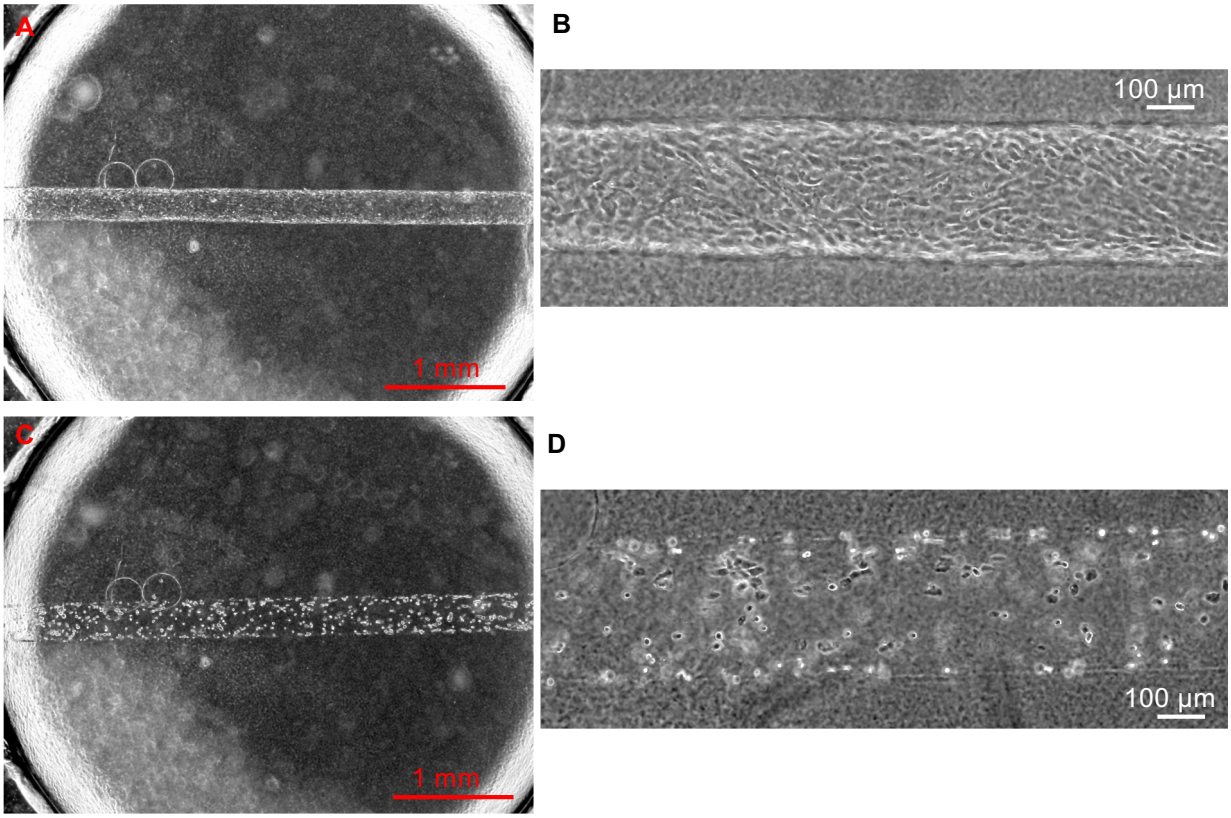


Figure 2.36: ECs perfused in the vessel at 10 dynes/cm^2 - experiment 2 (n=1 vessel). A-B: Endothelial cells have formed a confluent monolayer inside the vessel 24 hours post cell seeding before attaching the device to the perfusion system. C-D: After perfusion at 10 dynes/cm^2 for 24 hours the vessel had undergone significant cell death.

2.3.7 Molecular analysis in the blood vessel-on-a-chip model

In order for the blood vessel-on-a-chip model to be a useful tool in vascular science, it needs to be accessible for molecular analysis. The model has been optimised to study protein expression using immunocytochemistry with confocal microscopy as well to study gene expression using both bulk qPCR and single-cell qPCR, on cells extracted from the vessel.

2.3.7.1 Immunocytochemistry

For immunofluorescent staining, a similar protocol to staining ECs in 2D was used. The main difference in the microfluidic device is the possibility of solutes to diffuse into the collagen and therefore the washing steps are more challenging.

Problem 1: Prolonged cell exposure to formaldehyde, referred to as over fixation, significantly reduced the junctional staining that could be detected in the vessel.

Details: Formaldehyde fixation causes covalent cross-linking between molecules, including proteins, to glue them together and form an insoluble mesh (Kim et al., 2017). It proved particularly difficult to wash away the formaldehyde solution in the blood vessel-on-a-chip model following the fixation step of the staining protocol. Figure 2.37 shows two vessels that were stained at the same time, using the same staining protocol; one had been stored at 4°C prior to staining, following formaldehyde fixation and washing with PBS (Figure 2.37 (A)) and one was stained on the same day following fixation (Figure 2.37 (B)). Results show a clear difference in staining for the junctional protein VE-cadherin between the two cases, where almost no VE-cadherin staining was visible in the vessel that had been stored prior to staining. We hypothesise that over fixation, resulting in over cross-linking of proteins, would damage the antigen-antibody binding properties for the VE-cadherin staining, resulting in significantly reduced antibody signal.

Outcome: The complete staining protocol should be performed on the same day to maximise antibody signal. Furthermore, since particles can get trapped in the collagen a higher concentration of 10% BSA was used to minimise background signal from non-specific antibody binding.

Problem 2: Geometrical distortion of the vessel cross-section when capturing z-stacks using confocal microscopy.

Details: Following immunofluorescent staining, the vessels were imaged using confocal microscopy. Due to the thickness of the collagen only the 10x magnification objective could be used for imaging the entire vessel

cross-section; however, it would be possible to use objectives with long working distances if higher magnification imaging is required in future experiments. Geometrical distortion was observed when capturing images in a z-stack, due to refractive index (RI) mismatch when moving from air (RI=1) into a watery specimen (RI=1.31), resulting in a shortened object. This phenomenon is referred to as the fishtank effect and resulted in the vessel cross sections appearing as an ellipse rather than a cylinder (Figure 2.38(A)).

Outcome: To correct for this, the distances between images should be divided by a correction factor for 3D reconstruction, according to Equation 2.12 (Scientific Volume Imaging). For an air lens and a watery specimen, a correction factor of 0.76 should be used. Applying this correction factor resulted in a cylindrical vessel cross section (Figure 2.38B).

$$Correction\ factor = \frac{RI_{lens}}{RI_{specimen}} \quad (2.12)$$

2.3.7.2 Single-cell qPCR

All samples were prepared by Josefin Jansson-Edqvist. The single-cell qPCR experimental protocol including bioinformatic analysis of the results was performed by Dr. Michela Noseda's laboratory at Imperial College London.

An experiment was performed to validate the use of single-cell qPCR on endothelial cells that had been isolated from the vessels (following the RNA extraction protocol described in the optimised methods section), pooling HUVEC from three vessels, and using HUVEC trypsinised from culture in a 6-well tissue culture plate as a positive control. Following EC extraction from the vessel, the below steps were followed for single-cell gene expression analysis using single-cell qPCR (Massaia et al., 2018).

1. Single-cell isolation through Fluorescence-activated cell sorting (FACS). HUVEC from the vessels and from the 6-well tissue culture plate were sorted into a 96-well qPCR plate, 24 cells from each condition were isolated and placed one cell per well.
2. Cell lysis
3. Reverse transcription
4. cDNA amplification of target genes. 48 target genes were used for each cell. A gene panel already available in Dr. Michela Noseda's laboratory was used).
5. Library preparation of the 48 target genes

6. Quantification of gene expression using the Fluidigm® microfluidic system

The full set of gene expression data obtained is shown in Appendix: Chapter 2, where each data point represents the gene expression of one cell for a given gene. Results for four endothelial-specific genes (VWF, PECAM1, CDH5 (VE-cadherin) and KDR (VEGF receptor 2)) are shown in Figure 2.39 (A). Results are shown as -DeltaCt values, representing the gene expression of a given gene after subtracting the expression of the housekeeping gene. For all these genes, the average expression was slightly higher for ECs cultured in the vessel compared to the 6-well tissue culture plate; however, heterogeneity within each sample was not observed. Gene expression of CLEC3B and BMPER is shown in Figure 2.39 (B), which confirms that heterogeneity within a cell population can be detected in the vessel using this method, showing bimodal distributions of gene expression for ECs cultured in the vessel but not for the HUVEC positive control. Gene expression signal for ECs culture in the vessel was captured for all genes that were detectable in HUVEC isolated from the 6-well tissue culture plate. These results are promising as they indicate that this technique can be used on cells isolated from the vessels, even though only a low cell number is available for FACS sorting. Single-cell qPCR could therefore be a useful technique for gene expression analysis in the blood vessel-on-a-chip model, specifically if endothelial cells are co-cultured with tissue-specific cells, which might result in heterogeneity in gene expression depending on location along the vessel.

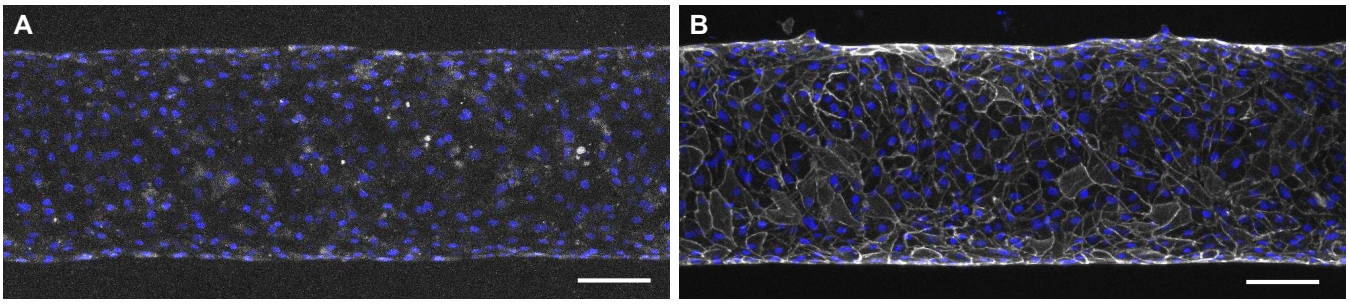


Figure 2.37: Over fixation significantly reduced the junctional staining that could be detected in the vessel. Immunofluorescent staining of the vessel, blue=nuclear staining DAPI, grey=junctional staining VE-cadherin. A: The vessel was fixed with 4% formaldehyde solution for 15 minutes at room temperature, washed with PBS for 15 minutes and then stored in PBS at 4°C for one week before performing the rest of the staining protocol, at which point the cell junctions have been destroyed. B: The complete staining protocol was performed on the same day, resulting in a good quality staining with clearly visible junctions. Representative images for n>10 vessels for each condition. Scale bars=100 µm.

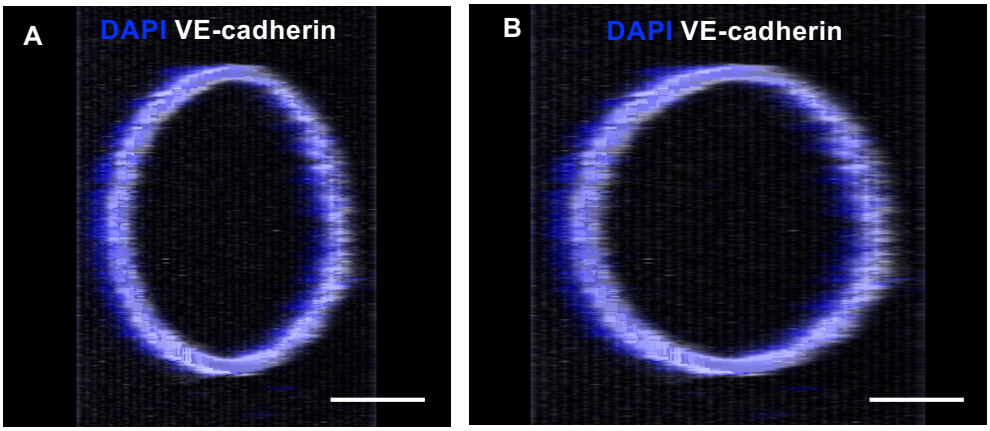


Figure 2.38: Geometrical distortion of the vessel cross-section using confocal microscopy. Immunofluorescent images showing the cross-section of the same vessel projected without correcting for the fishtank effect, resulting in an ellipse (A). When the correction factor is accounted for the true shape of a cylindrical vessel can be captured (B). Scale bars=100 µm.

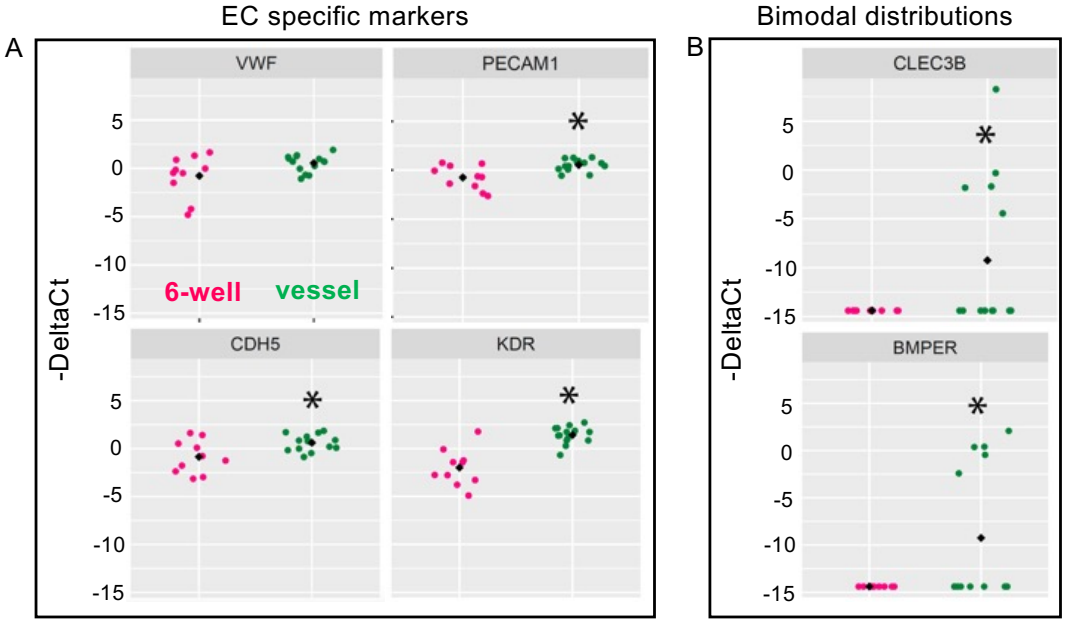


Figure 2.39: Gene expression data from single-cell qPCR. Gene expression data obtained from one single-cell qPCR experiment, comparing HUVEC cultured in the vessel (in green) to HUVEC cultured in a 6-well tissue culture plate (magenta). A: Gene expression of four endothelial-specific genes. B: Genes showing a bimodal distribution in the vessel but not in the 6-well tissue culture plate. Statistical significance indicated by * ($p<0.05$, Mann-Whitney U test).

Chapter 3: Application 1 – Permeability

3.1 Introduction

Endothelial barrier function refers to the transport of fluids (hydraulic conductivity) and solutes (permeability) across the endothelium. Permeability in the vasculature represents the rate at which different size molecules are transported across the endothelium, which is what this chapter will focus on. This transport is dependent on diffusion, where molecules move across a semipermeable membrane in response to a concentration difference, from higher to lower concentrations. The vasculature relies on a tightly regulated barrier function to supply tissues with oxygen and nutrients (as described in Chapter 1). A range of pathological conditions are associated with endothelial barrier dysfunction, where molecules are allowed to move more freely across the vessel wall, resulting in increased permeability. Consequently, measuring permeability is considered a key functional assay to validate the formation of a healthy endothelium *in vitro*. There are primarily two methods for doing this, Transendothelial electrical resistance (TEER) and using fluorescent tracer molecules to measure the change in solute concentration across the endothelium over time. TEER is a measurement of ion conductance, obtained by applying a voltage across the endothelium, where the measured values of resistance are indicative of monolayer integrity (Srinivasan et al., 2015). However, TEER is independent of molecular weight and therefore measuring permeability using fluorescent tracer molecules is more suitable to drug screening applications and consequently for disease modelling. This was the method chosen for quantifying permeability in the blood vessel-on-a-chip model. Bovine Serum Albumin (BSA) and dextran are commonly used fluorescent tracers. Dextran is available in a range of molecular weights and by using dextrans that are conjugated to different fluorescent molecules it is possible to simultaneously quantify the permeability of the endothelium to two or more molecular weights. Table 3.1 shows published *in vitro* endothelial permeability measurements of what the authors consider a functional endothelium, using different culture models (described in Chapter 1) and the same molecular weight of ~70 kDa.

Study	Model	Tracer molecule	Permeability (µm/s)
Wong and Searson (2014)	Needle	BSA (~70 kDa)	0.004-0.03
Chrobak et al. (2006)	Needle	BSA (~70 kDa)	0.06
Wang et al (2016)	Vasculogenesis	Dextran (70 kDa)	3-6 $x10^{-4}$
Sobrino et al. (2016)	Vasculogenesis	Dextran (70 kDa)	0.005
Offeddu et al. (2019)	Transwell	Dextran (70 kDa)	0.01
Offeddu et al. (2019)	Vasculogenesis	Dextran (70 kDa)	0.001
Kim et al. (2013)	3-channel	Dextran (70 kDa)	0.02

Table 3.1: *In vitro* permeability measurements of endothelial monolayers in different culture models.

These results vary within two orders of magnitude, which can be due to the type of endothelial cells used in the studies, the endothelial microenvironment or the method used for analysis. Different methods have been used for measuring permeability *in vitro*, which is discussed in the model development sections below.

3.1.1 Aims

The aims were to show that we can robustly measure permeability in the blood vessel-on-a-chip model and develop a suitable method for data analysis, which would allow us to correlate the permeability measurements to vessel formation.

3.2 Model development

3.2.1 Experimental setup

For each vessel, permeability was measured by replacing the media in the inlet reservoir with 3 ml dextran solution (65-85 kDa, tetramethylrhodamine isothiocyanate (TRITC) Dextran, Sigma, reconstituted in EGM2 cell culture media supplemented with 25 mM HEPES to a final concentration of 2 mg/ml). The 3D printed perfusion unit was placed on the confocal microscope stage and imaged with Time Lapse (7 seconds between images and 65 images total in a single plane, 12-bit 1024x1024 pixels image size). Microscopy settings were kept constant for all experiments (gain=600, 543 nm laser power=50, pinhole=1 Airy Unit resulting in a z-thickness of 12.8 µm). Following confocal imaging, the dextran solution in the inlet reservoir was replaced with EGM2 cell culture media (pre-conditioned to incubator temperature and gas concentration) and placed back in the incubator for continued cell culture. If permeability was measured on multiple vessels cultured in the same 3D printed perfusion unit, this protocol was performed sequentially before placing the unit back in the incubator for continued cell culture.

3.2.2 Capturing data

In the permeability assay, consecutive images were captured with a time difference of 7 seconds, which was the highest imaging frequency possible using the chosen microscopy settings. Figure 3.1 shows representative examples of a high permeability case (Figure 3.1 A-C), where dextran is transported across the vessel wall into the collagen, and a low permeability case (Figure 3.1 D-F), where no dextran is visible in the collagen at the end of the assay. The fluorescent images were captured just after the vessel had filled with dextran (at time=t) and 5 minutes later (at time=t+5 min). Intensity profiles (normalised by image width) for the two time

points are show in Figure 3.1 C and Figure 3.1 F for the high and low permeability cases, respectively. In the high permeability case, a fairly constant average intensity is reached of ~2700, which further remains constant between the two time points. In the collagen outside the vessel (located between 100<r<200 and -200<r<-100), intensity is increasing with time and decreasing with increased distance from the vessel wall, to reach zero intensity where there is no detectable dextran in the collagen. In the low permeability case, the same phenomenon is observed inside the vessel, maintaining a fairly constant average intensity of ~3200 between the two time points; however, in the collagen outside the vessel (located between 100<r<200 and -200<r<-100), the rate at which the intensity increases with time is significantly lower compared to the high permeability case, representing improved barrier function.

3.2.3 Data analysis

Having acquired the data, the below steps were followed for data analysis, which are described in detail in the subsequent sections. A dataset containing acquired images in the permeability assay for the same vessel on days 3, 5, 7 and 9 was used for method development, to represent differences in vessel barrier function. When measuring permeability in the same vessel on different days, the dextran solution in the ECM would diffuse into the vessel and get removed from the system during media turnover, resulting in zero fluorescent intensity in the collagen at the start of each permeability measurement.

1. Pre-process images in Fiji (ImageJ)
2. Locate the vessel boundaries
3. Account for radial diffusion into the collagen
4. Define the image interval to use for analysis and measure the dextran concentration inside the vessel
5. Calculate permeability

3.2.3.1 Pre-processing in Fiji (ImageJ)

The microscopy images were pre-processed in Fiji to convert to a tif format. If required, the image set was also rotated to achieve horizontal vessel boundaries, which is required for normalisation by image width.

3.2.3.2 Locate the vessel boundaries

The vessel boundaries were manually located for each image set based on the intensity profile. Figure 3.2 shows how the vessel boundaries were defined on the four different days of measuring permeability.

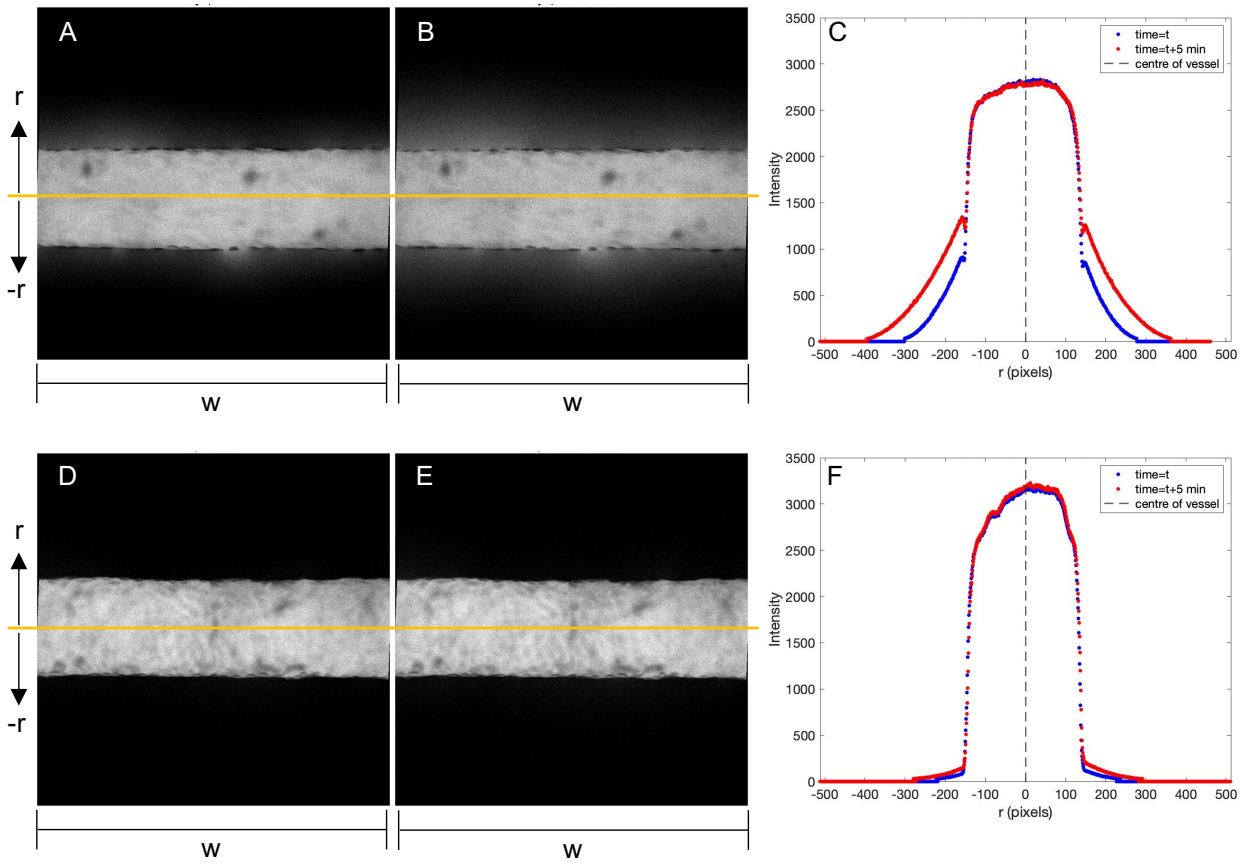


Figure 3.1: Fluorescent images and intensity profiles for a high and low permeability case. A-C: Permeability assay shown for a high permeability case. A-B: Fluorescent signal observed in the collagen represents dextran transported across the vessel wall. C: Intensity profile normalised by image width (w), showing a fairly constant intensity inside the vessel, which does not change with time. In the collagen outside the vessel (located between 100<r<200 and -200<r<-100), intensity is increasing with time and decreasing with increased distance from the vessel wall. D-E: No fluorescent signal is visible outside the vessel at any of the time points, indicating very low transport across the vessel wall. F: In the collagen outside the vessel (located between 100<r<200 and -200<r<-100), the rate at which the intensity increases with time is significantly lower compared to the high permeability case, representing improved barrier function.

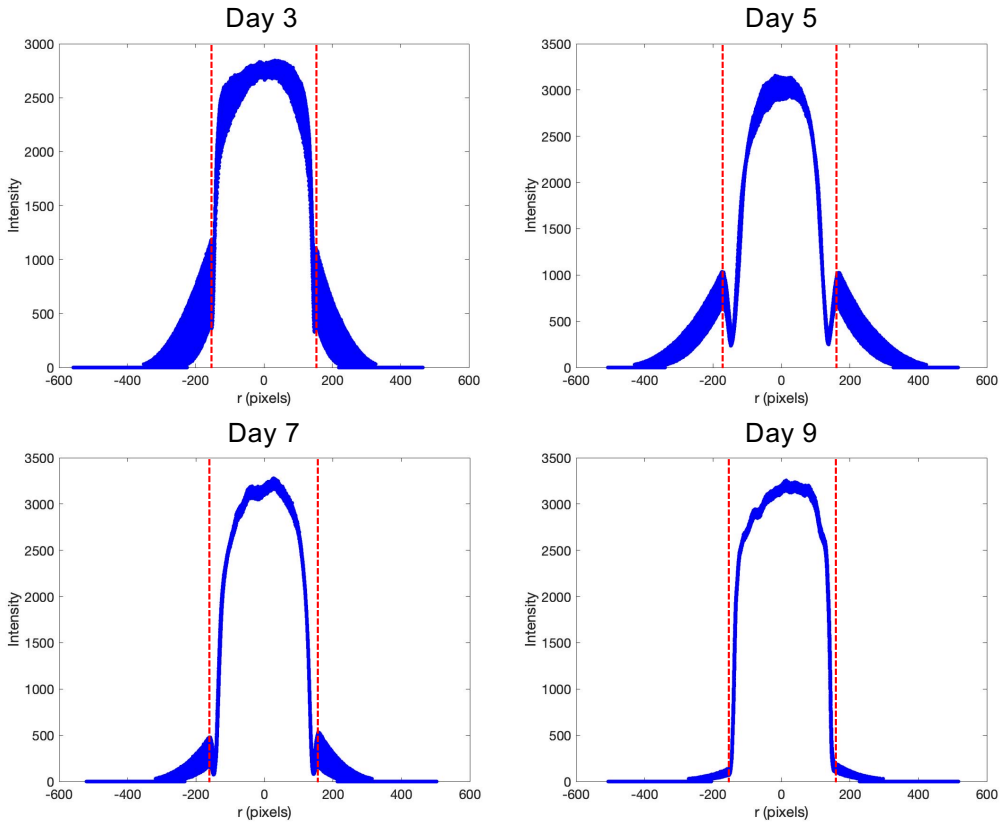


Figure 3.2: Using the intensity profile to locate the vessel boundaries. Intensity profiles obtained from measuring permeability on days 3, 5, 7 and 9 in the same vessel. The location of the vessel was manually defined for each image set, indicated by the red line.

Table 3.2 shows the vessel diameters resulting from using this method to locate the vessel boundaries. Slight variations in vessel diameters were observed, likely related to differences in focus during the permeability assay; however, all results are within ±10% of the expected vessel diameter of 300 μm, suggesting that this method can be used for locating the vessel boundaries. It would have been preferred to use automated detection of the vessel boundaries; however, a robust method for doing this has not yet been achieved.

	Vessel diameter (μm)
Day 3	284
Day 5	311
Day 7	292
Day 9	275

Table 3.2: Vessel diameters resulting from manual detection of the vessel boundaries.

3.2.3.3 Account for radial diffusion in the collagen

Due to the cylindrical geometry of the vessel, radial diffusion occurs through the wall and consequently, the diffusion volume outside the vessel (V_{ECM}) is a function of r (defined as the distance from the centre of the vessel) (Equation 3.1, derived from the volume of a cylinder where d_{vessel} is the vessel diameter). However, with confocal imaging, a 2D image is captured of a section with thickness *f* and width *w*, which results in a different diffusion volume outside the vessel (V_f), according to Equation 3.2 (derived from the volume of a 2D plane). Figure 3.3 (A-B) illustrates this difference in volume of collagen outside the vessel. Dextran concentration in the collagen, C, is directly proportional to volume, as shown by the equation for molar concentration (Equation 3.3), where $n_{dextran}$ represents the number of moles of dextran in a given volume ($V_{dextran}$). Therefore, it is important to account for radial diffusion when measuring permeability in the needle model.

$$V_{ECM}(r) = \pi w \left[r^2 - \frac{d_{vessel}^2}{4}\right] \quad (3.1)$$

$$V_f(r) = fw[r - \frac{d_{vessel}}{2}] \quad (3.2)$$

$$C = \frac{n_{dextran}}{V_{dextran}} \quad (3.3)$$

To account for radial diffusion, the dextran concentration in the collagen obtained from confocal imaging (C_f) was converted to radial coordinates (C_θ) by multiplying the captured data with a conversion factor, which

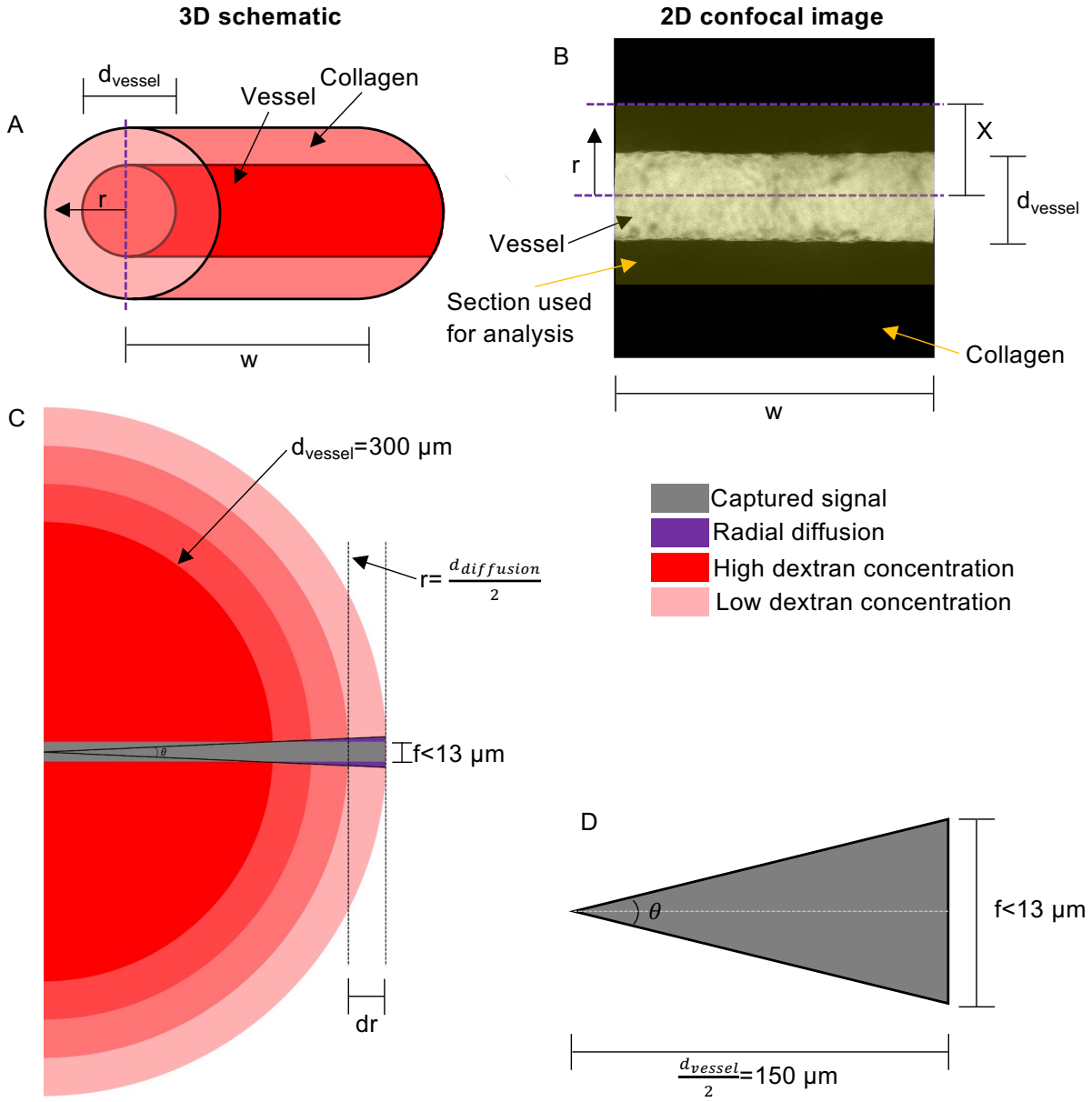


Figure 3.3: **Accounting for radial diffusion into the collagen in the needle model.** A-B: Images of the vessel illustrating differences in the volume of collagen, into which dextran diffuses, between 3D and 2D. C: Schematic illustrating diffusion through the collagen from the source of high dextran concentration inside the vessel. The volume of the captured signal as well as the volume for radial diffusion are drawn to scale for the given vessel diameter, d_{vessel}. D: zoomed-in schematic showing how θ is calculated based on dimensions of the vessel and the thickness of the image section captured using confocal microscopy.

increases with r, according to Equation 3.4. Only diffusion through the section of the vessel captured by confocal microscopy (with angle θ) was considered, which results in a diffusion volume of V_θ (Equation 3.5). Based on basic trigonometry (Figure 3.3 (D)), θ could be calculated according to Equation 3.6, which holds true in this case as f<<R_{vessel} (f<13 μm, d_{vessel}=300 μm).

$$C_\theta(r) = C_f \frac{V_\theta(r)}{V_f(r)} \quad (3.4)$$

$$V_\theta(r) = \frac{\theta}{2\pi} V_{ECM}(r) \quad (3.5)$$

$$\frac{\theta}{2} = tan^{-1} \frac{2f}{2d_{vessel}} \approx \frac{f}{d_{vessel}} \quad (3.6)$$

Considering diffusion through a small volume in the collagen, between $r = \frac{d_{diffusion}}{2}$ and $r = \frac{d_{diffusion}}{2} + dr$, a simplified expression of $C_\theta(r)$ could be derived using Equations 3.7-3.12. A schematic illustrating this is shown in Figure 3.3 (C), indicating diffusion through the collagen from the source of high dextran concentration inside the vessel.

$$V_f(r) = fwdr \quad (3.7)$$

$$V_\theta(r) = w\pi \frac{\theta}{2\pi} \left[(\frac{d_{diffusion}}{2} + dr)^2 - \frac{d_{diffusion}}{2}^2 \right] \quad (3.8)$$

$$V_\theta(r) = \frac{2wf}{2d_{vessel}} \left[\frac{d_{diffusion}}{4}^2 + dr^2 + 2dr \frac{d_{diffusion}}{2} - \frac{d_{diffusion}}{4}^2 \right] \quad (3.9)$$

$$V_\theta(r) = \frac{wf}{d_{vessel}} \left[dr^2 + 2dr \frac{d_{diffusion}}{2} \right] = \frac{wfdr}{d_{vessel}} \left[dr + 2 \frac{d_{diffusion}}{2} \right] \quad (3.10)$$

inserting into equation 3.4

$$C_\theta(r) = C_f(r) \frac{wfdr}{fwd_{vessel}dr} \left[dr + 2 \frac{d_{diffusion}}{2} \right] = C_f(r) \frac{1}{d_{vessel}} \left[dr + 2 \frac{d_{diffusion}}{2} \right] \quad (3.11)$$

Considering dr<<$\frac{d_{diffusion}}{2}$ and substituting r=$\frac{d_{diffusion}}{2}$

$$C_\theta(r) \approx C_f(r) \frac{2r}{d_{vessel}} \quad (3.12)$$

In the permeability assay, fluorescent intensity (I) is used to represent dextran concentration inside and outside of the vessel wall. To determine the relationship between intensity and dextran concentration, the system was calibrated by quantifying the fluorescent intensity corresponding to eight different dextran concentrations in the range 0-2.5 mg/ml, which were prepared through 1:2 serial dilution from the stock concentration of 2.5 mg/ml. The calibration was performed in a 96-well plate format. Figure 3.4 shows the calibration curves

obtained from this experiment, where each data point represents the average intensity of one image (1024x1024 pixels) captured at six different microscopy gains (550, 600, 650, 700, 800 and 900). The data used for creating the graphs is shown in Appendix: Chapter 3. Saturation is reached at an intensity of I=4095 and hence the concentrations measured during the permeability assay should always correspond to intensity values below this threshold. As expected, with higher microscopy gains, saturation was reached at lower dextran concentrations, limiting the range of concentrations that can be detected in the assay. Since the permeability assay is based on perfusing the vessel with a constant dextran concentration and measuring the concentration in the collagen, which starts at zero, a microscopy gain of 600 was chosen as it gave the largest detectable range of dextran concentrations. Figure 3.5 (A) focusses on the concentration curve for a gain of 600. The curve shows a linear relationship between intensity and concentration for concentrations of ~156-2500 µg/ml and intensities greater than ~I=30. Consequently, intensity values below this threshold could not be detected using this gain and therefore, all data in this range (I<30) was set to zero. Figure 3.5 (B) shows curve fitting of the data points in the linear region of the calibration curve, to obtain a conversion from concentration to intensity according to Equation 3.13 (linear fit with slope α and intercept b). The fit parameters α and b were obtained as $\alpha = 0.65 \pm 0.03$ and b=160 ± 51, both results presented with 95% confidence bounds on the linear fit.

$$C = \alpha I + \mathrm{b} \tag{3.13}$$

Permeability is measured by studying changes in dextran concentration in the collagen (ΔC) compared to the concentration inside the vessel (C_{vessel}). Therefore, if fit parameter b=0, intensity values in the collagen ($I_{time,1}$ and $I_{time,2}$) and inside the vessel (I_{vessel}) can be used rather than converting to concentration (Equation 3.14), as concentration becomes directly proportional to α, which cancels in this equation. If however b≠0, this condition does not hold true (Equation 3.15) and therefore intensity values should be converted to concentration for calculating permeability.

$$\frac{\Delta C}{C_{vessel}} = \frac{\alpha(I_{time,2} - I_{time,1})}{\alpha I_{vessel}} = \frac{(I_{time,2} - I_{time,1})}{I_{vessel}} \tag{3.14}$$

$$\frac{\Delta C}{C_{vessel}} = \frac{(\alpha I_{time,2} + b) - (\alpha I_{time,1} + b)}{(\alpha I_{vessel} + b)} \tag{3.15}$$

Figure 3.6 shows graphs comparing using intensity values in the collagen and converting to concentration for three different time points, imaged one minute apart, after accounting for radial diffusion as described above.

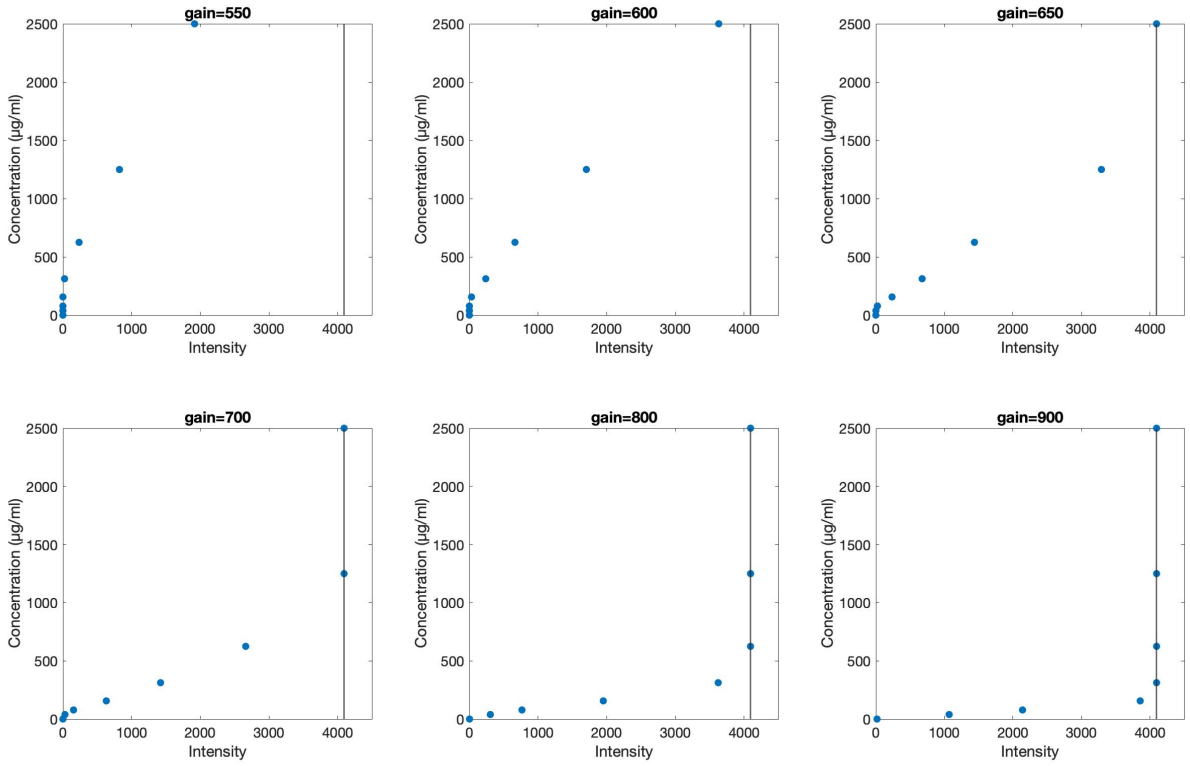


Figure 3.4: Calibration curves using different microscopy gains. Calibration of dextran at concentrations 0-2.5 mg/ml, for six different microscopy gains. The vertical line indicates pixel saturation at I=4095. Experiments performed sequentially for all concentrations in a 96-well tissue culture plate, using n=1 well per dextran concentration.

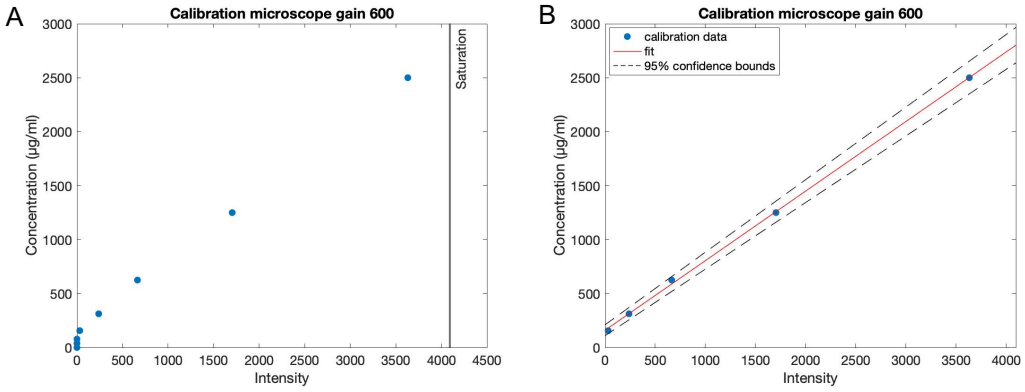


Figure 3.5: Dextran calibration curve shows relationship between intensity and concentration. A: Dextran calibration curve using a microscopy gain of 600. B: Graph showing the calibration data from A, including only data points in the linear region of the dataset. A linear fit was used in this region to establish the relationship between intensity and dextran concentration.

Results are shown for a high permeability case (day 3) and a low permeability case (day 9). For the low permeability case (Figure 3.6 (B)), results show increasing concentration in the collagen with increased distance from the vessel wall. This cannot be true as the vessel is the source of dextran from which diffusion occurs and consequently, the highest dextran concentration in the collagen should be measured closest to the vessel wall. From this we conclude that the conversion from intensity to concentration was incorrect and therefore, intensity rather than concentration was used for data analysis and for calculating permeability. The reason for this problem with conversion from intensity to concentration is unknown but could originate from differences in laser absorbance when capturing data in the blood vessel-on-a-chip model compared to in a plastic 96-well plate, where the calibration was performed.

3.2.3.4 Define the image interval and measure the dextran concentration inside the vessel

Permeability was calculated using a 5-minute imaging interval, which corresponds to 43 sequentially captured images. The interval was selected based on two criteria

i) Average intensity inside the vessel
ii) Total number of data points in the collagen

A larger imaging interval could have been chosen for analysis; however, we wanted to minimise the time required for performing the permeability assay to allow sequential imaging of multiple chips in the 3D printed perfusion platform without the vessels spending too much time outside the incubator.

3.2.3.4.1 Average intensity inside the vessel

Studying the average intensity inside the vessel, all imaging intervals were defined where the intensity changed by <±5%. When dextran solution is perfused through the vessel, the average intensity measured inside the vessel increases from zero (before adding dextran solution) to reach a stable value when all cell culture media inside the vessel has been replaced by dextran solution. A representative example is shown in Figure 3.7, indicating the image interval used for calculating permeability.

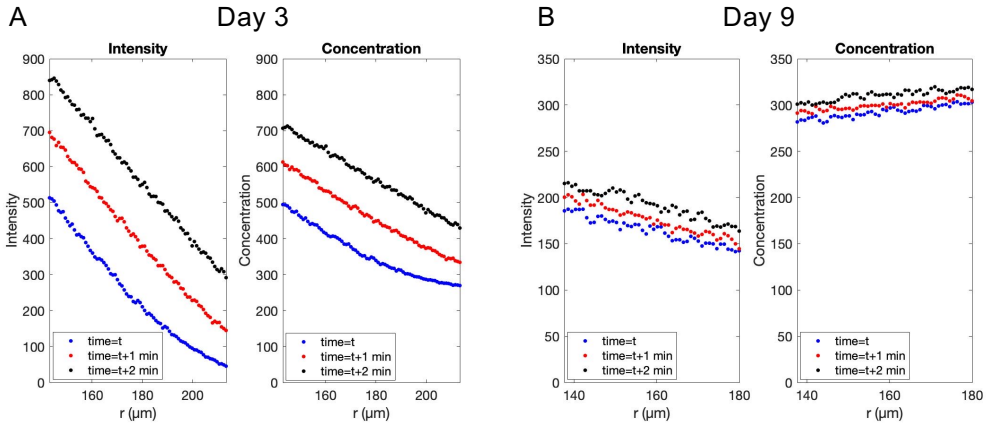


Figure 3.6: Intensity and dextran concentration profiles in the collagen. Graphs comparing using intensity values in the collagen and converting to concentration for three different time points, imaged one minute apart, after accounting for radial diffusion. A: Data captured on day 3, representing a high permeability case. B: Data captured on day 9, representing a low perme

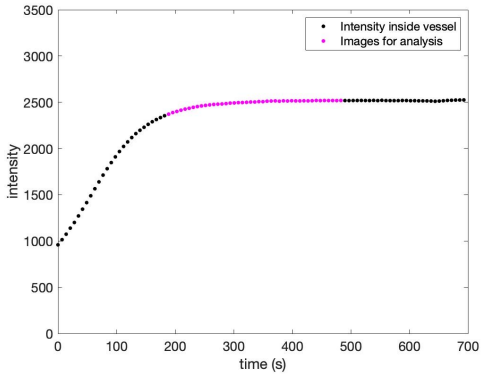


Figure 3.7: The average intensity inside the vessel as it is filling with dextran solution. Figure showing a representative example of the increase in average intensity inside the vessel with time. The first 5-minute interval where the average intensity changes by <±5% is indicated in magenta.

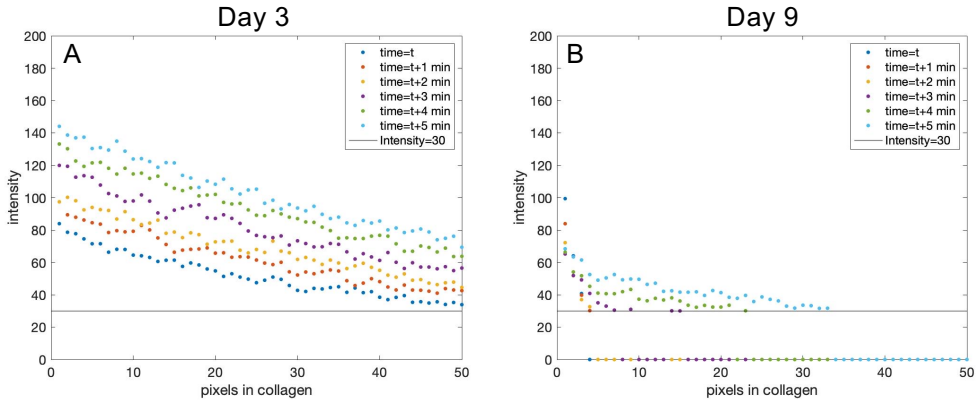


Figure 3.8: Defining the imaging interval based on positive data points in the collagen. Example cases using the first defined imaging intervals for a high permeability case (day 3) and a low permeability case (day9), showing five graphs representing five time points within the imaging interval (X=$\frac{d_{vessel}}{2}$+50 pixels). A: In the high permeability case, 50 data points were captured throughout time interval and therefore this imaging interval was used for calculating permeability. B: In the low permeability case, <50 data points were captured throughout the time interval and therefore, this imaging interval was not chosen for calculating permeability.

3.2.3.4.2 Total number of data points in the collagen

The number of positive data points in the collagen were quantified for all imaging intervals defined by the first criteria (described above), defining a data point as pixels with intensities of I>30. From these defined imaging intervals, the first one containing no zero data points in the collagen (for a given value of X) was chosen for calculating permeability. Figure 3.8 shows example cases using the first defined imaging intervals for a high permeability case (day 3) and a low permeability case (day 9), showing five graphs representing five time points within the imaging interval (from time=t to time=t+5 minutes, captured one minute apart). Here, X was chosen as $\frac{d_{vessel}}{2}$ + 50 pixels. Results show that in the high permeability case (Figure 3.8 (A)), 50 data points were captured throughout time interval and therefore this imaging interval was used for calculating permeability. However, in the low permeability case (Figure 3.8 (B)), <50 data points were captured throughout the time interval and therefore, a later time interval was chosen for calculating permeability, where this second criterium was met.

3.2.3.5 Calculate permeability

When permeability is studied *in vitro* in models that provide a liquid interface on both sides of the cell barrier, such as transwell models or microchannel models (primarily membrane models), Equation 3.16 can be used to calculate solute permeability (P_s), based on Fick's first law of diffusion. Here, the flux through the cell barrier (J_s) due to diffusion is measured by quantifying the change in solute concentration in the channel/compartment into which diffusion occurs (C_{diff}) between two given time points (t_1 and t_2). Average intensity values can be used to quantify concentration if the liquid is well mixed prior to sampling, hence assuming a constant concentration in the channel/compartment. A is the surface area of the cell barrier, V_{diff} is the volume of the channel/compartment into which diffusion occurs and Δc represents the concentration difference between the added solute concentration (C_{source}) and C_{diff}. Assuming $C_{source} >> C_{diff}$ within the sampling time and consequently, $\Delta c \approx C_{source}$, in which case small concentration gradients within C_{diff} would not significantly affect diffusion through the cell barrier. I_{source} and I_{diff} represent the measured fluorescent intensities corresponding to the added solute concentration and the concentration of solute that has diffused the cell barrier, respectively.

$$P_s = \frac{J_s}{A\Delta c} = \frac{1}{A\Delta c}\frac{V_{diff}(C_{diff,t2}-C_{diff,t1})}{(t_2-t_1)} = \frac{1}{AI_{source}}\frac{V_{diff}(I_{diff,t2}-I_{diff,t1})}{(t_2-t_1)} \quad (3.16)$$

In models that rely on solute diffusion into an ECM gel, the sample cannot be well mixed before sampling and therefore, there is a clear gradient in fluorescent intensity measured inside the ECM gel, representing a higher

concentration closer to so the cell barrier (as shown by intensity profiles earlier in this chapter). Three different methods are presented below for calculating permeability in microfluidic models where solutes are diffusing into an ECM gel. Method 1 and Method 2 are most frequently used in the field, both for measuring permeability in vasculogenesis models and in the needle model, and Method 3 is derived from first principles (derivation by my supervisor, Dr. Joseph van Batenburg-Sherwood).

3.2.3.5.1 Method 1

Price and Tien (2011) published a method for calculating permeability in the needle model (referred to as Method 1), which was derived from the study by Huxley et al. (1987), where permeability was measured in capillary beds *in vivo*. Using Method 1, a region of interest (ROI) is defined that captures both the vessel and the collagen (Figure 3.9 (A)) and the average intensity, I, inside this region is quantified at two given time points (t_1 and t_2) to calculate permeability (Equation 3.17). t1 is defined as the time when the vessel has filled with dextran solution and hence, reached a maximum intensity and d_{vessel} is the vessel diameter. The method assumes that the vessel intensity (I_{vessel}) remains constant during the time interval and consequently, that the increase in average intensity is due to diffusion of dextran into the collagen. Our experimental setup resulted in zero background intensity, I_b, defined as the intensity in the ROI before perfusing the dextran solution.

$$P_s = \frac{d_{vessel}}{4} \frac{1}{I_{vessel} - I_b} \frac{I_{ROI,t2} - I_{ROI,t1}}{\Delta t} = \frac{d_{vessel}}{4} \frac{I_{ROI,t2} - I_{ROI,t1}}{I_{vessel}(t_2 - t_1)} \quad (3.17)$$

Figure 3.9 (B-C) shows results for calculating permeability using Method 1 for a high permeability case (day 3) and a low permeability case (day 9). Results show that the calculated permeability varies with Δt and the size of ROI chosen; however, results stabilise at higher values of Δt, which is in line with the 6-minute time interval that the authors suggest. The main problem with this method is the significant dependence on X, which can give at least 3-fold change in permeability, depending on how the ROI is chosen. This makes it difficult to compare results between studies; however, it can be used to estimate permeability values within the same study, if a constant value for X is chosen. Comparing the high and low permeability cases, the permeability decreases by ~1 order of magnitude from day 3 to day 9, indicating improved barrier function. The reason for the dependence on X comes from using average intensities where pixels with zero intensity are included in the analysis. Average intensity is proportional to the total intensity and the number of pixels (Equation 3.18, arithmetic mean) and hence, including zero intensity pixels skews the data as this artificially lowers the average intensity without increasing the total intensity.

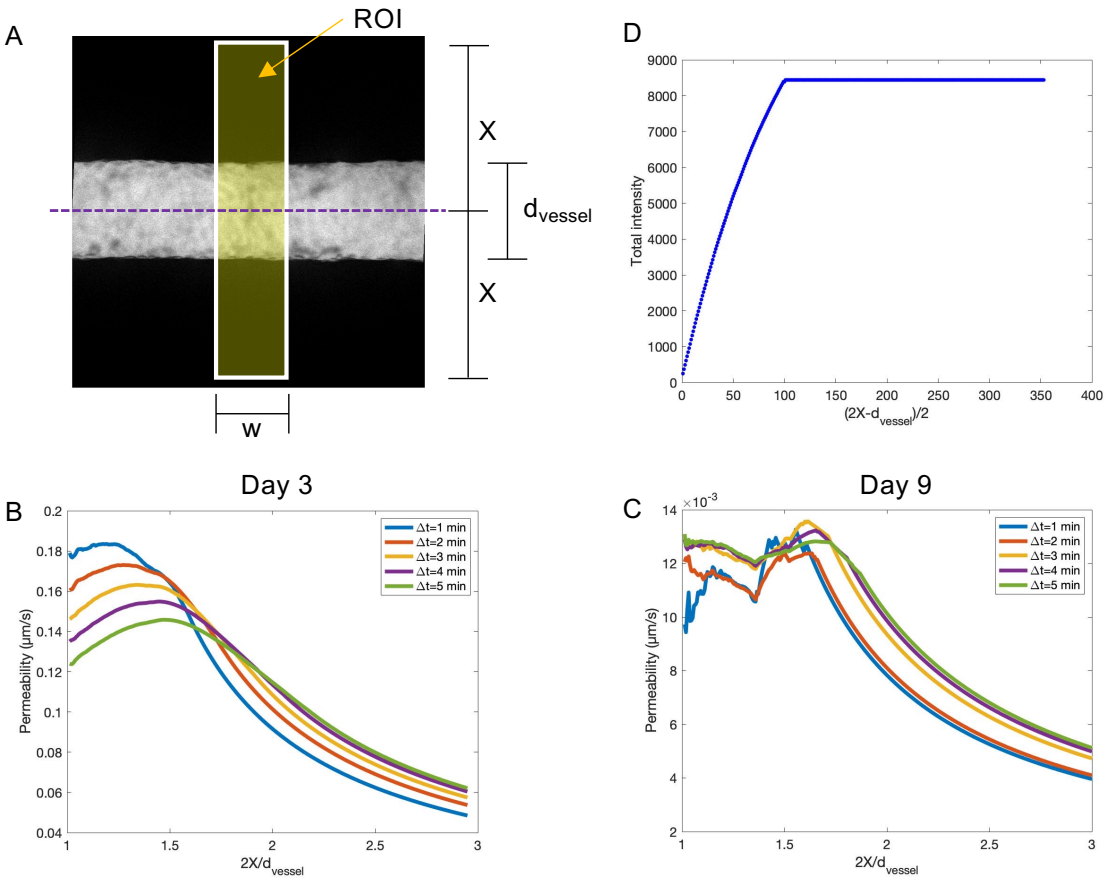


Figure 3.9: Calculating permeability using Method 1. A: ROI is chosen to capture both the vessel and the collagen. B-C: Results obtained when calculating permeability using Method 1 for a high permeability case and a low permeability case, day 3 and day 9 for the same vessel, respectively, using different values of X for defining the ROI and different time points Δt. D: The total intensity of the ROI increases with an increasing value of X as long as all pixel intensities are above zero.

$$average\ intensity = \frac{Total\ intensity}{nr\ of\ pixels} \quad (3.18)$$

This is shown in Figure 3.9 (D), where the total intensity is increasing as long as the pixel intensities are >0 (until $X=d_{vessel}/2+100$ pixels). The authors suggest using an as large ROI as possible, which consequently significantly underestimates the calculated permeability. Therefore, we did not trust this method for measuring permeability in the blood vessel-on-a-chip model.

3.2.3.5.2 Method 2

Method 2, described by Offeddu et al. (2019), is also based on the above-mentioned method for calculating permeability in the case of a liquid interface. In contrast to Method 1, this method separates the region of the vessel and the ECM, according to Equation 3.19, where A is the surface area of the vessel through which diffusion occurs ($A=\pi w d_{vessel}$), V_{ECM} is the volume of the ECM ($V_{ECM} = \pi w \frac{4X^2-d_{vessel}^2}{4}$). I_{ECM} and I_{vessel} are the average intensities in the ECM and vessel, respectively, where I_{vessel} is assumed to remain constant throughout the permeability assay.

$$P_s = \frac{V_{ECM}(I_{ECM,t2}-I_{ECM,t1})}{A\Delta I(t_2-t_1)} = \frac{\pi w(4X^2-d_{vessel}^2)(I_{ECM,t2}-I_{ECM,t1})}{4\pi w d_{vessel}(I_{vessel}-I_{ECM,t1})(t_2-t_1)} = \frac{(4X^2-d_{vessel}^2)(I_{ECM,t2}-I_{ECM,t1})}{4d_{vessel}(I_{vessel}-I_{ECM,t1})(t_2-t_1)} \quad (3.19)$$

The authors used this method to calculate permeability in a vasculogenesis model embedded in fibrin gel by capturing a z-stack of the vascular network. Applying this method to the needle model after accounting for radial diffusion, an image section can be used rather than a z-stack, since the average intensity of the section (in radial coordinates) should be the same as the average intensity for a z-stack (illustrated in the schematic in Figure 3.10). Equation 3.19 assumes a linear increase in I_{ECM} with time, in the form of $I_{ECM} = \alpha t + b$, where the slope of the linear curve, α, is calculated according to Equation 3.20 and the intercept, $b=I_{ECM,t1}$, representing the solute concentration in the ECM at the initial measurement when the concentration inside the vessel has reached a constant value.

$$\alpha = \frac{dI_{ECM}}{dt} = \frac{(I_{ECM,t2}-I_{ECM,t1})}{(t_2-t_1)} \quad (3.20)$$

Figure 3.11 shows I_{ECM} for all images in the selected 5-minute imaging interval for the four different vessels in the dataset used for method development (day 3, day 5, day 7 and day 9). Applying a linear fit to the data, the

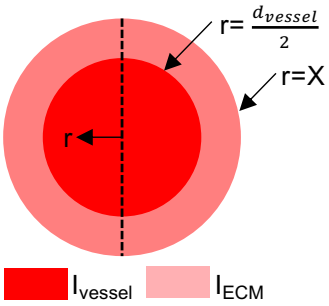


Figure 3.10: Schematic illustrating radial diffusion through the vessel wall. Dextran concentration is constant inside the vessel (I_{vessel}) and decreases in the collagen (I_{ECM}) with distance from the vessel wall r > $\frac{d_{vessel}}{2}$. I_{ECM} is constant for a given value of r.

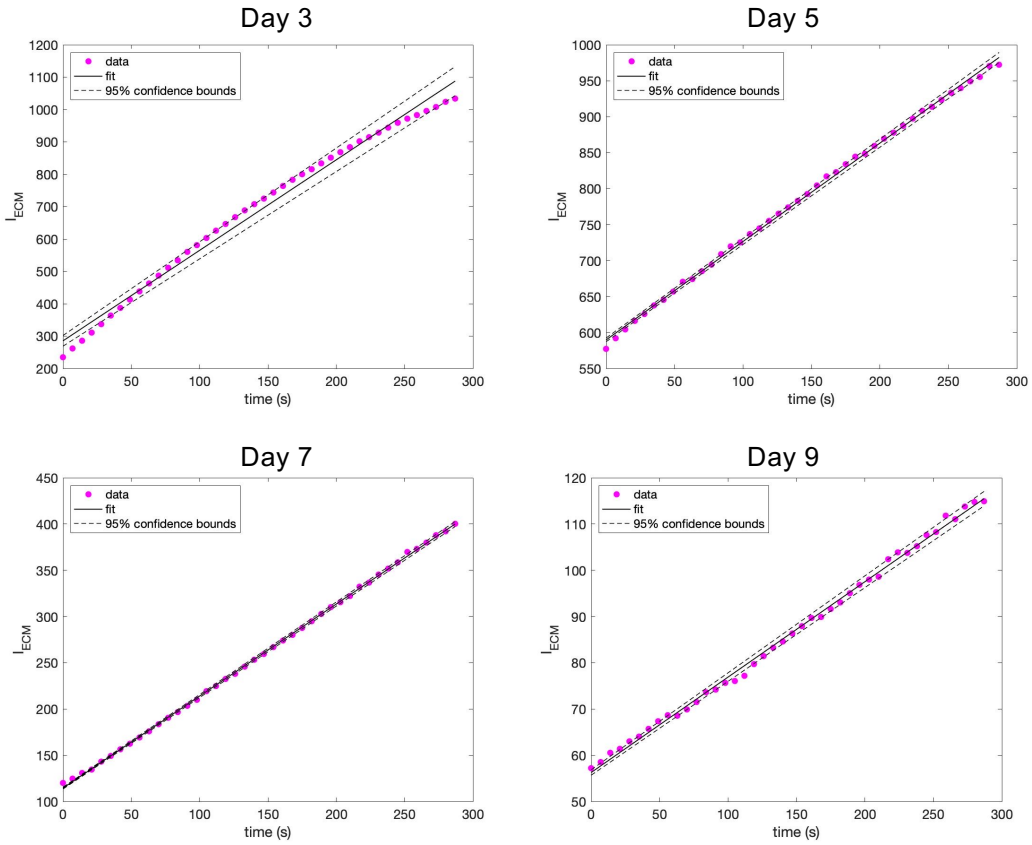


Figure 3.11: Linear fit of I_{ECM} for four vessels with different barrier function. Graphs showing the change in I_{ECM} with time for the 5-minute imaging interval for the same vessel imaged on four different days, representing for different barrier functions. A linear fit is applied to the the data in each graph and shown with 95% confidence bounds.

assumption of a linear increase in I_{ECM} with time is valid for all days except day 3, which represents the highest permeability of the four cases, corresponding to a subconfluent endothelial monolayer.

The concentration difference across the vessel wall ($\Delta I=I_{vessel}-I_{ECM,t1}$) considers the average intensity in the ECM, which is not a correct assumption as it does not account for the fact that the intensity in the ECM is not constant but decreases with distance from the vessel wall. Therefore, using the average intensity will overestimate the concentration difference and therefore overestimate permeability. However, for cases when $I_{ECM,t1} << I_{vessel}$ this does not have a significant effect as $\Delta I \approx I_{vessel}$. Table 3.3 shows $I_{ECM,t1}$ compared to the vessel intensity, showing that $I_{ECM,t1}$ is ~5-10 fold smaller than I_{vessel} for more leaky vessels (day 3 and day 5) and ~25-50 times smaller than I_{vessel} for vessels with tighter monolayers (day 7 and day 9), suggesting that this condition is unlikely to significantly affect the result for vessels with tight monolayers but might do so for more leaky vessels, which have a higher rate of diffusion through the vessel wall.

Day	$I_{ECM,t1}/I_{vessel}$
3	~0.1
5	~0.2
7	~0.04
9	~0.02

Table 3.3: Comparing $I_{ECM,t1}$ and I_{vessel} for the four different cases in the dataset used for model development.

It is unclear how X is defined, and consequently what region is used to obtain I_{ECM} in the study by Offeddu et al. (2019). This is important since including pixels with zero intensity will significantly affect the results as described earlier in this chapter. Therefore, to calculate permeability using Method 2, X was chosen to not include any pixels with zero intensity during the entire imaging interval. Figure 3.12 shows permeability calculated using Method 2 for the dataset using $X=2/3d_{vessel}$. The figure compares using two images captured at t_1 and t_2, referred to as the end-point-method, and using a linear fit between all images in the 5-minute imaging interval (substituting the fit parameters α and b into Equation 3.19). To maximise the number of data points obtained for the end-point-method, $\Delta t=t_2-t_1=7s$ was used, which corresponds to two consecutive images in the 5-minute imaging interval. The end-point-method (shown in blue) resulted in noisy data and was filtered using a Savitzky-Golay smoothing filter to reduce noise (shown in red). Using a larger Δt might slightly reduce noise, the authors use $\Delta t=12$ minutes; however, this analysis demonstrates that using only two data points to calculate permeability, the results will be directly correlated to which data points are chosen and therefore, very prone to bias. The trend obtained using the Savitzky-Golay smoothing filter does not show great dependence on t_1 (except for day 3), which is a promising result as it suggests that the calculated permeability

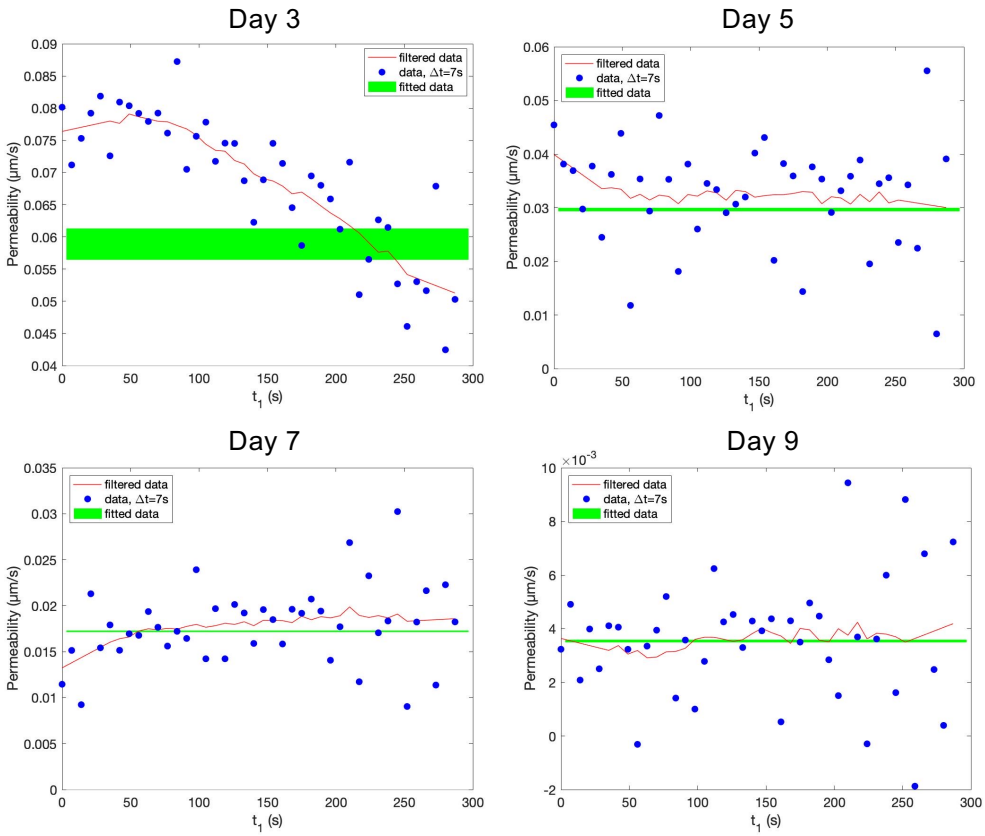


Figure 3.12: Permeability calculated using Method 2. Graphs comparing the end-point-method and the fit-method for the same vessel imaged on four different days.

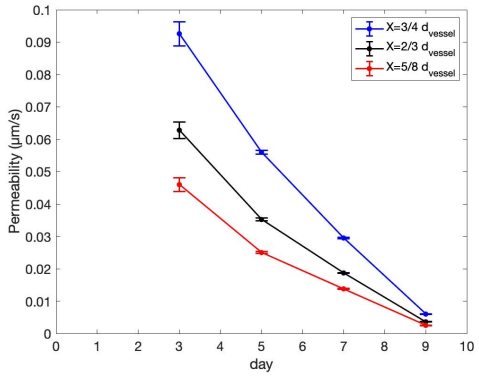


Figure 3.13: Dependence on X when calculating permeability using Method 2. Graph showing permeability calculated using Method 2 for the same vessel imaged on four different days, using different values of X. Results show that permeability calculated using Method 2 depends on the chosen value of X, where lower values of X result in lower calculated permeability. Error bars show ±2 standard deviations.

does not depend on the selected imaging interval. The fit-method resulted in a cleaner signal, shown in green with 95% confidence bounds on the fit; however, for the high permeability case (day 3) where the data did not show a linear trend, the fit-method underestimated permeability. Dependence on X was also investigated. Results are shown in Figure 3.13 for three different values of R_{ECM} (X=3/4d_{vessel}, X=2/3d_{vessel} and X=5/8d_{vessel}), using the fit-method to calculate permeability. Using this method, the calculated permeability show dependence on how X is defined (data shown in Appendix: Chapter 3). This is a limitation of this method, indicating that it is not completely accurate. However, in all three cases results show a clear and similar trend of decreasing permeability as the vessel is kept in culture, which correlates to improved barrier function. Furthermore, this suggests that as long as X is kept constant during analysis within the same study, Method 2 can be used to detect differences in permeability; however, it becomes difficult to compare the results to published data, especially since variables including X are commonly not defined or justified in published studies.

Method 2 proved to be a more accurate method to calculate permeability compared to Method 1 and therefore this was the method chosen for data analysis for model validation, using the below conditions

i) Using X=2/3d_{vessel}, choosing the 5-minute imaging interval to not include any pixels with zero intensity inside this region
ii) Using the fit-method, applying a linear fit to the I_{ECM} data to represent diffusion over time

3.2.3.5.3 Method 3

A significant limitation of Method 1 and Method 2 is that they do not account for the solute distribution in the ECM and consider a steady state of diffusion (according to Fick's first law) due to $I_{ECM} << I_{vessel}$. This problem is more pronounced for higher permeabilities and therefore becomes a problem when studying changes in barrier function, for example due to drug treatments. Derived from the advection-diffusion equation and Reynolds Transport Theorem we obtained a more complex expression for calculating permeability (Equation 3.21), which accounts for time-dependent changes in diffusion into the ECM and further does not require a linear decrease in solute concentration in the ECM (full derivation with assumptions in Appendix: Chapter 3).

$$P_s = \frac{1}{1-C^*\left(\frac{d_{vessel}}{2},t\right)}\left(\frac{2}{d_{vessel}}\frac{\partial}{\partial t}\int_{\frac{d_{vessel}}{2}}^{X} rC^*(r,t)\,dr - \frac{2X}{d_{vessel}}D\frac{\partial C^*(X,t)}{\partial r}\right) \quad (3.21)$$

The key terms in the equation are explained below and plotted in Figure 3.14 for a high permeability case (day 3) and a low permeability case (day 9).

- C^* is the concentration in the ECM, normalised to the concentration inside the vessel (Figure 3.14 (A-B))
- $C^*\left(\frac{d_{vessel}}{2}, t\right)$ is the normalised concentration in the ECM measured as close to the vessel wall (x=$\frac{d_{vessel}}{2}$) as allowed by imaging resolution (Figure 3.14 (C-D))
- $\int_{\frac{d_{vessel}}{2}}^{X} rC^*(r,t)\,dr$ is the number of normalised moles that have diffused into the control volume ($\frac{d_{vessel}}{2}$<r<X) (Figure 3.14 (E-F)). Since Method 3 does not assume a pre-defined relationship for diffusion over time, the fit that best suited the data can be chosen for each case. Here, a 2nd degree polynomial fit was used for the high permeability case and a linear fit for the low permeability case.
- D is the diffusivity of the solute in the given ECM. A robust method for calculating D has not yet been found. Therefore, D=10 $\mu m^2/s$ was used for calculating permeability, based on measurements by Ramanujan et al. (2002) in different concentration collagen gels and assuming a constant value of D within the control volume.
- $\frac{\partial C^*(X,t)}{\partial r}$ is the radial gradient of the normalised concentration evaluated at r=X, describing the solute diffusion out from the control volume (Figure 3.14 (G-H)). This data was obtained using a linear fit of C^* between the last 10 data points in the control volume between r=X-10 and r=X.

The data in Figure 3.14 was used to calculate permeability, using $X=2/3d_{vessel}$. Results for all four days (day 3, day 5, day 7 and day 9) are shown in Figure 3.15, applying a Savitzky-Golay smoothing filter to reduce noise. Results are within the same order of magnitude as for Method 2 and similarly don't show significant time-dependence. Dependence on X was also investigated and similar to Method 2, higher values of X (and thereby larger control volumes) resulted in higher calculated values of permeability (Figure 3.16, data shown in Appendix: Chapter 3). However, a clear decrease in permeability could be observed here as well with increased time in culture, which is a promising result. Work is ongoing to understand where this X-dependence comes from and consequently, which adjustments are required in the analysis to reach a robust method for calculating permeability both for vessels with high and low permeabilities.

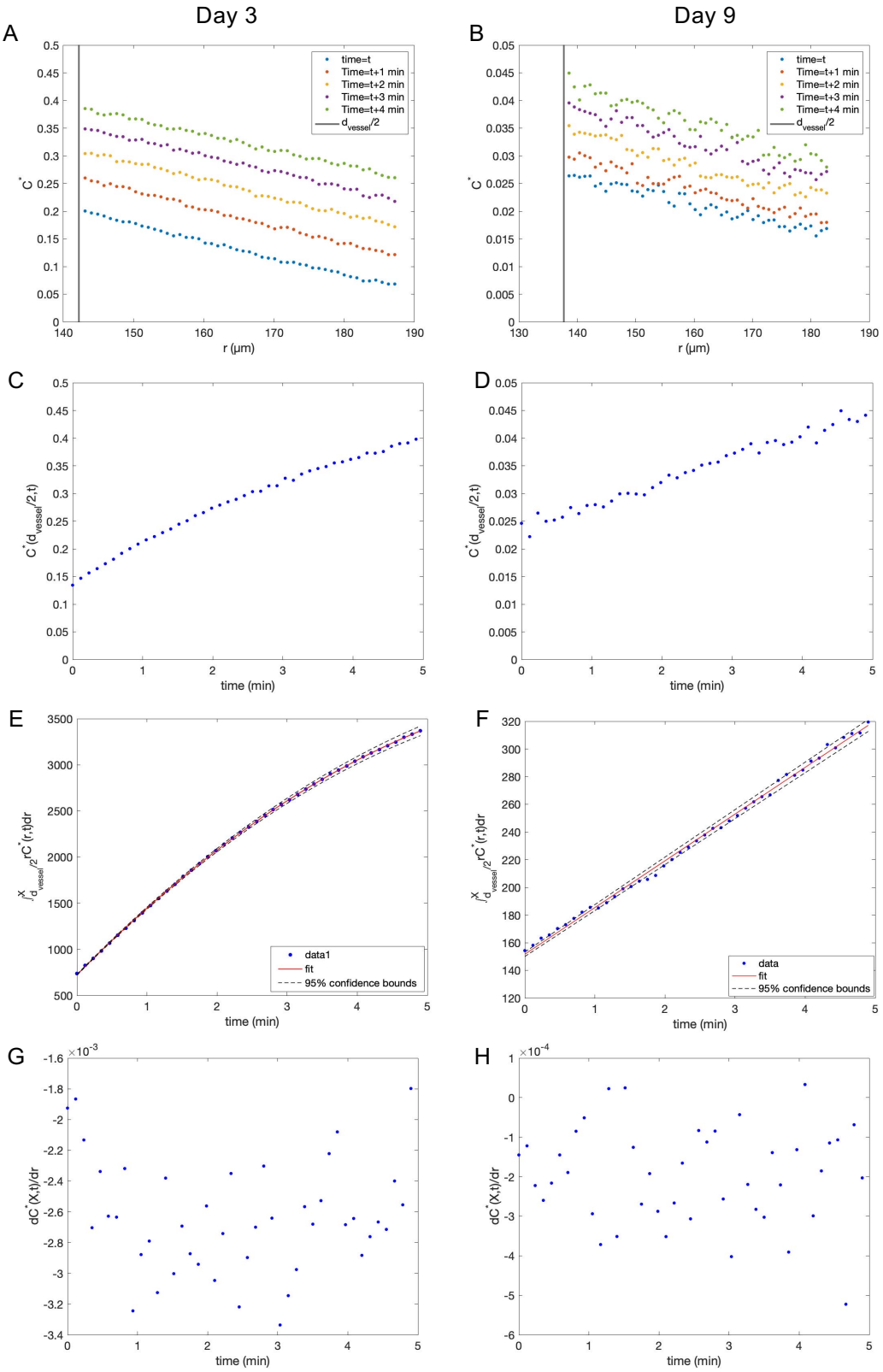


Figure 3.14: Graphs showing the key terms in the permeability equation for Method 3. Comparison of a high permeability case and a low permeability case, measured on day 3 and day 9 for the same vessel, respectively.

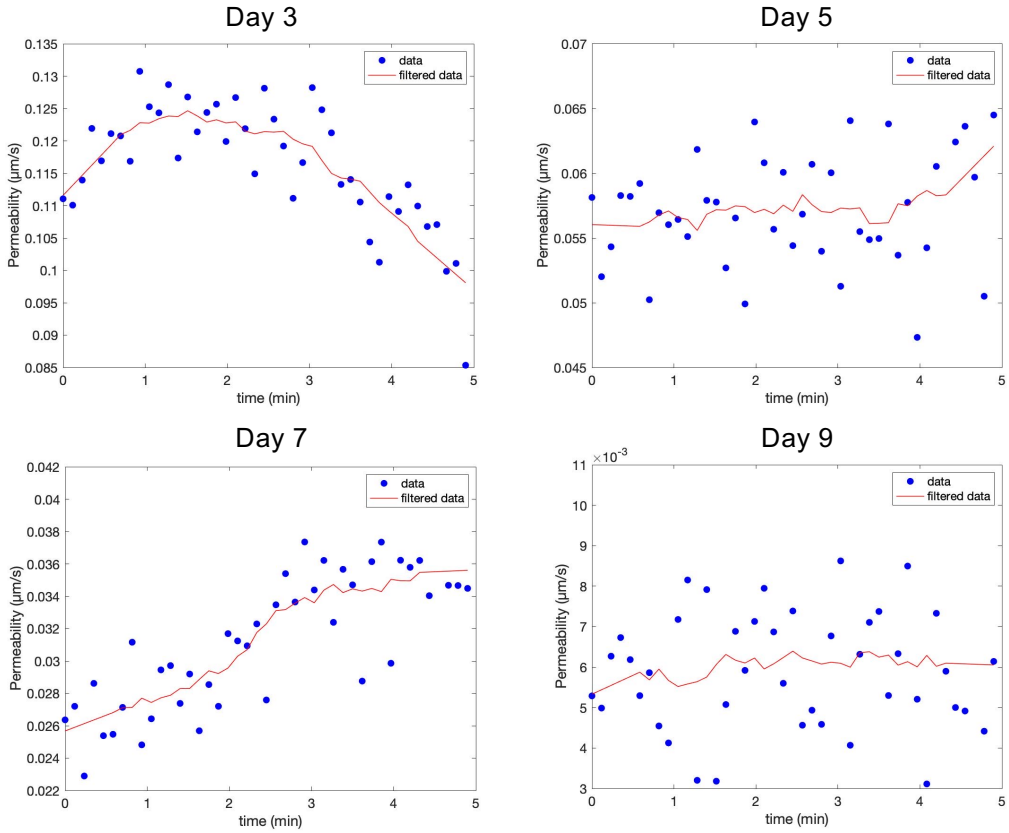


Figure 3.15: Permeability calculated using Method 3. Graphs showing permeability calculated using Method 3 for the same vessel imaged on four different days (day 3, day 5, day 7 and day 9). The data was filtered using a Savitzky-Golay smoothing filter to reduce noise.

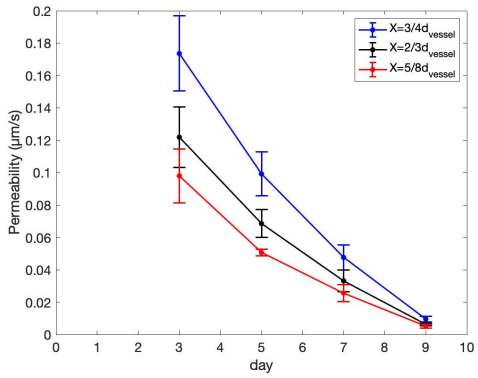


Figure 3.16: Dependence on X when calculating permeability using Method 3. Graph showing permeability calculated using Method 3 for the same vessel imaged on four different days, using different values of X. Results show that permeability calculated using Method 3 depends on the chosen value of X, where lower values of X result in lower calculated permeability. Error bars show ±2 standard deviations of the filtered data.

3.3 Model Validation

Permeability was measured for n=14 different vessels at different days post cell seeding to show that barrier function improves with time in culture and furthermore, that the blood vessel-on-a-chip model can be used as a functional assay to study permeability (this data was obtained using Method 2 for calculating permeability). Results are shown in Figure 3.17 (data shown in Appendix: Chapter 3), which suggests that the measured permeability can be divided into three main categories of barrier function, high permeability (P_s>0.05 μm/s), moderate permeability (0.015<P_s<0.05 μm/s) and low permeability (P_s<0.015 μm/s). The low permeability category is within the range of what has previously been considered a tight barrier in the literature, as shown earlier in this chapter (Table 3.1). Figure 3.17 (B) focusses on the moderate and low permeability groups. Furthermore, results indicate that it is not possible to rely on the number of days in culture to know when a certain barrier function is reached, as this can vary greatly between vessels, which is likely dependent on cell seeding density. Four datapoints are highlighted in the graphs in magenta, red, blue and green colour. They represent four different vessels that were seeded on the same day and permeability was measured on day 4 post cell seeding, where three vessels fall into the moderate permeability category and one vessel shows low permeability. The vessels were fixed the day after measuring permeability and stained for the junctional protein VE-cadherin and nuclear marker DAPI to study cell confluency in these vessels. Results for three of the vessels (magenta, red and blue) are shown in Figure 3.18, where all the vessels show a confluent monolayer. Two of the vessels with higher permeability (red and blue) are slightly deformed, but in terms of cell coverage or gaps in the monolayers, no obvious differences were observed compared to the lower permeability case (magenta). These results suggest that confluency alone is not always an accurate indication of barrier function. However, being able to measure permeability for the same vessel on multiple days shows that this assay does not significantly affect cell viability in the blood vessel-on-a-chip model but rather that permeability can be used as a real-time measurement to determine if a functional vessel has been formed (corresponding to a given baseline permeability), for use in other assays.

3.4 Discussion

The molecular weight of dextran used in this study was chosen to allow comparison of results to published studies in the field, which commonly use fluorescently labelled Bovine Serum Albumin (BSA) for validation of permeability, which corresponds to ~70 kDa dextran. This relatively high molecular weight is a useful tool for validating vessel formation; however, a lower molecular weight should be used to investigate the sensitivity of

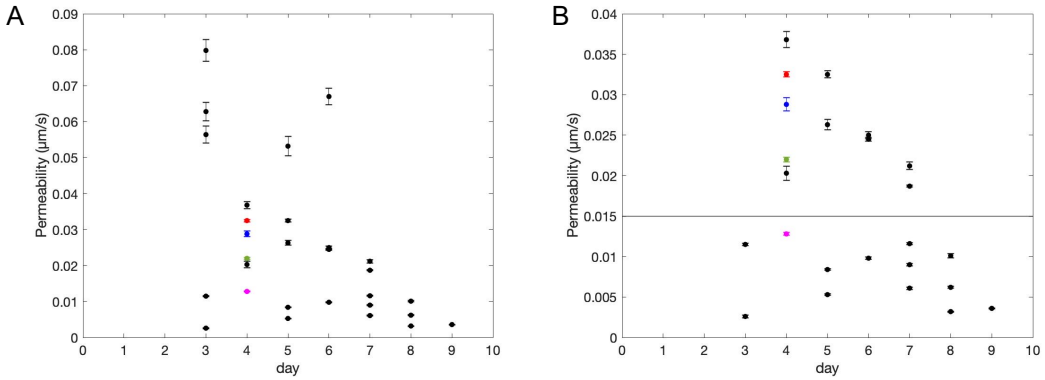


Figure 3.17: Permeability measurements at different days post cell seeding. Graphs showing permeability measurements for n=14 different vessels (total n=28 measurements, some vessels were measured on multiple days). The same data is shown in both graphs, where B considers only the moderate to low permeability measurements <0.05 µm/s. The coloured data points represent four vessels seeded on the same day. Error bars show ±2 standard deviations.

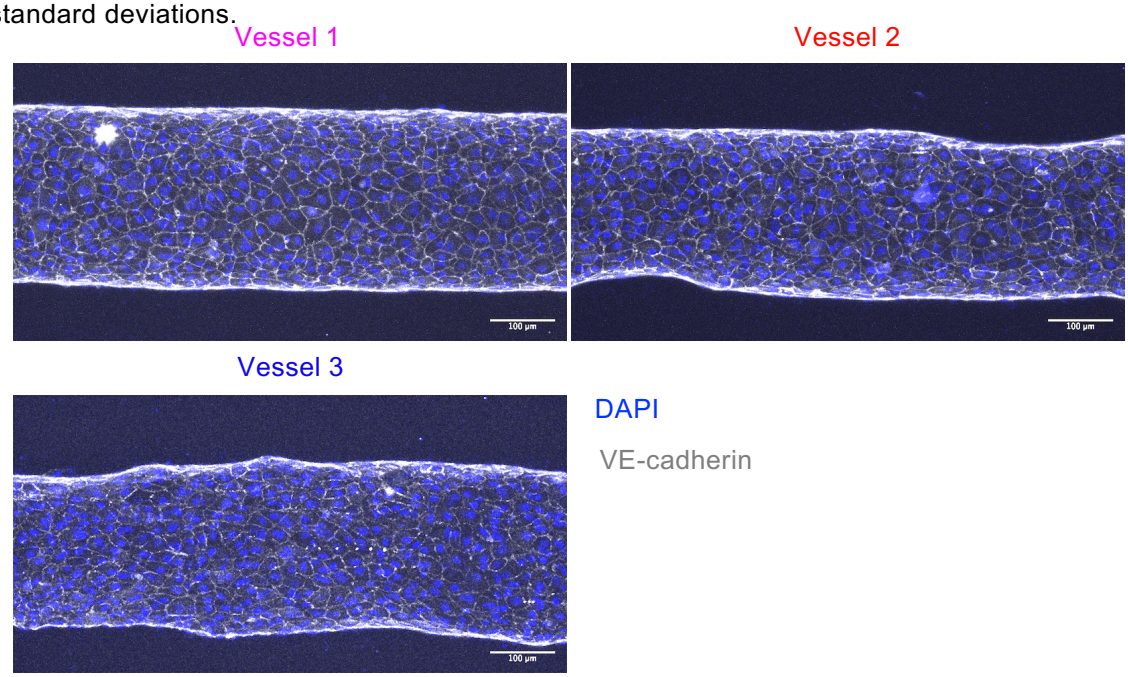


Figure 3.18: Immunofluorescent staining following permeability measurements. z-projected immunofluorescent images of n=3 vessels that were seeded on the same time and fixed the day after measuring permeability. The vessels are colour coded to correspond to the permeability data shown in Figure 3.17. All vessels show confluent monolayers without obvious gaps. Scale bar=100 µm.

the assay. In fact, there were a few cases where not enough dextran had leaked out from the vessel during the assay, and therefore even though these cases clearly represented high barrier function, permeability could not be quantified using this higher molecular weight dextran. To further validate the sensitivity of the model, permeability should be measured following stimulating the endothelium with agents or drugs that result in impaired or improved barrier function.

Comparing the different methods described for data analysis, it is clear that Method 1 is not reliable for quantifying permeability due to the significant dependence on how the ROI was chosen for analysis. Method 2, if using the fit-method and choosing X so that no zero-intensity pixels are included in the analysis, proved to be a robust method for detecting changes in permeability. However, since it considers a linear increase in solute concentration in the ECM and assumes $I_{vessel} >> I_{ECM}$ it is not suited for quantifying high permeabilities, which might be problematic if a lower molecular dextran is used. An advantage using the linear fit is the possibility to reduce the imaging interval used for analysis, since it does not account for time-dependence. Method 3 would be the ideal method to use as it allows time-dependent diffusion and high solute concentrations in the ECM; however, further optimisation of the analysis method is required to be confident in the absolute values of permeability calculated using this method. Results from both Method 2 and Method 3 showed dependence on X when calculating permeability. The reason for this is unknown but suggests that neither method in their current form gives accurate quantification of permeability in terms of absolute values. However, it should be noted that none of the published methods for quantifying permeability in a microfluidic model such as the needle model claims to be able to do this. In addition to the analysis methods, this effect could be related to data acquisition, including photobleaching of the fluorescent signal in the ECM and this should be investigated. Since the vessel is perfused during the permeability assay, the dextran solution inside the vessel is constantly being replaced and therefore is not sensitive to photobleaching. The same is not true for the dextran in the ECM, as diffusion through the vessel wall occurs much slower compared to perfusion along the vessel. Furthermore, additional calibration is required to understand the relationship between fluorescent intensity and dextran concentration. If the linear region of the calibration curve has an offset which is not accounted for in the analysis, as suggested by the current calibration data, this will affect lower intensities more than higher intensities and could therefore contribute to the observed X-dependent effects.

Chapter 4: Application 2 – Disease modelling of thrombosis

4.1 Introduction

Thrombosis is a leading cause of death worldwide. Despite decades of investigation into the mechanisms of coagulation, the role of endothelial cells and mural cells in the process are still not completely understood, which has implications for the discovery and development of treatments to manage this disease. In a healthy quiescent state the endothelium serves as an anticoagulant surface, which prevents interaction with circulating platelets and coagulation factors, and hence clot formation is unlikely to occur other than to stop bleeding if the vessel ruptures. However, endothelial activation results in dysfunctional regulation and loss of this anticoagulant capacity (to varying extent), and consequently clot formation can occur in the absence of vascular injury due to the presence of procoagulant agents. Tissue factor (TF) is a key procoagulant molecule, expressed by multiple cell types (including vascular cells) and is required for initiation of the extrinsic pathway in the coagulation cascade. There are different anticoagulant mechanisms involved in preventing platelet adhesion and fibrin deposition. Multiple pathways in the healthy, non-activated endothelium contribute to inhibit platelet adhesion, including pathways mediated by PAR receptors, which induce the release of nitric oxide and prostaglandin. For preventing fibrin deposition, TFPI (tissue factor pathway inhibitor) is released by endothelial cells and has an important role, together with its co-factor Protein C, for inhibiting free factor Xa (coagulation factors described in Chapter 1), which is required for initiation of the common pathway. Thrombomodulin (TM) is a transmembrane protein expressed by resting endothelial cells; TM regulates activation of protein C, which also inhibits circulating coagulation factors. TM binds to thrombin to inhibit its activity before thrombin is converted to fibrinogen (Yau et al., 2015); however, TM expression, as well as other anticoagulant mechanisms, is downregulated by inflammation. This highlights the importance of a healthy endothelium in preventing thrombosis. Understanding how to revert the endothelium back to a healthy anticoagulant state is therefore relevant for drug discovery. Furthermore, differences in the pro and anti-thrombotic phenotype of endothelial cells between vascular beds may influence the clinical picture of patients who present with localised vascular bed-specific thrombosis. However, studying vascular bed-specific thrombosis remains challenging both *in vivo* and *in vitro* (discussed in Chapter 1), which motivates the need for new models and tools for disease modelling to improve the understanding of the contribution of the vascular endothelium in thrombotic disease.

The blood vessel-on-a-chip model (described in Chapter 2) was used to develop an *in vitro* 3D thrombosis assay as a research tool for modelling thrombotic disease in a controlled microenvironment using human cells. The model was validated for studying thrombosis using HUVEC and ECFC, perfusing whole blood through the

vessel and studying coagulation during real-time imaging. Furthermore, model sensitivity was investigated using blocking antibodies. The 3D thrombosis assay was carried out after culturing endothelial cells in the blood vessel-on-a-chip platform (at <1 dyne/cm^2) until a confluent monolayer was established. The key experimental steps required for the 3D thrombosis assay are listed below

1. Endothelial activation through stimulation with proinflammatory cytokines
2. Blood collection and handling
3. Fluorescent labelling of blood components
4. Blood recalcification
5. Blood perfusion during real-time imaging

The methods used in steps 1-2 were determined based on previous studies and are described below. Steps 3-5 of the 3D thrombosis assay required optimisation, which is described in the model development section of this chapter.

4.1.1 Endothelial activation

Activation of endothelial cells by different agents results in upregulation of pro-thrombotic pathways and downregulation of anti-thrombotic pathways. In this 3D thrombosis assay, coagulation is studied in the context of inflammation by global endothelial activation with Tumour Necrosis Factor-α (TNF-α). TNF-α is an inflammatory cytokine, which is released primarily by macrophages and is considered a “master regulator” initiating a cascade of inflammatory cytokine production in response to tissue damage or infection (Parameswaran and Patial, 2010). Consequently, TNF-α, together with other circulating inflammatory cytokines, play an important role in numerous inflammatory diseases including atherosclerosis, sepsis and rheumatoid arthritis. Endothelial cells are the principal targets of TNF-α (Pober, 2002) and therefore, this cytokine is commonly used for endothelial activation *in vitro*. Activation results in multiple pro-inflammatory events, including increased expression of leukocyte adhesion molecules such as E-selectin, VCAM-1 and ICAM-1 and increased vascular permeability, to allow leukocytes to adhere to ECs and migrate into the tissue through endothelial junctions and initiate an inflammatory response. In terms of coagulation, TNF-α has been shown to downregulate thrombomodulin expression and upregulate tissue factor expression in endothelial cells and thereby switch the endothelium to a pro-thrombotic state (Madge and Pober, 2001).

The vessels were activated with TNF-α (Peprotech) by replacing the cell culture media in the inlet reservoir with 3 ml EGM2 supplemented with 25 mM HEPES and 10 ng/ml TNF-α, which was perfused through the vessels for 4-6 h prior to blood perfusion and real-time imaging. In control vessels, cell culture media was replaced by 3 ml EGM2 supplemented with 25 mM HEPES but without TNF-α at the same time point. TNF-α was stored in aliquots of 100 µg/ml at -20°C until us and to minimise effects of cytokine degradation from repeated freeze-thawing, each TNF-α aliquot was thawed maximum three times and then discarded.

4.1.2 Blood collection and handling

All blood collection was performed by clinical members of the Vascular Science Section, Drs. Adam Hartley, Andrew Porter and Marta Peverelli. For the experiments described in this chapter, blood was collected ~30 minutes prior to starting the 3D thrombosis assay. Blood was collected from healthy volunteers (male and female) who had not taken any pain relief medication for the past two weeks. Blood was collected in 3.2% trisodium citrate (transferred from BD Vacutainer Citrate Tubes), using a syringe with a 21G butterfly needle (from BD vacutainer set). The first 3 ml of blood was discarded and following collection the blood was mixed by slowly inverting the collection tube. The blood was used for experiments within 3h following collection, during which time it was stored at room temperature.

Since the outcome of the 3D thrombosis assay is dependent on both the endothelium and the blood used for perfusion, blood collection and handling are important factors to consider for the assay. Three parameters were considered to assure reproducible blood collection and handling

1. Blood sample variability
2. Anticoagulant used for blood collection
3. Artificial platelet activation from phlebotomy

4.1.2.1 Blood sample variability

Collecting blood from different people will result in variations in blood composition, including coagulation factors, between individuals. When using blood from healthy volunteers, it is not always possible to know their medical history and due to time limitations when performing *in vitro* experiments, it is not always feasible to characterise every blood sample. However, when studying coagulation, it is important to realise that anti-coagulant medication and pain relief medications (non-steroidal anti-inflammatory drugs, aspirin and

paracetamol) can inhibit platelet aggregation for maximum the lifetime of a platelet (~8-9 days) (Driver et al., 2020), and consequently, using blood collected from individuals that have recently taken such medicines is likely to affect the results of the 3D thrombosis assay.

4.1.2.2 Anticoagulant used for blood collection

Using an anticoagulant for blood collection is crucial to avoid blood clotting in the collection tube through activation of the intrinsic pathway. Several different anticoagulants exist, where heparin, EDTA (Ethylenediaminetetraacetic acid), and citrate are most commonly used, which all target the common pathway in the coagulation cascade. Heparin inhibits thrombin and activated factor X and thereby also the downstream generation of fibrin. EDTA and trisodium citrate both bind to free calcium in the blood, which is an important co-factor required at multiple stages for progression through the common pathway (Bowen and Remaley, 2014). However, anticoagulation with EDTA is irreversible whereas a blood sample collected on trisodium citrate can be recalcified to allow coagulation by carefully matching the concentrations of trisodium citrate and recalcification buffer.

4.1.2.3 Artificial platelet activation from phlebotomy

It is known that platelets are sensitive to shear rate, where perfusion at higher shear rates can induce platelet activation and aggregation (Holme et al., 1997). When withdrawing blood into a syringe or vacutainer, the shear rate that the platelets experience during collection is directly proportional to the velocity at which blood enters the collection tube. Toshima et al. (2008) used a laser light scattering method to study spontaneous platelet aggregation in blood samples following collection to investigate how variable parameters in phlebotomy affected spontaneous activation of blood components during blood collection. The study found that higher gauge needles, the use of a tourniquet and using vacutainers (rather than manually withdrawing blood with a syringe) resulted in increased platelet aggregation following blood collection.

4.2 Model development of the 3D thrombosis assay

4.2.1 Fluorescent labelling of blood components

Following blood collection, the blood was aliquoted into working volumes for each vessel by transferring 1.2 ml blood into 7 ml bijou tubes, using a 5 ml stripette, withdraw and dispense at low speed to minimise spontaneous platelet aggregation.

4.2.1.1 Fluorescent labelling of platelets

To visualise platelet adhesion and aggregation during the 3D thrombosis assay, platelets were labelled using a Phycoerythrin (PE) conjugated anti-human CD41 antibody (BioLegend), which was added to the blood sample at a concentration of 10 µl antibody per ml of blood. CD41 is primarily expressed on platelets and megakaryocytes and is commonly used in flow cytometry as a marker to identify platelets in whole blood or plasma.

4.2.1.2. Fluorescent labelling of fibrinogen

To visualise fibrin deposition during the 3D thrombosis assay, Alexa Fluor 647-conjugated fibrinogen from human plasma (Thermo Fisher Scientific) was added to the blood sample at a concentration of 5 µg/ml. The fluorescently labelled fibrinogen was stored in aliquots of 5 mg/ml at -20°C and defrosted only once for use in the 3D thrombosis assay. The concentration used was optimised based on preliminary experiments using a concentration of 20 µg/ml, as described by Mathur et al. (2019). However, this higher concentration resulted in high fluorescent signal outside of the vessel, which was obstructive for data analysis in terms of quantifying fibrinogen deposition inside the vessel, shown in Figure 4.1 (for reference to an image without fibrinogen signal outside the vessel, refer to Figure 4.5). Simply lowering the microscope gain was not sufficient to solve the problem with fibrinogen outside the vessel as this would lose the signal inside the vessel due to the significantly lower fluorescent intensity. An important difference between our blood vessel-on-a-chip model and the parallel channel based microfluidic model used by Mathur et al. (2019) is that whilst in our model endothelial cells are cultured in a 3D collagen gel, Mathur et al. (2019) cultured endothelial cells on a PDMS surface; here, radial diffusion outside the vessel would not be possible and therefore, any fibrinogen extravasation would not have been noticed in such a model.

4.2.2 Blood recalcification

As the last step, <5 minutes before blood perfusion, the blood sample was recalcified to allow coagulation to occur and thus fibrin deposition to take place in the 3D thrombosis assay. This was achieved by adding recalcification buffer (100 mM $CaCl_2$, 75 mM $MgCl_2$ reconstituted in PBS) to the blood sample in the 7 ml bijou tube at a 1:10 ratio (Mathur et al., 2019) and mixing by inverting the tube.

Two different approaches were investigated for blood recalcification: recalcification of the blood sample prior to perfusion (Figure 4.2 (A)) and recalcification during perfusion (Figure 4.2 (B)). The objective was to perfuse

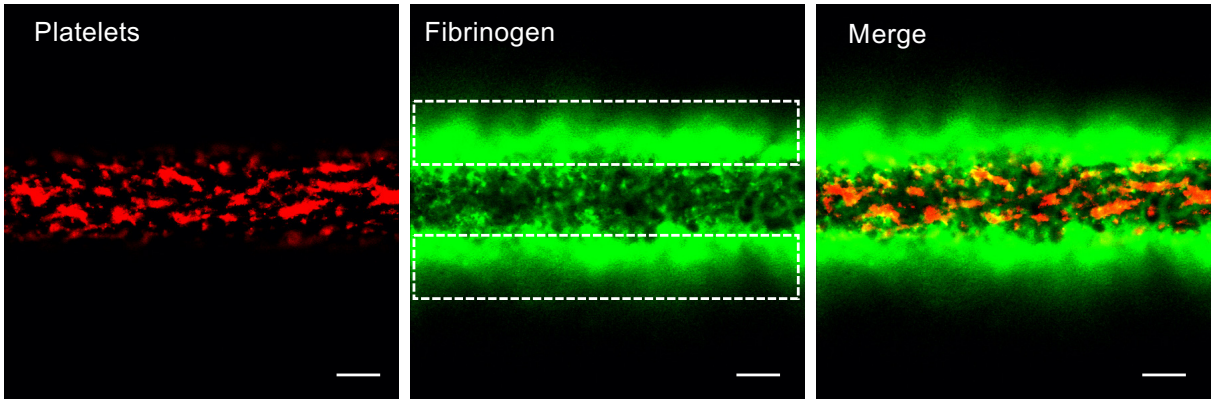


Figure 4.1: High fibrinogen concentrations result in fluorescent signal outside the vessel. Platelet adhesion (red) and fibrinogen deposition (green) in a TNF-α activated vessel. Adding 20 µg/ml labelled fibrinogen to the blood resulted in high fluorescent signal outside the vessel, indicated by the white regions. Representative images for n=3 vessels. Scale bars=100 µm.

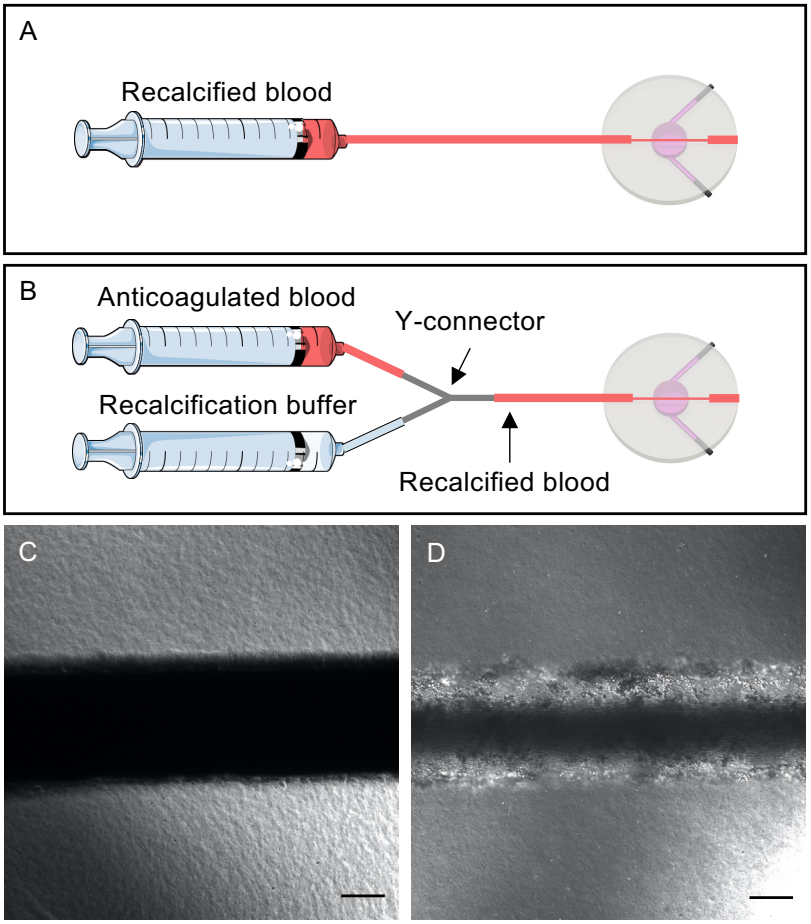


Figure 4.2: Different approaches for blood recalcification to avoid clotting in the tubing. A-B: Two different approaches for blood recalcification were investigated, recalcification of the blood sample prior to perfusion (A) or recalcification during perfusion (B). C-D: Brightfield images of the vessel during blood perfusion with a recalcified blood sample with no clotting in the tubing (C) or with clotting in the tubing (D), where separation of blood components was clearly visible (observed for n=3 vessels perfused with the same blood sample). Scale bars=100 µm.

blood through the vessel for 20 minutes without having clotting inside the tubing, which would obstruct blood flow through the vessel. In the first approach, the blood sample was recalcified as described above and then transferred into a syringe and perfused through the vessel. In the second approach, two different syringes were used in the perfusion setup and perfused at the same flow rate: one syringe containing anticoagulated blood and one containing the recalcification buffer. A Y-connector was used to connect tubing from the two syringes resulting in blood recalcification in the tubing just prior to entering the vessel. The second approach delays recalcification and should therefore be able to prevent clotting in the tubing for longer time periods, compared to the first approach. However, within the set time period of 20 minutes, neither of the two approaches resulted in clotting in the tubing during the optimisation experiment. Recalcification during perfusion (the second approach) required a more involved perfusion setup and resulted in significant dilution of the blood sample. Therefore, the first approach of recalcification of the blood sample prior to perfusion was used for all experiments in the 3D thrombosis assay. In all the experiments carried out in the 3D thrombosis assay, clotting in the tubing occurred only once, which was assumed to be due to donor variability and these experiments were discarded. If clotting in the tubing occurred, it was easily detectable in the brightfield channel, as it resulted in separation of blood components (Figure 4.2 (C-D)) and only plasma (yellow colour) was perfused through the vessel.

4.2.3 Blood perfusion during real-time imaging

4.2.3.1 Perfusion setup

The perfusion setup used for the 3D thrombosis assay is shown in Figure 4.3. A syringe pump was used to perfuse blood sample through the vessel, which was placed on the confocal microscope stage attached to the 3D printed unit. Unless otherwise stated, a flow rate of 40 µl/min was used for perfusion, which corresponds to a shear stress of ~10 dyne/cm^2, considering the non-Newtonian fluid properties of blood and a shear rate of ~250 s^{-1}. This flow rate was chosen for validation purposes; due to the haemodynamic properties of blood, including the higher viscosity compared to cell culture media, hydrostatic pressure in the 3D printed perfusion unit was not sufficient to facilitate blood perfusion through the vessel. Therefore, in these experiments blood had to be perfused at a higher shear stress compared to EC culture conditions. 10 dyne/cm^2 was chosen as the perfusion flow rate, as it is commonly used for *in vitro* studies with in HUVEC. A 1 ml syringe with recalcified blood was placed on the syringe pump and silicone tubing (ID=0.8 mm, OD=2.4 mm, Cole Parmer) was attached to the syringe through a luer fitting (Female Luer to Hose Barb Adapter, 1/16", Cole Parmer). To minimise dead volume in the perfusion circuit a custom designed PDMS connector was used to connect the

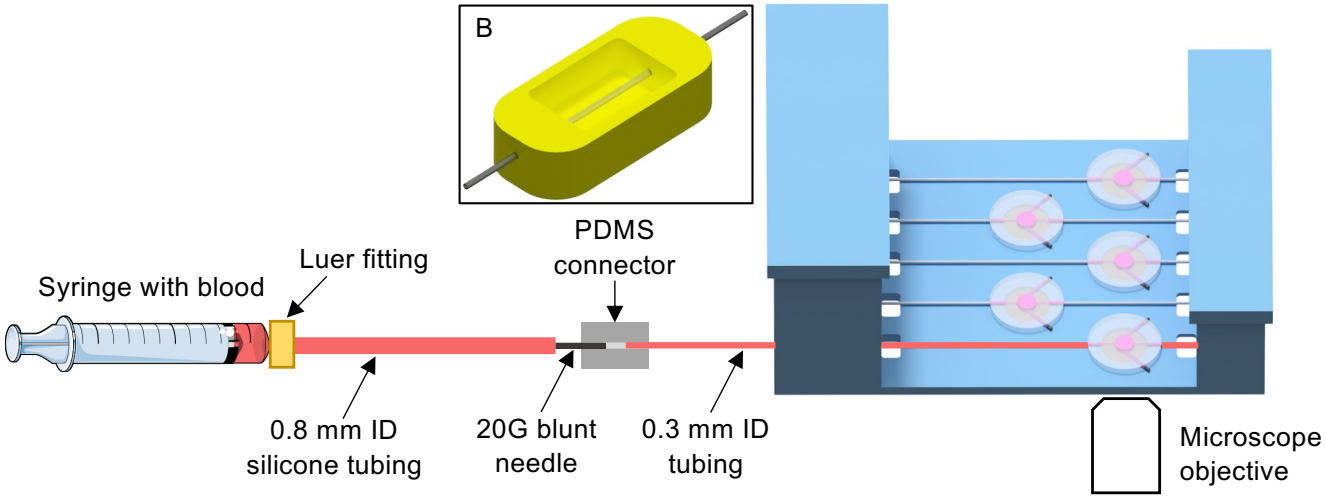


Figure 4.3: **The setup used for perfusing blood through the blood vessel-on-a-chip during real-time confocal microscopy.** The syringe with blood is attached to a syringe pump for blood perfusion and a PDMS connector is used to connect the tubing in the 3D printed perfusion unit to the tubing attached to the syringe. B: The 3D printed mould used for creating the PDMS connector, where PDMS is polymerised around tubing, which is inserted across the mould to create a hollow cylindrical channel.

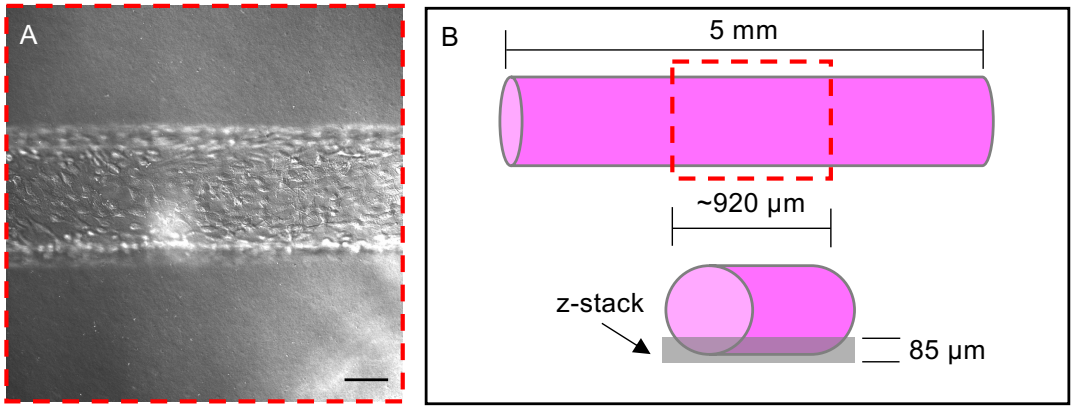


Figure 4.4: Acquiring data for the 3D thrombosis assay using confocal microscopy. A: Brightfield image in 10x magnification focussing of the bottom surface of the vessel prior to starting blood perfusion. B: In the 3D thrombosis assay data was captured in one region along the vessel, corresponding to a vessel length of ~920 µm, compared to the total vessel length of 5 mm. A z-stack was used to capture the coagulation response at the bottom surface of the vessel. Scale bar=100 µm

tubing attached to the syringe to the tubing used in the 3D printed unit, which was removed from the inlet reservoir and attached to the PDMS connector. The PDMS connector was simply manufactured by casting PDMS in a 3D printed mould around one piece of tubing (OD=0.61 mm) inserted across the mould to create a hollow cylindrical channel (Figure 4.3 (B)). The PDMS connector could be attached to the silicone tubing using the metal part of a 20G blunt needle, which was removed from the plastic luer fitting by submerging the needle in 70% ethanol for a few days, which dissolved the glue holding the two parts together.

4.2.3.2 Acquiring data

In the 3D thrombosis assay, the coagulation response, namely platelet adhesion and fibrinogen deposition, was studied at the bottom surface of the vessel with live imaging over a time interval of 20 minutes. To acquire data the vessel was imaged at 10x magnification, focussing on the bottom surface of the vessel in the brightfield channel (Figure 4.4 (A)) prior to starting blood perfusion. Using the brightfield channel to determine the location of the vessel surface proved difficult and therefore a z-stack with 14 images (~85 µm depth) was captured, rather than only one imaging plane. The depth of the z-stack is indicated as the grey region in Figure 4.4 (B). To allow quantification of fluorescent signal the gain, laser power and pin hole microscope settings were kept constant for all experiments (543 nm laser: gain: 650, laser power: 50.0, pinhole: 1 Airy Units, 633 nm laser: gain: 610, laser power: 20.8, pinhole: 1 Airy Units). Using 12-bit resolution resulted in captured images with 1024x1024 pixels, corresponding to imaging a region of the vessel with length ~920 µm, which is around 1/5 of the total vessel length of 5 mm. For a 20-minute time interval, this resulted in capturing four z-stacks for each vessel. Figure 4.5 shows a characteristic response of platelet adhesion and fibrinogen deposition at the end point of the assay, after 15-20 minutes of perfusion for a HUVEC vessel stimulated with TNF-α compared to a control vessel. The TNF-α stimulated vessel shows significant platelet adhesion and fibrinogen deposition compared to a background platelet signal and almost no fibrinogen deposition in the control. The time point of 20 minutes was chosen as the end point for the assay as this is comparable to the previous *in vitro* thrombosis studies (described in Chapter 1) and proved sufficient to capture a clear coagulation response in the TNF-α stimulated vessel. Ideally, the imaging time should be minimised to allow performing the 3D thrombosis assay on multiple vessels sequentially within the 3h time limit of using the collected blood. Following these preliminary experiments, the image size was decreased to 512x1024 pixels, which allowed capturing 10 z-stacks in the 20-minute time interval, indicated as the white regions in Figure 4.5, and therefore provided additional data points to the assay to better capture the dynamic coagulation response. Since the region used for data analysis was only ~1/5 of the total vessel length, the coagulation

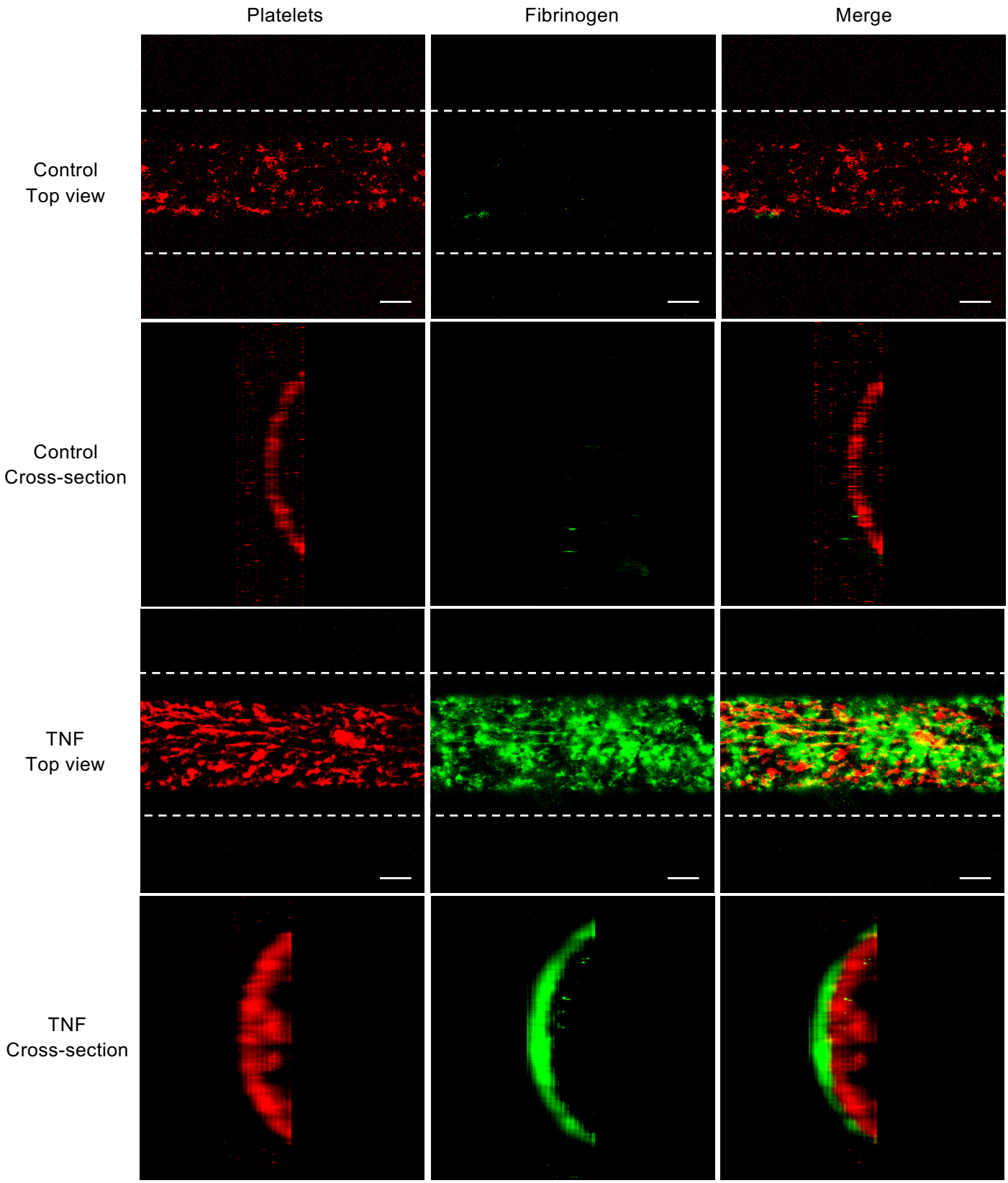


Figure 4.5: Characteristic response of platelet adhesion and fibrinogen deposition in the 3D thrombosis assay. Projected z-stacks showing a characteristic response of platelet adhesion and fibrinogen deposition at the end point of the 3D thrombosis assay, after 15-20 minutes of perfusion, for vessels stimulated with TNF-α compared to controls. The TNF-α stimulated vessel shows significant platelet adhesion and fibrinogen deposition compared to a background platelet signal in the control and almost no fibrinogen deposition. The white lines indicate a reduced image height of 512 pixels to allow additional z-stacks to be captured within 20 minutes. Scale bars=100 μm.

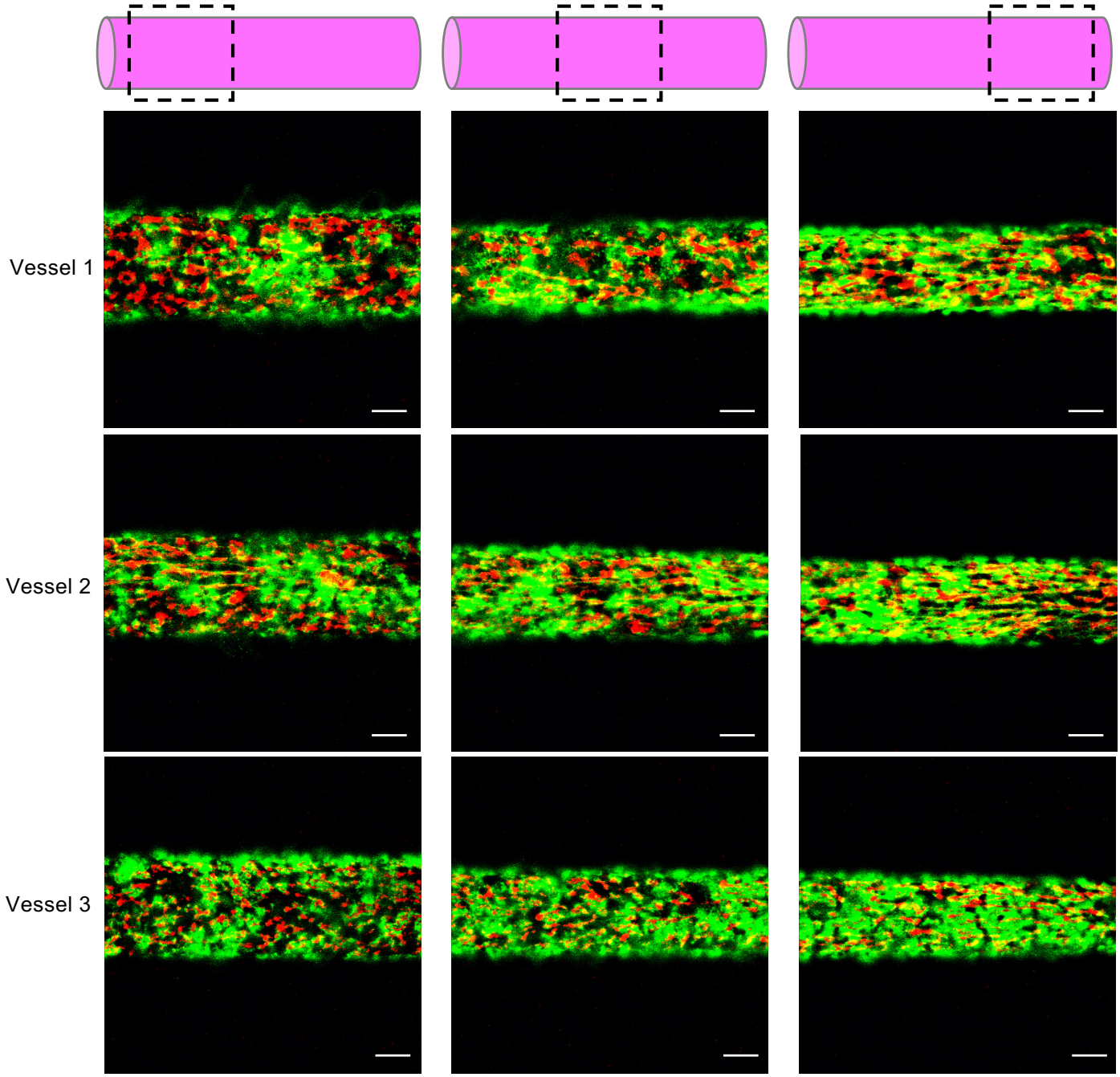


Figure 4.6: Coagulation response along the vessel. Projected and merged z-stacks showing platelet adhesion (red) and fibrinogen deposition (green) in three different locations along the same vessel (inlet, centre, outlet) for n=3 different TNF-α stimulated vessels. Scale bars=100 μm.

response was captured in different regions of the vessel (inlet, centre and outlet) to investigate variability along the vessel, for three separate TNF-α stimulated vessels (Figure 4.6). Since the images in the different regions were captured sequentially, they do not correspond to the same time point and are therefore not directly comparable but indicate a clear coagulation response along the entire vessel, even though local variations in platelet adhesion and fibrinogen deposition might occur. Based on the optimisation described above, in the final protocol for capturing data the decreased imaging size of 512x1024 pixels was used, resulting in capturing 10 z-stacks in the 20-minute imaging interval, and the inlet regions of the vessel was used.

4.2.4 Data analysis

The needle model, which our blood vessel-on-a-chip model is based on, has not previously been used for studying thrombosis. None of the *in vitro* thrombosis models described in Chapter 1 have a cylindrical vessel geometry and hence don't capture data in a z-stack format. Therefore, optimisation of data analysis was required to quantify the coagulation response. Following data acquisition, the images were pre-processed in Fiji (ImageJ) and analysed using a custom-written algorithm in Matlab, quantifying the amount of platelet adhesion and fibrinogen deposition. The method of analysis is outlined in the flow diagram in Figure 4.7 and can be divided into three parts: pre-processing in Fiji, pre-processing in Matlab and data analysis in Matlab, which are described below. Using an automated image processing protocol was chosen for efficiency as well as for minimising bias during the analysis.

4.2.4.1 Pre-processing in Fiji

Using the optimised method for data acquisition described above, the 3D thrombosis assay captured 10 z-stacks, each containing 14 images (84.81 μm), in three channels: brightfield, platelets (555) and fibrinogen (647) (total 140x3 images). Fiji was used to import the microscopy images, divide them into the three different channels and convert to tif format (140 images per channel) for interfacing with Matlab (Mathworks). Since quantification of platelet adhesion and fibrinogen deposition relies on identifying positive signal in the images, a built-in median filter "despeckle" was applied to all fluorescent images to remove "salt and pepper noise" by replacing each pixel with the median value in its 3x3 neighbourhood and thereby removing areas with individual positive pixels.

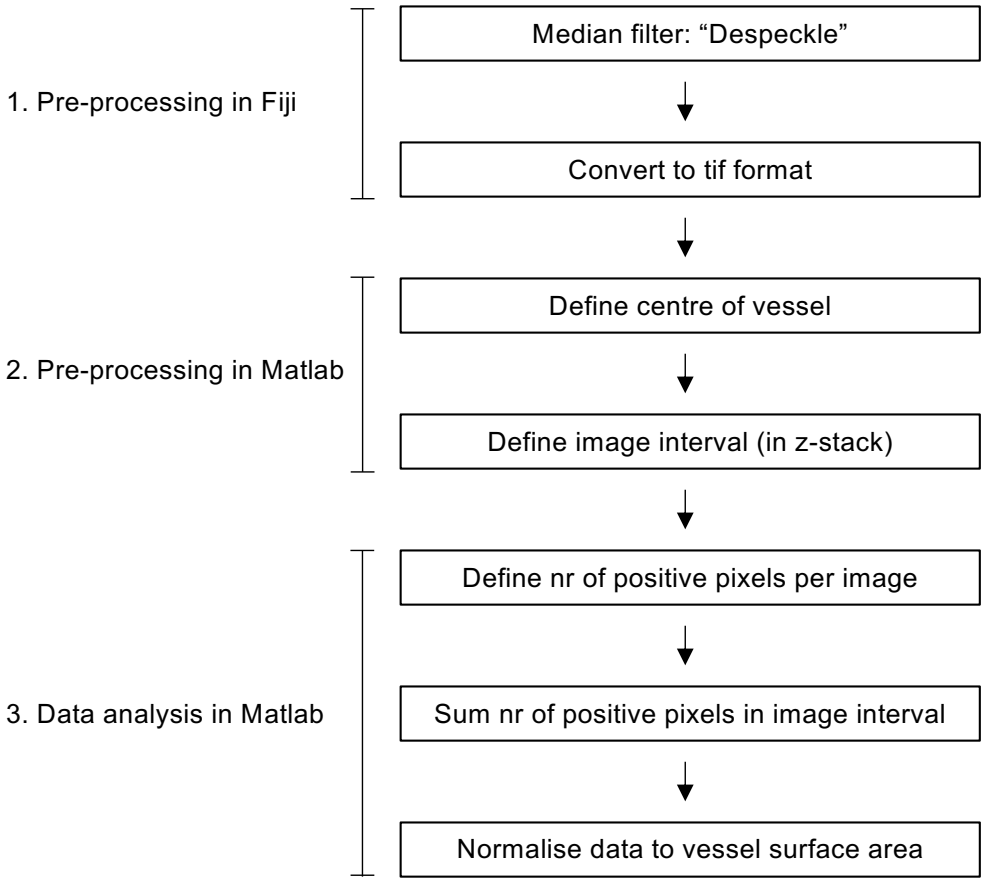


Figure 4.7: Flow diagram for data analysis of the 3D thrombosis assay.

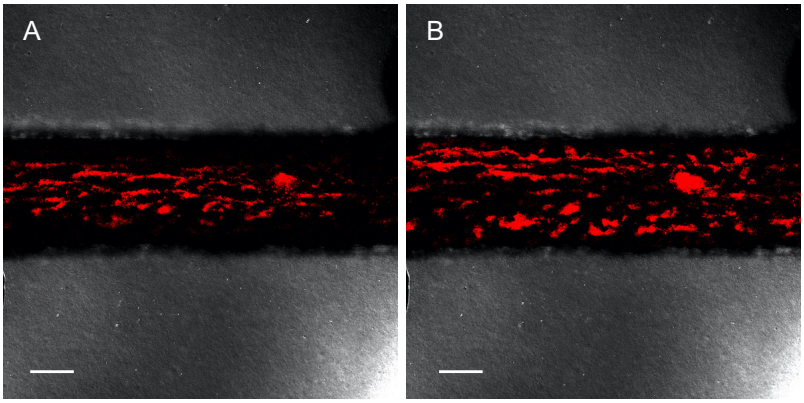


Figure 4.8: Investigating the use of the brightfield channel for identifying the vessel boundaries. Moving through the z-stack the brightfield channel cannot capture the vessel curvature. The platelet channel was therefore used for determining the vessel dimensions rather than the brightfield channel. A-B: Merged image of the brightfield (vessel in black) and platelet channels of image nr 2 from the bottom surface of the vessel (A) image nr 4 (B), indicating how the dimensions in the platelet channel change with z-location but not in the brightfield channel. Scale bars=100 µm.

4.2.4.2 Pre-processing in Matlab

Since the method of capturing data required manually defining the imaging range of the z-stack, this was a source of variability in the quantification of the 3D thrombosis assay. The platelet channel in the last z-stack (final time point) was used to identify the location of the vessel and the range of images to be included in the analysis. The platelet channel was chosen for this as platelet signal was captured both in TNF-α stimulated vessels and in controls, which was not the case for fibrinogen. The brightfield channel was considered for this purpose; however, the brightfield channel does not capture confocal images and could therefore not be used to distinguish the location of the vessel boundaries throughout the z-stack (Figure 4.8). By combining the signal from all images (referred to as z-projecting) in the last z-stack (final time point) in the platelet channel and quantifying the number of positive pixels per row (one row is 1x1024 pixels), the vessel boundaries could be identified as the first and last rows with >1% positive pixels per row. The centre of the vessel was defined as the row located at an equal distance between the defined boundaries. Figure 4.9 (A) shows positive platelet signal in red and the detection of vessel boundaries using this method. In case <1% positive platelet signal would be detected, the vessel would be considered to have zero platelet adhesion. The last z-stack was chosen for this step as platelet signal is expected to increase over time and using this approach therefore relies of the assumption that the vessel boundaries did not move over time. The pixel rows detected as vessel boundaries for all z-stacks are shown in Figure 4.9 (B). No movement was defined as no data points are exceeding five pixel-rows beyond the boundaries in the last z-stack (final time point).

The image interval used for data analysis was defined by studying the platelet signal in the individual images in the last z-stack (final time point) and specifically the platelet signal ±10 pixels from the centre of the vessel (yellow region in Figure 4.10 (A)). All image planes where >1% of pixels in the yellow region were positive for platelet signal were used for data analysis. Figure 4.10 (B) shows platelet signal in an untreated vessel in the first image plane used for analysis, where the majority of the signal was detected at the centre of the vessel. Figure 4.10 (C) shows the last image plane, where no platelet signal was detected at the centre of the vessel as a result of moving away from the bottom surface of the vessel. This image plane was not included in the analysis. From this figure it is also clear that there is large variability in intensity values both within the same image plane and between different planes. The reason for this in unclear, which is why absolute intensity values were not used for data analysis.

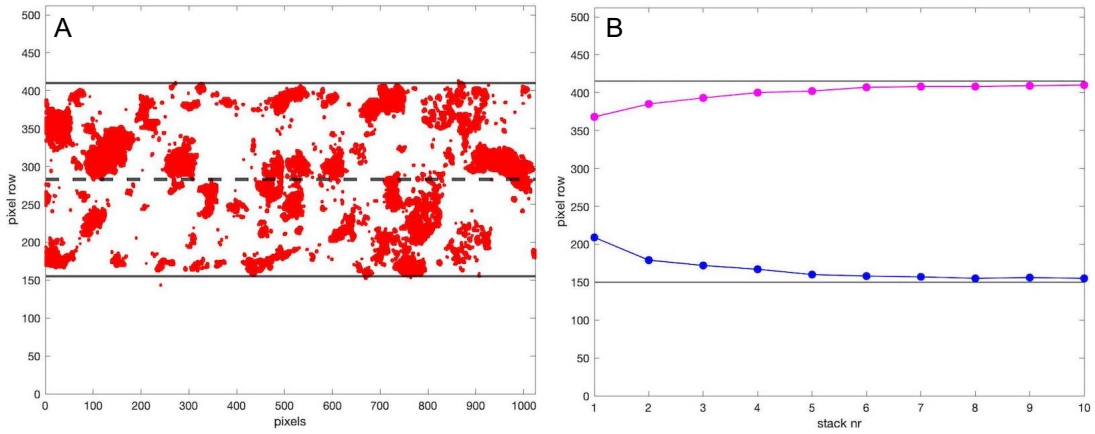


Figure 4.9: Using the platelet channel to define the vessel boundaries. A: The centre of the vessel (dashed line) was defined at an equal distance from the vessel boundaries (solid lines). Red indicates platelet signal and white is the background (zero signal). The vessel boundaries were defined by quantifying the positive signal for each pixel row and selecting the first and last pixel rows with >1% signal per row. B: The vessel boundaries located for each z-stack, where the values obtained from the last z-stack was used for analysis. The vessel was considered to have no movement in the x-y direction if both vessel boundaries remained <5 pixels beyond the final vessel boundaries defined in the final z-stack, indicated by solid lines in the graph.

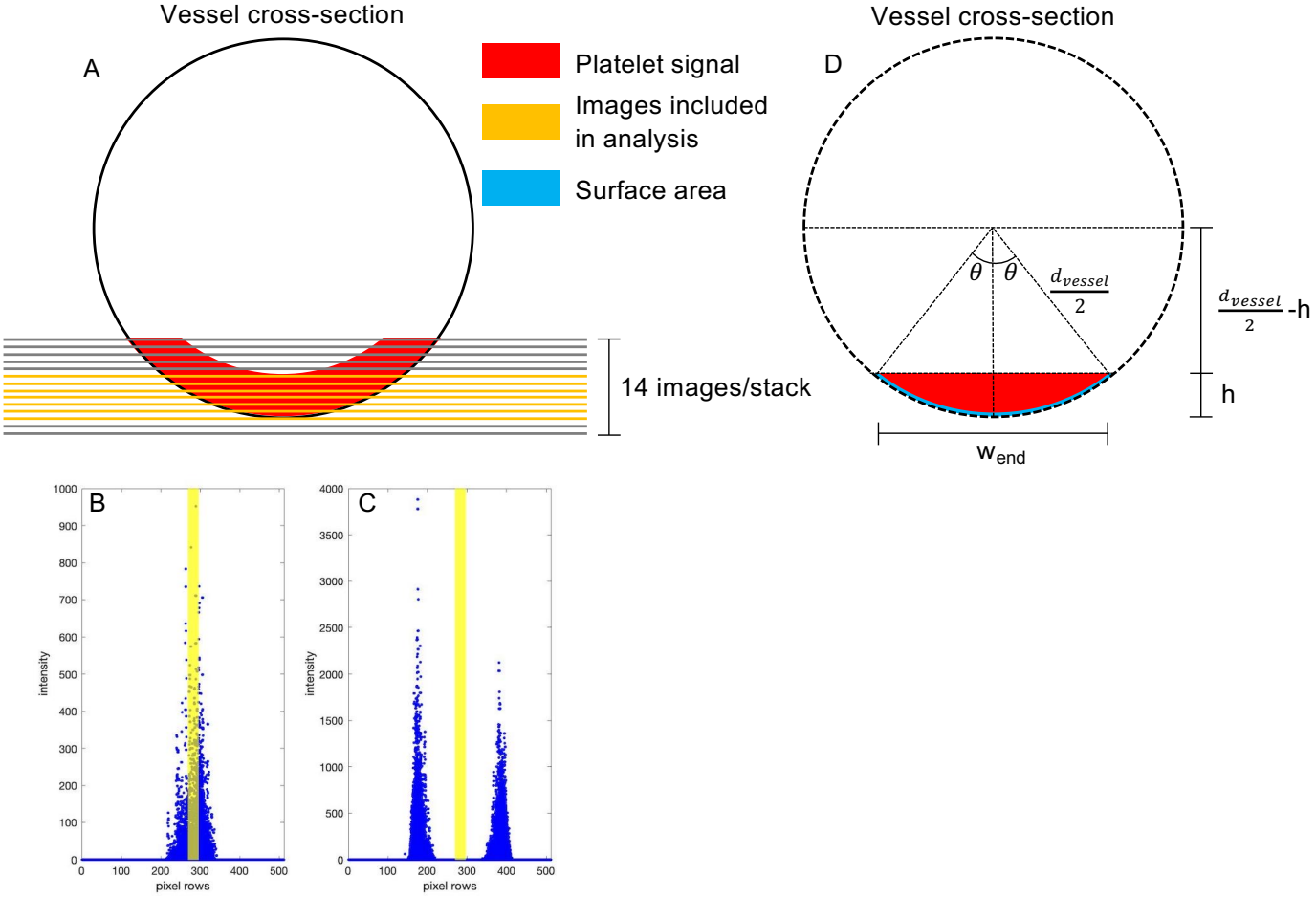


Figure 4.10: Defining the image interval used for data analysis. A-C: Defining the image interval (yellow image planes in fig A) for data analysis. Studying platelet signal (blue), all images in the image interval had >1% positive signal in the yellow region (±10 pixels from the centre of the vessel). B shows an image plane where this criteria is met and C shows an image plane where it is not. D: Calculating the vessel surface area (blue) based on acquired data of w_{end} and h.

4.2.4.3 Data analysis in Matlab

Having defined the location of the vessel as well as the image interval to use for data analysis, the number of positive pixels within the vessel boundaries were quantified for all images individually in both the platelet and fibrinogen channels (the background in both channels had zero intensity). The total number of positive pixels were quantified for each timepoint by adding the results of all images in the defined image interval for each channel (fibrinogen and platelets) referred to as *positive signal*. The same vessel boundaries and image intervals were used for all timepoints. This result was normalised to the vessel surface area ($A_{surface}$) captured in the image interval (Figure 4.10 (D), Equation 4.1), to obtain a value for norm. positive signal for each time point and channel. The vessel surface area was calculated according to Equations 4.2-4.5, where L is the length of the vessel, d_{vessel} is the vessel diameter, w_{end} is the identified vessel width of the last image included in the image interval, h is the height of the image interval and θ is the angle in radians. The parameters w_{end}, h and l were obtained from imaging while R and θ were calculated using basic trigonometry (Figure 4.10 (D)), assuming a circular vessel cross-section.

$$\text{norm. postive signal} = \frac{positive\ signal}{A_{surface}} \tag{4.1}$$

$$A_{surface} = L \times \pi d_{vessel} \frac{2\theta}{2\pi} = L \times \theta d_{vessel} \tag{4.2}$$

$$d_{vessel}^2 = \left(\frac{w_{end}}{2}\right)^2 + \left(\frac{d_{vessel}}{2} - h\right)^2 \tag{4.3}$$

$$d_{vessel}^2 = \frac{{w_{end}}^2}{8h} + \frac{h}{2} \tag{4.4}$$

$$\sin(\theta) = \frac{w_{end}}{d_{vessel}} \tag{4.5}$$

Quantification of positive signal normalised to surface area was carried out for all time points, resulting in 10 data points per vessel for each parameter. These results are from here on referred to as norm. platelet adhesion and norm. fibrinogen deposition and represent platelet adhesion and fibrinogen deposition, respectively.

4.3 Model validation

The 3D thrombosis assay has been validated using two types of endothelial cells, namely HUVEC and ECFC isolated from blood samples of healthy donors. The sensitivity of the assay was validated using HUVEC and

healthy donor ECFC were used to investigate the potential of using the assay with a different source of endothelial cells with a higher relevance in disease modelling.

4.3.1 3D thrombosis assay using HUVEC

The response of platelet adhesion and fibrinogen deposition after endothelial stimulation with TNF-α is shown in Figure 4.11, comparing results at the end time point of the 3D thrombosis assay (at t=18-20 minutes) for vessels perfused with blood samples from five different donors. Since these experiments were also used for method optimisation, the experiments might have different number of data points due to vessel damage or problems with imaging (vessel movement or defining the image interval not meeting the analysis criteria). Figure 4.11 (A) and Figure 4.11 (D) show the quantification of norm. platelet adhesion and norm. fibrinogen deposition, respectively. Control vessels show platelet adhesion <1 and around zero fibrinogen deposition in all cases. Results indicate a wider spread for the TNF-α stimulated vessels, ~1.5-4 for platelet adhesion and ~3-10 for fibrinogen deposition. To investigate the effect of blood donor variability, the platelet adhesion data for the TNF-α stimulated vessels was normalised by platelet adhesion in the control sample for the same blood donor (or normalised to the average of the control samples if there was more than one data point). This is shown in Figure 4.11 (B), as the fold change increase in platelet adhesion compared to control vessels. TNF-α stimulated vessels show a ~3.5-30 fold increase in platelet adhesion compared to controls and interestingly, the vessels group according to blood sample, suggesting that the variability in platelet adhesion is more dependent on blood sample variability rather than vessel variability. The same analysis could not be carried out for fibrinogen deposition, since the control vessels have zero signal; however, as seen in Figure 4.11 (D), these results do not suggest grouping based on blood sample but rather indicate vessel variability. This might be due to limitations in experimental design as only fluorescently labelled fibrinogen will be detected in the 3D thrombosis assay. Normal fibrinogen levels in blood from healthy donors is 2-5 g/l (Poon et al., 2012) (corresponding to 2000 µg/ml), which is expected to have significant contribution to the coagulation response in this assay, since only 5 µg/ml fluorescently labelled fibrinogen was added to each blood sample. However, the contribution of this non-fluorescently labelled fibrinogen was not captured and consequently, vessels that show lower fibrinogen deposition in the 3D thrombosis assay might have a higher proportion of fibrinogen deposition from non-fluorescently labelled fibrinogen. Due to the low number of data points for the same blood sample as well as the different number of data points between blood samples, statistical analysis for this data set proved challenging. A Mann-Whitney U test was used to determine if there were statistically significant differences between the treatment groups (TNF and control); however, this analysis did not account for blood

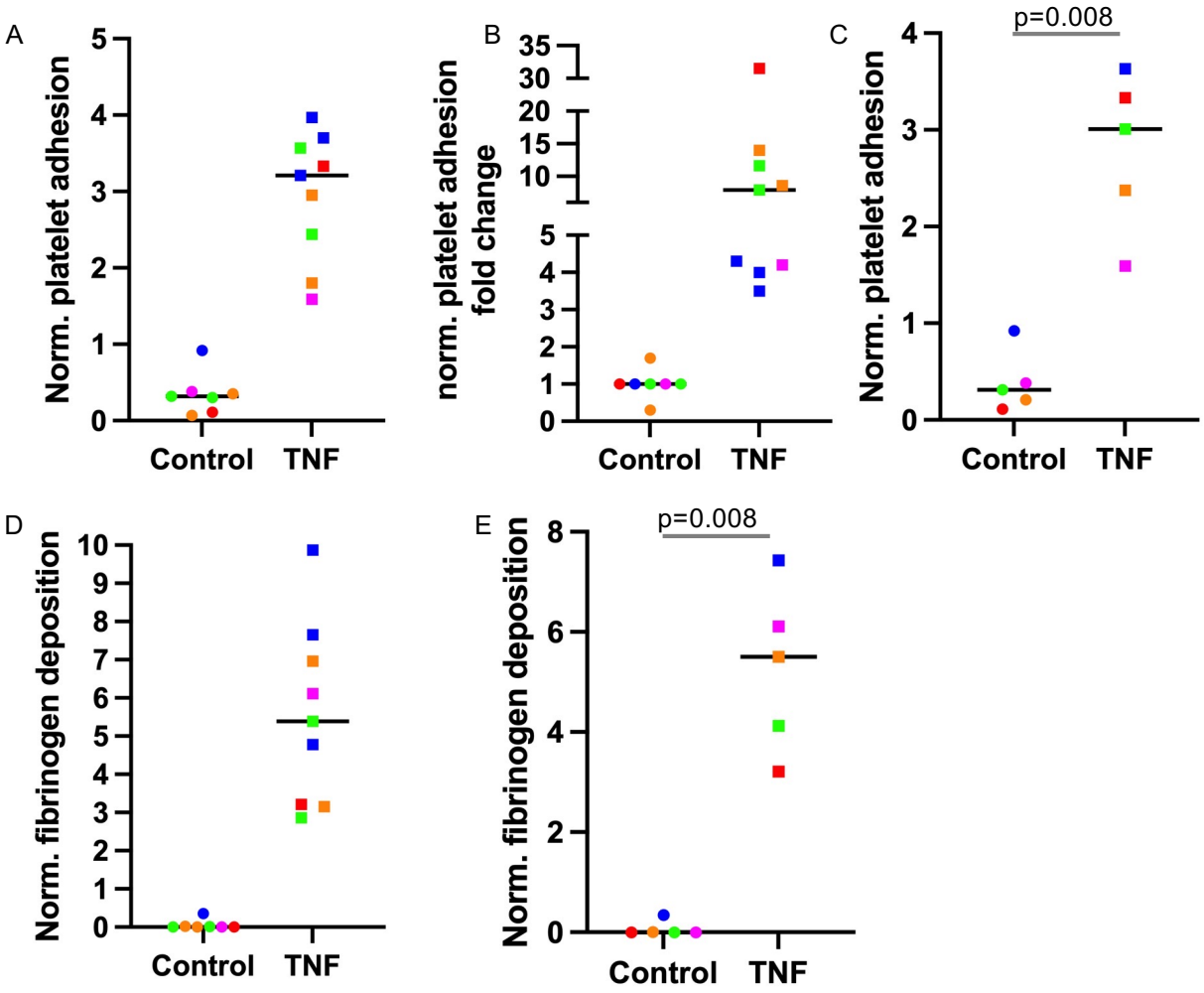


Figure 4.11: Platelet adhesion and fibrinogen deposition in HUVEC vessels. Results of platelet adhesion and fibrinogen deposition at the end time point of the 3D thrombosis assay, comparing TNF-treated and control vessels perfused with different blood samples. Each colour represents a different blood sample and each data point represents a different vessel (total n=5 different blood samples and n=16 different vessels). The black horizontal lines represent the median in each treatment group. A-C: Platelet adhesion. B: Platelet adhesion normalised to the control blood sample, indicating dependence on blood donor. C: Using a Mann-Whitney U test to determine if there were statistical differences between the two treatment groups (creating independent samples by using the average of the data points from the same blood donor). Results confirm statistical difference in platelet adhesion between the groups. D-E: Fibrinogen deposition, all data points (D), creating independent samples by using the average of the data points from the same blood donor (E). Results confirm statistical difference in fibrinogen deposition between the groups, based on a Mann-Whitney U test.

donor variability. The Mann-Whitney U test assumes independent samples, and therefore the average value was used for data points from the same blood donor, resulting in one data point per blood sample and treatment group for the analysis. This is shown in Figure 4.11 (C) and Figure 4.11 (E), for platelet adhesion and fibrinogen deposition, respectively (data shown in Appendix: Chapter 4). Results show significant differences in both platelet adhesion and fibrinogen deposition ($p<0.05$) between the control and TNF treatment groups, $p=0.008$ for both platelet adhesion and fibrinogen deposition.

In addition to studying total platelet adhesion and fibrinogen deposition at the end point of the 3D thrombosis assay, the increase in platelet adhesion and fibrinogen deposition over time was also analysed, applying the same method of data analysis to each individual z-stack. This is shown in Figure 4.12, where two different blood donors (Blood donor 1 and 2, labelled in magenta and red) were used as representative examples, as they showed different levels of platelet adhesion and fibrinogen deposition in the end point analysis. In both cases, platelet adhesion is increasing in a linear manner throughout the assay but reaching different levels of platelet adhesion at the end point. Blood donor 1 (magenta) shows higher background platelet adhesion in the control vessel; however, compared to the TNF-α stimulated vessel, this signal reaches steady-state towards the end of the 3D thrombosis assay. The onset of fibrinogen deposition takes place earlier for blood donor 1 and plateaus at the end of the 3D thrombosis assay, compared to blood donor 2, where fibrinogen deposition is still increasing at the end point. In both cases, fibrinogen deposition in the control vessels is almost zero. Furthermore, this data indicates a delayed onset of fibrinogen deposition, compared to platelet adhesion in both cases. Differences in dynamic response in the 3D thrombosis assay might explain the large range of fibrinogen deposition in the TNF treatment group. Efforts were made to fit this data as an additional approach for characterising the outcome of the 3D thrombosis assay; however, a robust method for doing that has not yet been found. Even though platelet adhesion and fibrinogen deposition can be evaluated at any of the 10 time points throughout the assay, being able to characterise the dynamic response between different treatment groups would allow us to evaluate treatment outcome more accurately by potentially predicting both the onset and the steady-state value for both parameters.

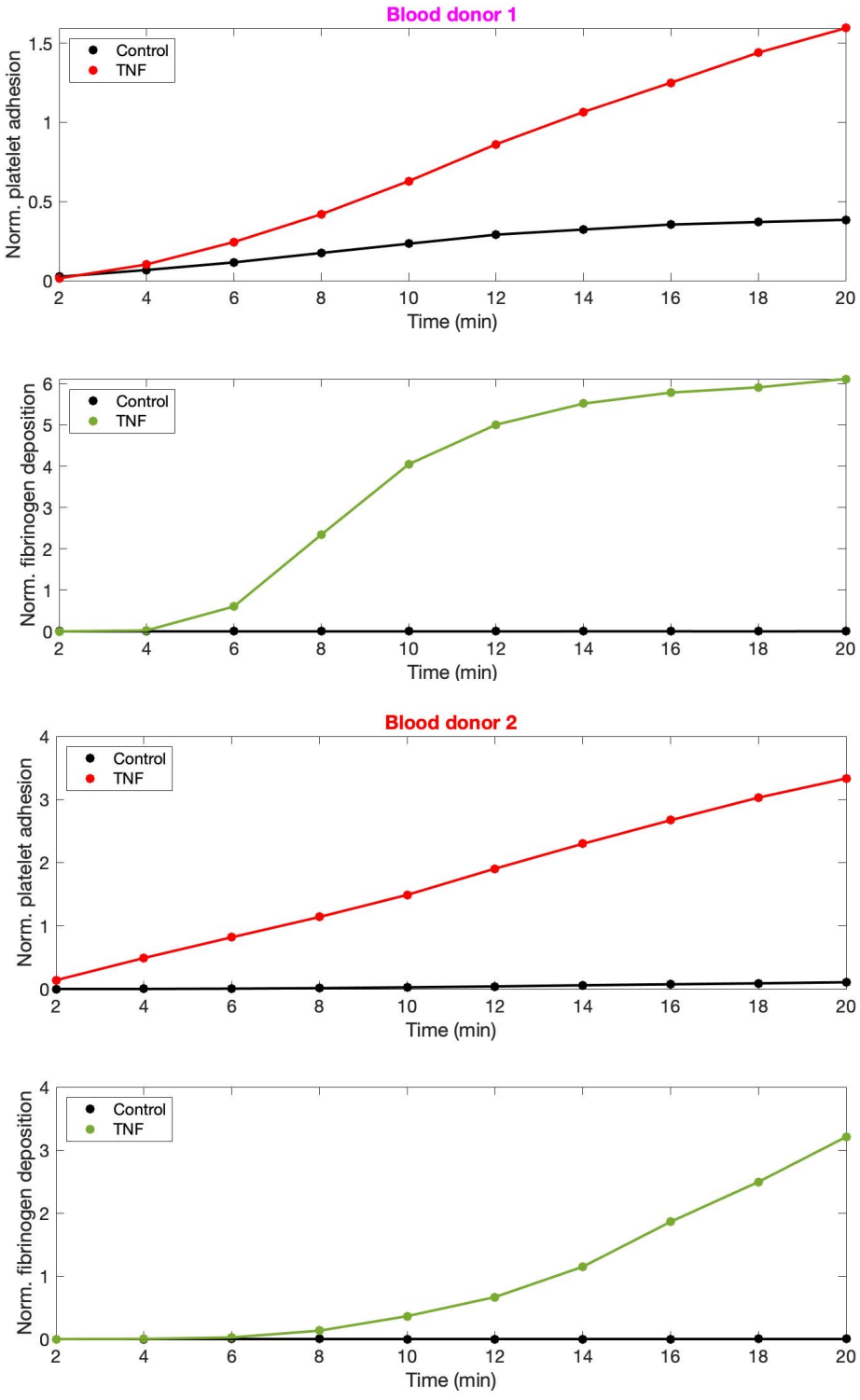


Figure 4.12: HUVEC dynamic response of platelet adhesion and fibrinogen deposition. Graphs showing the dynamic response of platelet adhesion and fibrinogen deposition for the 10 data points captured in the 3D thrombosis assay for perfusion with blood from two different blood donors (The end-point results are shown in Figure 4.11 as the red and magenta coloured data points).

4.3.1.1 The role of TF in the 3D thrombosis assay

To validate the contribution of the vessel wall on clot formation in the 3D thrombosis assay, tissue factor (TF) expression was blocked on the endothelial surface to prevent clot formation through initiation of the extrinsic pathway in the coagulation cascade. TF was blocked following 4-6h TNF-α stimulation, using an anti-TF antibody (25 µg/ml, mouse monoclonal, IgG_{2a}, Enzyme Research Laboratories) diluted in cell culture media to the correct concentration and incubated with the vessel for 20 minutes prior to blood perfusion. An IgG_{2a} control was used to confirm antibody specificity, using the same concentration and incubation time as the blocking antibody. Figures 4.13-4.14 show the results of blocking TF on platelet adhesion and fibrinogen deposition compared to TNF-α stimulated vessels and controls (data shown in in Appendix: Chapter 4). Results show a significant effect on both platelet adhesion and fibrinogen deposition by blocking TF, bringing both platelet adhesion and fibrinogen deposition down to baseline under these experimental conditions ($p=0.036$ using a Mann-Whitney U test when considering independent samples). No significant difference was observed between the control and anti-TF treatment groups ($p=0.79$ for both platelet adhesion and fibrinogen deposition using a Mann-Whitney U test when considering independent samples). This suggests that coagulation in this model is TF-dependent and occurs through the extrinsic pathway of the coagulation cascade, mimicking coagulation *in vivo*. Furthermore, it suggests that platelet adhesion is dependent on the activation of the extrinsic pathway under these experimental conditions, potentially through thrombin, which is a well-known platelet activator.

4.3.1.2 The role of thrombin in the 3D thrombosis assay

Thrombin was blocked by adding hirudin (Sigma) to the blood sample, at the same time as labelling blood components, prior to blood perfusion of TNF-α stimulated vessels, to study the contribution of coagulation factors in the blood in the 3D thrombosis assay. A titration curve was generated by sequentially adding different concentrations of hirudin, 25, 250, 500 and 1000 ATU (anti-thrombin units), where 1 ATU is defined as the amount of hirudin that neutralises 1 NIH unit of thrombin. Results show thrombin-dependent coagulation, with reduced platelet adhesion and fibrinogen deposition in response to increased hirudin concentration, where 1000 ATU completely blocked both platelet adhesion and fibrinogen deposition (Figures 4.15-4.16). Spearman's rank correlation statistical test was used to measure the degree of correlation between hirudin concentration and platelet adhesion and fibrin deposition. The analysis confirmed a statistically significant correlation, $p=0.02$ in both cases, considering TNF-treatment as zero hirudin concentration and using the average of the two TNF data points to represent this condition (considering independent samples).

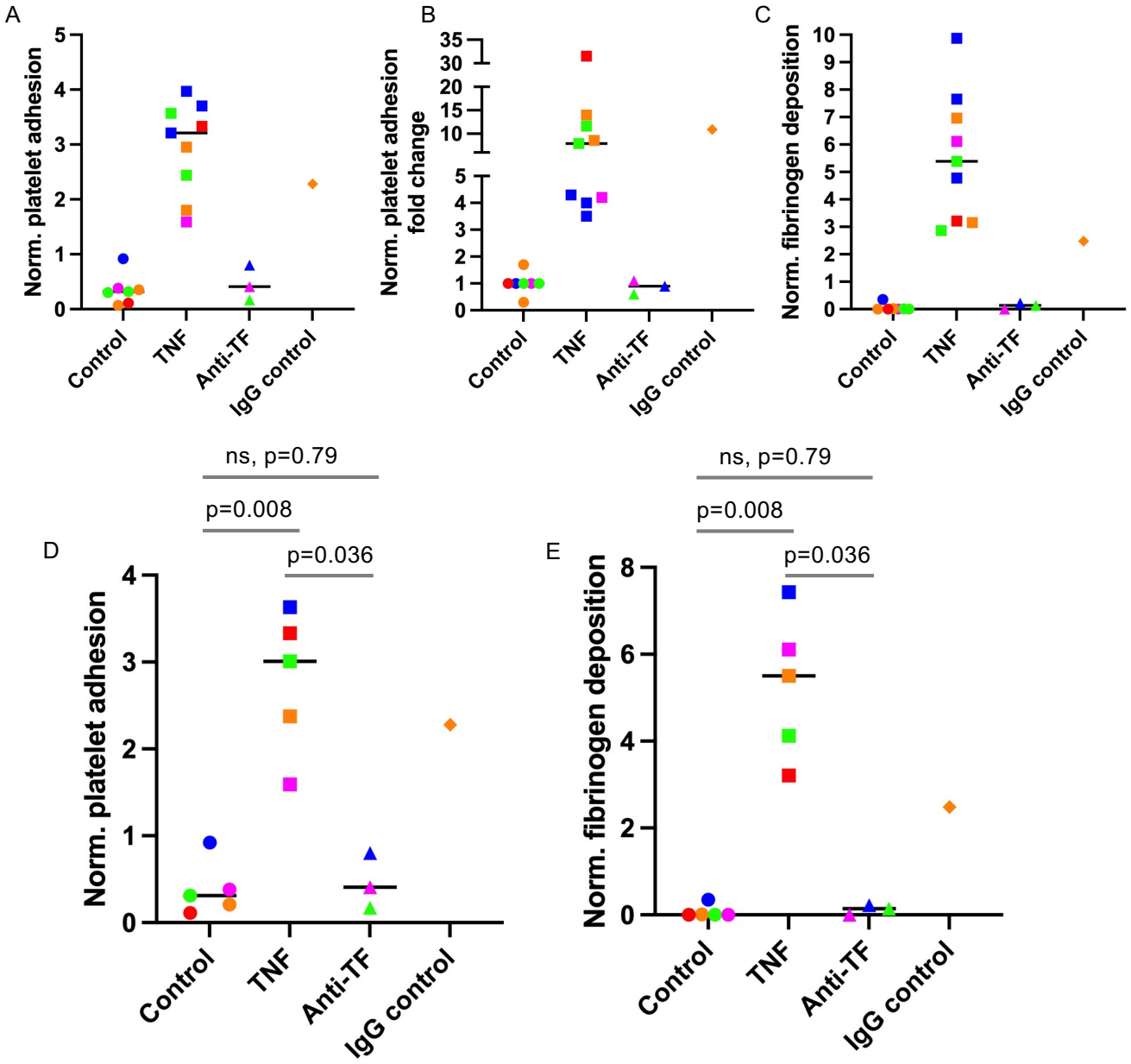


Figure 4.13: The effects of blocking TF on platelet adhesion and fibrinogen deposition. Blocking TF on endothelial cells following TNF treatment blocks both platelet adhesion and fibrinogen deposition and brings the results to a comparable level to control vessels (n=3 vessels, n=3 blood samples) . An IgG control (n=1 vessel, n=1 blood sample) was used to confirm antibody specificity, which does not block platelet adhesion and fibrinogen deposition. A-B: Platelet adhesion. C: Fibrinogen deposition. D-E: Creating independent samples by using the average of the data points from the same blood donor. Results confirm statistical difference (based on Mann-Whitney U test) in platelet adhesion (D) and fibrinogen deposition (E) between the TNF and Anti-TF treatment groups, but not between the Control and Anti-TF treatment groups.

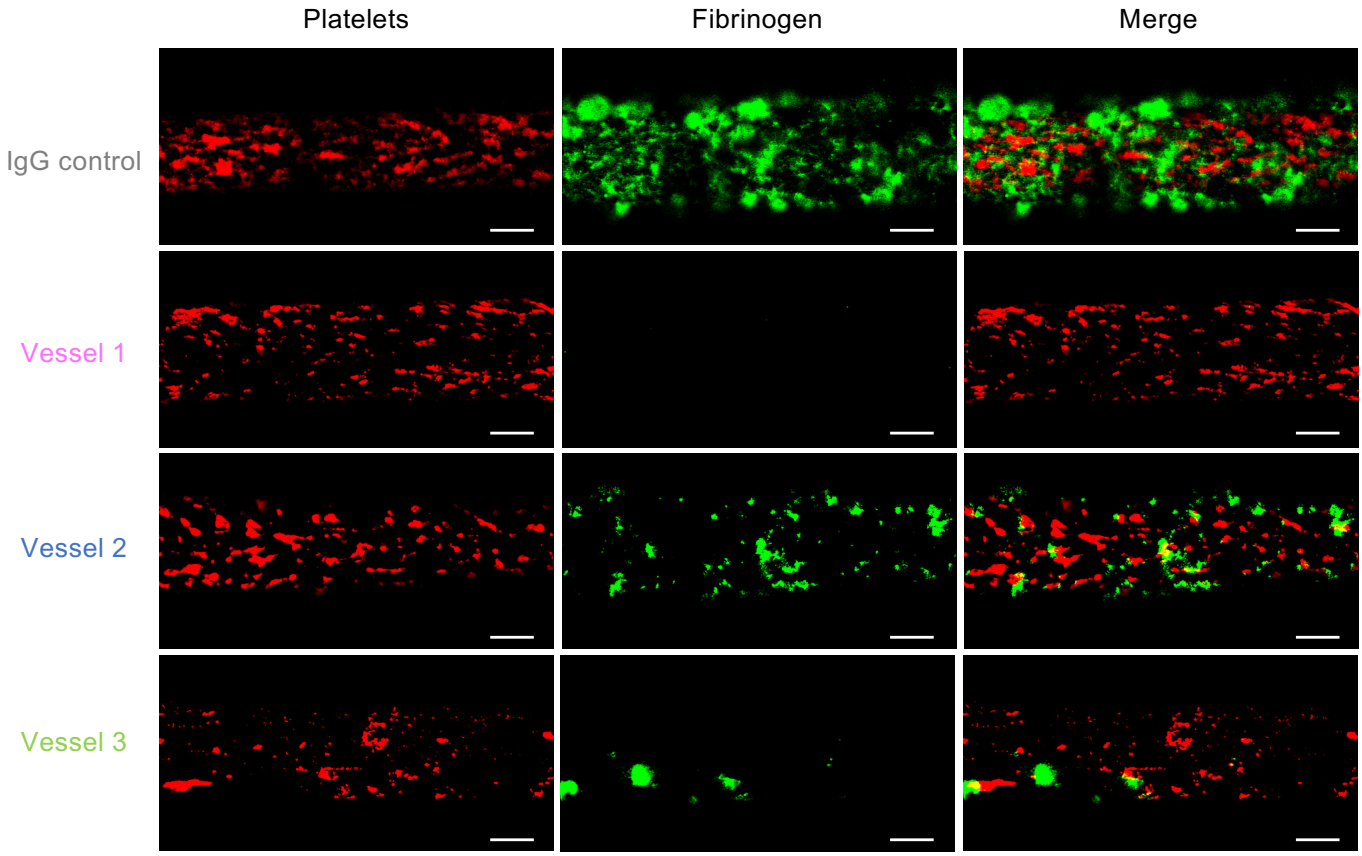


Figure 4.14: Immunofluorescent images showing the effect of blocking TF on coagulation. 2D projection of the z-stack images for the n=3 anti-TF treated vessels and the n=1 IgG control, showing reduced platelet adhesion and fibrinogen deposition following treatment. Scale bars=100 μm.

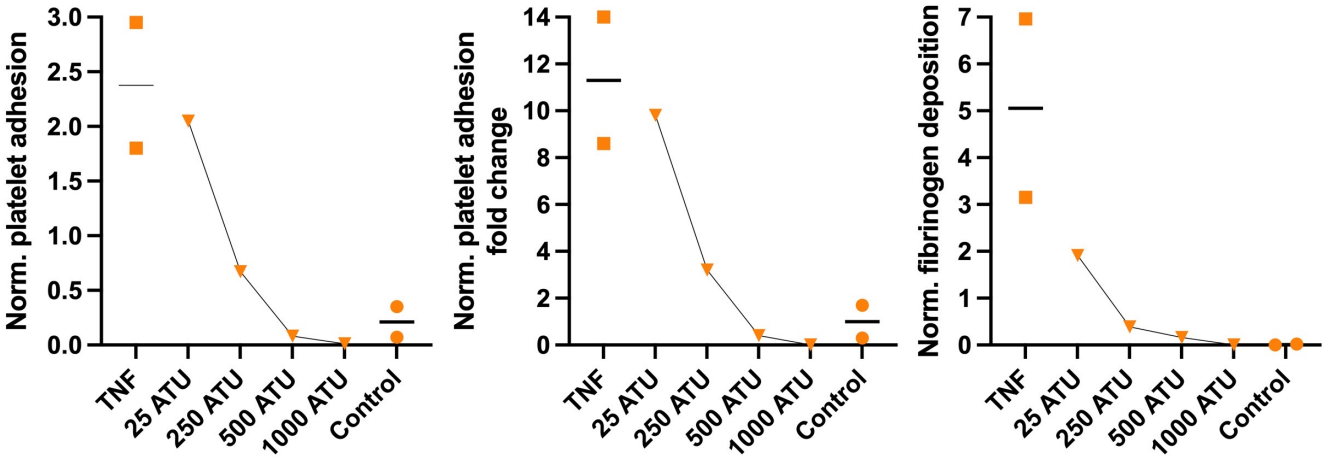


Figure 4.15: **The effects of blocking thrombin on platelet adhesion and fibrinogen deposition.** Blocking thrombin in the blood by adding hirudin inhibits coagulation by blocking both platelet adhesion and fibrinogen deposition. The titration curve of hirudin shows reduced signal in both channels in response to increasing hirudin concentration. ATU=anti-thrombin unit. Experiment including n=8 vessels perfused with the same blood sample, supplemented with different concentrations of hirudin. Statistical significant correlation between thrombin and coagulation (both platelet adhesion and fibrinogen deposition) using a Spearman's rank correlation test (p=0.02, using the average of the TNF condition to consider independent samples).

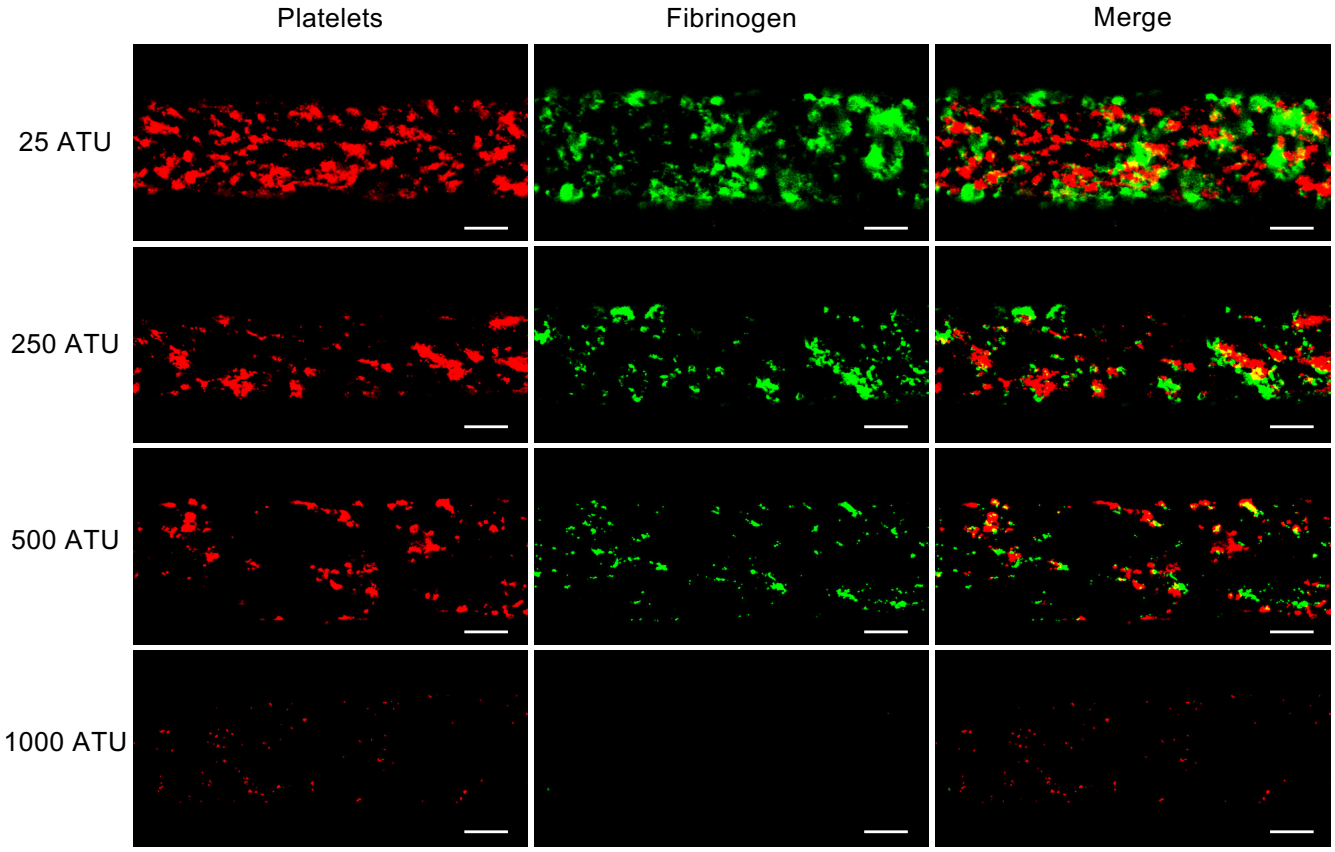


Figure 4.16: Immunofluorescent images showing the effects of blocking thrombin on coagulation. 2D projection of the z-stack images for n=4 TNF-α stimulated vessels perfused with blood treated with different concentrations of hirudin, showing reduced platelet adhesion and fibrinogen deposition in response to increasing hirudin concentration. Scale bars=100 μm.

Furthermore, since thrombin converts fibrinogen to fibrin and adding hirudin blocks the signal in the fibrinogen channel, these results indicate that the recorded fibrinogen deposition is indeed fibrin deposition, which has been converted from the fluorescently labelled fibrinogen and not an accumulation of recombinant fibrinogen.

4.3.2 3D thrombosis assay using ECFC

ECFCs were used in the 3D thrombosis assay to validate the potential of using patient cells for disease modelling in this assay. A pool of ECFCs isolated from five healthy donors was used for all thrombosis experiments in order to limit the effects of donor variability (described in Chapter 2). Since the 3D thrombosis assay requires the presence of a confluent endothelial monolayer, the ability of ECFCs to form a confluent monolayer was validated by culturing ECFCs in the blood vessel-on-a-chip model; phase contrast microscopy and immunofluorescent staining with VE-cadherin were used to visualise the vessel and assess confluency. As shown in Figure 4.17, ECFCs formed a confluent monolayer at day 5 post cell seeding, with no visible gaps between endothelial junctions. This suggests that ECFC behave similarly to HUVEC in this model and reach confluency within similar time frames.

Figure 4.18 shows a characteristic response of platelet adhesion and fibrinogen deposition at the final time point in the 3D thrombosis assay in pooled ECFCs. Using blood from n=4 donors, quantification of the response of platelet adhesion and fibrinogen deposition shows that ECFCs have a similar response to HUVEC, where stimulation with TNF-α clearly increases both parameters. Furthermore, as in HUVEC, variability due to blood donors was observed for platelet adhesion as well as a large range in fibrinogen deposition (Figure 4.19). However, one of the blood samples (labelled in yellow in the graph) showed very low fibrinogen deposition; this might be due to multiple freeze/thaw cycles of the fibrinogen used in that specific experiment, resulting in reduced fluorescent signal. The same blood sample showed a platelet response similar to the other donors, supporting the hypothesis of a technical issue with the reagent. A Mann-Whitney U test showed statistically significant differences between the two treatment groups (TNF and control), considering independent samples, with p=0.02 in both cases (Figure 4.19 (D-E)). Figure 4.20 shows the dynamic response for two different experiments (blood donor 1 and blood donor 2, labelled in cyan and black), showing a comparable response to HUVEC for fibrinogen deposition with later onset compared to platelet adhesion in the TNF-treated vessels and a constant almost zero signal in the controls. Blood donor 1 also shows a similar response to HUVEC in platelet adhesion, with a linear increase in platelet adhesion in the TNF-treated vessel and a constant background signal in the control. However, in blood donor 2, platelet adhesion seems to have

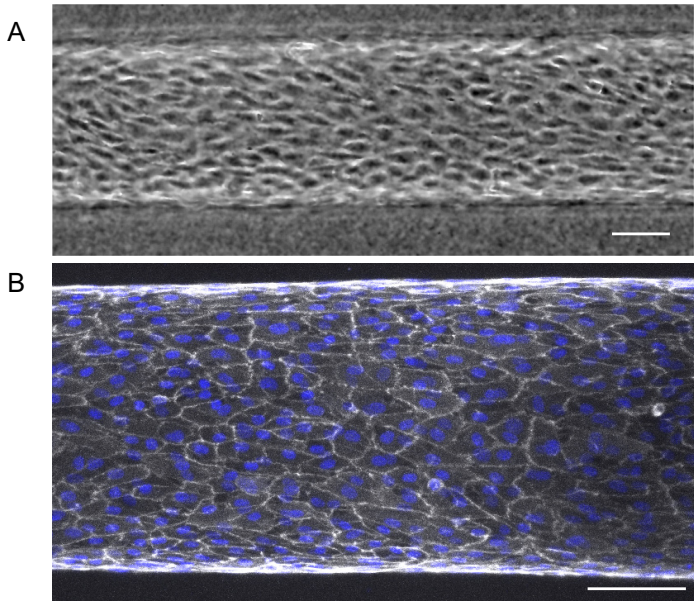


Figure 4.17: Representative images of ECFC cultured in the vessel, confirming the formation of a confluent monolayer. A: Phase contrast image showing a top-view of a vessel cultured with ECFCs isolated from healthy controls. B: Immunofluorescent staining of the same vessel, showing nuclear staining DAPI in blue and VE-cadherin in grey, which confirms the formation of a tight monolayer through the absence of gaps between the endothelial junctions. Scale bars=100 μm.

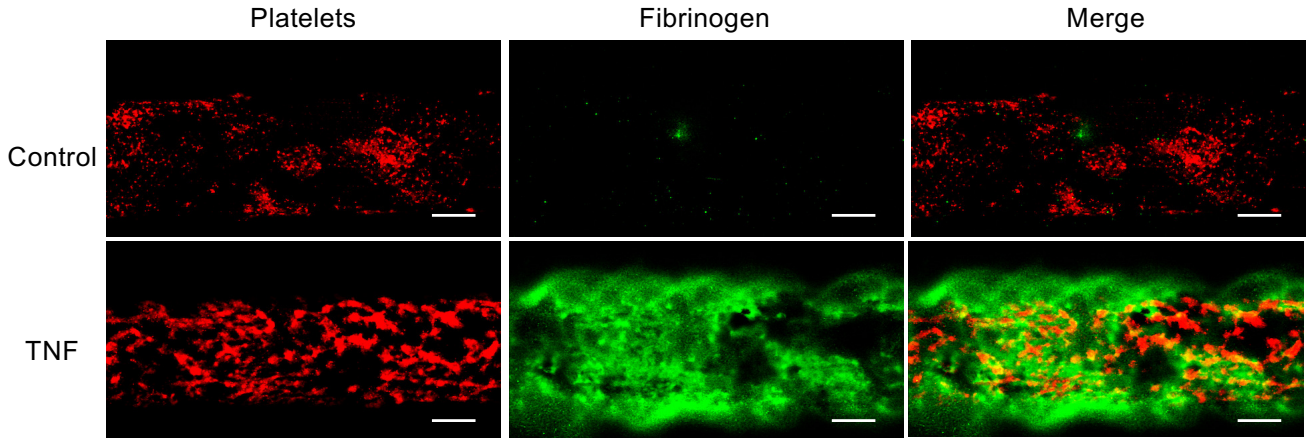


Figure 4.18: Characteristic response of platelet adhesion and fibrinogen deposition in ECFC vessels. Projected z-stack images of vessels created using ECFC, showing platelet adhesion and fibrinogen deposition at the final time point of the 3D thrombosis assay. Scale bars=100 µm.

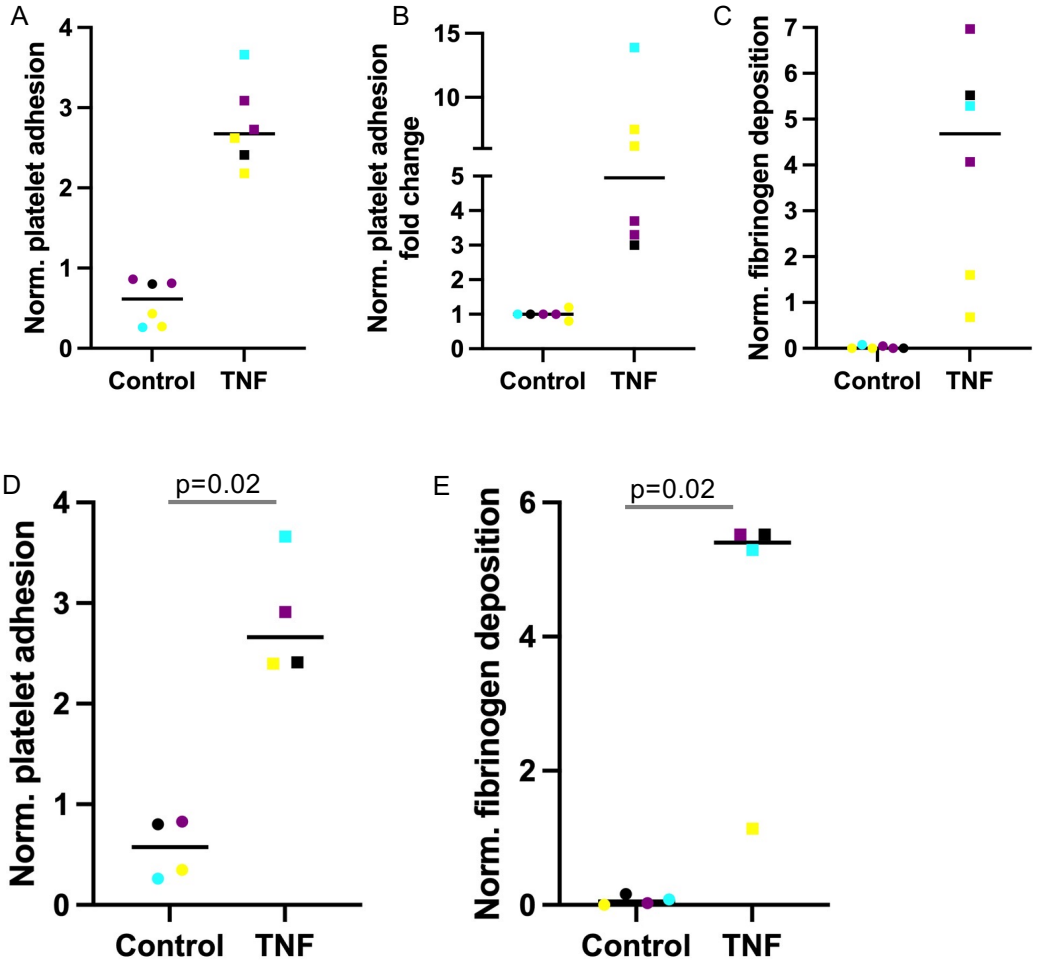


Figure 4.19: Platelet adhesion and fibrinogen deposition in ECFC vessels. Results for n=4 different blood samples and n=12 different vessels of platelet adhesion (A-B) and fibrinogen deposition (C) at the end time point of the 3D thrombosis assays for vessels created using ECFC, comparing TNF-treated and control vessels perfused with different blood samples. Each colour represents a different blood sample and each data point represents a different vessel. D-E: A Mann-Whitney U test determined statistically significant differences between the treatment groups for both platelet adhesion (D) and fibrinogen deposition (E), considering independent samples.

plateaued towards the end of the assay and there seems to be an onset of platelet adhesion in the control towards the end of the assay but maintaining significantly lower signal compared to the TNF-treated vessel.

4.3.3 Molecular profiling of EC activation

Bulk qPCR was used to study changes in gene expression following TNF-α stimulation in both HUVEC and ECFC vessels, compared to control. The protocol used for RNA extraction and qPCR is described in Chapter 2. Three confluent vessels were used in each treatment category (due to technical problems resulting in pipetting errors, only one control sample is included for HUVEC). ICAM1 was used as a marker to confirm endothelial activation following TNF-α stimulation (Figure 4.21). Results show >100-fold increase in gene expression in the HUVEC vessels and >35-fold increase in gene expression in the ECFC vessels compared to control vessels (and normalised to the housekeeping gene GAPDH), validating the method for endothelial activation with TNF-α in this model. In addition to ICAM1, a panel with seven genes (VE-cadherin, ERG, VWF, TM, TF, KLF2 and eNOS) was studied for each treatment condition, shown in Figure 4.22 (due to the low quantity of RNA extracted from each vessel, a total of nine genes can be investigated for one vessel). As expected, levels of TM and eNOS, which both are associated with an anticoagulant endothelium, were downregulated following TNF-treatment in both cell types. The procoagulant genes tissue factor and VWF showed the opposite response between the two cell types. TF gene expression was clearly upregulated in the ECFC vessels in response to TNF-treatment, which was expected based on the previous results shown in this chapter, confirming TF dependent coagulation in this model. However, TF expression in the HUVEC vessels did not show the same striking effect; the reason for this needs to be further investigated. The opposite effect was observed for VWF, which shows a clear upregulation following TNF-treatment in the HUVEC vessels but was not upregulated in the ECFC vessels. The response of other target genes to TNF-treatment was quite variable between samples, which is a problem as it limits the sensitivity of the analysis. Additional work is required to investigate if this is due to technical error and additional repeats of this experiment are required to characterise changes in endothelial phenotype in the vessels following stimulation with TNF-α. Due to the low quantity of RNA that can be extracted from each vessel, RNA quantity could not be measured prior to qPCR. Pooling multiple vessels might therefore reduce variability by using the same quantity of RNA in all samples.

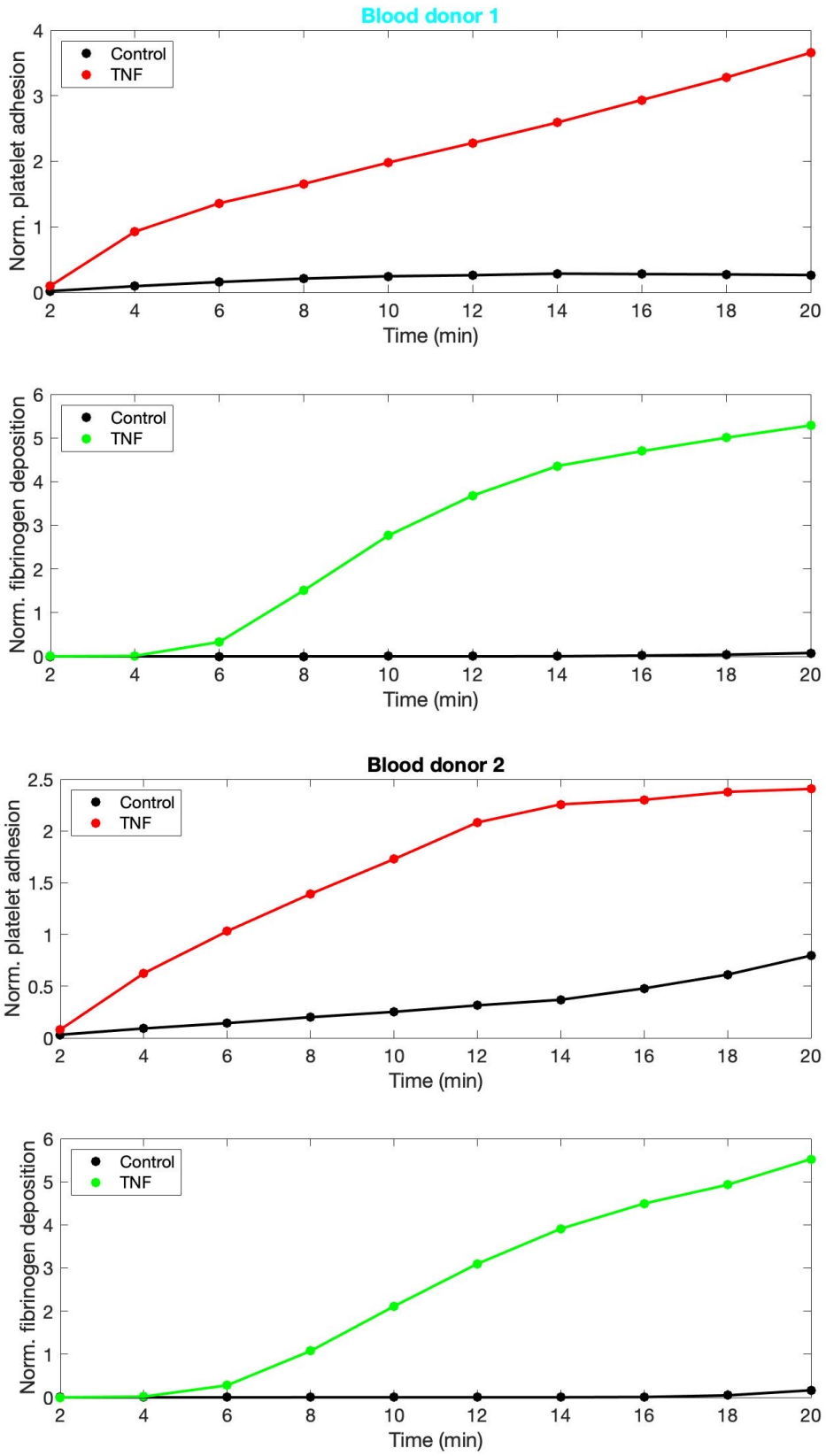


Figure 4.20: ECFC dynamic response of platelet adhesion and fibrinogen deposition. Graphs showing the dynamic response of platelet adhesion and fibrinogen deposition for the 10 data points captured in the 3D thrombosis assay for perfusion with blood from two different blood donors (The end-point results are shown in Figure 4.19 as the black and cyan coloured data points).

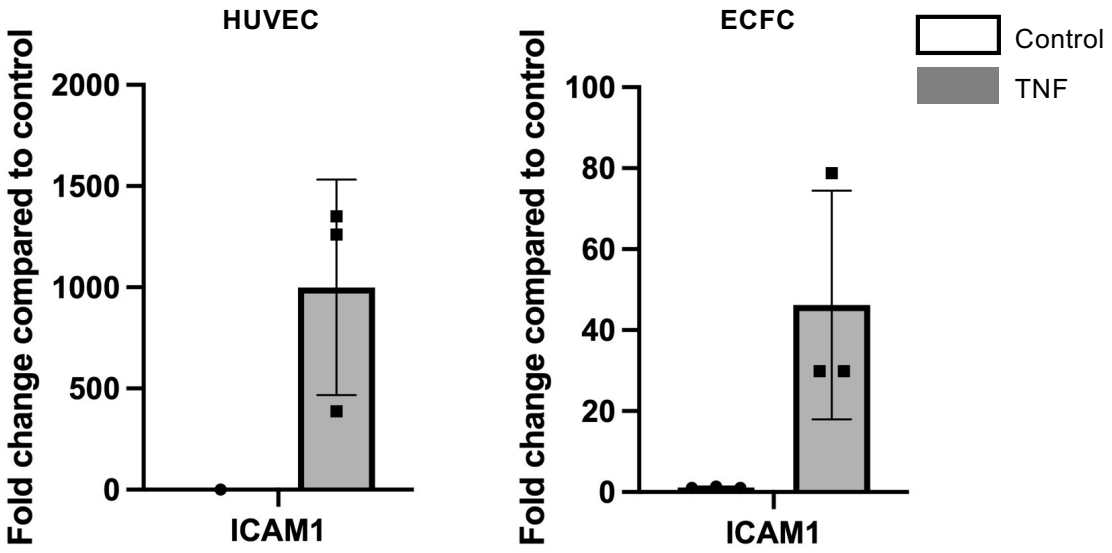


Figure 4.21: ICAM1 gene expression in HUVEC and ECFC vessels following TNF-treatment. Bulk qPCR data for HUVEC and ECFC, showing increased ICAM1 gene expression following endothelial activation with TNF-α compared to controls.

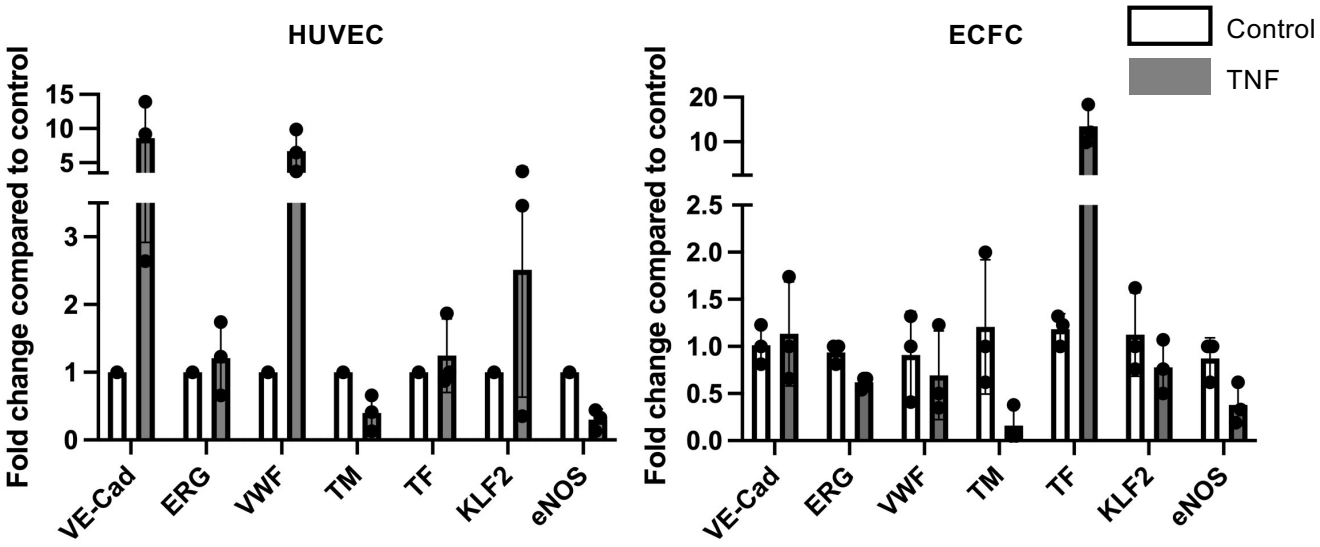


Figure 4.22: Bulk qPCR results for HUVEC and ECFC vessels following TNF-treatment. Results show changes in gene expression following endothelial activation with TNF-α compared to controls for a panel of genes.

4.4 Discussion

We have shown that the blood vessel-on-a-chip model can be used to study coagulation through activation of the extrinsic pathway, using real-time imaging to quantify platelet adhesion and fibrinogen deposition following vessel stimulation with the pro-inflammatory cytokine TNF-α. For validation purposes 10 ng/ml TNF-α was used, chosen as a positive control for endothelial activation in an *in vitro* setting. Having validated the model, more physiological stimulation could be used in the future, including tissue-specific cocktails of pro-inflammatory cytokines for disease modelling of thrombosis. Furthermore, using antibodies and compounds we have demonstrated that the model is sensitive to detecting changes in the coagulation response and for pathway detection. This model allows to manipulate the coagulation response from both the perspective of the endothelium and the blood. By blocking different coagulation factors in the context of studying the effect of anti-thrombotic drugs or blocking receptors on endothelial cells to determine the contribution of the vessel wall in the clotting process, this model presents an opportunity to dissect novel pathways and investigate the crosstalk between cellular and circulating regulators. In this context, ECFCs would be a valuable tool for mimicking a diseased endothelium, which could allow to create an autologous model of thrombosis, pairing ECFCs with blood isolated from the same patient. Anti-thrombotic drugs could then be investigated for rescuing a healthy phenotype. Furthermore, the advantage of using imaging to study coagulation is the flexibility in labelling different blood components. For example, the contribution of leukocytes could be investigated, which is relevant in inflammation and consequently would be expected to influence the thrombotic response.

Since studying coagulation in the 3D thrombosis assay relies on imaging, variability in captured signal between different vessels can be expected. For platelet adhesion, blood sample variability was found to influence the results. To address this, the blood sample could be characterised before using it in the assay, and the results could be used as a parameter for normalisation during data analysis to limit the influence of donor variability. However, there is an associated practical limitation of this as the blood sample should be used within 3 hours of collection. Furthermore, all control samples had background platelet adhesion, which was not a major problem for model validation as this concentration of TNF-α stimulation resulted in >3-fold increase in platelet adhesion compared to controls. However, the presence of background platelet adhesion could become a limitation if a different less powerful inflammatory stimulation is used. Since artificial platelet activation has been linked to needle size when collecting blood, due to an increase in shear rate, the source of this problem might be perfusion through the microtubing, which connects to the microfluidic device and has an inner diameter of 0.3 mm (compared to 0.5 mm for the 21G needle used for blood collection). Using hirudin, we

showed that both platelet adhesion and fibrinogen deposition were thrombin-dependent under the experimental conditions used in the validation experiments; this suggests that platelet adhesion in the TNF-α stimulated vessels was a result of activation of the extrinsic pathway in the coagulation cascade, which results in thrombin generation (described in Chapter 1). Since close to zero fibrinogen deposition could be detected in the control unstimulated vessels, this suggests that platelet adhesion in these vessels was not thrombin-dependent, but rather that the adhered platelets were already activated before entering the vessel. With respect to fibrinogen deposition, a possible source of variability is the presence of endogenous unlabelled fibrinogen in the blood sample, which is likely to influence the results; this cannot be investigated using the current experimental setup. It could be addressed by quantifying fibrinogen levels in the blood samples and potentially remove fibrinogen from the blood sample prior to the 3D thrombosis assay, to have the same amount of exogenous labelled fibrinogen in all experiments. A technical issue which may cause variability in fibrin deposition is related to the storage of labelled fibrinogen; multiple freeze/thaw cycles of the labelled fibrinogen was found to significantly reduce the fluorescent signal, which should be avoided for future experiments. Time-lapse imaging allowed capturing the dynamic response of platelet adhesion and fibrinogen deposition and results suggest that 20 minutes was a sufficient imaging time to capture differences in coagulation between the two treatment groups (control and TNF-α). As z-stacks require increased imaging time compared to a single plane, being able to analyse the dynamic response using curve fitting would be useful in case additional fluorescent channels are being imaged, which would result in increased imaging time and hence fewer data points being captured. Using z-stacks to capture data was important in this model to be able to capture the surface area of the vessel; however, the current method for data analysis relies on the platelet channel for defining the vessel boundaries. This might result in an underestimation of the vessel boundaries, especially in the control vessels with lower platelet coverage and might therefore become a problem if artificial platelet activation is reduced in this model. Fluorescently labelled endothelial cells (through cytoplasmic of junctional staining) could be used for more accurately defining the vessel boundaries. This would also provide higher accuracy for determining the start point of the z-stack, and thereby fewer images might be required per z-stack, which would reduce the imaging time per z-stack. Furthermore, labelled endothelial cells would allow to image the endothelium in real time during the 3D thrombosis assay. However, achieving this might be challenging as reagents used for live cell staining are commonly toxic to cells and would therefore require substantial optimisation; more reliable methods for fluorescent labelling, including lentivirus, can reduce cell viability in long-term culture and this would further be practically inconvenient to implement with ECFCs isolated from patients.

Chapter 5: Other applications

In addition to studying vessel barrier function and clot formation, preliminary results were obtained for using this platform to create a co-culture model with pericytes and to study angiogenesis by inducing sprouting from the vessel wall. Model development for these additional applications is shown below; however, validation of these models has not yet been carried out.

5.1 Co-culture with perivascular cells

The motivation for establishing an endothelial-pericyte co-culture model was to capture vascular bed specificity and investigate the contribution of paracrine signalling between endothelial cells and pericytes in thrombosis. The blood vessel-on-a-chip platform would be a suitable model for doing this as it should have the potential to fully capture the crosstalk through direct cell-cell interactions between the two cell types when they share the same ECM without separation by a barrier, which would not be possible using for example membrane-based models.

5.1.1 Introduction

As mentioned in Chapter 1, mural cells (smooth muscle cells and pericytes) contribute to vessel function and to vascular bed specificity, as the composition of the vascular wall varies throughout the vasculature. In capillaries, pericytes share a basement membrane with endothelial cells, resulting in direct contact between the two cell types through focal adhesions, which facilitate cell signalling. Furthermore, one pericyte typically contacts multiple endothelial cells to coordinate communication between neighbouring cells along the vessel (Armulik et al., 2005). Similar to endothelial cells, pericyte morphology and molecular signatures vary in different tissues. The highest pericyte coverage is found in the brain, contributing to regulating transendothelial transport across the blood-brain-barrier, as well as in the retina, where high glucose levels in the blood can result in pericyte loss, which is an early sign of diabetic retinopathy and can cause blindness. There is significantly lower pericyte coverage in capillary beds that require efficient exchange, including the lungs and the kidneys. There are no pericyte-specific markers; however, expression of SMA (Smooth muscle actin), Desmin, NG-2 and PDGFR-β (Platelet-derived growth factor receptor β) is associated with pericytes, with expression levels varying depending on pericyte location. The role of pericytes in regulating vascular function has been studied *in vitro* in the context of angiogenesis, where they are required for vessel stabilisation and maturation, and pericyte-endothelial co-culture models have also been used to study the restricted permeability of the blood-brain-barrier (Stone et al., 2019). However, the contribution of pericytes in

coagulation has not been extensively studied *in vitro* and not in a co-culture model that supports blood perfusion.

5.1.1.1 The role of pericytes in coagulation

It is well known that pericytes contribute to haemostasis. As described in Chapter 1, the baseline expression of tissue factor is much greater in mural cells compared to endothelial cells, which provide an antithrombotic surface. Following vascular injury, tissue factor expressed on the surface of mural cells is exposed to the circulating blood, initiating the extrinsic pathway of the coagulation cascade to form a blood clot and stop bleeding. Therefore, it is very relevant to consider the contribution of mural cells when studying coagulation *in vitro*. Bouchard et al. (1997) confirmed tissue factor expression on human brain pericytes cultured *in vitro* and further showed that the rate of thrombin generation (from TF-dependent initiation of the coagulation cascade) was 50-100 times greater, when performing this assay with pericytes alone compared to endothelial cells. In haemostasis, vascular injury, and thereby exposure of TF on the surface of mural cells to circulating blood, is key for endothelial activation and for the initiation of the coagulation cascade. Thrombosis however can occur following endothelial activation from additional stimuli that do not necessarily result in mechanical damage or vessel rupture, including inflammation and altered flow characteristics. Consequently, the contribution of pericytes in thrombosis is likely be different compared to haemostasis, however; this has not been thoroughly investigated. Matsumoto et al. (2014) studied pericyte response to pro-inflammatory cytokines and showed that pericytes cultured *in vitro* released a mixture of cytokines and chemokines, including Interleukins such as IL-1 and IL-6, following stimulation with TNF-α (20 ng/ml for 24h). This suggests that there could be differences in endothelial response when TNF-α is used for endothelial activation in the presence of co-culture with pericytes, which consequently could alter the coagulation response.

Endothelial cells and pericytes are known to communicate through the PDGF-β/ PDGFR-β and angiopoietin-1 (Ang-1)/Tie2 pathways, which also might play a role in coagulation. PDGF-β is secreted by endothelial cells during angiogenesis and contributes to recruiting pericytes to the newly formed vessels by anchoring to the PDGF-β receptor (PDGFR-β) on the pericyte cell surface (Armulik et al., 2005). However, PDGF-β is also stored in platelet granules, is released upon platelet activation and plays an important role in regulating angiogenesis during wound healing (Blair and Flaumenhaft, 2009), suggesting that this signalling pathway might be present in thrombosis as well. Ang-1 is secreted by mural cells, including pericytes, and is a ligand for Tie-2, which is an endothelial-specific receptor. The Ang-1/Tie2 pathway plays an important role in

angiogenesis for promoting vessel maturation and quiescence, and thereby maintaining a healthy and anticoagulant endothelium (Haase et al., 2019). Daly et al. (2018) identified thrombomodulin as another receptor for Ang-1, which further supports this as thrombomodulin is a known inhibitor of coagulation. A vessel co-cultured with pericytes could therefore result in a more protective phenotype against thrombosis, if the pericytes are not exposed to blood during the 3D thrombosis assay.

5.1.1.2 Aims

The following aims were used for developing the blood vessel-on-a-chip model to support co-culture with pericytes

1. Investigate cell seeding strategies for co-culture with endothelial cells and pericytes
2. Validate formation of a functional endothelium in the presence of pericytes

5.1.2 Model development

5.1.2.1 Cell seeding

In the pericyte-endothelial co-culture experiments, Red Fluorescent Protein (RFP) labelled Human Brain Microvascular Pericytes (HBMVP) (purchased from Angio-Proteomie) were seeded in the vessel using the same method for cell seeding and for long-term culture in the 3D printed perfusion unit as described in Chapter 2. Briefly, this method requires injecting cell suspension into the vessel twice, where the vessel is incubated for 30 minutes and then rotated 180° before the second cell seeding. Both cell types were used in the blood vessel-on-a-chip model at passage 3-6 and were cultured in a 6-well tissue culture plate format before cell seeding, trypsinising one well for each cell seeding. Using a 1:5 ratio of pericytes to endothelial cells it was found that the pericytes at this cell seeding density required longer time for cell adhesion to the collagen, compared to the 30 minutes observed for cell seeding of HUVEC alone (data shown in Chapter 2). Figure 5.1 shows pericytes seeded in the vessel at time points 2h and 6h post cell seeding; the cells have a round morphology at 2h and have spread out and adhered to the collagen at 6h. The time required for pericyte adhesion to the collagen was only investigated in the absence of endothelial cells, to allow distinguishing between the two cell types when studying changes in cell morphology using phase contrast microscopy. It was not feasible to increase the incubation time from 30 minutes to 6h between cell seedings. Therefore, HUVEC alone were first seeded on the top surface of the vessel and following a 30-minute incubation at 37°C, the chip was rotated 180° and the Pericyte/HUVEC mix (1:5 ratio) was seeded on the bottom surface of the vessel,

resulting in a total cell ratio of 1:10 pericytes to HUVEC. The chips were incubated at 37°C for 4h before connection to the 3D printed culture unit.

5.1.2.2 Studying vessel formation

Immunofluorescent staining was used to investigate cell coverage in the vessel; staining for the junctional protein VE-cadherin was used to confirm the formation of an endothelial monolayer in the presence of pericytes. When the vessels had grown to confluency (based on phase contrast microscopy), from culture in the 3D printed perfusion unit, they were fixed and stained with DAPI and VE-cadherin (following the immunofluorescent staining protocol described in Chapter 2). Imaging using confocal microscopy showed that an endothelial monolayer could be established in this model in co-culture with pericytes and even though pericytes were only seeded on one side of the vessel, results suggest that these cells were able to proliferate and/or migrate around the vessel lumen. However, reproducibility was a major issue associated with these studies. Figure 5.2 (A-D) shows z-stack projections (images captured with confocal microscopy and processed in Fiji) of four different vessels, which were fixed and stained 10 days post cell seeding and which were all seeded on the same day and using cells from the same cell suspension. Significant variability in vessel formation was observed; Vessels A and B show a larger number of pericytes and reduced VE-cadherin staining with patches of endothelial cells along the vessel. On the contrary, vessels C and D both show confluent endothelial monolayers but the vessels have significantly fewer pericytes. These results suggest that pericyte density may influence the ability of ECs to form a confluent monolayer in the blood vessel-on-a-chip model. Furthermore, variability in pericyte coverage along the same vessel could also be observed (Figure 5.2 (E-F)); however, this did not correlate with the formation of a confluent endothelial monolayer in the different regions along the vessel.

5.1.3 Discussion

The preliminary results presented in this chapter suggest that co-culture with endothelial cells and pericytes can be achieved in the blood vessel-on-a-chip model. However, additional model validation is required to understand how different parameters of the experimental setup influence vessel formation in this setting. Reproducibility in creating vessels where the vessel wall comprises endothelial cells and pericytes is essential to be able to use this co-culture model for functional assays, both to assure that an endothelial monolayer is formed and to expect a similar level of cellular signalling crosstalk between different vessels. To achieve this, future work should focus on optimising the below parameters

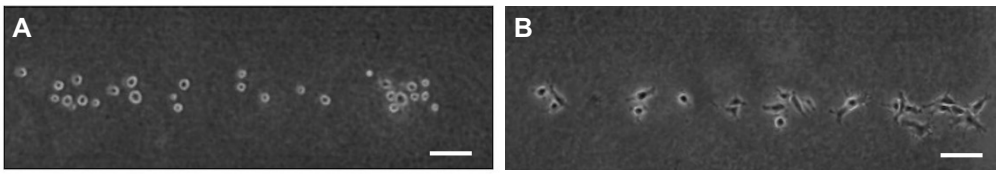


Figure 5.1: Cell adhesion of pericytes to collagen. Phase contrast images of pericytes seeded in the vessel A: 2h post cell seeding the cells still have a round morphology. B: 6h post cell seeding the cells have adhered and started to spread out on the collagen surface. Scale bars=100 μm.

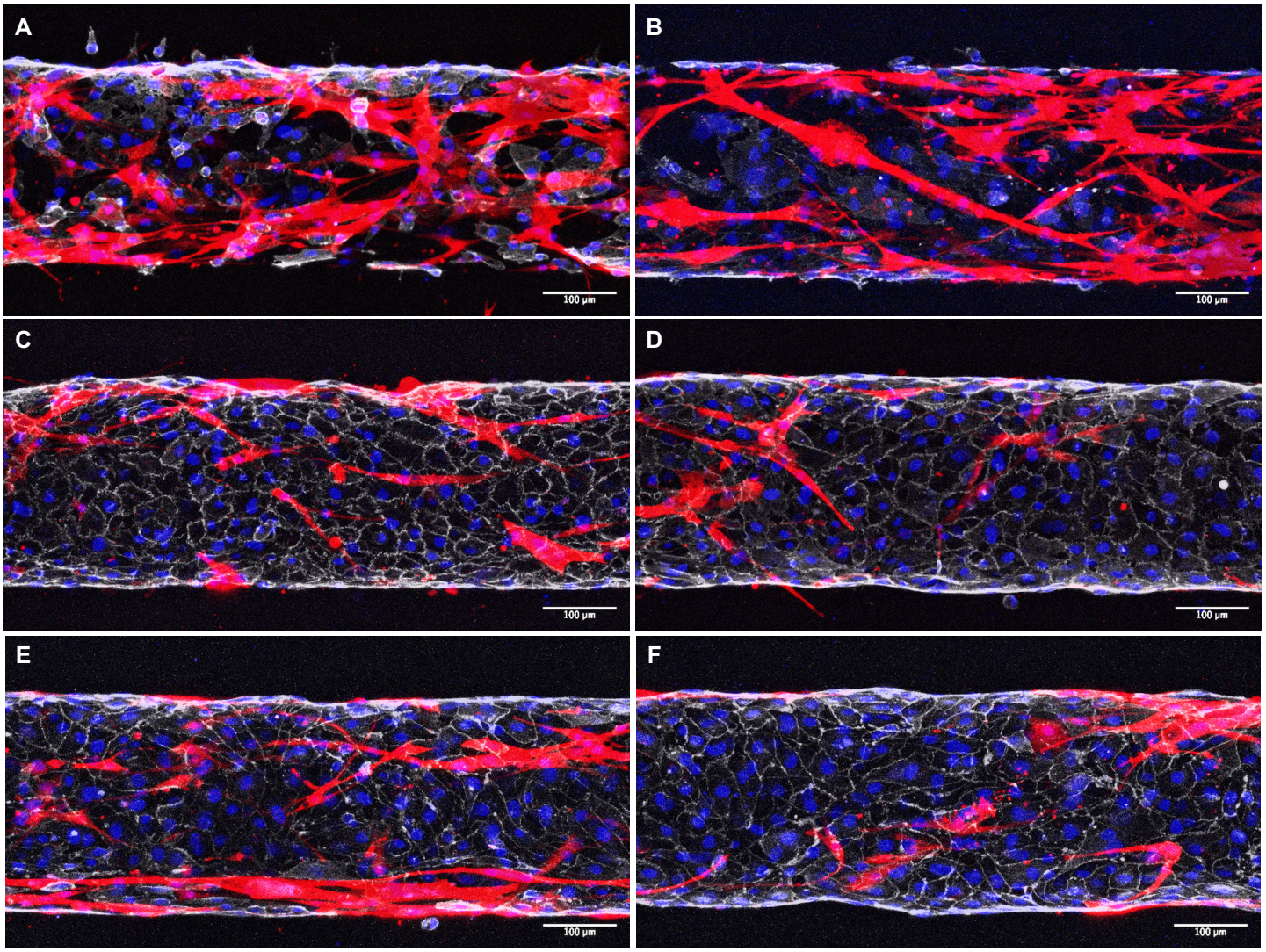


Figure 5.2: Immunofluorescent images showing vessel formation during co-culture with pericytes. Vessels co-cultured with HUVEC and HBMVP. Images show z-stack projections of immunofluorescent staining with DAPI (blue), RFP pericytes (red) and VE-cadherin (grey). A-D: n=4 different vessels seeded on the same day from the same cell suspension and fixed 10 days post cell seeding. A-B have much higher pericyte coverage compared to C-D, which prevents the formation of a continuous endothelial monolayer. E-F: Difference in pericyte coverage along the same vessel but a continuous endothelial monolayer is observed in both areas.

i) The cell seeding density to use (total nr of cells injected per vessel)

ii) Reproducibility of cell ratio between different vessels

iii) Using fluorescently labelled endothelial cells in the model

The total number of cells injected into the vessel, and consequently what confluency the vessel has at the cell seeding stage, could affect how the two cell types migrate, proliferate and survive in the presence of each other. Live fluorescent staining of both cell types, or potentially fixation and IF staining of the vessel closely following cell adhesion, could be used to count the number of endothelial cells and pericytes seeded in the vessels to investigate the reproducibility of both cell seeding density and cell seeding ratio between different vessels. Furthermore, real-time imaging of the RFP labelled pericytes could be used to determine if vessels with a large pericyte coverage at the experimental end point were initially seeded with a larger number of pericytes, or if this is due to variability in pericyte proliferation between different vessels. To address variability in cell ratio, a larger number of cells could be used (perhaps 2-4 wells in a 6-well tissue culture plate) to achieve a more homogeneous cell suspension and thereby reducing pipetting errors so that a similar number of pericytes are seeded in the vessel every time. The issue with heterogeneity of pericyte coverage along the vessel is more challenging to optimise as it is impossible to control where the cells adhere along the vessel. In addition to the RFP labelled pericytes, real-time imaging showing endothelial junctions, such as endothelial cells transduced with lentivirus to fluorescently tag VE-cadherin, will be essential to verify the formation of an endothelial monolayer prior to using the vessel for functional assays. If images similar to those shown in Figure 5.2 could be captured before starting the assay, it would be possible to refer back to these in case there was variability between experiments and furthermore, similar sections of a vessel could be chosen for the assay, for example regions with sparse or high pericyte coverage. Furthermore, the optimal ratio of endothelial cells to pericytes could be investigated using single-cell qPCR to study how endothelial gene expression may change in the presence of pericytes, including up or downregulation of genes associated with the pericyte-dependent pathways described earlier in this chapter. Such characterisation would be very relevant for establishing a vascular bed-specific endothelium in this model.

5.2 Angiogenesis

Developing the blood vessel-on-a-chip model to support angiogenesis was motivated by studying vascular malformations in vascular bed-specific and tissue-specific microenvironments, incorporating endothelial cells, pericytes and potentially tissue-specific cells mixed in the ECM, in the context of VWD (von Willebrand

disease). Model development for inducing angiogenesis in the blood vessel-on-a-chip model is described in this section; however, the model has not yet been used in the context of VWD.

5.2.1 Introduction

Angiogenesis is the process where new blood vessels are formed by sprouting from the existing vasculature in response to cues from the microenvironment, including growth factors released from surrounding tissue in response to hypoxia to request blood flow in that location. The vessel will continue to grow towards the growth factor source until the sprout can connect to another blood vessel and thereby support blood flow. Angiogenesis occurs in adult tissue during wound healing and tissue regeneration to meet metabolic demands. However, dysregulated angiogenesis is also associated with many diseases, including ischemia, due to insufficient vessel growth, cancer, where angiogenesis is required for tumour growth (Carmeliet, 2003) and vascular malformations, characterised by abnormal vascular remodelling and excessive angiogenesis.

5.2.1.1 Vascular malformations in VWD

VWD is a genetic disorder where patients have deficiency or dysfunction of VWF. In addition to the well-known role of VWF in coagulation, VWD has been associated with the formation of vascular malformations, referred to as angiodysplasia, which often present in the gastrointestinal (GI) tract of patients with VWD and can cause gastrointestinal bleeding. Angiodysplasia has been linked to dysregulated angiogenesis (Randi et al., 2013); however, the mechanisms involved and why this condition presents in the GI tract specifically are not well understood.

5.2.1.2 *In vitro* models to study angiogenesis

Vessel formation has been studied in the presence of pericytes using vasculogenesis models. Haase et al. (2019) formed microvascular networks in a microfluidic device by mixing endothelial cells and pericytes in a fibrin gel and allowing the vessels to self-assemble over time. The study found that endothelial cells alone did not form sustainable vascular networks but in the presence of pericytes the model was viable in culture for 1-2 weeks, where the presence of VEGF and crosstalk through the Ang/Tie2 signalling pathways was essential for regulating vessel growth. Even though pericytes play an important role in regulating angiogenesis *in vivo*, angiogenesis by sprouting from a pre-defined endothelium has not been extensively studied *in vitro* in direct co-culture with pericytes.

Sprouting angiogenesis from a vessel wall comprising only endothelial cells has been studied in static conditions using the fibrin bead assay and in microfluidic devices, in 3-channel models and in the needle model. In the fibrin bead assay, microbeads are coated with endothelial cells and mixed into a fibrin gel. Fibroblasts are seeded on top of the gel, which secrete growth factors, resulting in a growth factor gradient through the gel towards which endothelial sprouting occurs (Nakatsu et al., 2007). Even though this model can capture multiple steps of the angiogenic process, the sprouts do not originate from a parent vessel and it has limited potential for altering the microenvironment, such as incorporating pericyte co-culture. Similar to the fibrin bead assay, 3-channel models can be used in co-culture with fibroblasts to drive endothelial sprouting across a fibrin gel towards the fibroblast channel and this has been shown in co-culture with pericytes, which move across the gel in accordance with the endothelial cells (Kim et al., 2015). In the needle model, Takahashi et al. (2017) and Pauty et al. (2018) induced sprouting by supplementing the cell culture media with VEGF (50 ng/ml) delivered through the vessel lumen. This resulted in sparse spouting density along the vessel, which could be problematic if using this model to study angiogenesis under different treatment conditions (such as +/- VWF). Nguyen et al. (2013) presented a modified version of the needle model, which included two parallel vessels, one which was endothelialised and one without endothelial cells where a cocktail of proangiogenic factors was added, which allowed chemokines to diffuse into the ECM to create a growth factor gradient in the collagen. This resulted in a more robust angiogenesis model with sprouting densities and characteristics similar to those achieved using the 3-channel model. Wang et al. (2020) also used this modified version of the needle model with two parallel vessels to study the effects of collagen density (3-6 mg/ml) and growth factor cocktail (composition and concentration) on sprouting characteristics. The study found that lower collagen concentrations resulted in longer sprouts and higher collagen concentrations resulted in higher sprouting densities. Furthermore, the study showed that composition of the growth factor cocktail, in particular the concentration of the individual growth factors, regulated the synergistic response of cell proliferation and migration. If cell migration was too dominant, this resulted in migration of individual cells into the collagen rather than endothelial sprouting, where a continuous lumenised capillary could attach to the parent vessel. In conclusion, these studies have shown that sprouting angiogenesis can be studied in custom-designed microfluidic models based on the needle model and the 3-channel model, and therefore provided valuable insight during the model development phase when modifying the blood vessel-on-a-chip model to support angiogenesis.

5.2.1.3 Aims

The aim of this work was to establish a robust strategy for studying angiogenesis in the blood vessel-on-a-chip model described in Chapter 2. Three different approaches for achieving this were investigated

1. Perfuse a growth factor cocktail through the vessel lumen
2. Establish a growth factor gradient in the collagen
3. Co-culture with fibroblasts mixed in the collagen

5.2.2 Model development

Since parameters including ECM and composition of growth factor cocktail have been shown to influence angiogenic response *in vitro*, the growth factor cocktail used throughout the model development phase was chosen based on the already established angiogenesis model presented by van Duinen et al. (2019), which used a 3-channel model and achieved lumenised sprouts after six days in culture. This growth factor cocktail (50 ng/ml VEGF, 2 ng/ml PMA and 500 nM S1P) was chosen as the study used the same ECM as we use in the blood vessel-on-a-chip model (4 mg/ml collagen), and therefore, this would allow comparing results between assays during this phase of the project.

5.2.2.1 Perfusing a growth factor cocktail through the vessel lumen

The approach of perfusing growth factors through the lumen of the vessel was investigated as the first attempt to induce sprouting from the vessel wall based on convenience of delivery. The blood vessel-on-a-chip model was created as described in Chapter 2 and cultured in the 3D printed perfusion unit. Three days following cell seeding, when the vessels had formed a confluent monolayer, the cell culture media was supplemented with the growth factor cocktail. The vessels were cultured for four additional days, replacing the cell culture media containing the growth factor supplements daily. Images on days 4-7 following cell seeding are shown in Figure 5.3 for two different vessels (Vessel A and Vessel B) cultured in parallel. Increased sprouting density was observed over time; however, there was significant variability between the two vessels, with vessel A showing more sprouting at day 7 compared to vessel B. Furthermore, results indicated cell migration into the collagen, observed as cells in the collagen, which are detached from the vessel wall; however, this could not be confirmed with phase contrast microscopy alone.

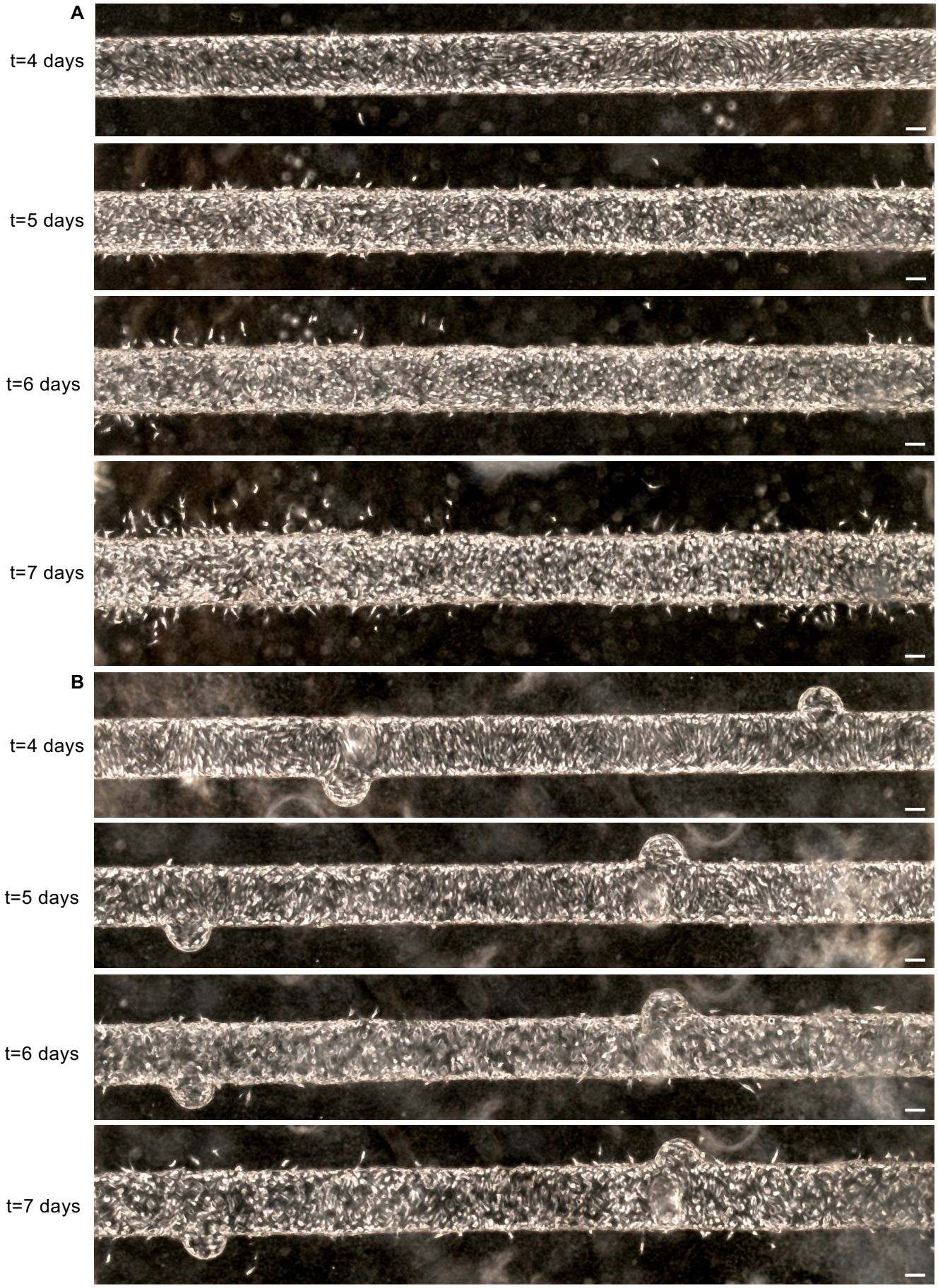


Figure 5.3: Inducing angiogenesis by perfusing a growth factor cocktail through the vessel lumen. Phase contrast images showing n=2 different vessels (A and B) on days 4-7 post cell seeding, following supplementing the cell culture media with the growth factor cocktail at day 3. A: Sprouting starts at day 5 and increases over time, however, variability in sprouting density is observed along the vessel. B: Very low sprouting density from day 6 onwards. Scale bars=100 μm.

5.2.2.2 Establish a growth factor gradient in the collagen

Two different approaches were investigated to establish a growth factor gradient in the collagen

i) Perfusing the growth factor cocktail through the ECM inlets

ii) Incorporate a growth factor chamber in the microfluidic device

5.2.2.2.1 Perfusing the growth factor cocktail through the ECM inlets

Since the ECM inlets are located parallel to the vessel at the edge of the ECM chamber, the aim was to take advantage of this design by opening both ECM inlets, connecting tubing to one ECM inlet and perfusing the growth factor cocktail through the collagen towards the vessel as the device remained connected to the 3D printed perfusion unit. By elevating the tubing, hydrostatic pressure could be used for perfusion to replace a proportion of the liquid in the collagen, which could escape from the other ECM inlet on the opposite side of the vessel. If a tight monolayer is established when introducing the growth factor cocktail, the majority of the perfused fluid is expected to travel around the vessel, rather than through the vessel wall, due to the significantly lower resistance ($R_{collagen} << R_{wall}$). A lumped parameter model of the fluid perfusion from ECM inlet 1 through the collagen and escaping through ECM inlet 2 is shown in Figure 5.4 (A), where the fluid is expected to follow the path around the vessel indicated in red. Fluorescent dextran (mol wt=65-85 kDa) was used as proof-of-concept for this technique to show that solutes could be introduced into the collagen. Figure 5.4 (B) shows the distribution of dextran inside the collagen 30 minutes after perfusion, using widefield microscopy to capture images of the entire ECM chamber. A lower molecular weight fluorescent dextran (20 kDa) was used to mimic growth factor size (VEGF molecular weight ~19 kDa) when investigating the timescales for maintaining this gradient in the collagen following delivery. Similar to the higher molecular weight dextran, the 20 kDa dextran could be injected through the ECM inlet and visualised in the collagen 30 minutes after perfusion using widefield microscopy (Figure 5.4 (C)). However, it was found that after overnight culture of the same chip connected to the 3D printed perfusion unit, there was a significant reduction in fluorescent intensity, which represents growth factor concentration inside the collagen (Figure 5.4 (D)) (all images in Figure 5.4 were captured using the same microscope settings). These results suggest that using this technique for establishing a growth factor gradient in the collagen requires frequent delivery of growth factors to achieve a stable gradient, which is not practical due to technical challenges associated with growth factor delivery. Due to the small perfusion volumes (~10-20 µl) it was difficult to confirm that the solutes had been delivered to the collagen

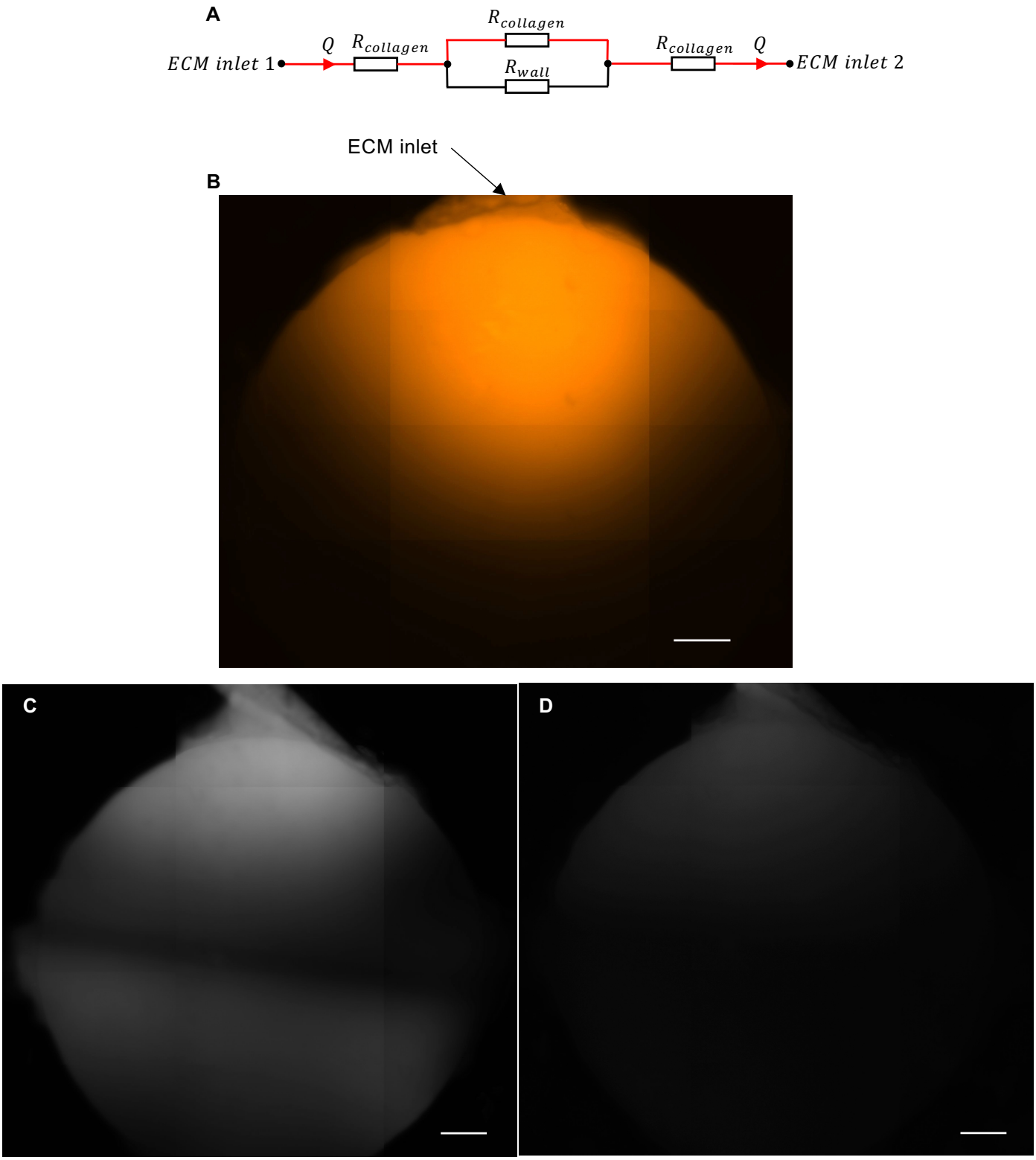


Figure 5.4: Perfusing a growth factor cocktail through the ECM inlets. A: Lumped parameter model for perfusing cell culture media supplemented with the growth factor cocktail from ECM inlet 1, through the collagen and fluid escaping from ECM inlet 2. If $R_{collagen} << R_{wall}$, the majority of fluid will be perfused through the collagen, indicated by the red path in the diagram. B: Fluorescent dextran (mol wt=65-85 kDa) can be delivered to the collagen using this technique. Images taken using widefield microscopy 30 minutes after perfusion (n=1 vessel). C: Widefield image showing 20 kDa fluorescent dextran in the collagen 30 minutes after perfusion (n=1 vessel). D: Following overnight culture connected to the 3D printed unit a significant reduction in fluorescent intensity from the 20kDa dextran was observed. Scale bars=500 μm.

without fluorescent imaging. Furthermore, due to the relatively high resistance of the collagen, the delivery process was slow as using a very large pressure drop could result in deforming the collagen.

5.2.2.2.2 Incorporate a growth factor chamber in the microfluidic device

To improve reproducibility of delivering growth factors to the collagen, the microfluidic device was modified to incorporate a growth factor chamber in direct contact with the ECM chamber, where a liquid growth factor cocktail could be injected and allowed to diffuse through the collagen. The growth factor chamber was placed 1.8 mm from the centre of the vessel and replaced one of the ECM inlets. It was designed with vertical inlets to allow access from the top of the device, to make interfacing with the device more practical when connected to the 3D printed perfusion unit (Figure 5.5). The vertical inlets were created by punching holes through the PDMS using a blunt needle before attaching the glass coverslip; tubing (ID=0.4 mm, OD=0.8 mm) was inserted into the holes and glued in place using PDMS. To create the vessel, collagen was injected from the ECM inlet until the edge of the growth factor chamber. The collagen was pre-polymerised for 15 minutes at room temperature after which cell culture media was injected into the growth factor chamber and the device was incubated overnight at 37°C, placed in a petri dish with PBS to prevent it from drying out. After a confluent endothelial monolayer had been established, the liquid in the growth factor chamber was replaced with cell culture media supplemented with the growth factor cocktail. Using this approach, directional sprouting was achieved from the vessel wall towards the growth factor chamber, starting two hours after injecting the growth factor cocktail and clearly visible after 24h (Figure 5.6). Reproducibility when injecting the collagen into the ECM chamber was the main limitation associated with this design; it was found that fluid from the growth factor chamber would often escape around the collagen, by the edges of the ECM chamber, and thereby not establishing a growth factor gradient. Therefore, this clear directional sprouting shown in Figure 5.6 was only achieved in one chip and since the vessel was fixed at 24h post cell seeding, it is unclear what long-term angiogenic response can be achieved using this method.

5.2.2.3 Co-culture with fibroblasts mixed in the collagen

As mentioned previously, angiogenesis models commonly use either proangiogenic factors supplemented in cell culture media or co-culture with fibroblasts, which secrete growth factors that induce sprouting. Using the microfluidic device without a growth factor chamber, human cardiac fibroblasts (isolated by Oisín King, Imperial College London) were mixed into the collagen (10,000 fibroblasts/device) prior to injection. Collagen was polymerised at 37°C for 2h, after which the needle was withdrawn and endothelial cells were seeded in the

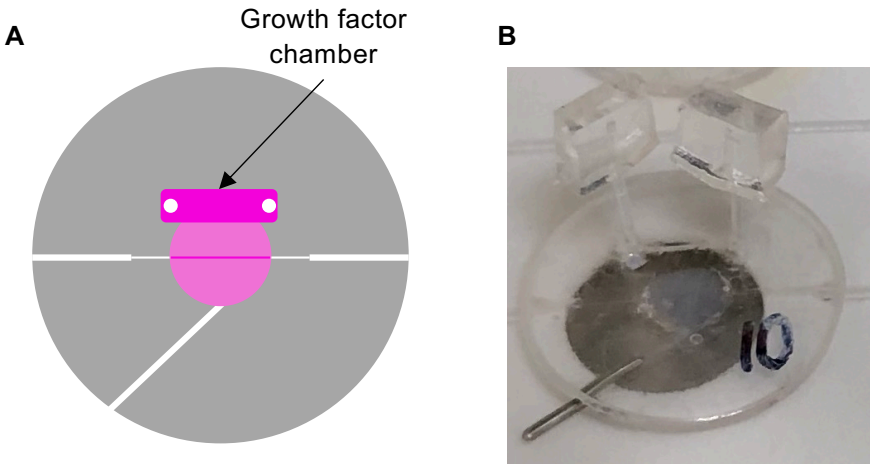


Figure 5.5: The altered design of the microfluidic device to include a growth factor chamber. A: top view of the altered design of the microfluidic device incorporating a growth factor chamber, which replaces one of the ECM inlets. B: Photo showing the device in culture and attached to the 3D printed unit. Tubing is attached to the growth factor chamber in the vertical direction and PDMS plugs are used to seal the inlets.

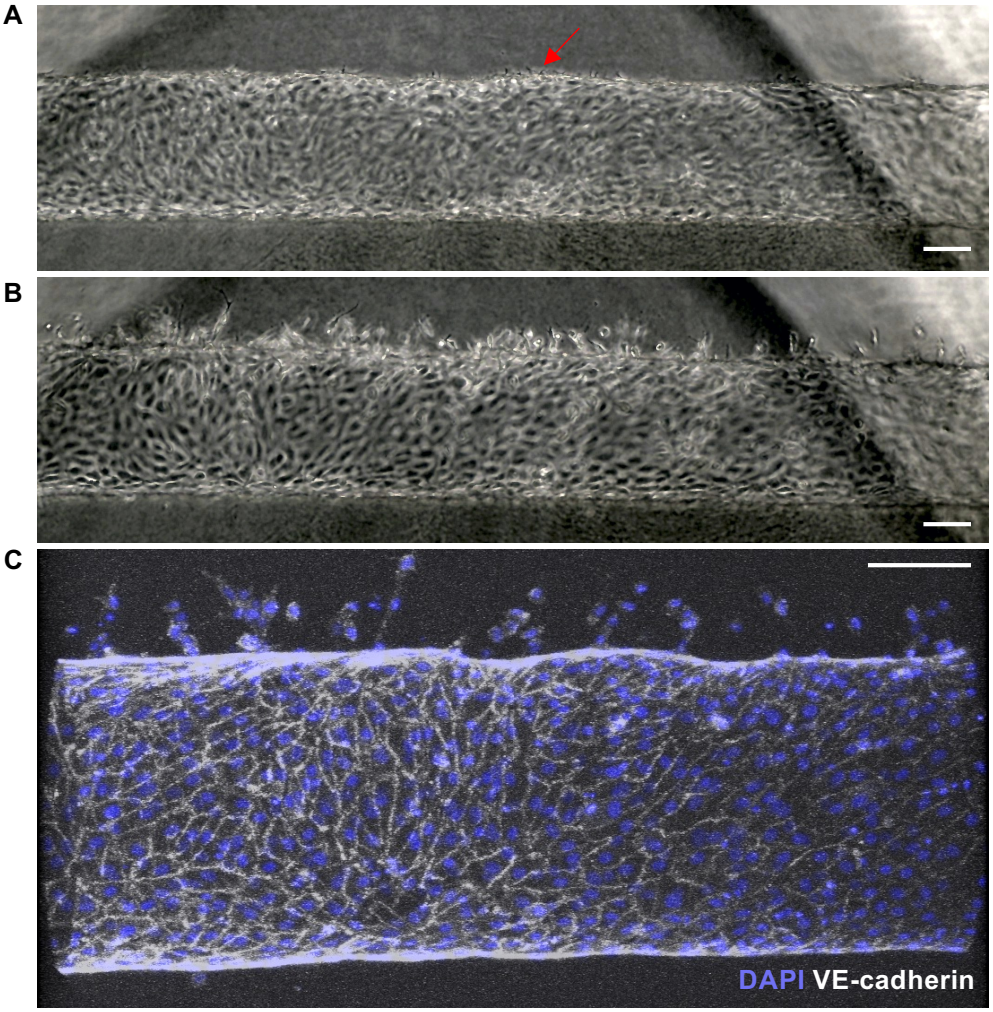


Figure 5.6: EC sprouting from the vessel wall in response to a growth factor gradient in the collagen. Directional sprouting from the vessel wall was achieved using the microfluidic device incorporating a growth factor chamber (n=1 vessel). A: Sprouting is initiated around 2h after injecting the growth factor cocktail. B-C: brightfield and immunofluorescent images taken 24h after injecting the growth factor cocktail, clearly showing sprouting towards the growth factor chamber. Scale bars=100 μm.

vessel. Figure 5.7 shows phase contrast images of the same device at days 1, 2, 3 and 5 following cell seeding, from which it is clear that endothelial cells maintained a confluent monolayer in the vessel in co-culture with fibroblasts. However, no (or very little) sprouting was observed from the vessel in this model. From the phase contrast images it seems like the fibroblasts are either proliferating or spreading inside the collagen over time, which suggests that the cells are viable five days post cell seeding. However, a live/dead assay is required to validate fibroblast viability. Furthermore, co-culture with fibroblasts did not seem to deform the collagen or the vessel, which was a promising result for future co-culture studies. In terms of using this co-culture model to induce angiogenesis, the source of fibroblasts and thereby their capacity to secrete pro-angiogenic growth factors has been identified as a critical parameter in other models, such as the fibrin bead assay, which commonly use lung fibroblasts. Thus, the lack of effect in our model may be due to the type of fibroblasts used.

5.2.3 Discussion

Incorporating a growth factor chamber to establish a chemical gradient in the collagen was the most successful attempt for inducing angiogenesis in the blood vessel-on-a-chip model. However, obtaining high reproducibility in this model would require re-designing the microfluidic device. Design improvements include introducing PDMS pillars or a phase guide to separate the growth factor chamber from the ECM chamber and provide a better seal between the ECM and growth factor chambers. However, these modifications to the mould used for casting PDMS are not well suited for 3D printing. Another option could be to significantly reduce the height of the growth factor chamber and thereby achieve a similar effect of using surface tension to obtain a barrier between the collagen and growth factor cocktail; however, this will also reduce the volume in the growth factor chamber, which consequently might require re-filling more frequently. How often the growth factor chamber requires re-filling to maintain a stable gradient in the collagen requires further investigation. Previous models (discussed earlier in this chapter) have used a second vessel in the needle model as a growth factor chamber, placed parallel to the endothelialised vessel. This has been shown as an efficient approach for inducing sprouting from the vessel wall. Even though this would be straightforward to incorporate in the current design, accessing these inlets during cell culture when the microfluidic device is attached to the 3D printed perfusion unit would be challenging and might therefore sacrifice reproducibility. Considering the above-mentioned challenges associated with optimising the blood vessel-on-a-chip model to support angiogenesis, it might be more sensible to use a different model for this application, such as the commercially available MIMETAS OrganoPlate, which already exists in a high-throughput format.

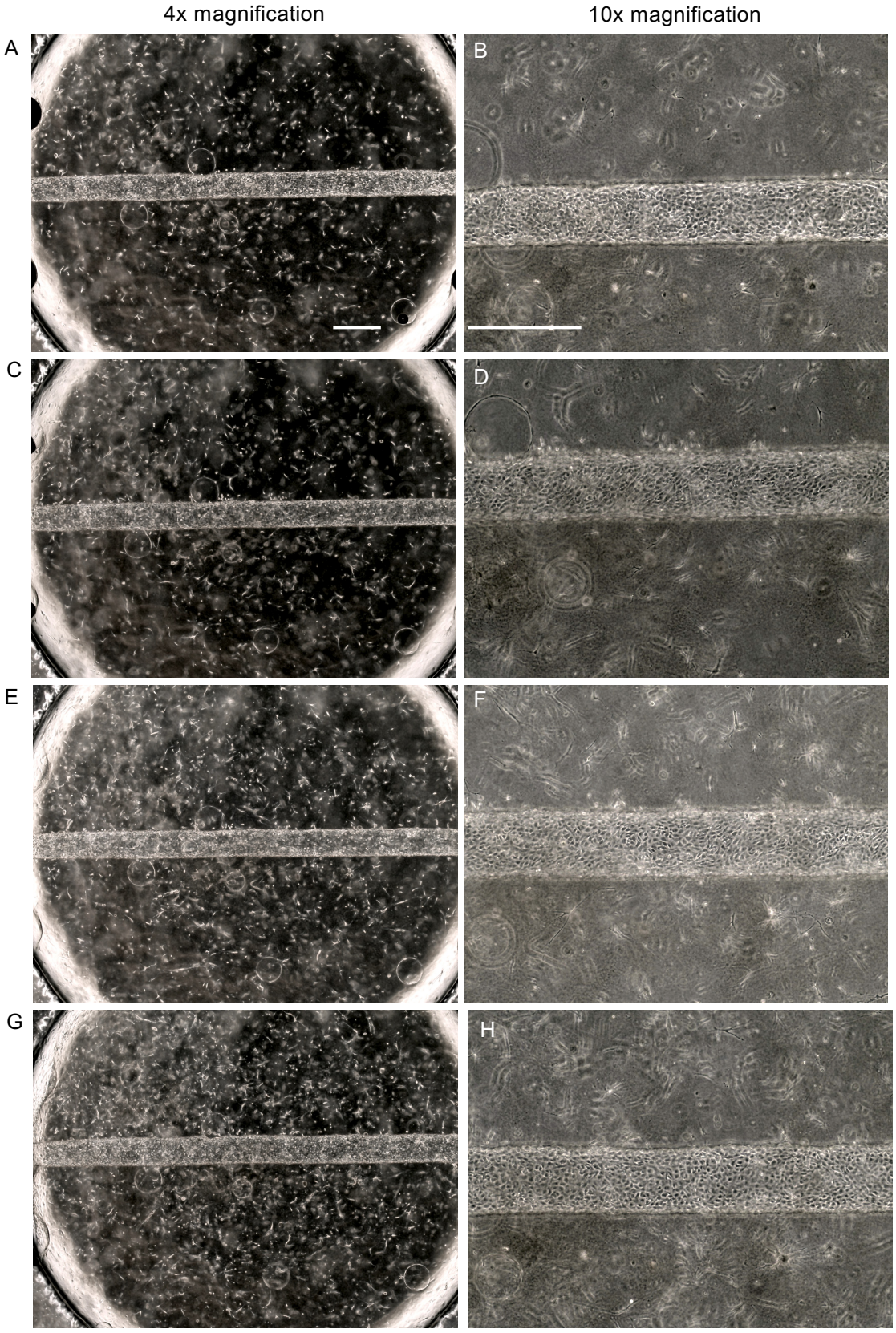


Figure 5.7: Co-culture model of endothelial cells seeded inside the vessel and human cardiac fibroblasts mixed in the collagen. Endothelial cells form a confluent monolayer in the presence of fibroblasts, however, very little sprouting could be observed in this model. 4x and 10x phase contrast images taken on day 1 (A-B), day 2 (C-D), day 3 (E-F) and day 5 (G-H) post cell seeding (representative images for n=2 different vessels). Scale bars=500 µm (applies to all images).

Chapter 6: Discussion

In this PhD project, a 3D blood vessel-on-a-chip platform was developed, comprising of a microfluidic device and a 3D printed perfusion unit. The platform allows independent control of three microenvironmental parameters, namely ECM, co-culture with tissue-specific cells and flow-induced shear stress, to mimic a tissue-specific microenvironment. The combination of all three parameters is commonly not captured *in vitro*. Furthermore, the model supports both molecular assays (qPCR and immunofluorescent staining) and functional assays (permeability and thrombosis). Having validated vessel formation in the platform, using permeability to demonstrate endothelial barrier function comparable with previous studies, we focussed on using the model to study thrombosis. Therefore, altering the microenvironment to affect endothelial phenotype and function fell beyond the scope of this project and the same ECM (collagen) and shear stress (<1 dyne/cm^2) was used in all experiments, without co-culture with tissue-specific cells. However, the method of creating the vessel by polymerising ECM around a needle suggests that a different ECM could be used in this model, at least one that polymerises with temperature or pH similar to collagen. Preliminary results indicate that the model supports perfusion at physiologically relevant shear stress (investigated at 10 dyne/cm^2) without collagen damage when connected to an external perfusion system; however, interfacing with the external perfusion system at this higher shear stress resulted in cell death in the vessel. The reason for this is unclear and requires further investigation. Pre-conditioning of the endothelium to physiological shear stress is a hurdle the field has not yet overcome, as most studies use static models or perfusion from hydrostatic pressure, which is limited in terms of the possible range of shear stress. Preliminary experiments were also carried out for co-culture with mural cells in this model; vessel formation with a confluent endothelial monolayer, validated using immunofluorescent staining of the junctional marker VE-cadherin, could be achieved in the presence of pericytes. However, results from studies using fluorescently labelled pericytes indicated problems with reproducibility and therefore, further optimisation is required before using the co-culture model for functional assays.

The blood vessel-on-a-chip platform was designed to support perfusion with whole blood during real-time imaging to study thrombosis, which has not previously been studied in the needle model or in an *in vitro* model where all three aspects of the endothelial microenvironment can be controlled. In this assay, platelet adhesion and fibrinogen deposition were measured; these were both upregulated following pro-inflammatory endothelial activation with TNF-α in HUVEC, which is in line with previous findings, both from *in vitro* and *in vivo* models. Furthermore, results indicate a physiologically relevant tissue factor dependent coagulation response, following the extrinsic pathway in the coagulation cascade, which was confirmed by blocking tissue factor on endothelial cells prior to the 3D thrombosis assay. Using hirudin as an inhibitor for thrombin, the final enzyme

in the common coagulation pathway, we investigated the sensitivity of the model, which was able to detect differences in clot formation in response to different hirudin concentrations. These results are promising for future studies, indicating that the model can be used to target specific coagulation factors in the coagulation cascade, potentially in the intrinsic, extrinsic and common pathways, which could have applications for studying anticoagulant drugs in the context of preventing thrombosis. Tissue factor dependent thrombosis and thereby clot formation through the initiation of the extrinsic pathway in the coagulation cascade has not been shown in any of the *in vitro* thrombosis models presented in Chapter 1, which highlights the physiological relevance of our model. Furthermore, thrombosis was also studied in vessels created from patient endothelial cells (ECFC), which showed a similar response to HUVEC with upregulation of platelet adhesion and fibrinogen deposition following stimulation with TNF-α. Human ECFCs have not previously been used in *in vitro* thrombosis models. Consequently, being able to use patient cells in this assay was an important outcome of this project, as this allows future studies to use the 3D thrombosis assay for disease modelling and potentially to evaluate thrombotic risk in patients.

From an engineering perspective and comparing to previously published studies based on the needle model design, significant effort was directed towards creating a platform with high reproducibility, where multiple vessels can be cultured in parallel and which supports real-time imaging with minimal user intervention during an experiment, to avoid user errors when handling individual devices (such as repeatedly connecting and disconnecting tubing). Furthermore, we focussed on developing a platform which could support both molecular and functional biological assays to create a research tool, which can be useful for a range of applications in vascular science and biomechanics. The main advantage of using only one specialised model is the possibility to directly compare and correlate results between studies, which is not possible if models with different endothelial microenvironments are used for different applications, as this can have significant impact on endothelial gene expression. However, the model has limitations. Similar to most microfluidic models, it provides relatively low throughput, is more difficult to use compared to conventional tissue culture techniques and requires increased experimental timescales. Therefore, for future use it would be sensible to focus on applications and research questions which require this level of complexity. Such an area is vascular bed-specificity or tissue-specificity, where this model can serve as a useful tool and presents an opportunity for *in vitro* disease modelling of the endothelium, particular in the context of thrombosis as this assay has been validated. Drug screening is a frequently discussed application of microfluidic devices, however, PDMS has been found to absorb small molecules, which is a limitation in the field (described in Chapter 2). The design presented in this study might be favourable compared to other models due to the very small surface area of

PDMS that is in contact with the perfused fluid, through which drugs or compounds would be delivered, however; this needs to be further investigated. In this design PDMS serves as the housing to the vessel, which is embedded in ECM and therefore when perfusing the vessel, the perfusate is only in direct contact with PDMS in the narrowed sections of the vessel inlets (length~2mm, diameter=300μm), where absorption of small molecules can occur. Due to the relatively low throughput of the blood vessel-on-a-chip platform, culturing five devices in parallel, we do not believe that this model can compete with conventional drug discovery platforms, which are based on 96-well or even 384-well formats. Instead, we see an opportunity to target the platform towards functional validation of drugs, as a potential downstream screening tool for investigating drug efficacy in a more physiologically relevant microenvironment or in personalised disease models, creating vessels from ECFCs isolated from specific patient groups. Furthermore, if a reproducible co-culture model can be established where tissue-specific cells are mixed in the collagen, these cells would obtain nutrients from the main vessel, which is a more physiological setting compared to transwell or membrane models, since tissue-specific cells are embedded in a 3D matrix *in vivo* and do not experience a liquid interface.

Bibliography

Aisenbrey, E. A., & Murphy, W. L. (2020). Synthetic alternatives to Matrigel. *Nat Rev Mater*, *5*(7), 539-551. https://doi.org/10.1038/s41578-020-0199-8

Armulik, A., Abramsson, A., & Betsholtz, C. (2005). Endothelial/pericyte interactions. *Circ Res*, *97*(6), 512-523. https://doi.org/10.1161/01.RES.0000182903.16652.d7

Ballermann, B. J., Dardik, A., Eng, E., & Liu, A. (1998). Shear stress and the endothelium. *Kidney Int Suppl*, *67*, S100-108. https://doi.org/10.1046/j.1523-1755.1998.06720.x

Barrile, R., van der Meer, A. D., Park, H., Fraser, J. P., Simic, D., Teng, F., Conegliano, D., Nguyen, J., Jain, A., Zhou, M., Karalis, K., Ingber, D. E., Hamilton, G. A., & Otieno, M. A. (2018). Organ-on-Chip Recapitulates Thrombosis Induced by an anti-CD154 Monoclonal Antibody: Translational Potential of Advanced Microengineered Systems. *Clin Pharmacol Ther*, *104*(6), 1240-1248. https://doi.org/10.1002/cpt.1054

Bastounis, E. E., Yeh, Y. T., & Theriot, J. A. (2019). Subendothelial stiffness alters endothelial cell traction force generation while exerting a minimal effect on the transcriptome. *Sci Rep*, *9*(1), 18209. https://doi.org/10.1038/s41598-019-54336-2

Blair, P., & Flaumenhaft, R. (2009). Platelet alpha-granules: basic biology and clinical correlates. *Blood Rev*, *23*(4), 177-189. https://doi.org/10.1016/j.blre.2009.04.001

Bode, M., & Mackman, N. (2014). Regulation of tissue factor gene expression in monocytes and endothelial cells: Thromboxane A2 as a new player. *Vascul Pharmacol*, *62*(2), 57-62. https://doi.org/10.1016/j.vph.2014.05.005

Bogorad, M. I., DeStefano, J., Wong, A. D., & Searson, P. C. (2017). Tissue-engineered 3D microvessel and capillary network models for the study of vascular phenomena. *Microcirculation*, *24*(5). https://doi.org/10.1111/micc.12360

Bouchard, B. A., Shatos, M. A., & Tracy, P. B. (1997). Human brain pericytes differentially regulate expression of procoagulant enzyme complexes comprising the extrinsic pathway of blood coagulation. *Arterioscler Thromb Vasc Biol*, *17*(1), 1-9. https://doi.org/10.1161/01.atv.17.1.1

Bowen, R. A., & Remaley, A. T. (2014). Interferences from blood collection tube components on clinical chemistry assays. *Biochem Med (Zagreb)*, *24*(1), 31-44. https://doi.org/10.11613/BM.2014.006

Braddock, M., Schwachtgen, J. L., Houston, P., Dickson, M. C., Lee, M. J., & Campbell, C. J. (1998). Fluid Shear Stress Modulation of Gene Expression in Endothelial Cells. *News Physiol Sci*, *13*, 241-246. https://doi.org/10.1152/physiologyonline.1998.13.5.241

Buresti, G. (2012). Elements of fluid dynamics. Imperial College Press.

Callister, W. D. (2007). *Fundamentals of materials science and engineering : an integrated approach* (3rd ed.). Wiley; John Wiley [distributor].

Carmeliet, P. (2003). Angiogenesis in health and disease. *Nat Med*, *9*(6), 653-660. https://doi.org/10.1038/nm0603-653

Chiu, J. J., & Chien, S. (2011). Effects of disturbed flow on vascular endothelium: pathophysiological basis and clinical perspectives. *Physiol Rev*, *91*(1), 327-387. https://doi.org/10.1152/physrev.00047.2009

Chrobak, K. M., Potter, D. R., & Tien, J. (2006). Formation of perfused, functional microvascular tubes in vitro. *Microvasc Res*, *71*(3), 185-196. https://doi.org/10.1016/j.mvr.2006.02.005

Costa, P. F., Albers, H. J., Linssen, J. E. A., Middelkamp, H. H. T., van der Hout, L., Passier, R., van den Berg, A., Malda, J., & van der Meer, A. D. (2017). Mimicking arterial thrombosis in a 3D-printed microfluidic in vitro vascular model based on computed tomography angiography data. *Lab Chip*, *17*(16), 2785-2792. https://doi.org/10.1039/c7lc00202e

Daly, C., Qian, X., Castanaro, C., Pasnikowski, E., Jiang, X., Thomson, B. R., Quaggin, S. E., Papadopoulos, N., Wei, Y., Rudge, J. S., Thurston, G., Yancopoulos, G. D., & Davis, S. (2018). Angiopoietins bind thrombomodulin and inhibit its function as a thrombin cofactor. *Sci Rep*, *8*(1), 505. https://doi.org/10.1038/s41598-017-18912-8

Davies, P. F. (2009). Hemodynamic shear stress and the endothelium in cardiovascular pathophysiology. *Nat Clin Pract Cardiovasc Med*, *6*(1), 16-26. https://doi.org/10.1038/ncpcardio1397

Davis, G. E., & Senger, D. R. (2005). Endothelial extracellular matrix: biosynthesis, remodeling, and functions during vascular morphogenesis and neovessel stabilization. *Circ Res*, *97*(11), 1093-1107. https://doi.org/10.1161/01.RES.0000191547.64391.e3

DeStefano, J. G., Williams, A., Wnorowski, A., Yimam, N., Searson, P. C., & Wong, A. D. (2017). Real-time quantification of endothelial response to shear stress and vascular modulators. *Integr Biol (Camb)*, *9*(4), 362-374. https://doi.org/10.1039/c7ib00023e

Dittrich, B. S. a. P. S. (2018). Microfluidics to Mimic Blood Flow in Health and Disease. *Annu. Rev. Fluid Mech*, *50*, 483-504. https://doi.org/https://doi.org/10.1146/annurev-fluid-010816-060246

Draoui, N., de Zeeuw, P., & Carmeliet, P. (2017). Angiogenesis revisited from a metabolic perspective: role and therapeutic implications of endothelial cell metabolism. *Open Biol*, *7*(12). https://doi.org/10.1098/rsob.170219

Driver, B., Marks, D. C., & van der Wal, D. E. (2020). Not all (N)SAID and done: Effects of nonsteroidal anti-inflammatory drugs and paracetamol intake on platelets. *Res Pract Thromb Haemost*, *4*(1), 36-45. https://doi.org/10.1002/rth2.12283

G.Firpo, E. A., L.Repetto, U.Valbusa. (2015). Permeability thickness dependence of polydimethylsiloxane (PDMS) membranes. *481*, 1-8. https://doi.org/https://doi.org/10.1016/j.memsci.2014.12.043

Gailani, D., & Renne, T. (2007). The intrinsic pathway of coagulation: a target for treating thromboembolic disease? *J Thromb Haemost*, *5*(6), 1106-1112. https://doi.org/10.1111/j.1538-7836.2007.02446.x

Gijsen, F. J., van de Vosse, F. N., & Janssen, J. D. (1999). The influence of the non-Newtonian properties of blood on the flow in large arteries: steady flow in a carotid bifurcation model. *J Biomech*, *32*(6), 601-608. https://doi.org/10.1016/s0021-9290(99)00015-9

Goveia, J., Rohlenova, K., Taverna, F., Treps, L., Conradi, L. C., Pircher, A., Geldhof, V., de Rooij, L., Kalucka, J., Sokol, L., Garcia-Caballero, M., Zheng, Y., Qian, J., Teuwen, L. A., Khan, S., Boeckx, B., Wauters, E., Decaluwe, H., De Leyn, P., Vansteenkiste, J., Weynand, B., Sagaert, X., Verbeken, E., Wolthuis, A., Topal, B., Everaerts, W., Bohnenberger, H., Emmert, A., Panovska, D., De Smet, F., Staal, F. J. T., McLaughlin, R. J., Impens, F., Lagani, V., Vinckier, S., Mazzone, M., Schoonjans, L., Dewerchin, M., Eelen, G., Karakach, T. K., Yang, H., Wang, J., Bolund, L., Lin, L., Thienpont, B., Li, X., Lambrechts, D., Luo, Y., & Carmeliet, P. (2020). An Integrated Gene Expression Landscape Profiling Approach to Identify Lung Tumor Endothelial Cell Heterogeneity and Angiogenic Candidates. *Cancer Cell*, *37*(1), 21-36 e13. https://doi.org/10.1016/j.ccell.2019.12.001

Grigoryan, B., Paulsen, S. J., Corbett, D. C., Sazer, D. W., Fortin, C. L., Zaita, A. J., Greenfield, P. T., Calafat, N. J., Gounley, J. P., Ta, A. H., Johansson, F., Randles, A., Rosenkrantz, J. E., Louis-Rosenberg, J. D., Galie, P. A., Stevens, K. R., & Miller, J. S. (2019). Multivascular networks and functional intravascular topologies within biocompatible hydrogels. *Science*, *364*(6439), 458-464. https://doi.org/10.1126/science.aav9750

Grover, S. P., & Mackman, N. (2019). Intrinsic Pathway of Coagulation and Thrombosis. *Arterioscler Thromb Vasc Biol*, *39*(3), 331-338. https://doi.org/10.1161/ATVBAHA.118.312130

Haase, K., Gillrie, M. R., Hajal, C., & Kamm, R. D. (2019). Pericytes Contribute to Dysfunction in a Human 3D Model of Placental Microvasculature through VEGF-Ang-Tie2 Signaling. *Adv Sci (Weinh)*, *6*(23), 1900878. https://doi.org/10.1002/advs.201900878

Harter, K., Levine, M., & Henderson, S. O. (2015). Anticoagulation drug therapy: a review. *West J Emerg Med*, *16*(1), 11-17. https://doi.org/10.5811/westjem.2014.12.22933

Heo, Y. S., Cabrera, L. M., Song, J. W., Futai, N., Tung, Y. C., Smith, G. D., & Takayama, S. (2007). Characterization and resolution of evaporation-mediated osmolality shifts that constrain microfluidic cell culture in poly(dimethylsiloxane) devices. *Anal Chem*, *79*(3), 1126-1134. https://doi.org/10.1021/ac061990v

Holme, P. A., Orvim, U., Hamers, M. J., Solum, N. O., Brosstad, F. R., Barstad, R. M., & Sakariassen, K. S. (1997). Shear-induced platelet activation and platelet microparticle formation at blood flow conditions as in arteries with a severe stenosis. *Arterioscler Thromb Vasc Biol*, *17*(4), 646-653. https://doi.org/10.1161/01.atv.17.4.646

Huh, D., Matthews, B. D., Mammoto, A., Montoya-Zavala, M., Hsin, H. Y., & Ingber, D. E. (2010). Reconstituting organ-level lung functions on a chip. *Science*, *328*(5986), 1662-1668. https://doi.org/10.1126/science.1188302

Hussey, G. S., Dziki, J.L. & Badylak, S.F. (2018). Extracellular matrix-based materials for regenerative medicine. *Nat Rev Mater*, *3*, 159–173. https://doi.org/https://doi.org/10.1038/s41578-018-0023-x

Huxley, V. H., Curry, F. E., & Adamson, R. H. (1987). Quantitative fluorescence microscopy on single capillaries: alpha-lactalbumin transport. *Am J Physiol*, *252*(1 Pt 2), H188-197. https://doi.org/10.1152/ajpheart.1987.252.1.H188

I D Johnston, D. K. M., C K L Tan and M C Tracey. (2014). Mechanical characterization of bulk Sylgard 184 for microfluidics and microengineering. *Micromech. Microeng*, *24*. https://doi.org/iopscience.iop.org/article/10.1088/0960-1317/24/3/035017

Iivanainen, E., Kahari, V. M., Heino, J., & Elenius, K. (2003). Endothelial cell-matrix interactions. *Microsc Res Tech*, *60*(1), 13-22. https://doi.org/10.1002/jemt.10238

Jackson, S. P., Darbousset, R., & Schoenwaelder, S. M. (2019). Thromboinflammation: challenges of therapeutically targeting coagulation and other host defense mechanisms. *Blood*, *133*(9), 906-918. https://doi.org/10.1182/blood-2018-11-882993

Jain, A., Barrile, R., van der Meer, A. D., Mammoto, A., Mammoto, T., De Ceunynck, K., Aisiku, O., Otieno, M. A., Louden, C. S., Hamilton, G. A., Flaumenhaft, R., & Ingber, D. E. (2018). Primary Human Lung Alveolus-on-a-chip Model of Intravascular Thrombosis for Assessment of Therapeutics. *Clin Pharmacol Ther*, *103*(2), 332-340. https://doi.org/10.1002/cpt.742

Jambusaria, A., Hong, Z., Zhang, L., Srivastava, S., Jana, A., Toth, P. T., Dai, Y., Malik, A. B., & Rehman, J. (2020). Endothelial heterogeneity across distinct vascular beds during homeostasis and inflammation. *Elife*, *9*. https://doi.org/10.7554/eLife.51413

Jimenez-Torres, J. A., Peery, S. L., Sung, K. E., & Beebe, D. J. (2016). LumeNEXT: A Practical Method to Pattern Luminal Structures in ECM Gels. *Adv Healthc Mater*, *5*(2), 198-204. https://doi.org/10.1002/adhm.201500608

Kim, J., Chung, M., Kim, S., Jo, D. H., Kim, J. H., & Jeon, N. L. (2015). Engineering of a Biomimetic Pericyte-Covered 3D Microvascular Network. *PLoS One*, *10*(7), e0133880. https://doi.org/10.1371/journal.pone.0133880

Kim, S. O., Kim, J., Okajima, T., & Cho, N. J. (2017). Mechanical properties of paraformaldehyde-treated individual cells investigated by atomic force microscopy and scanning ion conductance microscopy. Nano Converg, 4(1), 5. https://doi.org/10.1186/s40580-017-0099-9

Kim, S., Lee, H., Chung, M., & Jeon, N. L. (2013). Engineering of functional, perfusable 3D microvascular networks on a chip. *Lab Chip*, *13*(8), 1489-1500. https://doi.org/10.1039/c3lc41320a

Kintigh, J., Monagle, P., & Ignjatovic, V. (2018). A review of commercially available thrombin generation assays. *Res Pract Thromb Haemost*, *2*(1), 42-48. https://doi.org/10.1002/rth2.12048

Kolesky, D. B., Homan, K. A., Skylar-Scott, M. A., & Lewis, J. A. (2016). Three-dimensional bioprinting of thick vascularized tissues. *Proc Natl Acad Sci U S A*, *113*(12), 3179-3184. https://doi.org/10.1073/pnas.1521342113

Krogh, A. (1922). *The Anantomy and Physiology of Capillaries*. Yale University Press.

LaValley, D. J., Zanotelli, M. R., Bordeleau, F., Wang, W., Schwager, S. C., & Reinhart-King, C. A. (2017). Matrix Stiffness Enhances VEGFR-2 Internalization, Signaling, and Proliferation in Endothelial Cells. *Converg Sci Phys Oncol*, *3*. https://doi.org/10.1088/2057-1739/aa9263

Lei, D., Yang, Y., Liu, Z., Yang, B., Gong, W., Chen, S., Wang, S., Sun, L., Song, B., Xuan, H., Mo, X., Sun, B., Li, S., Yang, Q., Huang, S., Chen, S., Ma, Y., Liu, W., He, C., Zhu, B., Jeffries, E. M., Qing, F.-L., Ye, X., Zhao, Q., & You, Z. (2019). 3D printing of biomimetic vasculature for tissue regeneration [10.1039/C9MH00174C]. *Materials Horizons*, *6*(6), 1197-1206. https://doi.org/10.1039/C9MH00174C

Levental, I., Georges, P. C., & Janmey, P. A. (2007). Soft biological materials and their impact on cell function. *Soft Matter*, *3*(3), 299-306. https://doi.org/10.1039/b610522j

Li, R., Fries, S., Li, X., Grosser, T., & Diamond, S. L. (2013). Microfluidic assay of platelet deposition on collagen by perfusion of whole blood from healthy individuals taking aspirin. *Clin Chem*, *59*(8), 1195-1204. https://doi.org/10.1373/clinchem.2012.198101

Liu, J., Zheng, H., Poh, P. S., Machens, H. G., & Schilling, A. F. (2015). Hydrogels for Engineering of Perfusable Vascular Networks. *Int J Mol Sci*, *16*(7), 15997-16016. https://doi.org/10.3390/ijms160715997

Mackman, N. (2008). Triggers, targets and treatments for thrombosis. *Nature*, *451*(7181), 914-918. https://doi.org/10.1038/nature06797

Mackman, N. (2012). New insights into the mechanisms of venous thrombosis. *J Clin Invest*, *122*(7), 2331-2336. https://doi.org/10.1172/JCI60229

Madge, L. A., & Pober, J. S. (2001). TNF signaling in vascular endothelial cells. *Exp Mol Pathol*, *70*(3), 317-325. https://doi.org/10.1006/exmp.2001.2368

Martin-Ramirez, J., Hofman, M., van den Biggelaar, M., Hebbel, R. P., & Voorberg, J. (2012). Establishment of outgrowth endothelial cells from peripheral blood. *Nat Protoc*, *7*(9), 1709-1715. https://doi.org/10.1038/nprot.2012.093

Massaia, A., Chaves, P., Samari, S., Miragaia, R. J., Meyer, K., Teichmann, S. A., & Noseda, M. (2018). Single Cell Gene Expression to Understand the Dynamic Architecture of the Heart. *Front Cardiovasc Med*, *5*, 167. https://doi.org/10.3389/fcvm.2018.00167

Mathur, T., Singh, K. A., NK, R. P., Tsai, S. H., Hein, T. W., Gaharwar, A. K., Flanagan, J. M., & Jain, A. (2019). Organ-on-chips made of blood: endothelial progenitor cells from blood reconstitute vascular thromboinflammation in vessel-chips. *Lab Chip*, *19*(15), 2500-2511. https://doi.org/10.1039/c9lc00469f

Matsumoto, J., Takata, F., Machida, T., Takahashi, H., Soejima, Y., Funakoshi, M., Futagami, K., Yamauchi, A., Dohgu, S., & Kataoka, Y. (2014). Tumor necrosis factor-alpha-stimulated brain pericytes possess a unique cytokine and chemokine release profile and enhance microglial activation. *Neurosci Lett*, *578*, 133-138. https://doi.org/10.1016/j.neulet.2014.06.052

Miao Liu, J. S., Ying Sun, Christopher Bock and Quanfang Chen. (2009). Thickness-dependent mechanical properties of polydimethylsiloxane membranes. *JOURNAL OF MICROMECHANICS AND MICROENGINEERING*, *19*. https://doi.org/10.1088/0960-1317/19/3/035028

Miller, J. S., Stevens, K. R., Yang, M. T., Baker, B. M., Nguyen, D. H., Cohen, D. M., Toro, E., Chen, A. A., Galie, P. A., Yu, X., Chaturvedi, R., Bhatia, S. N., & Chen, C. S. (2012). Rapid casting of patterned vascular networks for perfusable engineered three-dimensional tissues. *Nat Mater*, *11*(9), 768-774. https://doi.org/10.1038/nmat3357

Murphy, S. V., & Atala, A. (2014). 3D bioprinting of tissues and organs. *Nat Biotechnol*, *32*(8), 773-785. https://doi.org/10.1038/nbt.2958

Nakatsu, M. N., Davis, J., & Hughes, C. C. (2007). Optimized fibrin gel bead assay for the study of angiogenesis. *J Vis Exp*(3), 186. https://doi.org/10.3791/186

Nashimoto, Y., Hayashi, T., Kunita, I., Nakamasu, A., Torisawa, Y. S., Nakayama, M., Takigawa-Imamura, H., Kotera, H., Nishiyama, K., Miura, T., & Yokokawa, R. (2017). Integrating perfusable vascular networks with a

three-dimensional tissue in a microfluidic device. *Integr Biol (Camb)*, *9*(6), 506-518. https://doi.org/10.1039/c7ib00024c

Nguyen, D. H., Stapleton, S. C., Yang, M. T., Cha, S. S., Choi, C. K., Galie, P. A., & Chen, C. S. (2013). Biomimetic model to reconstitute angiogenic sprouting morphogenesis in vitro. *Proc Natl Acad Sci U S A*, *110*(17), 6712-6717. https://doi.org/10.1073/pnas.1221526110

Nicolas, J., Magli, S., Rabbachin, L., Sampaolesi, S., Nicotra, F., & Russo, L. (2020). 3D Extracellular Matrix Mimics: Fundamental Concepts and Role of Materials Chemistry to Influence Stem Cell Fate. *Biomacromolecules*, *21*(6), 1968-1994. https://doi.org/10.1021/acs.biomac.0c00045

Offeddu, G. S., Haase, K., Gillrie, M. R., Li, R., Morozova, O., Hickman, D., Knutson, C. G., & Kamm, R. D. (2019). An on-chip model of protein paracellular and transcellular permeability in the microcirculation. *Biomaterials*, *212*, 115-125. https://doi.org/10.1016/j.biomaterials.2019.05.022

Pagano, G., Ventre, M., Iannone, M., Greco, F., Maffettone, P. L., & Netti, P. A. (2014). Optimizing design and fabrication of microfluidic devices for cell cultures: An effective approach to control cell microenvironment in three dimensions. *Biomicrofluidics*, *8*(4), 046503. https://doi.org/10.1063/1.4893913

Papaioannou, T. G., & Stefanadis, C. (2005). Vascular wall shear stress: basic principles and methods. *Hellenic J Cardiol*, *46*(1), 9-15. https://www.ncbi.nlm.nih.gov/pubmed/15807389

Parameswaran, N., & Patial, S. (2010). Tumor necrosis factor-alpha signaling in macrophages. *Crit Rev Eukaryot Gene Expr*, *20*(2), 87-103. https://doi.org/10.1615/critreveukargeneexpr.v20.i2.10

Pauty, J., Usuba, R., Cheng, I. G., Hespel, L., Takahashi, H., Kato, K., Kobayashi, M., Nakajima, H., Lee, E., Yger, F., Soncin, F., & Matsunaga, Y. T. (2018). A Vascular Endothelial Growth Factor-Dependent Sprouting Angiogenesis Assay Based on an In Vitro Human Blood Vessel Model for the Study of Anti-Angiogenic Drugs. *EBioMedicine*, *27*, 225-236. https://doi.org/10.1016/j.ebiom.2017.12.014

Peghaire, C., Dufton, N. P., Lang, M., Salles, C., II, Ahnstrom, J., Kalna, V., Raimondi, C., Pericleous, C., Inuabasi, L., Kiseleva, R., Muzykantov, V. R., Mason, J. C., Birdsey, G. M., & Randi, A. M. (2019). The transcription factor ERG regulates a low shear stress-induced anti-thrombotic pathway in the microvasculature. *Nat Commun*, *10*(1), 5014. https://doi.org/10.1038/s41467-019-12897-w

Petrosyan, A., Cravedi, P., Villani, V., Angeletti, A., Manrique, J., Renieri, A., De Filippo, R. E., Perin, L., & Da Sacco, S. (2019). A glomerulus-on-a-chip to recapitulate the human glomerular filtration barrier. *Nat Commun*, *10*(1), 3656. https://doi.org/10.1038/s41467-019-11577-z

Pober, J. S. (2002). Endothelial activation: intracellular signaling pathways. *Arthritis Res*, *4 Suppl 3*, S109-116. https://doi.org/10.1186/ar576

Pober, J. S., & Sessa, W. C. (2007). Evolving functions of endothelial cells in inflammation. *Nat Rev Immunol*, *7*(10), 803-815. https://doi.org/10.1038/nri2171

Poon, K. W., Lyng, F. M., Knief, P., Howe, O., Meade, A. D., Curtin, J. F., Byrne, H. J., & Vaughan, J. (2012). Quantitative reagent-free detection of fibrinogen levels in human blood plasma using Raman spectroscopy. *Analyst*, *137*(8), 1807-1814. https://doi.org/10.1039/c2an35042d

Potente, M., & Makinen, T. (2017). Vascular heterogeneity and specialization in development and disease. *Nat Rev Mol Cell Biol*, *18*(8), 477-494. https://doi.org/10.1038/nrm.2017.36

Price, G. M., & Tien, J. (2011). Methods for forming human microvascular tubes in vitro and measuring their macromolecular permeability. *Methods Mol Biol*, *671*, 281-293. https://doi.org/10.1007/978-1-59745-551-0_17

Price, G. M., Wong, K. H., Truslow, J. G., Leung, A. D., Acharya, C., & Tien, J. (2010). Effect of mechanical factors on the function of engineered human blood microvessels in microfluidic collagen gels. *Biomaterials*, *31*(24), 6182-6189. https://doi.org/10.1016/j.biomaterials.2010.04.041

Rafii, S., Butler, J. M., & Ding, B. S. (2016). Angiocrine functions of organ-specific endothelial cells. *Nature*, *529*(7586), 316-325. https://doi.org/10.1038/nature17040

Ramanujan, S., Pluen, A., McKee, T. D., Brown, E. B., Boucher, Y., & Jain, R. K. (2002). Diffusion and convection in collagen gels: implications for transport in the tumor interstitium. *Biophys J*, *83*(3), 1650-1660. https://doi.org/10.1016/S0006-3495(02)73933-7

Randi, A. M., Laffan, M. A., & Starke, R. D. (2013). Von Willebrand factor, angiodysplasia and angiogenesis. *Mediterr J Hematol Infect Dis*, *5*(1), e2013060. https://doi.org/10.4084/MJHID.2013.060

Raub, C. B., Putnam, A. J., Tromberg, B. J., & George, S. C. (2010). Predicting bulk mechanical properties of cellularized collagen gels using multiphoton microscopy. *Acta Biomater*, *6*(12), 4657-4665. https://doi.org/10.1016/j.actbio.2010.07.004

Riddel, J. P., Jr., Aouizerat, B. E., Miaskowski, C., & Lillicrap, D. P. (2007). Theories of blood coagulation. *J Pediatr Oncol Nurs*, *24*(3), 123-131. https://doi.org/10.1177/1043454206298693

Ruggeri, Z. M., & Mendolicchio, G. L. (2007). Adhesion mechanisms in platelet function. *Circ Res*, *100*(12), 1673-1685. https://doi.org/10.1161/01.RES.0000267878.97021.ab

Sabbagh, M. F., Heng, J. S., Luo, C., Castanon, R. G., Nery, J. R., Rattner, A., Goff, L. A., Ecker, J. R., & Nathans, J. (2018). Transcriptional and epigenomic landscapes of CNS and non-CNS vascular endothelial cells. *Elife*, *7*. https://doi.org/10.7554/eLife.36187

Sakariassen, K. S., Orning, L., & Turitto, V. T. (2015). The impact of blood shear rate on arterial thrombus formation. *Future Sci OA*, *1*(4), FSO30. https://doi.org/10.4155/fso.15.28

Sakurai, Y., Hardy, E. T., Ahn, B., Tran, R., Fay, M. E., Ciciliano, J. C., Mannino, R. G., Myers, D. R., Qiu, Y., Carden, M. A., Baldwin, W. H., Meeks, S. L., Gilbert, G. E., Jobe, S. M., & Lam, W. A. (2018). A microengineered vascularized bleeding model that integrates the principal components of hemostasis. *Nat Commun*, *9*(1), 509. https://doi.org/10.1038/s41467-018-02990-x

Sherwood, J. M., Reina-Torres, E., Bertrand, J. A., Rowe, B., & Overby, D. R. (2016). Measurement of Outflow Facility Using iPerfusion. *PLoS One*, *11*(3), e0150694. https://doi.org/10.1371/journal.pone.0150694

Sivarapatna, A., Ghaedi, M., Xiao, Y., Han, E., Aryal, B., Zhou, J., Fernandez-Hernando, C., Qyang, Y., Hirschi, K. K., & Niklason, L. E. (2017). Engineered Microvasculature in PDMS Networks Using Endothelial Cells Derived from Human Induced Pluripotent Stem Cells. *Cell Transplant*, *26*(8), 1365-1379. https://doi.org/10.1177/0963689717720282

Smith, S. A., Travers, R. J., & Morrissey, J. H. (2015). How it all starts: Initiation of the clotting cascade. *Crit Rev Biochem Mol Biol*, *50*(4), 326-336. https://doi.org/10.3109/10409238.2015.1050550

Sobrino, A., Phan, D. T., Datta, R., Wang, X., Hachey, S. J., Romero-Lopez, M., Gratton, E., Lee, A. P., George, S. C., & Hughes, C. C. (2016). 3D microtumors in vitro supported by perfused vascular networks. *Sci Rep*, *6*, 31589. https://doi.org/10.1038/srep31589

Song, J. W., & Munn, L. L. (2011). Fluid forces control endothelial sprouting. *Proc Natl Acad Sci U S A*, *108*(37), 15342-15347. https://doi.org/10.1073/pnas.1105316108

Srinivasan, B., Kolli, A. R., Esch, M. B., Abaci, H. E., Shuler, M. L., & Hickman, J. J. (2015). TEER measurement techniques for in vitro barrier model systems. *J Lab Autom*, *20*(2), 107-126. https://doi.org/10.1177/2211068214561025

Steffel, J., Luscher, T. F., & Tanner, F. C. (2006). Tissue factor in cardiovascular diseases: molecular mechanisms and clinical implications. *Circulation*, *113*(5), 722-731. https://doi.org/10.1161/CIRCULATIONAHA.105.567297

Stone, N. L., England, T. J., & O'Sullivan, S. E. (2019). A Novel Transwell Blood Brain Barrier Model Using Primary Human Cells. *Front Cell Neurosci*, *13*, 230. https://doi.org/10.3389/fncel.2019.00230

Takahashi, H., Kato, K., Ueyama, K., Kobayashi, M., Baik, G., Yukawa, Y., Suehiro, J. I., & Matsunaga, Y. T. (2017). Visualizing dynamics of angiogenic sprouting from a three-dimensional microvasculature model using stage-top optical coherence tomography. *Sci Rep*, *7*, 42426. https://doi.org/10.1038/srep42426

Toepke, M. W., & Beebe, D. J. (2006). PDMS absorption of small molecules and consequences in microfluidic applications. *Lab Chip*, *6*(12), 1484-1486. https://doi.org/10.1039/b612140c

Toshima, H., Sugihara, H., Hamano, H., Sato, M., Yamamoto, M., Yamazaki, S., Yamada, Y., Taki, M., Izumi, S., Hoshi, K., Fusegawa, Y., Satoh, K., Ozaki, Y., & Kurihara, S. (2008). Spontaneous platelet aggregation in normal subject assessed by a laser light scattering method: an attempt at standardization. *Platelets*, *19*(4), 293-299. https://doi.org/10.1080/09537100701883457

van Duinen, V., van den Heuvel, A., Trietsch, S. J., Lanz, H. L., van Gils, J. M., van Zonneveld, A. J., Vulto, P., & Hankemeier, T. (2017). 96 perfusable blood vessels to study vascular permeability in vitro. *Sci Rep*, *7*(1), 18071. https://doi.org/10.1038/s41598-017-14716-y

van Duinen, V., Zhu, D., Ramakers, C., van Zonneveld, A. J., Vulto, P., & Hankemeier, T. (2019). Perfused 3D angiogenic sprouting in a high-throughput in vitro platform. *Angiogenesis*, *22*(1), 157-165. https://doi.org/10.1007/s10456-018-9647-0

Wang, G., Kostidis, S., Tiemeier, G. L., Sol, W., de Vries, M. R., Giera, M., Carmeliet, P., van den Berg, B. M., & Rabelink, T. J. (2020). Shear Stress Regulation of Endothelial Glycocalyx Structure Is Determined by Glucobiosynthesis. *Arterioscler Thromb Vasc Biol*, *40*(2), 350-364. https://doi.org/10.1161/ATVBAHA.119.313399

Wang, W. Y., Lin, D., Jarman, E. H., Polacheck, W. J., & Baker, B. M. (2020). Functional angiogenesis requires microenvironmental cues balancing endothelial cell migration and proliferation. *Lab Chip*, *20*(6), 1153-1166. https://doi.org/10.1039/c9lc01170f

Wang, X., Phan, D. T., Sobrino, A., George, S. C., Hughes, C. C., & Lee, A. P. (2016). Engineering anastomosis between living capillary networks and endothelial cell-lined microfluidic channels. *Lab Chip*, *16*(2), 282-290. https://doi.org/10.1039/c5lc01050k

Warboys, C. M., Eric Berson, R., Mann, G. E., Pearson, J. D., & Weinberg, P. D. (2010). Acute and chronic exposure to shear stress have opposite effects on endothelial permeability to macromolecules. *Am J Physiol Heart Circ Physiol*, *298*(6), H1850-1856. https://doi.org/10.1152/ajpheart.00114.2010

Westrick, R. J., Winn, M. E., & Eitzman, D. T. (2007). Murine models of vascular thrombosis (Eitzman series). *Arterioscler Thromb Vasc Biol*, *27*(10), 2079-2093. https://doi.org/10.1161/ATVBAHA.107.142810

Wong, A. D., & Searson, P. C. (2014). Live-cell imaging of invasion and intravasation in an artificial microvessel platform. *Cancer Res*, *74*(17), 4937-4945. https://doi.org/10.1158/0008-5472.CAN-14-1042

Wong, K. H., Chan, J. M., Kamm, R. D., & Tien, J. (2012). Microfluidic models of vascular functions. *Annu Rev Biomed Eng*, *14*, 205-230. https://doi.org/10.1146/annurev-bioeng-071811-150052

Wu, W., DeConinck, A., & Lewis, J. A. (2011). Omnidirectional printing of 3D microvascular networks. *Adv Mater*, *23*(24), H178-183. https://doi.org/10.1002/adma.201004625

Wu, Y. (2015). Contact pathway of coagulation and inflammation. *Thromb J*, *13*, 17. https://doi.org/10.1186/s12959-015-0048-y

Yau, J. W., Teoh, H., & Verma, S. (2015). Endothelial cell control of thrombosis. *BMC Cardiovasc Disord*, *15*, 130. https://doi.org/10.1186/s12872-015-0124-z

Yeung, T., Georges, P. C., Flanagan, L. A., Marg, B., Ortiz, M., Funaki, M., Zahir, N., Ming, W., Weaver, V., & Janmey, P. A. (2005). Effects of substrate stiffness on cell morphology, cytoskeletal structure, and adhesion. *Cell Motil Cytoskeleton*, *60*(1), 24-34. https://doi.org/10.1002/cm.20041

Young, E. W., & Beebe, D. J. (2010). Fundamentals of microfluidic cell culture in controlled microenvironments. *Chem Soc Rev*, *39*(3), 1036-1048. https://doi.org/10.1039/b909900j

Yun, S. H., Sim, E. H., Goh, R. Y., Park, J. I., & Han, J. Y. (2016). Platelet Activation: The Mechanisms and Potential Biomarkers. *Biomed Res Int*, *2016*, 9060143. https://doi.org/10.1155/2016/9060143

Zeltz, C., & Gullberg, D. (2016). The integrin-collagen connection - a glue for tissue repair? *J Cell Sci*, *129*(6), 1284. https://doi.org/10.1242/jcs.188672

Zheng, Y., Chen, J., Craven, M., Choi, N. W., Totorica, S., Diaz-Santana, A., Kermani, P., Hempstead, B., Fischbach-Teschl, C., Lopez, J. A., & Stroock, A. D. (2012). In vitro microvessels for the study of angiogenesis and thrombosis. *Proc Natl Acad Sci U S A*, *109*(24), 9342-9347. https://doi.org/10.1073/pnas.1201240109

Zhu, W., Qu, X., Zhu, J., Ma, X., Patel, S., Liu, J., Wang, P., Lai, C. S., Gou, M., Xu, Y., Zhang, K., & Chen, S. (2017). Direct 3D bioprinting of prevascularized tissue constructs with complex microarchitecture. *Biomaterials*, *124*, 106-115. https://doi.org/10.1016/j.biomaterials.2017.01.042

Appendix: Chapter 2

Derivation for how the fluid level in the inlet reservoir changes with time, h(t), during hydrostatic pressure-driven perfusion in the 3D printed perfusion unit.

τ is shear stress, D is the vessel diameter, R is the total resistance in the fluidic circuit across which the pressure drop, ΔP, occurs. Q(t) is the flow rate through the vessel, μ is the fluid viscosity and L is the length of the vessel.

For Poiseuille flow in a cylindrical vessel

$$\Delta P = RQ(t) = \rho g h(t)$$

$$R = \frac{128\mu L}{\pi D^4}$$

$$\tau = \frac{D}{4}\frac{\Delta P}{L}$$

Substituting ΔP=RQ(t)

$$\tau = \frac{D}{4}\frac{\Delta P}{L} = \frac{DQ(t)}{4L}\frac{128\mu L}{\pi D^4} = \frac{32\mu Q(t)}{\pi D^3}$$

Perfusion through hydrostatic pressure will occur until there is no height difference between the fluid levels in the inlet and outlet reservoirs, $h(t)=h_{out}$. When h_{out} is kept constant, the volume in the inlet reservoir, V, changes with time

$$Q(t) = \frac{dV}{dt} = -\frac{\rho g h(t)}{R}$$

$$\frac{dh}{dt} = \frac{dV}{dt} \times \frac{dh}{dV}$$

Substituting V=Ah(t)

$$\frac{dV}{dt} = A\frac{dh}{dt}$$

$$\frac{dh}{dV} = \frac{1}{A}$$

$$\frac{dh}{dt} = -\frac{\rho g h(t)}{R} \times \frac{1}{A} = -\frac{\rho g h(t)}{RA}$$

$$\int \frac{1}{h} dh = -\int \frac{\rho g h(t)}{RA} dt$$

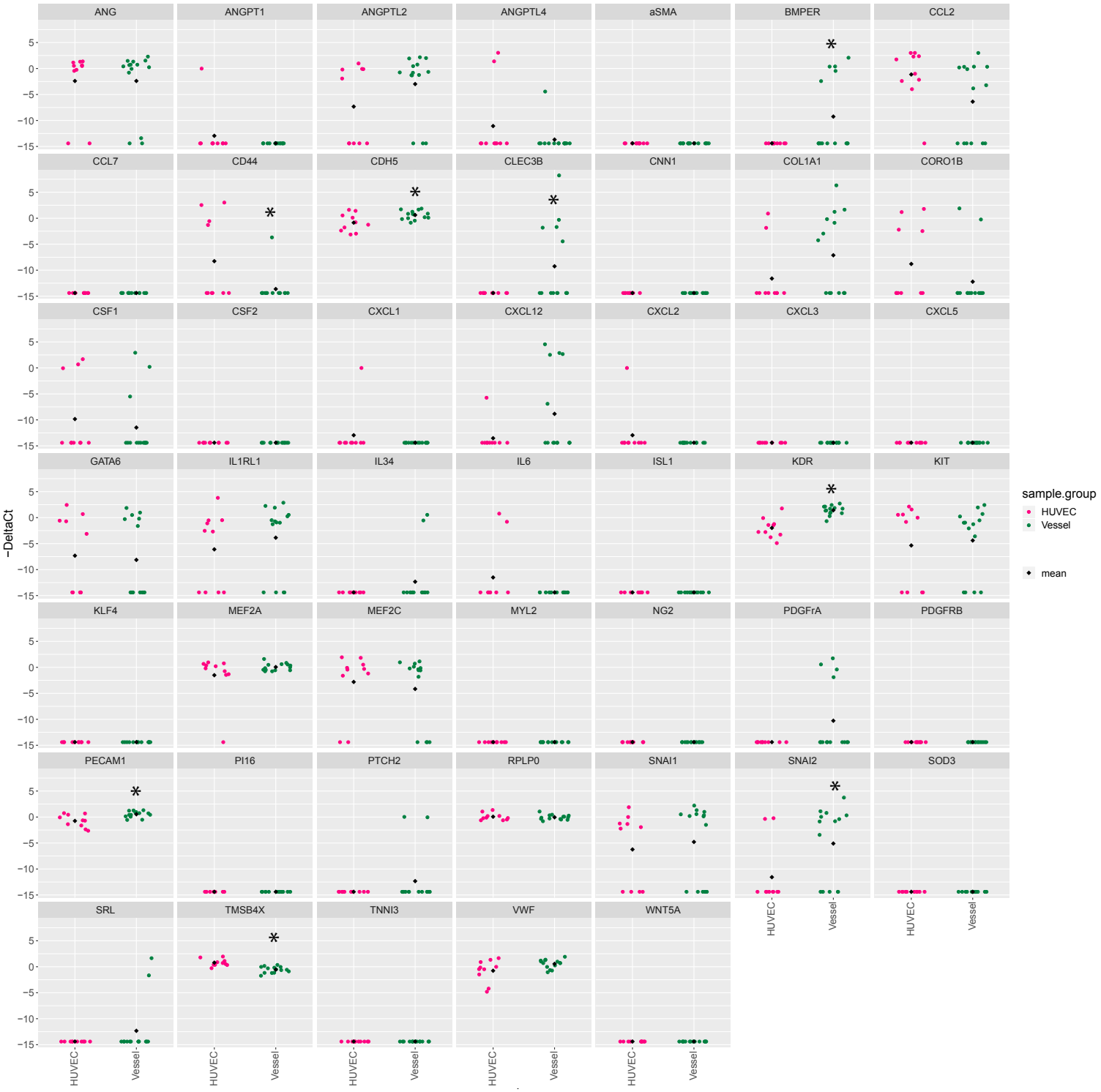
$$\ln(h) + C_1 = -\frac{\rho g h(t)}{RA} t$$

$$\mathrm{h(t)} = C_2 e^{-\frac{\rho g h(t)}{RA} t}$$

Boundary conditions: at t=0, $h(t)=h_0$ → $C_2=h_0$

$$\mathrm{h(t)} = h_0 e^{-\frac{\rho g h(t)}{RA} t}$$

Gene expression for the 48 genes studied using single-cell qPCR. The sample group “vessel” represents HUVEC cultured in the blood vessel-on-a-chip model and “HUVEC” represents HUVEC cultured in a 6-well tissue culture plate.



Appendix: Chapter 3

Dextran calibration data for characterising the relationship between intensity and concentration for different microscopy gains (Figure 3.4).

	Intensity values					
Dextran concentration	gain=550	gain=600	gain=650	gain=700	gain=800	gain=900
0	0	0	0.002	0.043	1.984	17.38
39	0	0.01	1.407	30.2	305.471	1069.621
78.125	0	0.358	23.292	154.69	765.787	2139.826
156.25	0.159	30.814	236.445	632.037	1950.388	3856.244
312.5	24.329	238.583	675.545	1421.95	3623.941	4094.789
625	235.553	664.09	1438.522	2662.26	4094.364	4095
1250	823.785	1703.878	3290.81	4094.805	4095	4095
2500	1917.528	3631.375	4095	4095	4095	4095

Data from Figure 3.13	Permeability (μm/s)		
	X=3/2 R_{vessel}	X=4/3 R_{vessel}	X=5/4 R_{vessel}
Day 3	0.093±0.004	0.063±0.003	0.046±0.002
Day 5	0.056±0.0006	0.035±0.0004	0.025±0.0003
Day 7	0.030±0.0002	0.019±0.0001	0.014±0.0002
Day 9	0.006±0.00009	0.004±0.00006	0.0025±0.00005

Data from Figure 3.16	Permeability (μm/s)		
	X=3/2 R_{vessel}	X=4/3 R_{vessel}	X=5/4 R_{vessel}
Day 3	0.17±0.02	0.12±0.02	0.10±0.02
Day 5	0.10±0.01	0.069±0.009	0.051±0.002
Day 7	0.048±0.008	0.033±0.007	0.026±0.005
Day 9	0.0095±0.002	0.0062±0.0007	0.0052±0.001

Data from Figure 3.17	**Day**	**Permeability**	**2 Std**
Vessel 1	3	0.0628	0.0026
Vessel 1	5	0.0325	4.40E-04
Vessel 1	7	0.0187	1.10E-04
Vessel 1	9	0.0036	6.20E-05
Vessel 2	3	0.0115	1.48E-04
Vessel 2	5	0.0084	9.59E-05
Vessel 3	3	0.0798	0.003
Vessel 3	4	0.0203	8.87E-04
Vessel 3	5	0.0053	7.23E-05
Vessel 4	6	0.067	0.0023
Vessel 4	7	0.0116	1.16E-04
Vessel 5	8	0.0032	6.51E-05
Vessel 6	5	0.0532	0.0027
Vessel 6	6	0.0245	2.46E-04

Vessel 6	7	0.0212	4.68E-04
Vessel 7	8	0.0101	2.40E-04
Vessel 7	7	0.009	1.42E-04
Vessel 7	6	0.0098	1.46E-04
Vessel 7	5	0.0263	6.49E-04
Vessel 7	4	0.0368	0.001
Vessel 7	3	0.0564	0.0024
Vessel 8	8	0.0062	1.24E-04
Vessel 8	6	0.025	4.50E-04
Vessel 9	3	0.0026	1.58E-04
Vessel 10	7	0.0061	1.44E-04
Vessel 11	4	0.0128	1.72E-04
Vessel12	4	0.0325	3.20E-04
Vessel 13	4	0.0288	8.10E-04
Vessel 14	4	0.022	2.78E-04

The derivation for obtaining the expression for calculating permeability using Method 3 (Equation 3.21) is shown below (R_0 in the derivation is referred to R_{vessel} in Chapter 3). *The full derivation and schematic were provided by my supervisor Joseph van Batenburg-Sherwood.*

Under the assumptions of infinite length and axisymmetry, the advection-diffusion equation reduces to

$$\frac{\partial C}{\partial t} = \frac{D}{r}\frac{\partial}{\partial r}\left(r\frac{\partial C}{\partial r}\right)$$

With boundary conditions

1) flux away from the vessel due to diffusion = flux through the vessel wall

$$-D\frac{\partial C(R,t)}{\partial r} = P_s\left(C_{in} - C(R)\right)$$

2) initial concentration at the wall equal to zero

$$C(R,0) = 0$$

3) concentration a long way away from the vessel being 0

$$C(r \to \infty) = 0$$

These equations have a highly complex analytical solution.
Instead of trying to fit to that, we break down the solution into simple components, which also allows a direct evaluation of the implicit assumptions that have been made in previous studies.

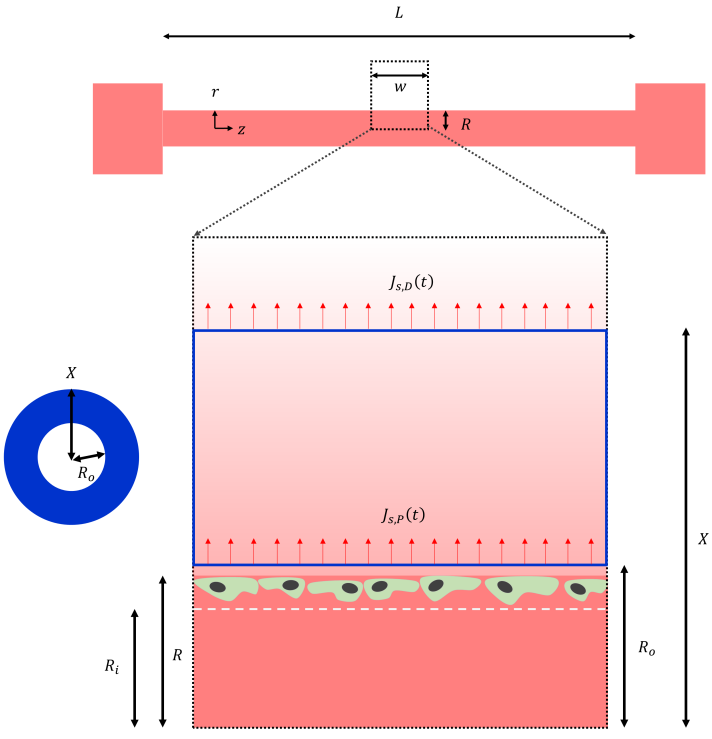


Figure 1: schematic of the whole vessel section and an imaging area, with mathematical terminology required for derivation and implementation

Permeability, $\boldsymbol{P_s}$

The solute flow rate J_s (mol/s) across the permeable layer lining the vessel at $r = R$ is given by

$$J_{s,P}(t) = P_s(\theta, z, t) S \Delta C(R, \theta, z, t) \quad (1)$$

- Assume equal hydrostatic and osmotic pressures on either side of the endothelium, hence no advective transport
- Assume P_s is not a function of space or time – but probe this in processing stage

$$J_{s,P}(t) = P_s(t) S \Delta C(R, t) \quad (2)$$

$\Delta C(R, t)$ is the transmural concentration difference

- Assume that the turnover of fluid in the vessel is sufficiently high, such that the internal concentration is a constant, $\overline{C_{in}}(t)$ – overbar indicates spatial averaging
- Assume that the concentration in the vessel is uniform, such that $C_{in}(R, t) = \overline{C_{in}}(t)$
- Assume the permeability of the collagen immediately next to the vessel wall is large compared to the permeability of the endothelium, such that P_S evaluated as follows is representative of P_S of the endothelium, and hence $C(R, t)$ can be replaced by $C(R_o, t)$. this is necessary because imaging immediately at R is not possible

$$\Delta C(R, t) = \overline{C_{in}}(t) - C(R_o, t) \quad (3)$$

S is a constant representing the surface area across which flux is occurring, with R_o and w the radius and length of the vessel section we are considering.

- Assume that vessel radius R_o is constant over the region w

$$S_o = 2\pi w R_o \quad (4)$$

Combining 2, 3 and 4, we have

$$J_{s,P}(t) = 2\pi w R_o P_s\big(C_{in}(t) - C(R_o, t)\big) \quad (5)$$

Diffusion

At $r = X$, solute diffuses out of the control volume due to the concentration gradient, following Fick's first law

$$J_{s,D}(t) = -D(\theta, z, t) S_X \frac{\partial C(X, t)}{\partial r} \quad (6)$$

where D is the diffusivity of the tracer in the collagen.

- Assume D is not a function of space or time – but probe this in processing stage

S is a constant representing the surface area across which flux is occurring. At the outer boundary of the control volume

$$S_X = 2\pi w X \quad (7)$$

Combining 6 and 7, we have

$$J_{s,D}(t) = -2\pi w X D \frac{\partial C(X, t)}{\partial r} \quad (8)$$

Reynold's Transport Theorem

If we define a region outside the vessel bounded by $r = R_o$ and $r = X$ (blue in Figure 1), then we can apply Reynold's transport theorem with extensive property B of number of moles, such that ρb is the concentration in mol/volume.

$$\frac{DN_{mol}}{Dt} = \frac{\partial}{\partial t}\int_{cv} C(r, t) dV + \oint_{cs} C(r, t)\vec{U}.\hat{n}\, dS \quad (9)$$

- Assume no reactions, hence N_{mol} for the system is constant
- Control volume does not change size
- Surface integral reduces to $J_{s,D}$ at $r = X$ and $J_{s,P}$ at $r = R_o$

Hence net solute flow rate across the control volume boundaries is given by

$$\oint_{cs} C(r, t)\vec{U}.\hat{n}\, dS = J_{s,D}(t) - J_{s,P}(t) \quad (10)$$

Letting $dV = 2\pi r w dr$, the total number of moles in the control volume region is given by

$$\int_{cv} C(r, t) dV = 2\pi w \int_{R_o}^{X} r C(r, t)\, dr \quad (11)$$

Equations 9, 10 and 11 yield

$$0 = 2\pi w \frac{\partial}{\partial t}\int_{R_o}^{X} r C(r, t)\, dr + J_{s,D}(t) - J_{s,P}(t) \quad (12)$$

Combining Equations 5, 8 and 12

$$P_s = \frac{1}{C_{in}(t) - C(R_o,t)} \frac{1}{R_o} \frac{\partial}{\partial t} \int_{R_o}^{X} rC(r,t)\, dr - \frac{X}{R_o} D \frac{\partial C(X,t)}{\partial r}$$

and dividing by $\overline{C_{in}}(t)$ such that $C^*(r,t) = C(r,t)/\overline{C_{in}}(t)$ yields the master equation

$$P_s = \frac{1}{1 - C^*(R_o,t)} \left(\frac{1}{R_o} \frac{\partial}{\partial t} \int_{R_o}^{X} rC^*(r,t)\, dr - \frac{X}{R_o} D \frac{\partial C^*(X,t)}{\partial r} \right) \quad (13)$$

Equation 13 fully describes a way to calculate the permeability at a given moment in time based on

- $P_s(t)$
  - The permeability of the endothelial cell layer and a small region of collagen that lies between R and R_o
- $C^*(R_o,t)$
  - Normalised concentration at a location close to the channel edge, but inside the gel at $r = R_o$.
- $\int_{R_o}^{X} rC^*(r,t)\, dr$
  - Total normalised number of moles in the control volume at time t
- D
  - The diffusivity of the solute in the collagen gel
- $\frac{\partial C^*(X,t)}{\partial r}$
  - The radial gradient of the normalised concentration evaluated at $r = X$.
  - Note that, if X is chosen such that $\frac{\partial C^*(X,t)}{\partial r} \approx 0$ then it would not be necessary to know the value of D. However, the ability to do this is limited by the restricted detection ability of the fluorescence imaging.

Appendix: Chapter 4

The below tables contain data from the figures in Chapter 4 and are colour coded based on blood donors.

Data from Fig. 4.11 (A)	Treatment	norm. Platelet adhesion
Vessel 1	Control	0.38
Vessel 2	TNF	1.59
Vessel 3	Control	0.11
Vessel 4	TNF	3.33
Vessel 5	Control	0.92
Vessel 6	TNF	3.21
Vessel 7	TNF	3.97
Vessel 8	TNF	3.7
Vessel 9	Control	0.32
Vessel 10	Control	0.3
Vessel 11	TNF	3.57
Vessel 12	TNF	2.44
Vessel 13	Control	0.35
Vessel 14	Control	0.07
Vessel 15	TNF	1.8
Vessel 16	TNF	2.95

Data from Fig. 4.11 (B)	Treatment	norm. Platelet adhesion (fold change)
Vessel 1	Control	1
Vessel 2	TNF	4.2
Vessel 3	Control	1
Vessel 4	TNF	31.5
Vessel 5	Control	1
Vessel 6	TNF	3.5
Vessel 7	TNF	4.3
Vessel 8	TNF	4
Vessel 9	Control	1
Vessel 10	Control	1
Vessel 11	TNF	11.6
Vessel 12	TNF	7.9
Vessel 13	Control	1.7
Vessel 14	Control	0.7
Vessel 15	TNF	8.6
Vessel 16	TNF	14

Data from Fig. 4.11 (C)	Treatment	norm. Platelet adhesion
Experiment 1	Control	0.38
Experiment 1	TNF	1.59
Experiment 2	Control	0.11
Experiment 2	TNF	3.33
Experiment 3	Control	0.92
Experiment 3	TNF	3.63
Experiment 4	Control	0.31
Experiment 4	TNF	3.01

Experiment 5	Control	0.21
Experiment 5	TNF	2.37

Data from Fig. 4.11 (D)	Treatment	norm. Fibrinogen deposition
Vessel 1	Control	0
Vessel 2	TNF	6.11
Vessel 3	Control	0
Vessel 4	TNF	3.21
Vessel 5	Control	0.35
Vessel 6	TNF	9.87
Vessel 7	TNF	7.65
Vessel 8	TNF	4.78
Vessel 9	Control	0.01
Vessel 10	Control	0
Vessel 11	TNF	2.86
Vessel 12	TNF	5.39
Vessel 13	Control	0.02
Vessel 14	Control	0
Vessel 15	TNF	3.15
Vessel 16	TNF	6.96

Data from Fig. 4.11 (E)	Treatment	norm. Fibrinogen deposition
Experiment 1	Control	0
Experiment 1	TNF	6.11
Experiment 2	Control	0
Experiment 2	TNF	3.21
Experiment 3	Control	0.92
Experiment 3	TNF	7.43
Experiment 4	Control	0
Experiment 4	TNF	4.12
Experiment 5	Control	0.01
Experiment 5	TNF	5.05

Data from Fig. 4.13 (A)	Treatment	norm. Platelet adhesion
Vessel 1	Control	0.38
Vessel 2	TNF	1.59
Vessel 3	Anti-TF	0.41
Vessel 4	Control	0.11
Vessel 5	TNF	3.33
Vessel 6	Control	0.92
Vessel 7	TNF	3.21
Vessel 8	TNF	3.97
Vessel 9	TNF	3.7
Vessel 10	Anti-TF	0.8
Vessel 11	Control	0.32
Vessel 12	Control	0.3
Vessel 13	TNF	3.57
Vessel 14	TNF	2.44
Vessel 15	Anti-TF	0.17
Vessel 16	Control	0.35

Vessel 17	Control	0.07
Vessel 18	TNF	1.8
Vessel 19	TNF	2.95
Vessel 20	IgG control	2.28

Data from Fig. 4.13 (B)	Treatment	norm. Platelet adhesion (fold change)
Vessel 1	Control	1
Vessel 2	TNF	4.2
Vessel 3	Anti-TF	1.1
Vessel 4	Control	1
Vessel 5	TNF	31.5
Vessel 6	Control	1
Vessel 7	TNF	3.5
Vessel 8	TNF	4.3
Vessel 9	TNF	4
Vessel 10	Anti-TF	0.9
Vessel 11	Control	1
Vessel 12	Control	1
Vessel 13	TNF	11.6
Vessel 14	TNF	7.9
Vessel 15	Anti-TF	0.6
Vessel 16	Control	1.7
Vessel 17	Control	0.7
Vessel 18	TNF	8.6
Vessel 19	TNF	14
Vessel 20	IgG control	10.9

Data from Fig. 4.13 (D)	Treatment	norm. Platelet adhesion
Experiment 1	Control	0.38
Experiment 1	TNF	1.59
Experiment 1	Anti-TF	0.41
Experiment 2	Control	0.11
Experiment 2	TNF	3.33
Experiment 3	Control	0.92
Experiment 3	TNF	3.63
Experiment 3	Anti-TF	0.8
Experiment 4	Control	0.31
Experiment 4	TNF	3.01
Experiment 4	Anti-TF	0.17
Experiment 5	Control	0.21
Experiment 5	TNF	2.37
Experiment 5	IgG control	2.28

Data from Fig. 4.13 (C)	Treatment	norm. Fibrinogen deposition
Vessel 1	Control	0
Vessel 2	TNF	6.11
Vessel 3	Anti-TF	0
Vessel 4	Control	0
Vessel 5	TNF	3.21

Vessel 6	Control	0.35
Vessel 7	TNF	9.87
Vessel 8	TNF	7.65
Vessel 9	TNF	4.78
Vessel 10	Anti-TF	0.22
Vessel 11	Control	0.01
Vessel 12	Control	0
Vessel 13	TNF	2.86
Vessel 14	TNF	5.39
Vessel 15	Anti-TF	0.14
Vessel 16	Control	0.02
Vessel 17	Control	0
Vessel 18	TNF	3.15
Vessel 19	TNF	6.96
Vessel 20	IgG control	2.48

Data from Fig. 4.13 (E)	**Treatment**	**norm. Fibrinogen deposition**
Experiment 1	Control	0
Experiment 1	TNF	6.11
Experiment 1	Anti-TF	0
Experiment 2	Control	0
Experiment 2	TNF	3.21
Experiment 3	Control	0.92
Experiment 3	TNF	7.43
Experiment 3	Anti-TF	0.22
Experiment 4	Control	0
Experiment 4	TNF	4.12
Experiment 4	Anti-TF	0.14
Experiment 5	Control	0.01
Experiment 5	TNF	5.05
Experiment 5	IgG control	2.48

Data from Fig. 4.15 (A)	**Treatment**	**norm. Platelet adhesion**
Vessel 1	TNF	1.8
Vessel 2	TNF	2.95
Vessel 3	25 ATU	2.05
Vessel 4	250 ATU	0.67
Vessel 5	500 ATU	0.08
Vessel 6	1000 ATU	0.01
Vessel 7	Control	0.35
Vessel 8	Control	0.07

Data from Fig. 4.15 (B)	**Treatment**	**norm. Platelet adhesion (fold change)**
Vessel 1	TNF	8.6
Vessel 2	TNF	14
Vessel 3	25 ATU	9.8
Vessel 4	250 ATU	3.2
Vessel 5	500 ATU	0.4
Vessel 6	1000 ATU	0

Vessel 7	Control	1.7
Vessel 8	Control	0.7

Data from Fig. 4.15 (C)	Treatment	norm. Fibrinogen deposition
Vessel 1	TNF	3.15
Vessel 2	TNF	6.96
Vessel 3	25 ATU	1.91
Vessel 4	250 ATU	0.39
Vessel 5	500 ATU	0.16
Vessel 6	1000 ATU	0
Vessel 7	Control	0.02
Vessel 8	Control	0

Data from Fig. 4.19 (A)	Treatment	norm. Platelet adhesion
Vessel 1	Control	0.26
Vessel 2	TNF	3.66
Vessel 3	Control	0.86
Vessel 4	Control	0.81
Vessel 5	TNF	3.09
Vessel 6	TNF	2.73
Vessel 7	Control	0.43
Vessel 8	Control	0.27
Vessel 9	TNF	2.62
Vessel 10	TNF	2.18
Vessel 11	Control	0.8
Vessel 12	TNF	2.41

Data from Fig. 4.19 (B)	Treatment	norm. Platelet adhesion (fold change)
Vessel 1	Control	1
Vessel 2	TNF	13.9
Vessel 3	Control	1
Vessel 4	Control	1
Vessel 5	TNF	3.7
Vessel 6	TNF	3.3
Vessel 7	Control	1.2
Vessel 8	Control	0.8
Vessel 9	TNF	7.5
Vessel 10	TNF	6.2
Vessel 11	Control	1
Vessel 12	TNF	3

Data from Fig. 4.19 (C)	Treatment	norm. Fibrinogen deposition
Vessel 1	Control	0.08
Vessel 2	TNF	5.29
Vessel 3	Control	0
Vessel 4	Control	0.05
Vessel 5	TNF	6.97
Vessel 6	TNF	4.07
Vessel 7	Control	0

Vessel 8	Control	0
Vessel 9	TNF	0.68
Vessel 10	TNF	1.6
Vessel 11	Control	0.16
Vessel 12	TNF	5.52

Data from Fig. 4.19 (D)	Treatment	norm. Platelet adhesion
Experiment 1	Control	0.26
Experiment 1	TNF	3.66
Experiment 2	Control	0.83
Experiment 2	TNF	2.91
Experiment 3	Control	0.35
Experiment 3	TNF	2.4
Experiment 4	Control	0.8
Experiment 4	TNF	2.41

Data from Fig. 4.19 (E)	Treatment	norm. Fibrinogen deposition
Experiment 1	Control	0.08
Experiment 1	TNF	5.29
Experiment 2	Control	0.025
Experiment 2	TNF	5.52
Experiment 3	Control	0
Experiment 3	TNF	1.14
Experiment 4	Control	0.16
Experiment 4	TNF	5.52

Appendix: Permission Documents

Schematics obtained from smart.servier.com are licensed under a Creative Commons Attributions 3.0 Unported License, where no permission is required for use.

Permission from Springer Nature Customer Service Centre GmbH: Springer Nature, Nature Reviews Molecular Cell Biology (Vascular heterogeneity and specialization in development and disease, Potente and Mäkinen), Copyright (2017) is shown on page 215.

Permission from SAGE Publications is shown on page 216.

SPRINGER NATURE LICENSE
TERMS AND CONDITIONS

Nov 27, 2021

This Agreement between Josefin Jansson-Edqvist ("You") and Springer Nature ("Springer Nature") consists of your license details and the terms and conditions provided by Springer Nature and Copyright Clearance Center.

License Number	5113760632934
License date	Jul 21, 2021
Licensed Content Publisher	Springer Nature
Licensed Content Publication	Nature Reviews Molecular Cell Biology
Licensed Content Title	Vascular heterogeneity and specialization in development and disease
Licensed Content Author	Michael Potente et al
Licensed Content Date	May 24, 2017
Type of Use	Thesis/Dissertation
Requestor type	academic/university or research institute
Format	electronic
Portion	figures/tables/illustrations
Number of figures/tables/illustrations	1
High-res required	no
Will you be translating?	no
Circulation/distribution	1 - 29
Author of this Springer Nature content	no
Title	Developing a 3D blood vessel-on-a-chip microfluidic in vitro model to study thrombosis in a controlled microenvironment
Institution name	Imperial College London
Expected presentation date	Aug 2021
Portions	Figure 1
Requestor Location	Josefin Jansson-Edqvist Krageholmsgatan 12 Malmo, 21619 Sweden Attn: Josefin Jansson-Edqvist
Total	0.00 GBP

Theories of Blood Coagulation

Author: James P. Riddel, Bradley E. Aouizerat, Christine Miaskowski, et al
Publication: Journal of Pediatric Oncology Nursing
Publisher: SAGE Publications
Date: 05/01/2007

Copyright © 2007, © SAGE Publications

Gratis Reuse

Permission is granted at no cost for use of content in a Master's Thesis and/or Doctoral Dissertation, subject to the following limitations. You may use a single excerpt or up to 3 figures tables. If you use more than those limits, or intend to distribute or sell your Master's Thesis/Doctoral Dissertation to the general public through print or website publication, please return to the previous page and select 'Republish in a Book/Journal' or 'Post on intranet/password-protected website' to complete your request.

BACK CLOSE WINDOW